Interactions of molybdenum and vanadium with iron nanoparticles

Loredana Brinza

Submitted in accordance with the requirements for the degree of Doctor of Philosophy.

The University of Leeds

School of Earth and Environment

June 2010

The candidate confirms that the work submitted is his own and that appropriate credit has been given where reference has been made to the work of others.

This thesis was carried out as a part of the

Bio-transformations of trace elements in aquatic systems

project.

The BIOTRACS Early-Stage Training (EST) Fellowships have been funded by the European Community under the Sixth Framework (FP6), Marie Curie Actions, contract number MEST-CT-2004-514262.

To Liane, Teodora and my family,

Declaration

Part of Chapter 4 is published in Mineralogical Magazine as:
Loredana Brinza, Liane G. Benning, Peter J. Statham, (2008), *Adsorption studies of Mo and V onto ferrihydrite*, ***Mineralogical Magazine***, Vol. 72(1), 107–110

The idea of quantifying the adsorption of molybdenum and vanadium onto ferrihydrite varying different parameters belongs to Loredana Brinza. The experiments were carried out partially at University of Leeds under the supervision of Prof. Liane G. Benning and partially at National Oceanography Center, Southampton under the supervision of Prof. Peter J. Statham (external supervisor). Data processing was done by Loredana Brinza and also their interpretation with valuable suggestions from both co-authors. Considerable acknowledgements are addressed to Dr. Juan Diego Rodriguez Blanco for his help in modeling adsorption kinetics.

Chapter 5 represents a manuscript in preparation for a journal like Environmental Science and Technology.
Loredana Brinza, and Liane G. Benning, (2010), *The fate of Mo and V and the speciation of Mo during ferrihydrite transformation to hematite*

The results from this manuscript were obtained by Loredana Brinza from her experiments based in the laboratory at Leeds and samples analyses at SRS Daresbury Laboratory, UK. Prof. Liane G. Benning wrote the XAS proposal for the molybdenum analyses in solid phases and help with the data acquisition. Data processing and interpretation was done by Loredana Brinza. The help of Prof. Liane G. Benning, Dr. Hong Phuc Vu and Dr. Samuel Shaw with the XAS data interpretation is acknowledged.

Chapter 6 reproduces a manuscript ready for submission to Crystal Growth and Design.
Loredana Brinza, Hong Phuc Vu, Samuel Shaw, Liane G. Benning, (2010), *The effect of molybdenum and vanadium on the crystallization of hematite from ferrihydrite at neutral pH,* **Crystal Growth & Design**

The original idea belongs to Prof. Liane G. Benning. She wrote the proposal for the synchrotron experiments. The first author carried out preliminary laboratory experiments and the Synchrotron based experiments at SRS Daresbury Laboratory, UK. Data processing as well as their interpretation was done by Loredana Brinza with helpful input of Prof. Liane G. Benning, Dr. Hong Phuc Vu and Dr. Samuel Shaw.

Acknowledgments

A PhD degree is a big achievement in everyone's life. It is a time full of up and down moments as life itself is. Although it is probably more intense, because the work is directed towards self satisfaction and because of the hard work we are responsible for but also because of the big reward from the end of the tunnel. For some of us it is also just a beginning of a career with high expectations for what is called science.

I started this experience back in 2005 with the believe that I can do it. Indeed, I had no doubt in any moment, I persevered in difficult moments although they never seemed to be more than small challenges (what I think science is all about – challenges!!). They were more at the beginning until I settled myself in/with this project and overcome the cultural differences of the international group I integrated in. After 6-7 months I started first experiments. I remember pleasantly how enthusiastic I was seeing that my ideas had positive outputs (e.g., potentiometric titration and first adsorption studies results). Slowly with time I found myself in a big world full of ideas for personal and professional development. From managing those ideas and planning their achievements and assimilation to actually have them applied and see the results was in fact the essence of this PhD experience. Personally, I think that it was not very easy to put the boundary of this project and to know what enough for this thesis is and when to stop. I finished my experimental work within two years and an half. Then, I started writing up when I found myself a bit tired, thus, I took few weeks holiday. During this time happened to catch up with my private life. Here I offered a part of my time to Dan. Shortly after that I carried out another "small" project, called – Teo. After few months happier and even more motivated, I was back to continue writing up.

However, this section is dedicated to all those people I interacted with during my PhD and who left with me a nice memory, a professional collaboration or a nice friendship.

Thus I will start with Prof. Liane G. Benning. Liane is the person who inspired my research conduit and who I will always admire for her enthusiasm, dedication to and commitment she made with science. She opened for me the vision of freedom of mind which science implies. I am very grateful to her for offering me the opportunity of heaving this international experience and tireless, guiding me throughout it. I thanks her for all those restless moments spent together at the SRS Daresbury Laboratory during my experiments, but also for all scientific chats we had and which motivated me even more in what I did. In addition, I appreciate her effort in training me how to use numerous analytical techniques which added a set of important skills for my professional development.

Professor Peter J. Statham is thanked for his supervision and useful support in the work I carried out at National Oceanography Centre, Southampton, as well as for directing the program which funded and made possible my research.

I shared valuable professional experiences with Dr Hong Phuc Vu, to whom I thank very much for exchanging his analytical and IT skills with me and for day and night hours we spent doing our experiments in Liane's labs at the University of Leeds and at the SRS Daresbury Laboratory, UK. His is a great team mate I had the opportunity to work with and hope we will keep a nice friendship.

I send my deepest considerations and best thoughts to my dearest Greek friend, Dr. Alexandra Xylouri who supported me in my personal life and cheered me up in everything I was doing research wise and also in our free time. Thank you very much, Alex – I am very happy to have met you.

Many thanks to: Dr. Samuel Shaw (for useful advices and interesting points of view on few of my results and also for his support during my experiments at Station 16.4, from the SRS Daresbury Laboratory); Dr. Dominique Tobler (although we did not interact as much I would have liked, I am very glad to have you as my Swiss friend); Dr. Juan Diego, Rodriguez Blanco (for your help in use of modeling software, nice chats and jokes – some of which took me some time to understand), Dr. Steve Bonneville (for your useful and interesting collaboration and for being so French); Ellen Avery (for sharing the office and Liane's labs with me for 4 years and with whom I should have spent more time); Adriana Matamoros – Velosa (for the little but meaningful time we spent together); Aryani Sumoondur (for sharing with me her interesting views, friendly moments and our room during "La Palma" Winter School); Gabriella Kakonyi (for her kind friendship), Cristina Moisescu (for nice experience sharing the same house), Dr. Zongbo Shi, Hellen Cope (for her support in delicate moments), Verity Payne, Pieter Bots, Dr. Lois Davidson, Dr. Jeny Rivas and Dr. Stefan Hunger for making my stay in Leeds so colorful and pleasant.

Dave Hatfield, Dr. Andy Brown, Dr. Eric Condliffe, Dr. Mike Ward, Dr. Dave Banks, Linda Forbes and Lesley Neve at the University of Leeds, Dr. Daryl Green at the National Oceanography Centre, Dr. Gary Fones at the University of Portsmouth; David J. Taylor and Dr. Andy Bennet at the SRS Daresbury Laboratory are acknowledged for helping me with the use of different techniques and probably others that I am forgetting.

Special thanks to my family (my sister - Otilia, mum and dad) - for their spiritual support; to Dan - for his monthly trips up to Leeds to see me and overcome the space barrier of our long relationship, his help in delicate moments, his hope that one day I will finish and I will have a less busy mind and lifestyle and to Dita - a lovely happy person, with a strong character. Finally to Teodora, who does not know yet, but she filled my life!

Abstract

Molybdenum, vanadium and iron are important micro and macro nutrients, respectively, for all living organisms. Their cycles and budgets in the natural environment is affected by - and affects many different processes.

Poorly ordered ferrihydrite nanoparticles characterised for their particle size (3-5nm), crystallinity, surface area (~200m^2g^{-1}) and surface charge (point of zero charge = 7.96) helped to understand better their adsorption and co-precipitation interactions mechanisms with molybdenum and vanadium.

Comparative studies of molybdenum and vanadium adsorbed onto or co-precipitated with ferrihydrite as well as the influence of different conditions such us pH, metal concentration, particles concentration and matrix composition were carried out. The obtained kinetic parameters were modelled with various geochemical software packages to evaluate their behavior.

Metastability of ferrihydrite under hydrothermal conditions was the second big theme of this thesis. The crystallisation kinetic (transformation rates) and thermodynamics (activation energies) of the hematite formation were assessd with in situ synchrotron-based difraction tehnique in the presence and the absence of molybdenum and vanadium under conditions mimicing the geochemistry of deep sea hydrothermal systems (ionic strength = 0.7, pH = 8). The data showed that hematite crystallization (from ferrihydrite) followed a temperature dependent trends and that the transformation requires an apparent activation energy of 26 $kJmol^{-1}$. The presence of molybdenum and vanadium delayed the transformation reaction by 32% and 38% respectively.

The transformation also leads to the sequestration of more than 90% of the initial ferrihydrite associated molybdenum and vanadium in the hematite structure, making it thus non-bioavailable for further reaction.

Finally, synchrotron-based X-ray Absorption Spectroscopy revealed that the initial molybdate speciation in the starting ferrihydrite changes bonding and coordination in the end-product hematite and molybdenum replaced iron in the hematite structure further supporting the fact that molybdenum is immobilized in the hematite structure.

List of contents

List of figures

List of tables

List of equations

EQ NO.	FORMULA	DESCRIPTION
Eq. 2.1.	$\alpha = 1 - e^{(-kt)^m}$	The Avrami-Erofe'ev equation
Eq. 2.2.	$\alpha = 1 - e^{-k(t-t_0)^m}$	The Johnson-Mehl-Avrami-Kolmogorov
Eq. 2.3.	$k = A \cdot e^{-E_a/RT}$	The Arrhenius equation
Eq. 2.4.	$E_a = -\ln k + \ln A/RT$	The Arrhenius equation rearranged
Eq. 2.5.	$\ln t^*_\alpha = const. - \ln A + (E_a/R)(1/T)$	"The time to a given fraction" equation
Eq. 2.6.	$\frac{dq}{dt} = k_{1,ads}(q_e - q)$	The Lagergren model – pseudo first order adsorption kinetic model
Eq. 2.7.	$\frac{dq}{dt} = k_{2,ads}(q_e - q)^2$	The pseudo-second order adsorption kinetic model
Eq. 2.8.	$q = \frac{V \cdot (C_i - C_f)}{S_a}$	Equation of mass balance of metal concentration in solution
Eq. 2.9.	$q = \frac{(C_{ia} - C_{fa})}{S} \cdot V_a$	Equation of mass balance of metal concentration in the adsorbent (after total digestion)
Eq. 2.10.	$q_e = \frac{q_{\max} \cdot b \cdot C_e}{1 + b \cdot C_e}$	The Langmuir isotherm
Eq. 2.11	$q_e = K_F \cdot C_e^{1/n}$	The Freundlich isotherm
Eq. 3.1	$d = \frac{\lambda L}{r}$	Equation for the *d*-spacing calculation from the SAED patterns
Eq. 3.2	$d(H) = \frac{kT}{3\pi\eta D}$	The Stokes Einstein equation
Eq. 3.3	$q^c = \frac{C^c}{S^c} \cdot V^c{}_d$	Equation of mass balance of metal concentration in the co precipitated samples (after total digestion)
Eq. 3.4.	$q_e = \frac{q_{\max} \cdot b \cdot C_e}{1 + b \cdot C_e}$	The Langmuir isotherm
Eq. 3.5.	$\frac{C_e}{q_e} = \frac{1}{q_{\max} b} + \frac{1}{q_{\max}} \cdot C_e$	Liniarized Langmuir isotherm

EQ NO.	FORMULA	DESCRIPTION
Eq. 3.6.	$q = \frac{V \cdot (C_i - C_t)}{S_a}$	Equation of mass balance of metal concentration in solution
Eq. 3.7.	$E = \frac{C_i - C_t}{C_i - C_f} \cdot 100$	Metal removal efficiency (%)
Eq. 3.8.	$\frac{dq_t}{dt} = k \cdot (q - q_e)$	The Lagergren model – pseudo first order adsorption kinetic model
Eq. 3.9.	$\frac{dq_t}{dt} = k \cdot (q - q_e)^2$	The pseudo-second order adsorption kinetic model
Eq. 3.10.	$q_e = K_F \cdot C_e^{1/n}$	The Freundlich isotherm
Eq. 3.11.	$\log q_e = \log K_F + \frac{1}{n} \log C_e$	Linearized Freundlich equation
Eq. 3.12.	$K_d = \frac{q_e}{C_e}$	The distribution coefficient equation
Eq. 3.13.	$\lambda = 2\, d_{hkl} \sin\theta$	The Bragg's Law
Eq. 3.14.	$E = hc/\lambda$	The Planck-Einstein equation
Eq. 3.15.	$E\, d_{hkl} \sin\theta = (hc/\lambda) \times (\lambda/2) = hc/2 = 6.19926$	Combination of Eq. 3.14. and Eq.3.15.
Eq. 3.16.	$E = 6.19926 / (d_{hkl} \sin\theta)$	Rearrangement of Eq. 3.15.
Eq. 3.17.	*E(keV) = [Channel Number]* b + a*	Equation used to calibrate ED-XRD detector.
Eq. 3.18.	$\alpha = (A_t - A_{min})/(A_{max} - A_{min})$	Equation used for empirical normalization of XRD peak areas to the degree of reaction
Eq. 3.19.	$\alpha = 1 - e^{-k(t-t_0)^n}$	The Johnson-Mehl-Avrami-Kolmogorov model
Eq. 3.20.	$k = A \cdot e^{-E_a / RT}$	The Arrhenius equation
Eq. 3.21.	$\ln k = \ln A_{(cryst.)} - \frac{E_{a(cryst.)}}{RT}$	Logarithmic form of the Arrhenius equation in terms of rate constant
Eq. 3.22.	$\ln t_0 = \ln A_{(nuc.)} - \frac{E_{a(nuc.)}}{RT}$	Logarithmic form of the Arrhenius equation in terms of induction time
Eq. 3.23.	$\ln t_\alpha = const. - \ln A + (E_a/R)(1/T)$	"The time to a given fraction" equation
Eq. 3.24.	$I = I_0 \cdot e^{-\mu x}$	The Beer's law

EQ NO.	FORMULA	DESCRIPTION
Eq. 3.25.	$\mu(E) \propto I / I_0$	The Beer's law – used for adsorption coefficient calculation in fluorescence mode
Eq. 3.26.	$q_r = \frac{V \cdot (C_f - C_i)}{S_r}$	The mass balance equation used for uptake capacity calculation of the resin in column adsorption studies
Eq. 4.1.	$q = \frac{V \cdot (C_i - C_e)}{S_a}$	Equation of mass balance of metal concentration in solution
Eq. 4.2.	$E = \frac{(C_i - C_e)}{C_i} \cdot 100$	Metal removal efficiency (%)
Eq. 4.3.	$\frac{dq_t}{dt} = k \cdot (q - q_e)^2$	The pseudo-second order adsorption kinetic model
Eq. 6.1.	$\alpha = (A_t - A_{min})/(A_{max} - A_{min})$	Equation used for empirical normalization of XRD peak areas to the degree of reaction
Eq. 6.2.	$\alpha = 1 - e^{-k(t-t_0)^n}$	The Johnson-Mehl-Avrami-Kolmogorov
Eq. 6.3.	$k = A \cdot e^{-E_a / RT}$	The Arrhenius equation
Eq. 6.4.	$E_a = -RT \ln (t^*_\alpha / A)$	The activation energy expressed in terms of "The time to a given fraction" equation
Eq. 6.5.	$Ea_{(HM)} = 14.6\ pH - 84.39$	Equation obtained from our data interpretation describing the E_a *vs.* pH dependence of HM formation
Eq. 6.6.	$E_{a(GT)} = -9.06pH + 157.87$	Equation obtained from our data interpretation describing the Ea *vs.* pH dependence of HM formation
Eq. 7.1.	$q_r = \frac{V \cdot (C_f - C_i)}{S_r}$	The mass balance equation used for uptake capacity calculation of the resin in column adsorption studies

Nomenclature

λ = wavelengths, Å;

2-θ = 2-theta

A = the frequency or pre-exponential factor in Arrhenius equation,

A_t = is the XRD peak area at time t,

A_{min} and A_{max} = the minimum and maximum peak area values of the specific XRD peak

b = the Langmuir equilibrium constant which is related to the affinity of the binding sites;

C = metal concentration in complete digested sample, mg L^{-1};

C_i = initial metal concentration in solution, mg L^{-1};

C_t = metal concentration in solution at time t, mg L^{-1};

d = *d*-spacing, Å;

D = translational diffusion coefficient;

d(H) = the hydrodynamic diameter;

*E*a = the activation energy, $kJmol^{-1}$,

I_0 = intensity of the incident beam which passes through the sample in the XAS setting;

I = intensity of the scatered beam which passed through the sample in the XAS setting

k = the Boltzmann's constant;

K = the Langmuir rate constant of adsorption, g $mmol^{-1}min^{-1}$;

k = the rate constant for the transformation reaction, s^{-1};

K_F = the Freundlich rate constant of adsorption, g $mmol^{-1}min^{-1}$;

m = variable that depends on the nucleation rate;

n = adsorption intensity;

q = metal uptake capacities;

q_{max} = the maximum amount of metal ion per unit mass of the ferrihydrite, mg g^{-1} ;

R = the gas constant (8.31451 J mol^{-1} K^{-1});

r = the radius of circles, mm;

S = dry weight of co precipitated sample digested, g;

S_a = dry weight of ferrihydrite per adsorption batch, g;

T = the absolute temperature in Kelvin (K).

t = time, s;

t_0 = the induction time, s;

t^*_α = time to a given fraction, sec;

V = solution volume, mL;

V_d = the acid volume used for sample digestion, L;

η = viscosity;

Prefixes

n – nano, 10^{-9} m

μ – micro, 10^{-6} m

m – milli, 10^{-3} m

Abbreviations

Å - Angstrom
BET - Brunauer, Emmett and Teller;
DLM - Diffuse Layer Model
DLS - Dynamic Light Scattering;
EDL - Electric Double Layer
EDX - Energy Dispersive X-Ray;
ED-XRD - Energy Dispersed X-Ray Diffraction;
EXAFS - Extended X- Ray Fine-Structure Spectroscopy.
FAAS- Flame Atomic Adsorption Spectrometer;
FEG-SEM - Field Emission Gun-Scanning Electron Microscopy;
FEG-TEM - Field Emission Gun-Transmission Electron Microscopy;
FHY – Ferrihydrite;
GIF - Gatan Imaging Filter;
GR - Green rust
GT- Goethite;
HM – Hematite;
ICP AES - Inductively Coupled Plasma Atomic Emission Spectrometer;
ICP MS - Inductively Coupled Plasma Mass Spectrometer;
IS - Ionic Strength;
MCA - Multi-Channel Analyzer;
MT - Magnetite
NOC - National Oceanography Centre;
SAED - Selected Area Electron Diffraction;
SRS – Synchroton Radiation Source;
SW – Schwertmanite;
TDS - Total Dissolved Solid;
TLM - Triple Layer Model;
XAFSS - X-Ray Adsorption Fine Structure Spectroscopy;
XANES - X-ray Adsorption Near Edge Spectroscopy
XRD – X-Ray Powder diffractometer;

Chapter 1
Introduction

1.1. Background

Chapter 1 summarizes the aims and objectives of this thesis and describes the motivation for this study. It also introduces the main research settings, experimental techniques and modeling packages used in answering the research questions. The chapter ends with an outline of the thesis.

Ferrihydrite (FHY) is a well known amorphous iron oxyhydroxide which forms in different environments under neutral conditions *(i.e.,* deep sea hydrothermal systems, soils, sediments, *etc.*). One of the most important characteristics of ferrihydrite is its high affinity to adsorb different cations and anions.

Although the interactions between ferrihydrite and a whole plethora of anions and cations has been studied for many years, the interactions between molybdenum (as molybdate) and vanadium (as vanadate) and ferrihydrite has so far been less studied and thus this thesis will focus on these interactions.

In deep-ocean hydrothermal plumes molybdenum and vanadium are known to be readily scavenged by freshly formed iron oxyhydroxides nanoparticles (*i.e.,* ferrihydrite) forming during the oxidation of hydrothermal vent fluids via mixing with seawater. These scavenging processes have important implications for the cycling and budget of molybdenum and vanadium in the ocean, yet, no quantitative information about the mechanisms that govern the interaction between ferrihydrite and molybdenum or vanadium are available. Thus, part of this thesis focused on processes that mimicked seawater reactions.

Molybdenum (Mo) and vanadium (V) are important micronutrients for all living organisms and a shortage of these elements may lead to functional enzymatic disequilibria. Molybdenum and vanadium cycling in the environment are controlled by adsorption, co-precipitation, ion exchange or complexation onto/with various bio-and geo-sorbents. Their sequestration and build up in sediments leads to the formation of concentration gradients across the sediment-water interface and therefore strongly influences the cycling of molybdenum and vanadium. However, neither the uptake mechanisms nor their partitioning and fate in the water - or sediment columns in ocean or other aquatic settings have ever been quantified. Adsorption and co-precipitation

quantification and characterisation of the kinetic of these reactions forms the first main part of this thesis.

Another important characteristic of the ferrihydrite is its metastability. Depending on environmental conditions, ferrihydrite transforms to more crystaline iron phases such: as goethite (GT), hematite (HM), schwertmanite (SW), magnetite (MT), green rust (GR), etc. The ferrihydrite transformation to hematite at neutral and oxic conditions made the second big topic of this thesis. The kinetics, thermodynamics and mechanisms of the ferrihydrite to goethite (GT)/ hematite (HM) transformation in the presence of coprecipitated anions (molybdate and vanadate), as well as the fate of the metals during this process were assessed using conventional as well as synchrotron-based techniques.

1.2. Aims and objectives

This thesis is focused onto two main research aims.

The first aim of the thesis was to study interactions (such as adsorption and co-precipitation) between iron nanoparticles (*e.g.,* ferrihydrite) and molybdenum and vanadium in order to understand their impact on controlling their availability, mobility and the budget at different media such seawater, freshwater, polluted effluents, soils, sediments, etc.

This aim was reached by addressing to the following objectives:

i. Ferrihydrite characterization;

ii. Modelling the speciation of molybdenum and vanadium;

iii. Adsorption and co precipitation studies of molybdenum and vanadium onto/with ferrihydrite in different environmental conditions;

iv. Modelling the adsorption experiments;

The second aim was to follow the fate of the molybdenum and vanadium after their interaction with iron oxyhydroxides. To approach this aim the following objectives were set:

i. Study the bonding environments of the molybdenum from adsorbed and co-precipitated ferrihydrite as well as from the ferrihydrite transformation end-product;

ii. Evaluate the thermodynamics and kinetics of ferrihydrite transformation into more stabile phases in the presence and absence of molybdenum and vanadium;

iii. Quantitatively evaluate the molybdenum and vanadium partitioning during ferrihydrite transformation to stabile iron oxyhydroxides phases.

Unfortunately just a few but valuable months were spent on assessing the feasibility of using an anionic resin to pre-concentrate molybdenum and vanadium from complex matrices (such as seawater). These preliminary studies were done for molybdenum and vanadium to be measured by ICP techniques and to reduce the possible interferences. These studies were performed at the University of Southampton, Uk during my three months stay as part of the BIOTRACS exchange program.

1.3. Experimental and modeling approaches

Details of all experimental methods and modeling approaches are described in Chapter 3, here just a brief overview is given.

Most of the work contained in this thesis was performed in the laboratory at the University of Leeds with additional time spent at the SRS Daresbury Laboratory , UK and three months spent at the University of Southampton, National Oceanography Centre, UK. Exceptions are the synchrotron Energy Dispersive X-ray Diffraction *in situ* experiments which were carried out and measurements were performed at Daresbury Laboratory, Station 16.4.

Laboratory studies were carried out using a variety of conventional experimental designs, techniques and apparatus. Various adsorption system such as batch reactors and column reactors (or flow-through systems) were used for molybdenum and vanadium adsorption onto ferrihydrite (Chapter 4) and anionic resin (Chapter 7), respectively.

Analytical techniques and apparatus such as spectrophotometry (Ultra Violet-Visible Spectrophotometer) and spectroscopy (Inductively Coupled Plasma - Optical Emission Spectroscopy, Inductively Coupled Plasma – Mass Spectroscopy) for liquid characterization were used to measure the Mo, V, Fe and P concentration in different aqueous solutions from the adsorption, co-precipitation and transformation experiments as well as the mineral digestions.

Solid phase *(i.e.,* ferrihydrite, hematite) chemical and physical characterization and identification was performed using X-Ray Diffraction, high resolution potentiometric titrations, high resolution microscopy (Scanning Electron Microscope and Transmission Electron Microscope), dynamic light scattering and BET.

A nanoscale view of the molybdenum species associated with the solid phases (*e.g.,* ferrihydrite and hematite) was possible with synchrotron based X-Ray Adsorption Spectroscopy at SRS Daresbury Laboratory.

In addition, the nucleation and growth of hematite nanoparticles from ferrihydrite were monitored *in-situ* and real time using Synchrotron based Energy Dispersive – X-Ray Diffraction. This technique allowed monitoring the mineral transformation by taking X-Ray Diffractogrames every minute. The data were used to obtain kinetic and thermodynamic information on the ferrihydrite transformation.

Finally, two geochemical modeling packages (Geochemist's Workbench® 6.0 and Visual MINTEQ 2.32) were used to assess molybdenum, vanadium, phosphorus and iron speciation and to simulate the molybdenum and vanadium adsorption experiments.

1.4. Thesis outline

This thesis consists of 9 chapters.

Chapter 1 includes the introduction and the motivation of studying ferrihydrite nanoparticle interactions with molybdenum and vanadium and their fate during ferrihydrite transformation to hematite.

Chapter 2 presents the state of the art in our current knowledge as a literature review.

A detailed description of all methodologies and theoretical backgrounds used throughout the research is given in Chapter 3.

This is followed by four results chapters:

Chapter 4 is one of the major chapters, which contains qualitative and quantitative studies for understanding the interaction mechanisms between molybdenum, vanadium and ferrihydrite.

Chapter 5 describes the nano-scale approach of quantifying Mo-associated ferrihydrite and its transformation end-product: Mo-associated hematite using X-Ray Adsorption Spectroscopy.

Chapter 6 details the transformation studies of the ferrihydrite in the presence and absence of molybdenum and vanadium from the thermodynamic and kinetic point of view via *in situ* Synchrotron based Energy Dispersive –X-Ray Diffraction.

Chapter 7 contains preliminary results on using an anionic resin, Toyopearl M60, for molybdenum and vanadium pre-concentration from seawater matrices with implications for trace metals measurements in complex matrices.

Finally, the results from the entire thesis are discussed and summarized in Chapter 8 together with an outlook of the entire work.

Chapter 2
Iron oxyhydroxide interactions in hydrothermal plumes – inorganic approach

2.1. Introduction

It is well known that iron is an important element for the metabolism of all living organisms and that the availability of iron compounds in the environment controls the iron biogeochemical cycle, which in turn is linked to other important global cycles (*i.e.,* P, S, C (Cornell and Schwertmann 2003).

Iron phases occur widely in waters and sediments as well as in cool and moist soils (Jambor and Dutrizac 1998; Poulton and Raiswell 2002) with goethite, schwertmanite, ferrihydrite and hematite being most commonly found.

The interactions between iron particles and various environmental parameters that affect geochemical cycles are important because they most often control the availability/uptake of other metallic (or/and organic) species, some of which are considered pollutants. Oxyhydroxides such as ferrihydrite, due to their poorly ordered nature, and their corresponding high surface area, adsorb or incorporate significant quantities of metals such as Cd, As, Mo, V, Zn, Co, Pb (Cornell and Schwertmann 2003; Dyer et al. 2003; Feely et al. 1998; Hongshao and Stanforth 2001; Kooner 1993; Loan et al. 2005; Shaw et al. 2005), yet many of the processes that control the pathways or kinetics of these reactions are still poorly understood. In addition, the transformation reactions from the poorly ordered phases to the more geologically stable ones (*i.e.,* goethite, hematite) although important in many settings is still not well quantified.

The inorganic pathways for the formation of the various iron oxyhydroxides have been studied intensively (Cornell and Schwertmann 2003; Jambor and Dutrizac 1998)}, yet there are still many open questions regarding the mechanism of scavenging/binding (*i.e.,* sorption and (co) precipitation), or transformation rates and mechanisms between the phases.

From all iron oxyhydroxides our attention fell on ferrihydrite – a poorly ordered phase which is primarily formed at near neutral pH and which has an very big surface area (200-250m^2g^{-1}) (Cornell and Schwertmann 2003). It is a metastable phase which

transforms into different crystalline iron (oxy) hydroxides such as goethite, hematite, green rust, magnetite, etc., depending on changes in environmental conditions (Cudennec and Lecerf 2006; Davidson et al. 2008; Schwertmann et al. 1999; Schwertmann and Murad 1983).

In addition, this thesis focuses on molybdenum and vanadium interactions with iron phases in seawater or fresh water because very few experimental studies have treated these interactions (Feely et al. 1998; Gustafsson 2003; Trefry and Metz 1989) and because in seawater environments, specifically in deep sea hydrothermal settings, scavenging of molybdenum and vanadium by oxidised particles from vent fluids and their deposition into adjacent sediments plays an important role in molybdenum and vanadium cycling (Feely et al. 1998; German et al. 1997; German et al. 2002; German and Sparks 1993; Jambor and Dutrizac 1998).

In this respect, in deep oceans, one of the important sources of iron are hydrothermal systems (Figure 2. 1.). The input of iron from hydrothermal vents although relatively small (14 ± 5 Tg $year^{-1}$) in comparison with the terrestrial weathering input, is nevertheless an important contribution in the iron budget of our oceans (Raiswell et al. 2006).

When the hydrothermal fluid is injected into seawater, the oxidation and changes in temperature and pH/ Eh (see Figure 2. 1.) affect the composition and mineralogy of the plume particles.

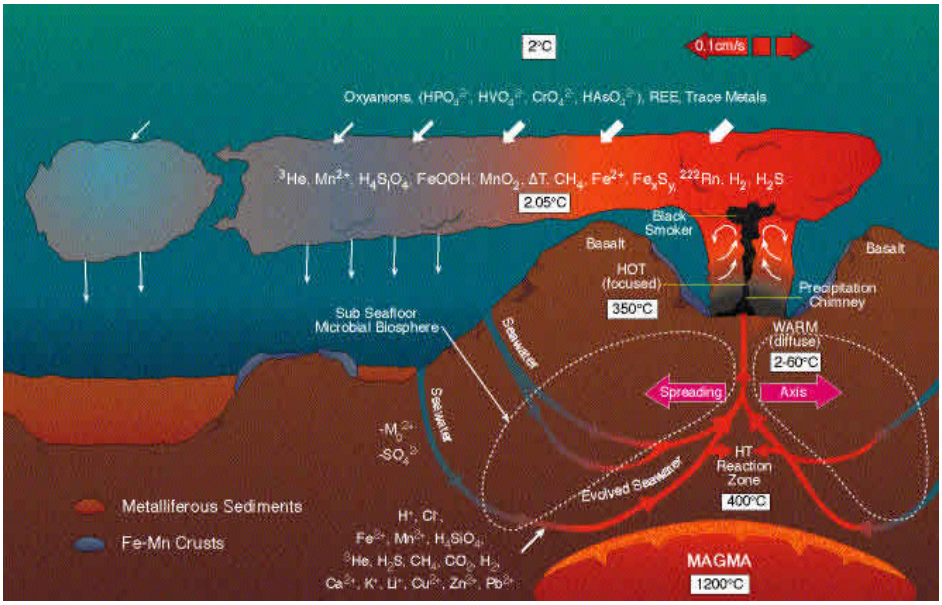

Figure 2. 1. Hydrothermal vents and transformations involved during the contact between hydrothermal fluid and seawater (http://www.indiana.edu).

The pH of the vent fluid is very low and in contact with the pH of seawater (7.8 – 8) it increases up to 4 in the reaction zone and higher in the buoyant plume. The acidic hydrothermal fluids contain high amounts of free sulphide and dissolved ferrous iron and these precipitate as sulphides. When in contact with seawater these particulates transform / oxidize to particulate Fe (III) phases which control the concentration of other elements via different scavenging processes (*e.g.,* absorption and co precipitation processes) (Field and Sherrell 2000).

These iron particles disperse horizontally away from the vent field and the particles eventually will settle from the buoyant plume. The particles that form and are transported in these plumes are enriched in Si, P, V, Mn, Cu, Zn As by factor of up to 20 or more relative to deep-ocean suspended matter, providing excellent tracer of hydrothermal plumes beyond the immediate region of the field vent. Overall, the most common iron oxyhydroxide formed in the hydrothermal plumes is believed to be ferrihydrite, goethite, hematite and lepidocrocite. Their preferential formation as well as subsequent deposition and scavenging capacities naturally depends on a whole plethora of changing physico-chemical conditions (Pichler and Veizer 1999).

The scavenging processes in the spreading plume affect the element/Fe ratios with increasing distance from the vent fields (Lilley et al. 1995). For example, Feely et al (1998) found a strong positive relationship between the molar P/Fe ratio in fresh hydrothermal Fe ferrihydrite precipitates and seawater–dissolved phosphate in a sample from Atlantic and Pacific Ocean. In contrast, they found that the molar V/Fe ratios in the hydrothermal plume are inversely correlated with dissolved phosphate. Their results indicate that inter ocean variations in dissolved phosphate control the P/Fe and V/Fe ratios in hydrothermal iron precipitates (Cornell and Schwertmann 2003; Feely et al. 1998). In addition, the deposition of these particles when they scavenged various metals (*i.e.,* molybdenum and vanadium) leads to an increase in the metals concentrations in the sediments formed from the deposited phases. Yet, these concentration and scavenging effects are poorly understood as the basic experimental data on the interactions between vanadium and molybdenum and iron oxyhydroxides precipitates and their transformation to more ordered phases have so far not been studied.

2.2. Iron oxyhydroxides

There are 16 iron oxides and hydroxides actually known and studied (see Table 2. 1). They are manly composed of Fe together with O^{2-} and HO^{-}. Some of them may contain other elements as chlorine and sulphur. In most of them iron is trivalent with few exceptions (*e.g.,* green rust, wurtite and magnetite) where iron is a combination of di and tri-valent species.

Table 2. 1. Iron oxides and oxyhydroxides (Cornell and Schwertmann 2003; Jambor and Dutrizac 1998)

MINERAL	**NOMINAL FORMULA**
Goethite	ά-FeOOH
Akaganeite	*β*-FeOOH
Lepidocrocite	γ-FeOOH
Feroxyhite	*δ*-FeOOH
Hematite	ά-Fe_2O_3
Maghemite	*γ*-Fe_2O_3
Magnetite	Fe_3O_4
Wustite	FeO
Bernalite	$Fe(OH)_3$
Ferrihydrite	Fe_5HO_8 $4H_2O$
Green rust	Fe_x^{III} $Fe_y^{II}(OH)_{3x+2y-z}(A^-)_z$; $A^- = Cl^-$; ½SO_4^{2-}
Schwertmannite	$Fe_{16}O_{16}(OH)_y(SO4)_z$ nH_2O
Not a mineral	$Fe(OH)_2$
Not a mineral	*β*-Fe_2O_3
Not a mineral	ε-Fe_2O_3
Not a mineral	High pressure FeOOH

There are a whole range of fields in which iron oxides have important implications and applications. Some of these are summarized in the Figure 2. 2

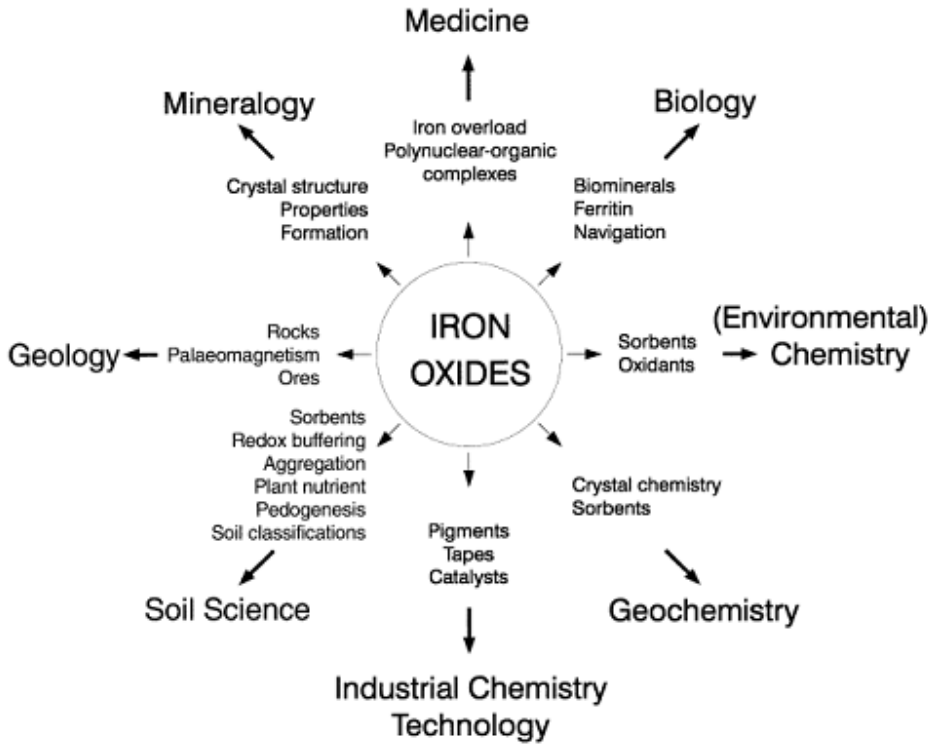

Figure 2. 2. Multidisciplinary use of iron oxyhydroxides and their appropriate research fields (Cornell and Schwertmann 2003).

From all of them, the present thesis will focus on ferrihydrite as main iron oxyhydroxide (starting material) and on hematite and goethite, as transformation end products.

Ferrihydrite is one of the amorphous iron oxyhydroxides, wide spread in various environments with neutral pH. It is also found in the human liver as a constituent of ferritin. Its importance in the geochemistry, soil sciences and environmental chemistry comes from the fact that it can be a very good sorbent (Figure 2. 2) because of its very high surface area. It has a dark-red or brownish colour and is a nano-particulate mineral forming usually small aggregates.

Goethite is a well crystallised iron oxyhydroxide, which occurs in rocks and in a variety of fields of the global ecosystem and is important also in industry where is used as a pigment. It has a chemical formula of ά-FeOOH and its well defined structure is based on hexagonal close packing of anions. It can occur in big crystals (few centimetres) as well as in nano-particulate size crystals (tens of nanometres).

Hematite is another crystalline iron oxide mineral which occurs in soil, sediments and rocks. Its stability makes it the usual end-product of a variety of other oxyhydroxides

transformation under specific environmental conditions. Its chemical formula is ά-Fe_2O_3 and as goethite, has a structure based on hexagonal close packing of anions. Similar as goethite, it is also used as a pigment. Hematite has a red bloodlike colour when powdered (nano-particulate plates) and a sparkling - grey colour when coarsely crystalline (Cornell and Schwertmann 2003).

All three minerals, along with others mentioned above, can undergo a variety of transformations in the environment and these transformations strongly depend on physical and chemical factors associated with the environments where they are present. Generally, the hydroxides can transform to oxides and vice-versa via de-hydroxylation and hydroxylation. Cornel and Schwertmann (2003) revised such inter-conversions in their book and a summary of these are presented in Table 2.2.

Table 2. 2. Iron oxyhydroxides transformations (Cornell and Schwertmann 2003).

PRECURSOR	**PRODUCT**	**TRANSFORMATION MECHANISM**	**PREFERRED MEDIUM**
Goethite	Hematite	Thermal or mechanical dehydroxilation	Gas/vacuum
Goethite	Hematite	Hydrothermal dehydroxylation	Solution
Goethite	Maghemite	Thermal dehydroxylation	Air+organic
Lepidocrocite	Maghemite Hematite	Thermal dehydroxylation	Gas/vacuum
Lepidocrocite	Goethite	Dissolution / reprecipitation	Alkaline solutions
Lepidocrocite	Magnetite	Reduction	Alcaline solutions with Fe(II)
Akaganeite	Hematite	Thermal dehydroxylation	Gas / Vacuum
Akaganeite	Goethite	Dissolution / reprecipitation	Alkaline solutions
Akaganeite	Hematite	Dissolution / reprecipitation	Acide solutions
Akaganeite	Magnetite	Dissolution / reduction	Alkaline solutions with N_2H_2
Feroxyhyte	Goethite	Dissolution / reprecipitation	Alkaline solutions
Ferrihydrite	Hematite Maghemite	Thermal hihydration/ dehydroxylation	Gas/vacuum
Ferrihydrite	Goethite	Dissolution / reprecipitation	Aqueous solutions pH 3-14

Table continued on next page

Ferrihydrite	Akaganeite	Dissolution / reprecipitation	Acidic media, presence of Cl^-
Ferrihydrite	Lepidocrocite	Dissolution / reprecipitation	pH 6 presence of cysteine
Ferrihydrite	Hematite	Aggregation, short range crystallization within ferrihydrite aggregates	Aqueous solution at pH 6-8
ferrihydrite	Substituted magnetite	Dissolution reprecipitation	Alkaline solutions with M”
Hematite	Magnetite	Reduction	Reducing gas
Hematite	Magnetite	Reduction-dissolution /reprecipitation	Alkaline solutions with N_2H_2
Magnetite	Maghemite/Hematite	Oxidation	Air
Maghemite	Hematite	Thermal conversion	Air

As seen in Table 2. 2. there are two types of transformation mechanisms: solution aided mechanisms (*e.g.,* dissolution / reprecipitation) and solid phase transformation mechanisms (*e.g.,* thermal dehydration or aggregation / rearangement).

Ferrihydrite, our starting material of interest, transforms to goethite and hematite via both types of mechanisms depending on physico-chemical settings of the system.

A more detailed description of the properties and transformation pathways of the ferrihydrite into more stable minerals are presented in the following sections (2.3. and 2.4.).

2.3. Ferrihydrite

Ferrihydrite is an iron oxyhydroxide often called “amorphous ferric oxide” or “hydrous ferric oxide,” which can be found in different environmental media such as soil, iron rich polluted waters (*e.g.,* mine waste and acid mine drainage), deep oceans and lake bottom sediments, hydrothermal vents or hot- and cold-spring deposits. Ferrihydrite is often associated with a variety of other amorphous or crystalline minerals (Cornell and Schwertmann 2003; Crawford et al. 1996; Jambor and Dutrizac 1998; Poulton and Raiswell 2002; Sunda 2000; Trivedi and Lisa 2001) and has a well-documented ability to adsorb or co-precipitate onto / with organic compounds and ions of many elements including toxic or trace metals (Cornell and Schwertmann 2003; Jambor and Dutrizac 1998).

Synthetic (2-line) ferrihydrite is the initial precipitate resulted from the rapid hydrolysis of a Fe (III) solution. Its structure is usually very poorly crystalline (Cornell and Schwertmann 2000; Cornell and Schwertmann 2003; Dyer et al. 2003; Dyer et al. 2004; Scheinost et al. 2001; Spadini et al. 2003; Trivedi et al. 2003; Trivedi and Lisa 2001; Waychunas et al. 2002; Waychunas et al. 1996).

Rapid hydrolysis of the acid Fe(III) solutions achieved either by briefly heating the solution (at 80ºC) or by rapidly rising the pH to ca. 7 with a base solution leads to the formation of a more crystalline mineral called 6 line ferrihydrite (Cornell and Schwertmann 2000).

However, from crystallographic principles at least two types of ferrihydrite can be distinguished: a so called 2-line ferrihydrite – which is characterized by a very poorly ordered structure and for which the XRD pattern has 2 broad peaks with d-spacing of 1.5 and 2.5 Å; and 6-line ferrihydrite – which is characterised by a slightly more ordered structure and has 6 peaks in its XRD pattern (Cornell and Schwertmann 2000; Cornell and Schwertmann 2003; Janney et al. 2000a).

Both, 2-line and 6-line ferrihydrite will transform to goethite and/or hematite if stored in water under different conditions. It has been observed that even in a dry state, the transformation can occur after several years, presumably due to the physical sorption of the H_2O onto the particle surface. Many studies were published on the transformation of the ferrihydrite into more ordered phases and these will be briefly discussed in the next sections.

The chemical formula and the crystalline structure of the ferrihydrite have been the subject of long time debates. Jambor and Dutrizac (1998) used a nominal ferrihydrite

formula: $5Fe_2O_3\ 9H_2O$ but $Fe_5HO_8\ 4H_2O$ is also used (e.g.,(Cornell and Schwertmann 2000; Cornell and Schwertmann 2003; Schwertmann et al. 1999; Schwertmann and Murad 1983). Cudennec et al., (2006) and Loan et al., (2005) used as ferrihydrite formula $Fe_5O_7(OH)\ 4H_2O$ and $5Fe_2O_3\ 9H_2O$, respectively.

Recently, based on an ideal structure obtained from the X-Ray diffraction patterns modelled with pair distribution function Michel et al., (2007) calculated a chemical formula for ferrihydrite of $Fe_{10}O_{14}(OH)_2$ (Michel et al. 2007).

However the exact structure of the ferrihydrite is still uncertain. The literature provides structures with a general agreement that iron in ferrihydrite is octahedrally coordinated in the core structure and tetrahedral coordinated at the surface (Jambor and Dutrizac 1998).

Jannney et al., 2000 suggested that synthetic two line ferrihydrite contains highly disordered material and nano-crystals with structures based on hexagonal (ABAB) and cubic (ABC) stacking of close-packed layers of O^{2-} and OH^- ions. They found that the ferrihydrite structure with cubic stacking is similar to maghemite and suggested that ~25% of the iron was in tetrahedral sites. The structure of hexagonal stacking consists of double chains of face-sharing iron octahedra each octahedron shares one face, two edges, and three corners with adjacent octahedra (Janney et al. 2000b).

Hiemstra and Riemsdijk (2009) suggested that single-coordinated surface groups dominate the surface of ferrihydrite and that these groups can be present in two structural configurations: the groups either form the edge of a single Fe-octahedron or are present at a single corner of two adjacent iron octahedra.

Michel et al., (2007) using real-space modelling of the pair distribution function (PDF), derived from the direct Fourier transformation of the total x-ray scattering, that ideal ferrihydrite structure containing 20% tetrahedral and 80% octahedral coordinated iron (Michel et al. 2007)

One of the main characteristic of ferrihydrite is its very high surface area. Values of surface area between 120 and 340 m^2g^{-1} have been found for synthetic and natural, 2 and 6 line ferrihydrite (Jambor and Dutrizac, 1998). As a result of this characteristic ferrihydrite can adsorb a variety of cations (*e.g.,* Cd^{2+}, Cu^{2+}, Pb^{2+}, Co^{2+}, Mn^{2+}, Cr^{3+}, Cr^{6+}, Ni^{2+}, Zn^{2+}, Ag^{+}), anions (*e.g.,* PO_4^{3-}, MoO_4^{2-}, HVO_4^{2-}, $VO_2(OH)_2^{-}$, $VO_3(OH)^{2-}$, WO_4^{2-}) and organics (herbicides: 7 chloro-3-methylquinoline-8-carboxylic acid, thiazafluron; mugineic acid and p-hydroxybenxoic acid) (Dzombak and Morel 1990; Gustafsson 2003; Jambor and Dutrizac 1998; Kooner 1993; Loan et al. 2005; Sannino et al. 2009; Trivedi and Lisa 2001).

A large surface area, high adsorption affinity for different inorganic and organic species and low synthesis cost, makes ferrihydrite a very attractive material for the treatment of wastewater and soil decontamination.

Other environmental implications are related with the effect of the ferrihydrite formation and transformation pathways on the availability and the budget of different elements in aqueous media. Most of the ferrihydrite transformations (biotic and abiotic) as well as the effect of different factors (pH, temperature, aging time, the presence of different ions) have already been studied; however there are still many unknown transformation pathways and influencing factors which deserve future research.

2.4. Ferrihydrite transformation

2.4.1. Background

Ferrihydrite, as a metastable amorphous mineral, can transform to more ordered iron oxides such as goethite, hematite, magnetite, green rust, etc under specific environmental conditions (Cornell and Schwertmann 2003; Schwertmann et al. 1999; Schwertmann and Murad 1983; Shaw et al. 2005; Sumoondur et al. 2008; Vu et al. 2010; Yee et al. 2006). All transformations are mainly and highly dependent on pH and oxic *vs.* anoxic conditions. In addition, temperature, ionic strength, redox potential; solid-solution ratios, the presence or the absence other ions (anions and cations) which can retard or enhance the transformation reaction need to be taken into consideration as they can have an important effect on these mineralogical transformations.

The most common transformation studies under oxic conditions have been carried out on ferrihydrite to hematite and goethite at low and high pH (Cornell and Schwertmann 2003; Schwertmann et al. 1999; Schwertmann and Murad 1983) or on schwertmanite to ferrihydrite and then goethite and hematite under alkaline conditions (Davidson et al. 2008) or only from ferrihydrite to goethite or hematite under alkaline conditions (Shaw et al. 2005; Vu et al. 2010).

Under anoxic conditions, transformation studies of ferrihydrite to magnetite (with green rust as intermediate phase) by Summoondur et al., (2008) and ferrihydrite to goethite (with Fe (II) as catalyst) by Yee et. al., (2006) are two examples found in the literature. In many of these mineral transformation / formation studies, the various authors aimed to derive mechanistic information as well as thermodynamic and kinetic transformation / formations parameters using either conventional methodologies (*e.g.,* digestions) or synchrotron based approaches.

A first long term transformation assessment was done by Schwertmann and Murad (1983) who found that storing ferrihydrite in aqueous solution at 24^{o}C for almost 3 years at different pH values resulted in the formation of goethite and/or hematite (Schwertmann and Murad 1983). They used oxalate extractions, XRD, TEM and Mössabauer spectroscopy to follow and record the ferrihydrite transformation. Their results suggest that at pH between 7 and 8 hematite was preferentially formed via a internal rearrangement and dehydration, while at pH 4 and 12 goethite formed via dissolution/re-precipitation.

The most recent paper which revises the mechanism of ferrihydrite transformation to hematite or goethite is from Cudennec and Lecerf (2006). Taking into consideration Schwertmann's previous work they proposed the following scheme for ferrihydrite transformation in acidic and alkaline media:

Acidic solutions: 0<n<3

$$5Fe_2O_3, 9H_2O_{(s)} + (30\text{-}10n)H_3O^+_{(aq)} + (6+10n)\ H_2O \leftrightarrow 10[(Fe(OH)_n(H_2O)_{(6-n)}]^{(3-n)+}_{(aq)}$$

Alkaline solutions: 3<n<6

$$5Fe_2O_3, 9H_2O_{(s)} + (10n\text{-}30)OH^-_{(aq)} + (66\text{-}10n)\ H_2O \leftrightarrow 10[(Fe(OH)_n(H_2O)_{(6-n)}]^{(3-n)-}_{(aq)}$$

At pH above 7, iron is dissolved as the complex anions, $Fe(OH)_4(H_2O)_2^-$ (n = 4), $Fe(OH)_5(H_2O)^{2-}$ (n = 5) and at very alkaline pH, as $Fe(OH)_6^{3-}$(n = 6). At these pH values the solubility of iron increases but is still very low, and therefore goethite is favoured.

Conversely, at pH around 7, H_3O^+ and OH^- concentrations are too low for dissolving enough ferrihydrite for the formation of goethite through solution. Here, the transformation take place mainly in the "solid state", favouring hematite formation in solutions enhanced by the minimum solubility for the ferrihydrite. Actually, at this pH the main dissolved species is the neutral complex $Fe(OH)_3(H_2O)_3$ and hematite is obtained as follows:

$$5Fe_2O_3{\cdot}9H_2O_{(s)} \leftrightarrow 5\ \acute{\alpha}\text{-}Fe_2O_{3(s)} + 9H_2O$$

They suggested that the dehydration of ferrihydrite $Fe_5O_7(OH)$, $4H_2O$, is the mechanism of hematite formation and they explained that the structure of ferrihydrite is contracted by about 2% during its transformation into hematite. In addition, the fact that in the formula chosen for ferrihydrite, $Fe_5O_7(OH)$, $4H_2O$, even if the O/OH rate is not necessarily fixed and it can probably vary around a value near seven (Cudennec and Lecerf 2006).

Schwertmann (1983) was the first to find that high temperature favours the formation of the oxide hematite. Later, Liu et. al., (2008) in their transformation experiments (from room temperature to 100°C) of ferrihydrite with addition of Fe(II) (Fe(II)/Fe(III) molar ratio of 0.02) showed that at high temperatures the formation of hematite is favoured whereas low temperatures favours the dissolution re-precipitation mechanism as well as the formation of goethite (Liu et al. 2008).

Many studies followed more complicated systems due to the presence of other ions in solution or in the iron oxyhydroxides structure: cations like Fe^{2+} (Liu et al. 2008; Liu et al.

2007; Yee et al. 2006), Pb^{2+} (Vu et al. 2010), Cd^{2+} (Lin et al. 2003) , Zn^{2+} (Jambor and Dutrizac 1998), Mn^{2+}(Cornell and Schwertmann 2003), Ni^{2+} (Punnoose et al. 2004), Al^{3+} (Jentzsch and Penn 2006) or anions like Cl^{-} (Liu et al. 2008), CO_3^{2-} (Hiemstra et al. 2009), SO_4^{2-} (Liu et al. 2008), (Davidson et al. 2008), PO_4^{3-} (Shaw et al. 2005) certainly influence the results of the transformation reactions.

The substitution of these ions in the iron oxyhydroxides structure can lead to changes in the iron oxyhydroxide cell edge length or volume (Cornell and Schwertmann 2003). On the other hand, the presence of these ions in the iron oxyhydroxide structure can catalyze or inhibit the transformation of ferrihydrite to specific end-products under appropriate conditions.

Studies before 1998 on the effect of many of these anions and cations, as well as some organic molecules onto transformation of the ferrihydrite under different conditions are revised by Jambor and Dutrizac (1998) in their comprehensive review. Later in 2003, an updated view about these transformations was given by Cornell and Schwertmann (2003) in their book. Below, only few recent examples are given.

In the presence of Fe (II) under limited oxic conditions (N_2 bubbled into reaction vessels) and at pH 7 and 9, Liu et al., (2008) showed that ferrihydrite transforms to goethite and hematite at pH 7 and hematite only at pH 9, and this was catalyzed by the presence of Fe(II). Under fully anoxic condition Yee et. al., (2006) followed the same transformation *in situ* using synchrotron based technique diffraction but with an Fe(II)/Fe(III) ratio that lead to pure goethite and they found that the activation energy of goethite formation in the presence of Fe(II) was ca. 60% smaller that in its absence. Thus, the catalytic effect of Fe (II) decreases the energetic barrier which the system needs to overcome to form goethite. They also mentioned that depending on Fe(II)/Fe(III) ratio and reaction time the transformation end-product can be magnetite (5 times higher Fe(II)/Fe(III) ration and longer time) or goethite.

Vu and collaborators (2010) showed that the presence of lead in the ferrihydrite structure (adsorbed) at alkaline pH (13) enhanced the formation of hematite and reduced the induction time by ca. 20-30%. They also first found that at this pH, goethite is an intermediate phase (Vu et al. 2010).

An example of a cation effect on ferrihydrite transformation is Shaw et al., (2005) work on the phosphate effect on ferrihydrite transformation to goethite and hematite under alkaline conditions. Using synchrotron based diffraction they found that the apparent activation energy of nucleation at pH 13.7 for the phosphate-doped ferrihydrite system was three times higher than the apparent activation energy without phosphate and that the presence of phosphate retarded the ferrihydrite transformation.

Despite all these studies very little is known about the effects of molybdenum and vanadium on ferrihydrite stability and transformation at different temperatures, under neutral conditions in seawater *vs.* freshwater systems. Thus, this was the main part of the present thesis which focused on ferrihydrite characterisation and transformation at different temperatures, under neutral conditions in seawater *vs.* freshwater systems

2.4.2. Kinetic and thermodynamic approaches

Kinetic approach

In order to obtain kinetic rate constants from mineral formation /transformation or mineral nucleation and growth reactions the Johnson-Mehl-Avrami-Kolmogorov (JMAK) kinetic model is one the most common model used (Davidson et al. 2008; Shaw et al. 2005; Sumoondur et al. 2008; Vu et al. 2010; Yee et al. 2006).

The Johnson-Mehl-Avrami-Kolmogorov kinetic model (JMAK) was derived by Johnson and Mehl (1939), Avrami (1939, 1940) and Kolmogorov (1937) and it has been widely used to describe re-crystallization processes but also phase transformation processes.

This model is based on the Avrami-Erofe'ev equation (Eq 2.1.), which is the basic model often used for quantifying the kinetics of crystal growth in solution (Croker et al. 2009), as well as in solid state (Khawam and Flanagan 2006; Zhang and Du 2008).

$$\alpha = 1 - e^{(-kt)^m} \qquad \textbf{(}\text{Eq. 2.1.}\textbf{)}$$

where k is the rate constant for the reaction (s^{-1}), t is time (s) and m is a variable that depends on the nucleation rate, reaction mechanism, and dimensionality of growth (Hulbert 1969).

The JMAK model attempts to predict the fraction of crystallized material at every given point in time with the following assumptions (Cahn 1956) (Tobler 2008):

- the new phase nucleates as infinitely small, rigid, independent units that are able to overlap;
- nucleation occurs randomly and uniformly;
- the nucleation rate is time-independent;
- the sample is of infinite size and boundary effects can be ignored, and
- grain growth continues until impingement occurs.

The model can be written as:

$$\alpha = 1 - e^{-k(t-t_0)^m} \quad \textbf{(}\text{Eq. 2.2.}\textbf{)}$$

where *k* is the rate constant for the reaction (s^{-1}), *t* is time (s), t_0 is the induction time (s) and *m* is a variable that depends on the nucleation rate, reaction mechanism, and dimensionality of growth (Hulbert 1969).

The JMAK model has been applied before in various studies of oxyhydroxide formation kinetics (*e.g.,*(Davidson et al. 2008; Shaw et al. 2005; Sumoondur et al. 2008; Vu et al. 2010; Yee et al. 2006)). It is applied for kinetic determination of new phase nucleation (on grain boundary surface, grain edges, or grain corners) and/or new phase growth.

Kalu and Warydoba (2007) argued that the JMAK model should only be used to analyze the kinetics of re-crystallization and grain growth, but is inadequate for quantifying the recovery (dislocation, annihilation, dislocation rearrangement and subgrain growths phenomena) kinetics.

Thermodynamic approach

The Arrhenius equation is the most common formula used for activation energy determination. Previously the Arrhenius equation was applied to calculate activation energy of hydrothermal crystallization of many minerals (*e.g.,* calcium titanate, (Croker et al. 2009); iron oxides (Davidson et al. 2008; Shaw et al. 2005; Vu et al. 2010; Yee et al. 2006)

Its expression is:

$$k = A \cdot e^{-E_a / RT} \quad \text{(Eq. 2.3.)}$$

where *k* is the rate constant; *A* is the frequency or pre-exponential factor; E_a is the activation energy (kJ mol^{-1}), R is the gas constant (8.314 J mol^{-1} K^{-1}) and *T* is the absolute temperature in Kelvin (K).

Rearranging Eq. 2.3, E_a can be extracted as:

$$E_a = -\ln k + \ln A/RT \quad \text{(Eq. 2.4.)}$$

Another method for activation energy determination is the “time to a given fraction method” (Putnis 1992). This method was used to determine the activation energy of crystallization of albite from analcime and quartz (Putnis 1992). This approach relies solely on the time to a given fraction of transformation (t^*_α) and can be expressed as:

$$\ln t^*_\alpha = const. - \ln A + (E_a/R)(1/T) \quad \text{(Eq. 2.5.)}$$

The “time to a given fraction method” determines the activation energy, E_a, independent of the fraction transformed in the rate equation and also makes it possible to test whether E_a varies during the course of a transformation (Putnis 1992). The superscripts term “α” represents a certain fraction of transformation chosen randomly.

No comparative studies on activation energy determinations via the Arrhenius approach *vs.* “time to a given fraction” could be found in literature. Thus, in order to validate these two approaches, we applied them to our thermodynamic quantification of the ferrihydrite transformation under neutral conditions in seawater *vs.* freshwater systems in the presence and the absence of molybdenum and vanadium anions.

2.5. Adsorption and co precipitation

2.5.1. Theoretical background

A short summary of interactions which can occur at the solid-water interface is important in order to give a strong base to the topic.

A full understanding of adsorption requires a careful characterization of the adsorbent - adsorbate interaction as a function of the physical and chemical proprieties of the adsorbate (Stumm, 1992). Table 2. 3. presents an overview of the types of interaction and their mechanisms.

Table 2. 3. Types of interactions between adsorbent and adsorbate and their possible mechanisms (Polihrohiade 1967)

Type of interaction	**Mechanism**
Chemical reaction with surface	Surface hydrolysis Surface complexation Surface ligand exchange Hydrogen bond formation
Electrical interaction at surface	Electrostatic interaction Polarization interaction
Interaction with solvent	Hydrophobic expulsion

First a few definitions: (1) adsorption is a phenomenon which assumes that the adsorbate is bound in a multilayer, non-stoichiometrically onto the adsorbent surface; (2) in contrast, an ion exchange binding mechanism only takes place stoichiometrically (equimolecular rate) between exchangeable ions; (3) precipitation is a phenomenon which takes place in a system where the concentration of a specific ion overcomes its saturation limit in solutions. Co-precipitation is a process in which along with the saturated ion there is another component which is sequestered in the precipitated structure during its formation.

Laboratory experimental designs of adsorption and co precipitation require different settings. Adsorption differs from co precipitation in terms of formation of a colloid substrate in the presence of metal ion (absorbate / co-precipitate) studied. When the adsorbate is added after the formation of the adsorbent then adsorption takes place. In the case of co

precipitation the adsorbate is added prior to or during the adsorbant formation (Crawford et al. 1996).

Mass transfer to the adsorbent-sorbent interface

The main stages of mass transfer for the adsorption are:

- Adsorbate migration into the mobile liquid layer from the surface of adsorbent;
- Adsorbate migration through the fixed liquid layer from the adsorbent surface;
- Adsorbate transport through liquid solid interface;
- Adsorbate diffusion into the adsorbent pores;

From the kinetic point of view one of these stages is considered reaction determinant and will drive the reaction rate (Polihrohiade 1967).

The adsorption as well as co-precipitation capacities can be influenced by a variety of factors, some of which are presented in Table 2. 4.

Table 2. 4. Factors which can affect sorption and co-precipitation of metals on to/with minerals:

Type of factors	**Factors**
Physicochemical or environmental factors	• pH; • Temperature; • Ionic strength; • Oxygen concentration (oxic or anoxic media); • Biomass presence; • Metal ion concentrations • Metal ion to solid ratio; • Competitive ions (*e.g.,* PO_4^{3-} or SO_4^{2-}); • Inhibiting components from seawater (*e.g.,* complexants)
Substrate (minerals) factors:	• Surface functional groups; • Particle/aggregate size; • Surface area; • Crystallographic defined surface (un/ordered); • The ability of the absorbent (particle bonded) to act as a reductant or oxidant for metal ions that exist in different oxidation states;

Table continued on next page

Metal forms and ligand types	• Hydration lever of metal ions; • Ligands types (*e.g.,* soft, middle and hard); • Precipitate/aggregate/polymerized forms; • Solubilisation capacity of metal species; • Complexing state of metal ions (coordination chemistry of aqueous metal ion and possible change in coordination chemistry during sorption, including cation coordonation number, valence state and hydrolysis; • Toxicity of metal compounds; • The bonding environment of adsorbate to the adsorbant surface *e.g.,* inner-sphere, outer-sphere, or asa surface precipitate.
Microorganisms	• Type of radicals from cell wall (*e.g.,* carboxyl, phosphate, amino, carbonyl, thio etc); • Electrostatic and trans-membrane potential of microorganisms cell wall; • Enzyme types from cell synthesis; • Chemical transformation capacity of micro-organisms; • Flocculation and aggregation of colloids; • Genetic factors (morphology, physiology, metabolism).

Regarding inorganic and also biogenic adsorption experiments, in order to assess and understand the effect of these factors, the topic must be separated into small defined issues and then studied at a fundamental level.

2.5.2. Kinetics of metal sorption

A number of models with various degrees of complexity have been developed to describe the kinetics of metal sorption in batch systems.

The kinetic models used to fit experimental data of metals sorption onto various media (e.g., microorganisms, minerals, resins, zeolites, etc) were the Lagergren model, (which describes pseudo first order kinetic or first order kinetic) and pseudo second order (which is based on the assumption that sorption follows second order kinetics).

The pseudo – first order model, called Lagergren model, considers that the rate of adsorption or site occupation is proportional to the number of unoccupied sites

$$\frac{dq}{dt} = k_{1,ads}\left(q_e - q\right) \quad \textbf{(}\text{Eq. 2.6.}\textbf{)}$$

Where: q_e and q are the amounts of adsorbed metal ions onto the adsorbent at equilibrium and at any time t, respectively (mg g^{-1}), and $k_{1;ads}$ is the Lagergren rate constant of the first-order adsorption (Cruz et al. 2004).

The second model is based on the fact that metal ions displace alkaline-earth ions from adsorbent bonding sites and, therefore, with respect to the sorption sites the sorption can be considered to follow a pseudo-second order kinetic (Cruz et al. 2004). The observed kinetics can be modeled assuming that the rate of occupation of adsorption sites is proportional to the square of the number of unoccupied sites

$$\frac{dq}{dt} = k_{2,ads}\left(q_e - q\right)^2 \quad \text{(Eq. 2.7.)}$$

Where: $k_{2;ads}$ is the rate constant of the second-order adsorption (g mg^{-1} min^{-1}).

2.5.3. Sorption equilibrium modelling

Many mathematical models have been developed to describe sorption equilibria. Most commonly used, are Langmuir and Freundlich isotherm models (Volesky 2004).

The Langmuir equation for adsorption of metals to soils, clays or micro-organisms has been derived and applied in many studies (Bradl 2005; Brinza et al. 2005; Herrero et al. 2006).

This model can be applied for single ion solution studies and also for multi-ion solutions, by modifying the expression for competitive species on the adsorption sites (called competitive Langmuir model).

The simple expression of the Langmuir adsorption model examines the relationship between adsorbed (q_e) and metal concentration (C_e) at equilibrium.

To obtain the equilibrium data for this model the experiments can be designed in two ways:

- Initial metal concentration is varied while the adsorbent weight is kept constant - this is the most common approach;
- Initial metal concentration is kept constant and adsorbent weight is varied (Ting and Mittal 1999)

The basic formulas used in determining the maximum uptake capacities of metals (using Langmuir or Freundlich adsorption models) by different adsorbents are based on mass balance of metal in solution and adsorbed metal as described by Eq. 2.8. (Ofer et al. 2004):

$$q = \frac{V \cdot \left(C_i - C_f\right)}{S_a} \qquad \text{(Eq. 2.8.)}$$

Where: q = metal uptake capacities (mg metal g^{-1} dry adsorbent)

V_a = solution volume (mL)

C_{ia} = initial metal concentration before the adsorption test (mg L^{-1})

C_{fa} = final metal concentration after the adsorption test (mg L^{-1})

S_a = dry weight of adsorbent sample (g)

The uptake capacity of adsorbent calculated as a function of metal concentration in the adsorbent (after total digestion) uses the following mass balance formula (Ofer et al. 2004):

$$q = \frac{\left(C_{i\,a} - C_{fa}\right)}{S} \cdot V_a \qquad \text{(Eq. 2.9.)}$$

Where: q = metal uptake capacities (mg metal g^{-1} dry adsorbent)

V_a = digested adsorbent sample volume (mL)

C_{ia} = metal concentration in completely digested adsorbent sample (mg L^{-1})

C_{fa} = metal concentration in completely digested adsorbent sample after the adsorption test (mg L^{-1})

S = dry weight of adsorbent sample (g)

The expressions of these two models are described as follows.

The Langmuir model (Langmuir 1916; Polihrohiade 1967; Volesky 2004):

$$q_e = \frac{q_{\max} \cdot b \cdot C_e}{1 + b \cdot C_e} \qquad \text{(Eq. 2.10.)}$$

where: q_{max} (mg g^{-1}) is the maximum amount of metal ion per unit mass of adsorbent and

b is the equilibrium adsorption constant which is related to the affinity of the binding sites.

q_{max} represents a practical limiting adsorption capacity when the surface is fully covered with metal ions and allows the comparison of adsorption performance, particularly in the cases where the adsorbent did not reach its full saturation in the experiments.

The empirical Freundlich equation (Polihrohiade 1967; Volesky 2004), based on sorption onto a heterogeneous surface, can be derived assuming a logarithmic decrease in the enthalpy of the adsorption with the increase in the fraction of occupied sites and is given by:

$$q_e = K_F \cdot C_e^{1/n} \qquad \text{(Eq. 2.11.)}$$

Where: K_F and n are the Freundlich constants characteristics of the system,

K_F - indicating the adsorption capacity and

n - adsorption intensity describing the adsorbate affinity for the adsorbent suface sites. Values of 1/n between 0.1<1/n<1 represent good adsorption, whereas the lower values 1/n suggest that weak adsorption forces are operative on the surfaces

2.6. Uptake mechanisms

2.6.1. Coordination or complex formation

The metal removal from solution can also take place by complex formation on the surface sites after the interaction between metal and active groups occurred. This phenomenon involves electrostatic forces and covalent coordination links.

Some micro organisms can also produce organic acids which can chelate metals (*i.e.,* with siderophores), resulting in metal-organic complexes which can be then adsorbed or complexed onto / by different adsorbents.

2.6.2. Chelation

Chelates are complexes formed with multidentate ligands and the phenomenon has been called chelation.

Although this terminology is typically employed for aqueous complexation with small ligands, the terms are often applied in the literature when dealing with more complex organic molecules.

The terms *inner-sphere* and *outer-sphere* complex are used to distinguish between binding which is, respectively, largely covalent in character or electrostatic in nature.

Regarding *inner-sphere* complexes, the interacting ligand is immediately adjacent to the metal cation. The *inner-sphere* adsorption of metals occurs through the loss of the water of hydratation and the formation of direct chemical bonds with the mineral surface, typically via oxygen atoms (Figure 2.4). It can be distinguished by the number of surface oxygen atoms to which the adsorbate binds, where one, two or more chemical bonds results in mono-dentate, bi-dentate and (rarely) tridentate or tetra-dentate *inner-sphere* surface adsorption complexes (Bradl 2005).

With regards to outer-sphere complexes, ions of opposite charge are attracted and approach each other within a critical distance and effectively form what is termed an ion pair. In *outer-sphere* complexes, the metal ion or the ligand or both generally retain their coordinated water when the complex is formed (Figure 2. 3). In other words, the metal ion and the ligands are most often separated by one or more water molecules (Brown et al. 1999). The binding forces involved in *outer-sphere* adsorption are usually a combination of hydrogen bonds and electrostatic long-range Coulombic forces.

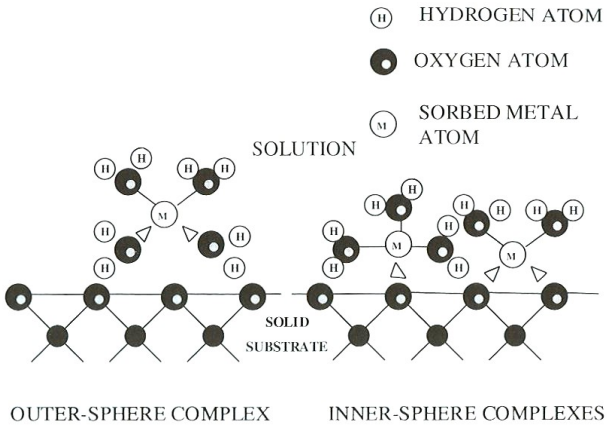

Figure 2. 3. Schematic sketch of possible sorption complexes at mineral /water interface (Bradl et al., 2005)

Typically inner-sphere complexes are more tightly bound to the surface comparing with outer-sphere complexes, thus they are less easily removed through desorption.

Outer-sphere and *inner-sphere* adsorption can be expressed by the following reactions:

$SOH + M^{2+}$ (aq) = SOHM2+ (aq) *outer-sphere* adsorption

$SOH + M^{2+}$ (aq) = $SOM^{+} + H^{+}$ monodentate *inner-sphere* adsorption

$2SOH + M^{2+}$ (aq) = $(SO)_2 M^{0} + 2 H^{+}$ bidentate *inner-sphere* adsorption

Generally the effect of the surface charge can be used to distinguish outer-sphere adsorption from *inner-sphere* adsorption, but is also possible that both types can occur in the same system.

Theoretically, increasing the ionic strength, or concentration of a background electrolyte, usually decreases the metal adsorption densities measurably due to a neutralization of the surface charge. This way, the attractive forces that encourage outer-sphere adsorption are reduced. An example: of such behavior is the adsorption of Ba and Pb onto goethite as described by Bradl et al (2005).

In case of *inner-sphere* adsorption, the adsorption is intense and is a function of surface charge, with metal uptake capable of taking place at pH near the point of zero charge or even when the adsorbent surface is positively charged. As an example: the studies of Pb adsorption onto ferrihydrite by (Dyer et al. 2003; Trivedi et al. 2003), showed via XANES and XAFS studies that Pb(II) ions predominantly sorb onto ferrihydrite via *inner-sphere* complexation, releasing their primary hydration shell upon sorption. In addition they found

that the configuration of the sorption complexes does not depend on the adsorbate concentration.

Adsorption as ternary surface complexes represents a sorption mechanism in which, the adsorbate either serves as a bridge between the ligand L and the surface or it is bound to the surface indirectly via intermediate bridging ligands. Such complexes are defined as *Type A ternary complex* and *Type B ternary complex*, respectively (Figure 2. 4), and can be represented:

$SOH + M^{2+}(aq) + L^{-} = SOML + H^{+}$ Type A ternary complex

$SOH + L^{-} + M^{2+}(aq) = SLM + OH^{-}$ Type B ternary complex

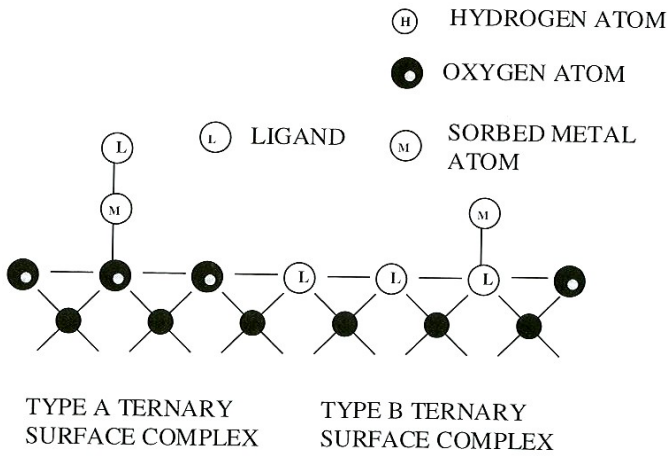

Figure 2. 4. Schematic sketch of *Type A ternary complex* and *Type B ternary complex* involving the metal, mineral surface, and ligand, which may bond directly to the surface or primarily via the adsorbate (Bradl 2005).

Some examples of inorganic ligands which can be found in seawater are: bicarbonate, carbonate, chloride, nitrate, phosphate, sulfate, and sulfide, while organic ligands such as amino, carboxylic, fulvic and humic acids are also common. For biosorption pathways, the prime responsible agents for binding are various organic compounds (*e.g.,* polysaccharides) from the cell wall of microorganism which contain functional groups like carboxyl, hydroxyl, etc (Brinza and Gavrilescu 2003; Volesky and Holan 1995).

Surface properties of iron oxyhydroxides

Physical, chemical and mineralogical proprieties of iron oxyhydroxides are variable, but usually in the presence of water iron phases are completely hydroxilated. This can be

understood as a two step reaction which is shown schematically in Figure 2.5 (Haese 2000).

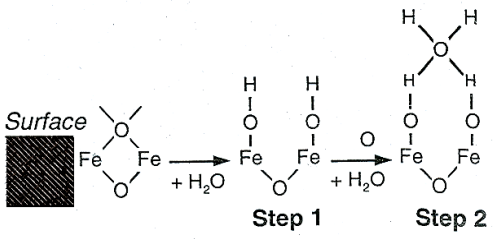

Figure 2. 5. The hydroxylated surface of iron oxides

The hydroxylated surface of implies that most metal – iron oxide binding mechanisms are the outer-sphere type. However the large variations where iron phases preclude a full generalization of this mechanism due to the fact that metal species present in the system (anions, cations complexes) can vary dramatically as a function of changing environmental conditions. Thus, a full and individual characterization of the adsorbent (*e.g.,* chemical surface properties) as well as of the adsorbate (*e.g.,* geochemical modelling) in the conditions of interest is needed in order to understand the surface bonding mechanisms.

2.6.3. Micro-precipitation

Multinuclear complexation is also possible in certain cases. When the sorption densities is high a monolayer of adsorbed metal atoms often forms a solid surface layer of the metal (*e.g.,* hydroxide or oxide phase) phenomenon which is called precipitate (Figure 2. 6). The appearance of precipitate is strongly correlated with metal concentration (saturation index of metal ion), pH and its solubility product (Bradl 2005).

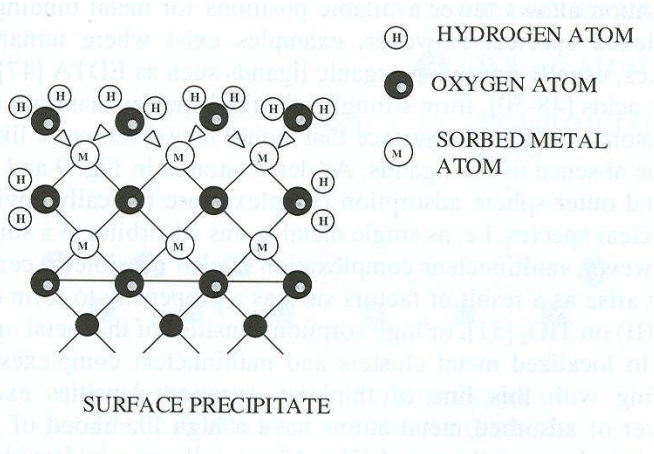

Figure 2. 6. Schematic sketch of surface precipitation at the mineral /water interface (Bradl 2005).

Precipitation can take place when the pH of a solution or/and element concentration varies near the stability field of the appropriate solid phase (*e.g.,* as a consequence of cellular metabolism or pure chemical mixing of an acidic solution with an alkaline one). The metal uptake from solution is sometimes associated with active defence of biomass (bio-mineralization), producing compounds which favour precipitation (*e.g.,* sulphate-reducing bacteria producing sulphuric acid which decreases the pH of the surrounding environment) via following reactions:

$$2S + 3O_2 + 2HOH \text{ ------> } 2H_2SO_4 \text{ (}\textit{Thiobacillus thiooxidans}\text{)}$$

$$12FeSO_4 + 3O_2 + 6HOH \text{ ------> } 4Fe_2(SO_4)_3 + 4Fe(OH)_3 \text{ (}\textit{Thiobacillus ferroxidans}\text{)}$$

2.7. Surface complexation modelling of metal sorption onto oxyhydroxides

Adsorption of metal species onto oxyhydroxides is often modelled with the following models: Constant Capacitance Model (CCM), CD-Music layer model (1-pK CDM) (Gustaffson, 2003; Goldberg et al., 2002), triple layer model (TLM) or diffuse layer model (DLM: 2-pK DLM) (Bradl 2005). The aim of the modelling is to determine the mechanisms and calculate intrinsic constants of the complexes formation.

CCM is generally described as the surface complexation model which gives information about binding mechanism as either momo - or bidentate complexes (Goldberg et al. 2002; Gustafsson 2003).

CDM was used by Hiemstra and Van Riemsdijk (1996) and Bourikas et al., (2001) to describe MoO_4^{2-} sorption onto titanium oxides and their results suggested that at low pH adsorption was dominated by bidentate complex formation, while at high pH monodentate complex formation dominated. For the molybdenum adsorption onto goethite, using the same model, Gustafsson (2003) added the $FeOMo(OH)_5^{-0.5}$ specie with a log K_{int} = 18.28 to fit the adsorption data at low pH better. His study suggested that the adsorption of MoO_4^{2-} onto ferrihydrite can be described with two monodentate surface complexes via both, CDM and DLM, surface complexation models (Gustafsson 2003).

(Dzombak and Morel 1990) suggested the DLM model as the most suitable for modelling ion adsorption onto iron oxyhydroxides. In addition the TLM model has been used for modelling metal adsorption data onto kaolinite and illite as well as soils and sediments (Sarkar et al. 2000; Wen et al. 1998) .

The diffuse double layer model combines the chemo-sorption approach with the electric double layer (EDL) theory proposed by Gouy-Chapman (Dzombak and Morel 1990). An illustration of the two layer concept (a surface layer and a diffuse layer of counter-ions in solution) representing the diffuse layer model for oxide/water interface is given in Figure 2. 7.

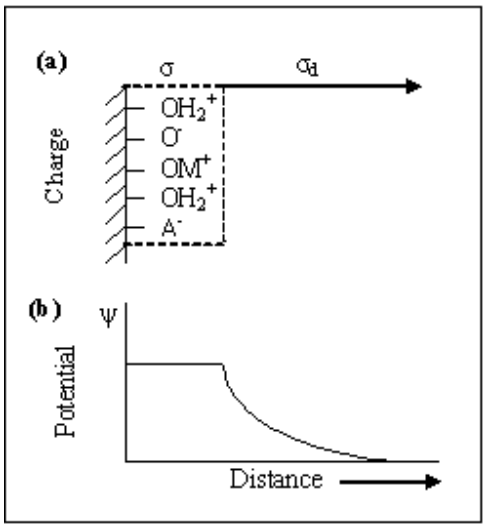

Figure 2. 7. Schematic representation of ion binding on an oxide surface: (a) surface charge distribution; (b) potential decay in the diffuse layer (after (Dzombak and Morel 1990)).

A detailed description of the theoretical background and the appropriate equations is given in Dzombak and Morel (1990) and Langmuir (1997).

The DLM is a default model included in the Visual MINTEQ 2.32 software and is usually used for surface modelling of many ions onto a variety of adsorbents, including iron oxides. As shown above, modelling of molybdenum adsoption onto ferrihydrite at different pH values has so far been poorly studied (Gustafsson, 2003), modelling studies of vanadium adsorption onto ferrihydrite at different pH have not so far been done. Thus, in this work modelling of vanadium and molybdenum adsorption onto ferrihydrite at pH 4-9 with the DLM in the Visual MINTEQ 2.32 code was carried out and the results were compared with the experimental results in order to validate the default models for these two metals.

2.8. Molybdenum

2.8.1. Chemistry

Molybdenum has the atomic number 42 and an atomic weight of 95.94 $gmol^{-1}$. It is a silvery white metal of great hardness with melting point of 2617 ºC and a density of 10.22 g cm^3. It occurs in the oxidation states of II, III, IV, V and VI, with oxidation states V and VI predominantly in nature. In these oxidation states it has an affinity for oxides and for sulphur and oxygen containing groups. In dilute oxic solutions, the predominant form is the molybdate anion (MoO_4^{2-}), while under reducing conditions the stable oxidation state is Mo (IV). Sometimes molybdenum is enriched in marine sediments overlaid by an anoxic water column, as MoS_2. However, the sulfide concentration of the water column of most lakes is too low to allow the precipitation of pure Mo-sulfide phases.

In aqueous systems, molybdenum forms soluble anionic species. Below pH 4 $HMoO_4^-$ and H_2MoO_4 are the most common species; above this pH, MoO_4^{2-} becomes the major species (Figure 2. 8).

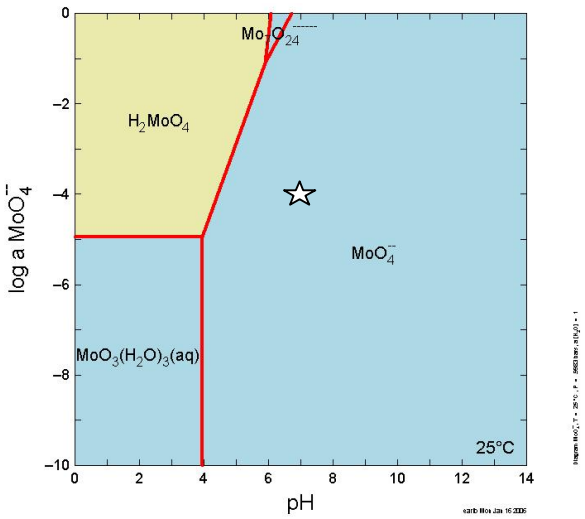

Figure 2. 8. Molybdenum speciation as a function of pH and concentration (activity). The blue zone indicates aqueous phases whereas yollow zone indicates solid phases. Diagram was drawn, in standard conditions (pressure of 1 atm, temeprature of 25°C and fCO_2 of 0.0035) using the Geochemist's Workbench® 6.0 code. The star indicates molybdenum concentration used in most of experimental studies from this thesis

Molybdenum adsorption onto iron oxides is strongly pH dependent and increases with decreasing pH (Bradl 2005).

Molybdenum in concentrations above 100µM and at low pH values tends to polymerize to form different polymolybdate species (Goldberg et al. 2002; Gustafsson 2003). In oxic lakes molybdenum is present as MoO_4^{2-}. Schaller et al., (1997) cited co-precipitation of molybdenum with manganese oxides as one of the main processes for molybdenum removal from the water column. Along with co-precipitation of Mo (VI) with mixed $FeS{\cdot}MoS_3$ phases as well as diffusive transport of dissolved Mo (VI) into the sediment they suggested these processes as the main mechanisms for molybdenum removal. They also suggest that the oxidation of dissolved Mn (II) at the redox gradient could promote the adsorption of molybdenum onto the freshly formed oxide surfaces (Schaller et al. 1997).

At low concentrations, molybdenum is an essential micronutrient for plant growth, but it can be also considered a pollutant when its concentration is high in environmental media (Goldberg et al. 2002). In seawater it is present as molybdate (MoO_4^{2-}), in concentrations varying around 0.1 $\mu molL^{-1}$ (or 9 -13 μgL^{-1}(Hanson et al. 1977) or 9 -11 (Furnace and Rainbow 1990)). However, matrix interferences, makes molybdenum determination in seawater difficult and therefore this research topic is still under the attention of many analytical chemists (See chapter 7).

2.8.2. Molybdenum determination in seawater and complex matrices

Flame atomic absorption spectrometry (FAAS), inductively coupled plasma optical emission spectrometry (ICP-OES), graphite furnace atomic absorption spectrometry (GFAAS) are analytical techniques which can be used for molybdenum determination as a function of sample type and the concentration expected to be found. Because of low concentration in different media, including seawater, its determination might require a pre-concentration step (Ferreira et al. 2004; Ferreira et al. 2002; Ferreira et al. 2001)
Some molybdenum pre-concentration methods for different types of samples are presented as follow:

- Pre-concentration procedures by co-precipitation;
- Pre-concentration by liquid–liquid extraction;
- Pre-concentration by solid–liquid phase extraction.

Pre-concentration procedures by co-precipitation are characterized by the formation of insoluble compounds. The phenomenon can be associated with metal adsorption onto a precipitated surface. This pre-concentration method has been proposed mainly for water samples analysis. For example, molybdenum determination in seawater samples as well as biological samples can be pre-concentrated through the co-precipitation procedure using as precipitant ammonium pyrrolidine-1-carbodithioate (APDC) and dissolvent methyl izo-butyl ketone (MIBK) or HNO_3 1M. These are analyzed by GFAAS with a limit of detection of about 0.5 μgL^{-1} (Fujiwara et al. 1986; Jin et al. 1987). Due to the fact that these procedures are laborious and time consuming, they are little used.

Pre-concentration by liquid-liquid extraction is based on the absorption principle. Two immiscible liquid phases and a molybdenum complexed phase are transferred from one liquid (usually the sample) into another organic liquid (absorbent). Even if this method has the disadvantage of using high amount of toxic organic solvents, it is still the most used technique for molybdenum pre-concentration. An example of a pre-concentration method using the solvent extraction procedure for seawater samples, is given by Mcleod et al., (1981), who has used dithiocarbamate as an extracting agent and chloroform as a solvent before using an ICP-OES for analysis. For GFAAS analyses Monien et al., (1980) has chosen tetramethylenedithio-carbamate as an extractant. Ferreira and collaborators (2001) cited other complexing reagents for liquid-liquid extraction: *e.g.,* caffeic acid and 5,5'- ethylene-disalicylohydroxamic acid (Ferreira et al. 2001).

Pre-concentration procedures using solid–liquid extraction consist of the adsorption of a metal ion in the form of a complex onto a solid material (adsorbent), with a latter desorption using an eluent. This technique has been very often used in pre-concentration procedures for molybdenum determination (Ferreira et al. 2004 and references therein). A solid matrix of the activate carbon or specific adsorption resins (e.g. Amberlite XDA-4) was used and as a reagent calmagite was used for ICP-OES and sodium bis-(2-hydroxyethyl) dithio-carbamate for GFAAS, respectively (Ferreira et al. 2004).

Recently, researchers were looking for new procedures which can reduce the time for the pre-concentration protocol and determination, thus they developed on line systems for pre-concentration and determination of molybdenum. Some of these new techniques achieve a very good limit of detection (limit of detection 0.2µg L^{-1}) and relative standard deviation (relative standard deviation of about 2-5% using activate alumina and as eluate NH_3 2M) (Greenfield et al. 1989).

For molybdenum analysis from iron matrices, Ferreira et al., (2001, 2004) recommend an additional preparation step due to major interferences with iron which can occur during determination.

Iron as well as other elements (*e.g.,* Al, Ti) oxides are considered important mineral sorbents for molybdenum (MoO_4^-) as they acquire positive charge at low pH. Gustafsson (2003) referenced that the binding mechanism of (MoO_4^-) onto ferrihydrite is by surface complexation with the formation of either momo- or bidentate complexes.

Despite of all these studies so far, more studies, in term of new sorbents or ion exchange resins can be tested to pre-concentrate molybdenum from seawater matrices.

2.9. Vanadium

2.9.1. Chemistry

Vanadium has the atom number 23 and a atomic weight of 50.94 $gmol^{-1}$.

Vanadium is an essential trace element for plants and animals that acts by stimulating the synthesis of chlorophyll in plants and promoting the growth of young animals (Ferreira et al. 2002).

The distribution of vanadium among different oxidation states plays an important role in its environmental chemistry. In aqueous solutions vanadium can exist in the II, III, IV, and V oxidation states. The two most common forms, principally present in natural waters, are IV and V, which have different toxicities. Vanadium (V) is more active than other species and occurs as VO_2^{+} (vanadyl) and VO_4^{3-} (vanadate) in acid and alkaline media, respectively. In reducing environments, the usual form which has been detected is V(IV). In contrast, it was predicted that V(V) species are thermodynamically predominant in oxic environments. Vanadium (IV) is present as the oxo-vanadium cation, which is stable in acidic media and can be oxidised to V(V) in alkaline solutions. The literature contains reports about the presence of a mixture of V(V) and V(IV) in solution (Naeem et al. 2007).

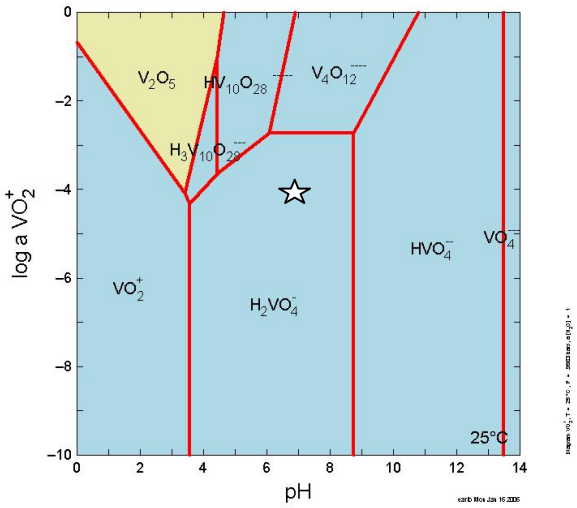

Figure 2. 9. Vanadium speciation as a function of pH and concentration (activity). The blue zone indicates aqueous phases whereas yollow zone indicates solid phases. Diagram was drawn, in standard conditions (pressure of 1 atm, temeprature of 25°C and fCO_2 of 0.0035) using the Geochemist's Workbench® 6.0 code. The star indicates vanadium concentration used in most of experimental studies from this thesis.

It is accepted that vanadium (V) exists in environments which are in contact with atmospheric oxygen and vanadium (IV) is most likely to be present in reducing environments. Different factors affect the distribution of vanadium between these two oxidation states: for example the presence of organic matter (*e.g.,* humic acids) and the acidity of the environment. For instance, at low pH (3.5) vanadium (IV) is also stable in the presence of oxygen, this oxidation state changes above this pH. Thus, the control of vanadium valences in aqueous solutions is a major problem. However, in seawater system vanadium was found to be as pentavalent vanadium whereas in anoxic sediments it may exist in its reduced form, also.

Of major interest is the V/Fe ratio in hydrothermal plume particles which are sensitive indicators for dissolved phosphate concentration at depths where ferrihydrite forms. Feely et al., (1998) suggested that ferrihydrite particles form in the oxidic plume and scavenge vanadium. The V/Fe ratio remains constant as they disperse away from the vent field. Feely et al., (1998) sited German et al., (1997) who have observed a very high V/Fe ratio in plume particles near the Rainbow vent field on the Mid-Atlantic Ridge (Feely et al. 1998). They found a V/Fe ratio of 0.0030 in the superficial sediments collected approximately 8 Km away from the vent field of Juan de Fuca Ridge. The ratio is about the same in hydrothermal plume particles in the overlying water column. Taking into account the relationship between the V/Fe ratio and the dissolved phosphate concentration in hydrothermal plume particles and sediments on site and off site of hydrothermal vents, the V/Fe ratio in mid ocean sediments might provide significant information about long term variation of dissolved phosphate concentration in deep seawaters.

Vanadium concentrations in typical fresh waters and seawaters are quite low (2-3 $\mu g\ L^{-1}$ (Ferreira et al. 2002)) and as a result, especially in seawater, vanadium determination in such complex matrices is not very easy. Thus, new pre-concentration techniques are being developed to avoid interferences caused by matrix content during vanadium quantification.

2.9.2. Vanadium determination in seawater and complex matrices

The concentration of vanadium in seawater is between 2-3 $\mu g\ L^{-1}$ (or about 39 $nmolL^{-1}$) (Ferreira et al. 2002) and up to 40 nmol L^{-1} (Abbasse et al. 2002) while in the deep ocean Feelly et al (1998) cite as vanadium being uniformly constant at about 0.000687-0.0007263 $\mu g\ L^{-1}$.

Lilley and co-workers (1995) detected vanadium concentrations in seawater of 35-37 nmol kg^{-1}. The average concentration of vanadium in Northeast Pacific deep ocean particulate matter collected from depths ranging between 1800-2800m at 50º 08.1'N, 140º 19.6'W was 0.013 ± 0.007 nmol L^{-1}, while in the neutrally buoyant plume of the vent fields over the Juan de Fuca Ridge, the average concentration of vanadium was 0.26 nmol L^{-1} (Lilley et al. 1995)

Due to the overall low concentration of vanadium in seawater, Ferreira and collaborators (2002) and Abbasse et al., (2002) have developed pre-concentration methods for vanadium determination in seawater prior to measurement with ICP techniques. Such methods include: solvent extraction, precipitation, co-precipitation, and ion exchange. Solvent extraction and co-precipitation have been commonly used for the pre-treatment of vanadium, but they are laborious and carry a risk of contamination and the possibility of interference effects.

In the 80`s several scientists examined the pre-concentration and separation techniques of vanadium from complex matrices using chelating resins containing the imino-diacetate group (*e.g.,* Chelex-100). To separate the V(V) and V(IV) the method used at that time was based on sorption of both V(V) and V(IV) at pH 4.5 and separation by stripping V(V) under basic conditions (pH ~10) and then V(IV) under acidic condition (pH~0.8). Another method used ethylene-diamine-triacetate (EDTA) immobilised on silica gel for separation of V(V) and V(IV). In this method both V(V) and V(IV) were eluted under acidic conditions using HCl 6 mol L^{-1} (Abbasse et al. 2002).

Abbasse (2002) also discussed chelating organic ligands such as 8 - hydroxyquinoline, luminol, or dithizone which were added individually to filtered seawater samples at different pH in order to complex dissolved vanadium species; the resulting vanadium–organic complexes were then sorbed on to a C_{18} column. Another procedure investigated was direct percolation of filtered seawater samples at different pH over different chelating resins such as chelamine, chelex-100, and immobilised 8-hydroxyquinoline. Vanadium ions sorbed onto these resins were then desorbed using small quantities of acidic solutions and then analyzed with ICP–AES.

Ferreira et al., (2002) have studied and then optimized a pre-concentration method which used 1-(2-pyridylazo)-2-naphthol (PAN) as a complexing reagent on a solid phase matrix such as active carbon. For metal determination they used an ICP-OES. They also mentioned the recent work of some other authors, who have used matrices such as: Naphthalene, Amberlite XAD-2000; alumina; Amberlite XAD-2; Amberlite XAD-4; and chloromethylated polystyrene, as well as cloud-point extraction.

In 1988, Shieh and Duedall, conducted adsorption experiments of dissolved vanadium V(V) onto synthetic amorphous ferric oxyhydroxide using synthetic seawater medium. They found that adsorption of V(V) onto amorphous $Fe_2O_3 \cdot H_2O$ in seawater was rapid and reached a quasi-equilibrium condition within 1 hour under laboratory conditions. The pH was the major factor influencing adsorption of V(V) onto amorphous $Fe_2O_3 \cdot H_2O$ (Shieh and Duedall 1988).

Chapter 3
General methods

3.1. Introduction

The studies presented in this thesis were performed under laboratory conditions and no field work is included. The experimental setup, protocols, as well as the tehniques used to analyse liquid and solid samples are described in this chapter.

Briefly, the sythesis of the starting material studied along with common and high resolution characterization techniques are first desribed. The characterization of the staring material was a compulsory topic for further interactions and transformation investigations. Thus, solid phase characterization tehniques such as: Scanning Electron Microscopy Transmission Electron Microscopy (particles and aggregates visual and semi-quantitative characterization), BET (particles surface area), Dynamic Light Scaterring (particles and aggregates size range), high resolution potentiometric titrations (surface charge properties), X-Ray Diffraction (solid phases chemical characterization/ identification) provided an excellent physico-chemical characterisation of our nanoparticulate and very amorphous starting material.

In the next part of the thesis, sets of laboratory based experiments and their protocol are detailed. These experiments were conducted to quantify molybdenum and vanadium uptake onto and with ferrihydrite and identify the mechanisms of their interactions under different environment conditions. Typical batch experimental setups were used for mineral synthesis as well as for adsorption studies. Solution phase analysis (from adsorption, desorption, co-precipitation and digestion experiments) were done with different Inductively Coupled Plasma techniques such as Optical Emission Spectrometry and Mass Spectrometry, as they were available time planning and financially. Solid samples from adsorption, coprecipitation and transformation experiments were characterized with diffraction techniques.

Ferrihydrite transformation is another important topic of this thesis. The experiments were carried out at different temperatures (from 4 to 140°C) using common laboratory appliances, such as fridges and digital ovens, but also specific hydrothermal chambers for high temperatures *in-situ* synchrotron experimental setups.

Tw types of synchrotron tehniques were used at the SRS Daresbury Laboratory, UK. At Staion 16.4, *in-situ* Energy Dispersive-X-Ray Difraction transformation experiments

of ferrihydrite with and without molybdenum and vanadium under different environmental conditions were performed. Such techniques allowed recording the kinetic and interpreting the thermodynamic of ferrihydrite transformation into more stable phases such as hematite and the effect of molybdenum and vanadium associated (via coprecipitation and adsorption) with ferrihydrite as well as the effect of ionic strenghts. X-Ray adsorption Spectroscopy was used to assess the speciation of molybdenum in adsorbed and co-precipitated ferrihydrite as well as to confirm its fate in ferrihydrite transformation end-product.

In addition to the above mentioned experimental and measuring techniques, two bio-geochemical modeling packages were used to understand solution chemistry prior to adsorption studies, but also to compare the adsorption experimental results with their simulation outputs. Thus, Act2 module of the Geochemist's Workbench® 6.0 code was used to draw speciation and solubility diagrams of molybdenum and vanadium in fresh and seawater systems under standard conditions (pressure 1 atm and temperature of 25°C). Visual MINTEQ 2.32 code was used to simulate molybdenum and vanadium pH - dependendance set of experiments and allow the comparison of theoretical modeled outputs with experimentally obtained uptake capacities.

A series of basic (e.g. Microsoft Office (Microsoft ®), Origin Pro 8 software (OriginLab 2007)) and specific (e.g. X-fit (Cheary and Coelho 1996), EXCALIB, EXBROOK, EXSPLINE (Dent and Mosselmans 2003; Spadini et al. 2003) and EXCURV98 (Binstead 1998)) softwares were used for data processing, interpretation and display.

3.2. Ferrihydrite synthesis and characterization

3.2.1. Pure ferrihydrite

2-line ferrihydrite (FHY) was synthesized following the method of Cornell and Schwertmann (2000). Briefly, a 0.127 M Fe $(NO_3)_3$ $9H_2O$ solution (constantly bubbled with nitrogen, N_2, gas to avoid CO_2 equilibration) was brought to pH 7.2 under constant stirring by adding drop-size 1 M NaOH solution. The iron solution was prepared from nitrate iron salt (analytical grade from Ficher Scientific) which was used carefuly after opening the container (as is a hygroscopic salt). Care was taken to seal the container properly after each use.This change in pH lead to the precipitation of a yellow-brown slurry which was repeatedly centrifuged and washed with18.2 MΩ deionised water (to eliminate the salt content). Consecutive washing treatments were done until the total dissolved solid (TDS) concentration (measured with Water PAL Sprinte™ Industries TDSmeter) was close to zero (~10 ppm). The resulting slurry was subsequently stored in a sealed plastic bottle at 4^{o}C and pH 7. This method resulted in the precipitation of about 10 g of a heavily aggregated amorphous phase consisting of 2-line ferrihydrite (Cornell and Schwertmann 2000). The slurry was used for all adsorption and transformation studies (Chapters 4 to 6) within three months (tests showed that the ferrihydrite remained stable if kept as slurry and at low temperatures).

Note that in all experiments described below the ferrihydrite was used as slurry and not as dried material, because upon drying the ferrihydrite changes surface area, particles size, crystallography, etc. It was also observed that if the ferrihydrite slurry was kept at temperatures below 0ºC, the properties of the slurry change upon freezing (i.e., increasing aggregation). All results described in the subsequent chapters will be expressed in terms of dried weight ferrihydrite. The conversion from wet slurry to dried weight ferrihydrite was done taking into account the density of the slurry after synthesis. Aliquots (in triplicate) of the ferrihydrite slurry were dried overnight at 40-50 ºC and the density was calculated from the difference between the dried weight and the wet weight. The samples were also dried in the oven either at 40ºC overnight or freeze dried (with an EC Modulyo freeze drier at -50ºC and 7 mbar) for Brunauer, Emmett and Teller (BET) and X Ray Diffraction (XRD) measurements, respectively.

3.2.2. Ferrihydrite co-precipitated with molybdenum and vanadium

Specific amounts of molybdenum (VI) and vanadium (V) were added to the ferrihydrite synthesis solutions. A molybdenum salt (Na_2MoO_4 – 99.0-101.0% for analysis Certified AR, Ficher Scientific) was dissolved in a 0.127 M NaOH solution while a vanadium salt (Na_3VO_4 – 99% m.p., Acros Organics, Ficher Scientific) was dissolved in the starting 0.127M Fe $(NO_3)_3 \cdot 9H_2O$ solution to avoid precipitation of molybdenum or vanadium phases and to respect the metals speciation in the aqueous solutions (see also below). The aim was to have molybdenum present as MoO_4^{2-} and vanadium present as VO_2^+. The co-precipitation experiments were carried out using initial concentrations of molybdenum and vanadium between 1 and 50 000 µM. Each synthesized co-precipitated ferrihydrite batch resulted in ca. 10g of material containing between 0.001% and 50% metal:Fe molar ratios. Note that in all subsequent descriptions these samples are referred to as 0.001%; 0.01%; 0.1%; 0.5%; 1% 5% 10% and 50% molybdenum or vanadium co-precipitated ferrihydrite.

3.2.3. Ferrihydrite characterization

(a) Metal concentrations

The amounts of co-precipitated molybdenum and vanadium were determined by measuring the concentration of molybdenum and vanadium that remained in the supernatant after ferrihydrite precipitation (*i.e.,* not removed by the co-precipitation), as well as by measuring the concentrations of molybdenum and vanadium in the digested solid phases (see below). All molybdenum and vanadium analyses were carried out either by Inductively Coupled Plasma Mass Spectrometery (ICP-MS) or by Inductively Coupled Plasma Optical Emission Spectrometery (ICP-OES). An ICP-MS Agilent 7500ce, Octopole Reaction System using helium gas and 10 ppm Rh internal standard was used for molybdenum and vanadium measurements for the particle concentration effect studies, phosphorus competitive studies and co-precipitation and adsorption isotherms studies. For the rest of the experiments (partitioning experiments, studies of pH effect on adsorption, studies of molybdenum and vanadium adsorption in different matrices) an ICP-OES (Perkin Elmer Optima 4300DV) was used to measure the molybdenum and vanadium

concentration in the adsorption supernatants. Three measurement replicates were run for each sample using three different wavelengths. For molybdenum λ = 202.021, 203.835 and **204.588nm** and for vanadium λ = 290.867, 310.215 and **309.299nm**, respectively. The wavelengths in bold were choosen as the best from the axial (for Mo) and the radial (for V) intensity readings. Regression factor of the calibration curve for the chosen concentration interval were close to 1. For the samples co-precipitated with low concentration of molybdenum or vanadium (below 1%, metal:Fe initial molar ratios), the quantification of the molybdenum and vanadium concentrations in the supernatant was more difficult due to the presence of high sodium concentrations in the matrix which could have caused problems to the injection system (an desirable dilution required for sodium would not be appropriate for molybdenum analysis). For these samples the total concentrations of molybdenum and vanadium in the solid phase were derived from a sequential extraction approach (see below). In contrast, for the samples co-precipitated with high concentrations of molybdenum or vanadium (above 1%) the supernatant measurements were confirmed by, and were in agreement with, the quantitative measurements obtained from the solution from the digested solid.

The amount of molybdenum retained via absorption was calculated from the supernatant analysis using mass balance equation.

The choice of ICP-OES *vs.* ICP-MS was made by their availability at the specific experimental timing and financial respects.

(b) Iron phase sequential extractions

Iron phase sequential extractions were used: (i) to quantify the amount of molybdenum and vanadium associated with the ferrihydrite (as starting material) as well as with its transformation end-product (see subchapter 3.4 and 3.8) and (ii) to quantify the ferrihydrite transformation progress in the off-line transformation experiments (see subchapter 3.6). .

Generally, poorly ordered iron oxyhydroxides such as ferrihydrite, lepidocrocite schwertmanite can be extracted in ammonium oxalate and oxalic acid.
Cornell and Schwertmann (2000) recommend this technique to estimate the degree of transformation of goethite and hematite when they are formed from ferrihydrite under different conditions.

In the absence of light, the oxalate buffer solution, which consists of 0.2 M ammonium oxalate brought to pH 3 with 0.2 M oxalic acid, reductively dissolves ferrihydrite within 2 hours while leaving the crystalline goethite (and hematite) essentially undissolved.

The ratio of oxalate soluble Fe to total Fe (derived by complete digestion of the samples using 6M HCl) gives the proportion of ferrihydrite in the sample. During the extraction, the samples were stirred to ensure total dissolution of the solid phase. Due to the fact that in the presence of light some of the iron phases may dissolve (possible photo-reduction of Fe^{3+}), light has been excluded by wrapping the digestion vessel in aluminum foil.

To avoid precipitation of Fe (II) oxalate in the filtrate extracts and thus to avoid underestimation of the oxalate soluble iron, the amount of oxalate used was never below 1mL per mg oxalate soluble Fe (Cornell and Schwertmann 2000); thus 10 mg ferrihydrite (or mineral mixtures) were dissolved in 10 mL oxalate (or HCl for total Fe measurement) for all digestions.

The iron concentrations in the solutions from both extractions (oxalate and hydrochloric acid), after appropriated dilutions, were measured using the colorimetric Ferrozine method (Viollier et al. 2000).

(c) Field Emission Gun - Scanning and Transmission Electron Microscopy (FEG-SEM/FEG-TEM)

FEG SEM/TEM allowed the evaluation of the size and morphology of individual particles and aggregates as well as the identification of the solid mineral phase composition and their crystallographic parameters.

FEG – SEM imaging was performed with a *LEO 1500* Series microscope with a GEMINI column. Images were collected at 3 keV at a working distance of 3-6 mm with the samples deposited on an Al stub and after coating with 3 nm of Platinum.

TEM investigations were carried out with a FEI CM200 FEG-TEM operating at 197kV which was fitted with a Gatan Imaging filter (GIF 200). Selected area electron diffraction (SAED), bright field images (BFI) and energy dispersive X Ray Spectrometric (EDS) analyses were used to obtain quantitative diffraction patterns (SAED) and semi-quantitative molar ratios for Mo:Fe and V:Fe (EDS). In all cases the EDS analyses were collected on at least 3 different points on a sample to assess the homogeneity of the element distribution in the samples.

Selected area electron diffraction (SAED) patterns from the examined area were obtained at each electron dose and compared with standard XRD tables of *d*-spacing for reference iron oxides.

The values of the *d*-spacing from the SAED patterns were calculated using the following equation:

$$d = \frac{\lambda L}{r} \qquad \text{(Eq. 3.1.)}$$

where: *d* is *d*-spacing (in Å), λ (beam energy wavelength); L (the distance between the beam source and the sample stub) is 24·1 (Åmm) and *r* is the radius of the sample's circle from SAED pattern – mm.

(d) X-Ray Diffractions (XRD)

A PHILIPS PW 1730/10 X-Ray powder diffractometer was used to identify the mineralogical composition and purity of the starting pure as well as metal co-precipitated ferrihydrite. In addition, transformation intermediate products and end-products (see subchapter 3.6.2) were also characterized using XRD.

Dried samples (overnight in the oven at 40ºC) were deposited onto a silicon sample holder and a diffraction pattern was collected using a CuKα radiation source with a wavelength 1.54Å. Data were collected for 2-θ (2-theta) between 5 – 70° at a scan rate of 0.08 ^{o}/minute; a step size of 0.01º, and working at 40kV and 30mA. These settings lead to long scans (~14h) which insured that the presence of even small quantities of other phases could be identified. Scans of the experimental materials were compared with standard traces from the JCDD database.

(e) BET – surface area

The Brunauer, Emmett and Teller (BET) technique is one of the best-known methods for surface area measurements (Brunauer et al. 1938).

In this study a Micromeritics Gemini V Series analyzer, using He gas, was used to measure ferrihydrite surface area. A known amount of freeze dried ferrihydrite was degassed under N_2 with a VacPrep degasser for 12 hours and the surface area was determined at a fixed gas (He) evacuation rate of 100 mmHg min^{-1}, an optimum pressure of 765 mmHg and an equilibration time of 5 sec.

(f) Dynamic Light Scattering (DLS) and Laser Diffraction (Mastersizer)

Dynamic Light Scattering is a technique that uses a laser light and which can provide information on the size and polydispersity of particles, generally in a submicron range. DLS measures the intensity of back-scattered laser light caused by the Brownian motion of particles suspended in a solution. This technique assumes that all particles are spherical in shape.

For this work a Zetasizer Nano ZS, unit from Malvern Instruments was used to measure the ferrihydrite particle sizes.

The hydrodynamic diameter of the particles was derived from the transitional diffusion coefficient using the Stokes Einstein equation:

$$d(H) = \frac{kT}{3\pi\eta D} \qquad \text{(Eq. 3.2.)}$$

Where: *d(H) is* the hydrodynamic diameter in water; *D is* the translational diffusion coefficient in water; *k is* the Boltzmann's constant (1.38065×10^{-23} JK^{-1}); *T is* the absolute temperature in K and η is the viscosity in water (at 20°C being 100.2 N s/m^2).

Ferrihydrite particle size measurements were performed at different ionic strengths (0, 0.01, 0.7 and 1) with Mlavern Mastersizer and particle concentrations (0.001; 0.002; 0.004 and 0.006 gL^{-1}) with Malvern Zetasizer.

The measurements with Zeta sizer were performed in 1 cm plastic cuvettes at 21ºC using a laser beam with a λ= 633nm at an angle of the detector of 173º.

For the ionic strength effect on particle size study, the particle size was measured with another type of laser diffraction unit, called Mastersizer instrument. This technique releases a focused laser beam passed through a vessel where the particles are suspended in dynamic regime (mixing speed up to 3000 rpm). The light is scattered by the particles under specific angles which are inversely proportional to the particle size. A couple of photosensitive detectors measure the angular intensity of the scattered light. Thus, for comparison with Zetasizer Nano ZS (scattered light is collected by one detector fixed at 173º) the scattered intensity is collected by a series of detectors from different angles. The particle size is calculated from the projection of scattering intensity versus angle using the Mie scattering model. The Mastersizer 2000 software which contains this model is used to accuratelly measure the particle size (from 0.02 µm to 2000 µm) across a wide dynamic range (MalvernLab 2000).

(g) Potentiometric titrations

Potentiometric titrations were carried out to evaluate the surface charge properties of pure ferrihydrite and of ferrihydrite with co precipitated metals at different ionic strenghts (IS), in the presence and absence of CO_2 for the range of pH between 4 and 10.

All titrations were carried out with a Man -Tech Inc. auto-titration system equipped with an automatic burette (PC-Titrate^{TM}) with three ports: a glass pH electrode, a titrant injector and a thermometer. The data were recorded via interactive computer titration software. Experiments were conducted in 250 mL beakers on a magnetic stirrer plate (600 rpm). Prior to each titration, the pH electrode was manually calibrated using VWR certified pH standard solution. Working temperature was room temperature (21°C ± 0.5°C).
A standard titration protocol involved equilibrating a ferrihydrite suspension in 100mL of an electrolyte background solution and titrating both from high pH to low pH and from low to high pH with either HCl or NaOH to establish hysteresis effects. Sets of titrations were done as follows:

- 1. Titrations of ferrihydrite at different particle concentrations (1g and 2gL^{-1}), constant injection flow of 0.05mL min^{-1} and ionic strength 0.1.
- 2. Titrations of ferrihydrite at different contact times between base or acid injections (1min and 10 min) to allow homogeneous surface contact of the titrate, constant ferrihydrite concentration (1g L^{-1}) and ionic strength 0.1;
- 3. Titrations of ferrihydrite at different ionic strengths: (0.01; 0.1 and 1) by varying the electrolyte (NaCl) concentration but at constant titration flow (0.05mL min^{-1}) in order to assess the influence of ionic strength on the ferrihydrite surface charge properties;
- 4. Titrations of ferrihydrite with and without CO_2 present: to assess the influence of carbonic acid on the ferrihydrite surface in the pH interval between 4 - 10 at a solid concentration of 1gL^{-1}, 0.05mL min^{-1} N_2 gas flow and an ionic strength of 0.1. The CO_2 presence was avoided by titrating the ferrihydrite slurry in a closed system that was continuously purged with N_2 gas.
- 5. Titrations of ferrihydrite with and without co-precipitated molybdenum and vanadium (1% molar ratio): to assess the influence of co-precipitated metals on the surface properties; these titrations were carried out with 1gL^{-1} co-precipitated ferrihydrite and at an injection flow of 0.05 mL min^{-1} and at ionic strength 0.1.

The first two titration sets were conducted to determine the optimum titration parameters and the best titration conditions for latter three sets.

3.3. Geochemical modelling

The geochemical modeling carried out in this thesis had the goal of identifying the aqueous or solid species present and the saturation limits for molybdenum and vanadium in the studied systems and to determine the optimal conditions as well as the metal speciation as a function of pH for the experimental adsorption studies (Geochemist's Workbench® 6.0 code). In addition, modeling of the experimental adsorption studies were done to compare practical results obtained in the laboratory with the ones given by geochemical software (Visual Minteq 2.32 code) with respect to the given process conditions.

3.3.1. Geochemist's Workbench® 6.0

Speciation diagrams of Mo (VI) and V (II, III, IV and V) as a function of pH were calculated using the Geochemist's Workbench® 6.0 software (Bethke 2002) with the thermodynamic data at standard conditions (T = 25ºC, P = 1.013 bar and fCO_2 = 0.0035) using solution compositions representing either distilled water (18.2 MΩ) or a seawater system (Table 3.1.)

For modeling the speciation of molybdenum and vanadium with Geochemist's Workbench® software the databases: "thermo2000.dat" for molybdenum and "thermo_minteq.dat" for vanadium were used.

Molybdenum speciation was modeled only as Mo(VI) as all other oxidation states are not relevant because they are less available in common oxic environments. The distribution of vanadium among its various oxidation states plays an important role in its environmental chemistry because the two most common forms present in natural waters, V(IV) and V(V) have different degrees of toxicity. Vanadium III, IV and V speciation in distilled systems and for V(V) (in seawater as is the most common species in the seawater) were simulated.

Table 3. 1. Composition of the seawater (after Dr. J Floor Anthoni 2000, 2006) used in the modeling

Element	**Atomic weight**	**ppm* (mg/kg)**
Hydrogen	1.00	110,000
Oxygen	15.99	883,000
Sodium	22.98	10,800
Chlorine	35.45	19,400
Magnesium	24.31	1,290
Sulfur	32.06	904
Potassium	39.10	392
Calcium	10.08	411
Bromine	79.91	67.3
Molybdenum	95.94	0.01
Vanadium	50.94	0.0019

* (URL: http://www.seafriends.org.nz/oceano/seawater.htm)

3.3.2. Visual MINTEQ V 2.32

Visual MINTEQ V 2.32. (Gustafsson 2005) is a geochemical equilibrium and speciation program that can be used to compute equilibrium among dissolved, adsorbed, solid, and gas phases at specified conditions. It is based on the MINTEQA2 version 4.0. code which was compiled in Visual Basic 6.0 in 2005 (Gustafsson 2005).

The Visual-MINTEQ 2.32 software was used to assess and quantify the speciation of molybdenum and vanadium adsorbed at different pH values (4 to 9) and at constant metal concentrations (100 µM), as well as to simulate the adsorption experimental results.

The program includes an extensive database of thermodynamic data for metals ("vminteq"), but also options for surface complexation modeling (*e.g.,* diffuse layer model, DLM).

3.4. Metal uptake processes: molybdenum and vanadium co-precipitation with ferrihydrite

The uptake experimental set up for molybdenum and vanadium co-precipitation was described in paragraph 3.2.2.

The uptake capacities of molybdenum and vanadium via co precipitation were calculated as a function of metal concentration in the ferrihydrite samples after total digestion (see iron oxyhydroxides digestion methods described in the paragraph 3.2.3.B) using the following mass balance formula:

$$q^c = \frac{C^c}{S^c} \cdot V^c{}_d \qquad \text{(Eq. 3.3.)}$$

Where: q^c is the metal uptake capacity via co-precipitation, mg metal g^{-1} dry ferrihydrite

$V^c{}_d$ is the acid volume used for co-precipitated sample digestion, L;

S^c is the dry weight of the co-precipitated sample digested, g;

C^c is the metal concentration in the completely digested co-precipitated sample, mg L^{-1}.

3.4.1. Co-precipitation isotherm

The maximum uptake capacities of molybdenum and vanadium via co-precipitation with ferrihydrite were obtained from Langmuir type isotherms. The empirical Langmuir uptake model is usually applied to adsorption studies, but in this case was adapted also for the co-precipitation studies in order to compare the uptake capacitances of ferrihydrite for molybdenum and vanadium via adsorption and co-precipitation.
The Langmuir model is based on the equation:

$$q_e = \frac{q_{\max} \cdot b \cdot C_e}{1 + b \cdot C_e} \qquad \text{(Eq. 3. 4.)}$$

Where q_e is the metal uptake capacity at equilibrium; q_{max} is the maximum amount of metal ion per unit mass of ferrihydrite (mg g^{-1}), b is the equilibrium constant which is related to

the affinity of the metal for binding sites and C_e is the metal concentration in the supernatant at equilibrium.

The Langmuir parameters can be determined from the linearized form of the equation:

$$\frac{C_e}{q_e} = \frac{1}{q_{\max} b} + \frac{1}{q_{\max}} \cdot C_e \qquad \text{(Eq. 3.5.)}$$

Therefore, a plot of (C_e/q_e) *vs.* C_e gives a straight line with the slope of $1/q_{max}$ and the intercept $1/(q_{max}b)$.

The parameter q_{max} represents the practical limiting uptake capacity when the ferrihydrite is fully saturated with metal ions. This parameter allows the comparison of the ferrihydrite adsorption performance with other sorbants in similar specified process conditions.

3.5. Metal uptake processes: molybdenum and vanadium adsorption onto ferrihydrite

3.5.1. Batch experiments set up

Adsorption studies were carried out as typical batch experiments in 500 mL beakers. Specific amounts (quantified from the dried weight) of ferrihydrite slurry were equilibrated with a metal-containing solution (molybdenum or vanadium) and the experiments were carried out at room temperature (25ºC ±2) with the mixture being continuously stirred using a magnetic stirrer (300 rpm). For most of the adsorption studies (except for the set of experiments where the pH influence on molybdenum and vanadium adsorption capacity was tested) the pH was adjusted to 7 using 1M NaOH or HCl. The tests were conducted under N_2 atmosphere to assure the lack of or at least the minimization of CO_2 in the system. Solution samples were taken at a geometrical time scale (0; 10; 20; 40; 80; 160; 320 and 1280 minutes) and analyzed using ICP-OES or ICP-MS following the appropriate protocol (dilutions, matrix match, *etc.*). From quantitative measurements of the metal concentrations in the supernatant, the uptake capacities of the ferrihydrite for the metals, as well as the removal efficiencies of molybdenum and vanadium from the solution as a function of time were obtained (see below).

Adsorption experiments were carried out as a function of the following parameters:

(a)Metal concentration effects

The effect of metal concentration was studied in batch experiments as described above with 0.1gL^{-1} (dry weight) ferrihydrite and 1, 10, 100 and 1000 µM molybdenum and vanadium added.

(b) Particle concentration effects

Batch experiments were carried out at a metal concentration of 100 µM but at three different ferrihydrite concentrations: 0.1, 1 and 2 g L^{-1}, while all other conditions were kept as described above.

(c) pH effects

The effect of pH was studied in the pH interval between 4 and 9. All adsorption experiments were carried out with a potentiometric stat titrator (Radiometer 865 from Titra-Lab®) which maintained the pH constant. The required addition of base and acid were added by setting the titrator on Stat pH mode via the Stat Adaptive Addition Algorithm. During the titrations the pH was maintained constant, with a variation interval of 0.001 pH units, by adding appropriate amounts (min 0.001 mL) of acid (0.1N HCl) or base (0.1N NaOH) at a flow rate of max 1mL min^{-1}. Sets of data for: (a) pH *vs.* time; (b) acid and base volumes added vs. time and (c) T *vs.* time were monitored and collected by TitraMaster 85 (V4.0) which is a Titralab® PC software provided by Radiometer Analytical SAS.

The ionic strength varied during the titrations due to the acid and base addition (between 1 mL and 12 mL of acid or base to 500 mL of solution) averaging 0.01.

(d) Effect of phosphorus on molybdenum and vanadium adsorption onto ferrihydrite

A set of competitive adsorption studies were carried out using equal concentrations of individual metals (P, Mo or V at 100 μM) and 0.1g L^{-1} ferrihydrite. Combinations of binary metal: molybdenum and P, vanadium and P, molybdenum and vanadium, as well as single metal (P, Mo or V) experiments were carried out under the conditions described above for the batch experiments. The concentration of phosphate was analyzed using the standard acid acetate – molybdenum blue spectrophotometric method (Kuo 1996) (using spectrophotometer at λ=882nm), which has a detection limit of 10 μgL^{-1}.

(e) Matrix effects

Seawater (with and without organics) and double distilled water were used as matrices for the adsorption experiments in order to compare the laboratory data (which were carried out in metal-containing double distilled water) with a system that mimiced a seawater environment.

The seawater was collected by Dr. Micha Rijkenberg, National Oceanography Centre (NOC), Southampton, from the Canary Basin, North Atlantic: 25º. The seawater was filtered on site through 0.2 μm filter paper and then stored in a temperature controlled room at 4ºC.

The adsorption studies were carried out with 1000 µM metal concentration and 0.1 g L^{-1} ferrihydrite in the absence of light to avoid the photo-reduction of iron. For the experiments in seawater without organics, the organic compounds were removed from seawater by ultraviolet treatment available at the NOC.

3.5.2. Adsorption modeling and simulation

Adsorption kinetic

The kinetics of the adsorption was plotted as *q vs.* time or E *vs.* time; where *q* - is the metal uptake capacity (mg g^{-1}) and E is the uptake efficiency in %:

$$q = \frac{V \cdot (C_i - C_t)}{S_a} \qquad \text{(Eq. 3.6.)}$$

Where: *q* is the metal uptake capacity, mg g^{-1};

V is the solution volume, L;

C_i is the initial metal concentration in solution, mg L^{-1};

C_t is the metal concentration in solution at time t, mg L^{-1};

S_a is the dry weight of ferrihydrite per adsorption batch, g;

$$E = \frac{C_i - C_t}{C_i - C_f} \cdot 100 \qquad \text{(Eq. 3.7.)}$$

C_i is the initial metal concentration in solution, mg L^{-1};

C_t is the metal concentration in solution at time, t, mg L^{-1};

C_f is the final metal concentration in solution, mg L^{-1}.

To calculate adsorption kinetics and uptake capacities and derive information about the adsorption mechanism at the macro-scale level with regards to the rate limiting adsorption steps which can either be inter-particle diffusion (physical-sorption) or surface reaction (chemo-sorption) a pseudo-second order kinetic model was used.

The uptake rates were calculated by fitting the experimentally derived uptake capacities to an empirical pseudo second order model (Equation 3.9.) which is based on classical Lagergren kinetic (Equation 3.8.) (Herrero et al. 2006).

$$\frac{dq_t}{dt} = k \cdot (q - q_e) \qquad \text{(Eq. 3.8.)}$$

$$\frac{dq_t}{dt} = k \cdot (q - q_e)^2 \qquad \text{(Eq. 3.9.)}$$

Where k is the rate constant of adsorption, g mmol^{-1}min^{-1}; q_e is the amount of metal adsorbed at equilibrium (calculated with Equation 3.6.), mmol g^{-1} and q_t is the amount of metal adsorbed per g ferrihydrite, mmol g^{-1} at any time, t, min.

The data from the pH effect on molybdenum and vanadium adsorption experiments (molybdenum and vanadium adsorption) were fitted with the pseudo-second order model, and the regression factor which gives the goodness of fit allowed the identification of:

- the adsorption rates of molybdenum and vanadium at different pH values;
- the equilibrium concentrations predicted, $q_{e,calc}$, to be compared with experimental isotherm values, $q_{e,exp}$.
- the derivation of a macro scale adsorption mechanism, for the range of the studied pH, with regard to the limiting step of adsorption: a best fit of a pseudo-second order kinetic model implies a surface reaction dependent mechanism or a poor fit to this model implies a best fit of a first order kinetic model which describes an inter-particle diffusion dependent mechanism (Cheung, 2000).

Surface complexation or electrostatic adsorption model

The metal adsorption data for the pH dependent set of experiments were also fitted with a Diffuse Layer Model (DLM) in order to determine mechanistic information, with regards to surface complexes (inner-sphere *vs.* outer-sphere complexes; mono-dentate or bi-dentate complexes), to check if the experimental outputs are in agreement with modelling outputs (Bradl 2005; Dzombak and Morel 1990), and derive new dissociation constants where possible. The Diffuse Layer Model was chosen because it is one of the most used models for hydrous ferric oxides surface complexation and also because it can fit low ionic strength adsorption data (Dzombak and Morel 1990).

Visual MINTEQ software modeling and simulation

The set of data from the experiments that aimed at elucidating the effect of pH on the adsorption of molybdenum and vanadium onto ferrihydrite (hydrous ferric oxide, HFO) were simulated with the diffuse layer model (HFO with DLM) with the Visual MINTEQ 2.32 software following the approach described in (Gustafsson 2005) and using the thermo data: feo-dlm.mdb database.

Table 3. 2. Given fixed parameters used in the adsorption modeling**.**

Parameter	Value	Reference
Ionic strength	0.01	This study
Mo or V concentration	100 µM	This study
Ferrihydrite surface area	600 m^2g^{-1}*	(Gustafsson 2005)
Ferrihydrite surface area	200 m^2g^{-1}#	This study
Ferrihydrite particle concentration (Cp)	0.1g L^{-1}or 0.935mM±	This study
Ferrihydrite surface sites density	2.3 sites/nm^2*or 0.205 mol mol^{-1} Fe	(Gustafsson 2005)
Ferrihydrite molecular weight	106.86 $gmol^{-1}$*	(Gustafsson 2005)
Radius of a considered spherical particle	2 nm	This study
The ferrihydrite atoms stoichiometry, as Fe^{+3}:H_2O:H^+	1:3:-3*	(Gustafsson 2005)
log K's of the surface complexation reactions defining the formation of the protonated $FeOH_2^+$ species	7.29*	(Gustafsson 2005)
log K's of the surface complexation reactions defining the formation of the deprotonated FeO^- species	8.93*	(Gustafsson 2005)

* note that all parameters referenced as Gustafsson (2005) are preset parameters by the program author for ferrihydrite in the Visual MINTEQ 2.32 code;

[±] Cp in molality could be calculated as 0.935 mM (assuming a ferrihydrite stoichiometry of Fe:H_2OH:H of 1:3:-3, with a molecular weight of the ferrihydrite of 106.86 g mol^{-1}); [#]Measured surface area (200 $m^2 g^{-1}$) was used in modeling the adsorption in order to compare the experimental results with the modeled results. The software contains as a default for the diffuse layer model – a value for the surface area of 600 $m^2 g^{-1}$. This value was also used in an adjacent simulation in order to compare our results with the literature (*e.g.* Mo and W sorption experiments onto ferrihydrite run by Gustafsson, 2005)

The used parameters are presented in the Table 3. 2. The values referenced as "This study" are typed experimental values, whereas the ones referenced as "Gustafsson, 2005" are default values fixed within the code.

The results were compared with the adsorption experimental data from pH 4 to 9.

Adsorption isotherms

A plot that describes the amount of a species sorbed as a function of its concentration in solution, measured at constant temperature, is called an sorption isotherm plot (Stumm and Morgan 1996).

The most common adsorption isotherms can be described by the classical Langmuir and Freundlich methods. In this study these methods were used to quantify the maximum adsorption uptake capacities of the sorbate (molybdenum or vanadium) onto the sorbent (ferrihydrite), as well as to derive the adsorption equilibrium constants and saturation of the binding sites. In addition, adsorption isotherm plots were used to compare the maximum adsorption capacity of molybdenum and vanadium via adsorption onto ferrihydrite and co-precipitation with ferrihydrite. The set of data from the experiments that targeted the metal concentration effect (constant sorbent weight and variable concentrations of metal) were fitted with both models using the OriginPro 8 software (OriginLab 2007). A detailed description of these methods and the possible output information for both models are given below:

The **Langmuir isotherm** assumes a metal (here molybdenum and vanadium) adsorbes onto an adsorbent (here ferrihydrite) surface and creates a monolayer surface coverage; in addition, it is assumed that the energy of the adsorption is independent of the surface coverage {Stumm, 1996 #210; Langmuir, 1997 #197).
As described above the Langmuir isotherm and the Langmuir parameters were determined using Equations 3.4. and 3.5.

The empirical **Freundlich isotherm** is based on sorption on heterogeneous surface, and it can be derived assuming a logarithmic decrease in the enthalpy of

adsorption with the increase in the fraction of occupied sites. Thus, it assumes an infinite supply of non-reacted sorption sites and that the adsorption occurs in multilayer {Stumm, 1996 #210}.

The Freundlich isotherm is given by:

$$q_e = K_F \cdot C_e^{1/n} \qquad \text{(Eq. 3.10.)}$$

Where: K_F and n are the Freundlich constants characteristics of the system,

K_F is indicating the adsorption capacity;

Ce is the metal concentration at the equilibrium;

n is the adsorption intensity; values of 1/n between 0.1<1/n<1 represent good adsorption, whereas the lower values1/n suggest that weak adsorption forces are operative on the surfaces

The Freundlich equation can also be linearized via a logarithmic form and the Freundlich constants can be determined via

$$\log q_e = \log K_F + \frac{1}{n}\log C_e \qquad \text{(Eq. 3.11.)}$$

The distribution coefficient (or Solid Water Distribution Ratio), K_d

For a full interpretation of, and a comparison between the adsorption isotherms the distribution coefficients were also estimated for both (molybdenum and vanadium) adsorption systems.

The distribution coefficient, K_d, is the slope of an isotherm at the origin and usually it is expressed in mLg^{-1} or $mmolg^{-1}$. It can be expressed as:

$$K_d = \frac{q_e}{C_e} \qquad \text{(Eq. 3.12.)}$$

This coefficient is a conditional constant and is valid for a specific concentration range at a given pH only. At high sorbate concentrations, K_d describes the ratio of sorbate:sorbent at which all available sites are saturated. A value of 0 for K_d indicates a

non reactive surface of the sorbent while values of 100 or above describe very reactive surfaces (Langmuir 1997).

A correlation between the two models described above can show that:

(i) When values of C_e are very small the Langmuir isotherm is more or less equivalent to the Freundlich isotherm with $q_e = K_F C$, $n = 1$ and $K_F = K_d$;

(ii) When C_e is large, $q_e = q_{max} = K_d$ which is equivalent with Freundlich isotherm with $n = 0$ (Langmuir 1997).

Modeling and 3D plotting of the parameters which influence the adsorption process

In order to offer to the reader a few possible ways of using the experimental results from the present study to scale up, transpose or interpolate the results to different more realistic environments and to apply them in different research fields, various combinations of three parameters (e.g. pH, uptake capacity and particle concentration or pH, particle concentration and metal concentration) from the adsorption studies were plotted in 3D with the Origin Pro 8 software (OriginLab 2007).

3.6. Off-line ferrihydrite transformation

Off-line transformation experiments were carried out at:

- short-term (3 hours to max 5 days) dynamic (stirred) experiments at high temperatures (100ºC - 200ºC) and initial pH of 8 and ionic strength 0.01, to assess the transformation end products for both metals (Mo and V) and in both the adsorbed and co precipitated systems. They were carried out in order to gain insights into the adequate time length and optimal conditions for the Synchrotron experiments.The transformation reactions (including the appearance of intermediary products and the end-products) were quantified by quenching the reactions at various time steps. The solids were analized with XRD, whereas the transformation supernatant Fe concentration and the pH were analysed to determine the partitioning of the metals in the end products and assess if any dissolution occurred during transformation.

- Long-term transformation experiments: ferrihydrite samples with and without molybdenum and vanadium co-precipitated at various concentrations (0.001 - 1% metal: Fe, molar ratio), ionic strength 0.01 and pH 7, were stored in fridges at 4 and 10ºC (up to 34 months) to assess:

(i) The transformation time frame of ferrihydrite at low temperatures (Appendix C);
(ii) The influence of different concentrations of metal on the transformation rate
(iii) A comparison between high and low temperature transformation of ferrihydrite

Long-term transformations were followed by taking sub-samples every three months and analyzing them with XRD. For the samples at 4ºC additional digestions of the slurries were performed with respect to the protocol described in subchapter 3.2.3.b.

- Three different ionic strengths (0.01, 0.1 and 1) at 25ºC
- Constant pH (8) and ionic strength (0.01) – recording pH during the transformation.

One *off-line* transformation experiment was carried out at constant ionic strength (0.01), initial pH = 8 for 5.7days in a water bath at ~73ºC. The pH drift during the transformation was measured every 10 minutes with a PC controlled ORION 710A pH meter. The intermediate and end-products of the transformations were quantified via X-Ray Diffraction of the solids removed at specific times.

3.7. In situ Energy Dispersed X-Ray Diffraction

Energy Dispersed X-Ray Diffraction (ED-XRD) is a synchrotron based technique which was used to study *in situ* and time resolved processes and to derive the transformation kinetics and mechanism of the ferrihydrite conversion to hematite in the presence and absence of molybdenum and vanadium.

3.7.1. ED-XRD theory

ED-XRD is a technique that measures the intensity of X-rays diffracted by specific crystallographic planes of a mineral phase. In contrast to conventional X-ray diffraction, in ED-XRD the incident beam is a polychromatic white beam which scans the sample simultaneously at different energies, E (different wavelengths, λ) generating time resolved X-Ray diffractograms of the solid mineral phase (Newville 2008).

The relationship between the energy of a diffracted beam and the *d*-spacing of a mineral is given by Bragg's Law (Equation 3.13.):

$$\lambda = 2\, d_{hkl} \sin\theta \qquad \text{(Eq. 3.13.)}$$

Using the Planck-Einstein equation (Equation 3.14.), the energy, E, of a photon of wavelength, λ, is given by:

$$E\ (\text{keV}) = hc/\lambda \qquad \text{(Eq. 3.14.)}$$

Combining Equation 3.13 and Equation 3.14 gives:

$$E\, d_{hkl} \sin\theta = (hc/\lambda) \times (\lambda/2) = hc/2 = 6.19926 \qquad \text{(Eq. 3.15.)}$$

where: energy (E) is in keV, the wavelength (λ) is in Angstroms, h is the Planck's constant (41.35668×10^{-19} keV s), and c the speed of light in vacuum ($2.997\ 924\ 590 \times 10^{18}$ Å s^{-1}). Thus, $hc/2$ is in units of keV Å. Therefore the energy, E (in keV) is given by:

$$E\ (\text{keV}) = 6.19926 / (d_{hkl} \sin\theta) \qquad \text{(Eq. 3.16.)}$$

Equation 3.16. shows that the energy (E) of a diffracted beam arising from a particular *d*-spacing in a sample is inversely proportional to the sine of half of the 2θ angle of the detector.

3.7.2. Off-line test experiments for the ED-XRD

A series of off-line test experiments were carried out at the SRS Daresbury Laboratory, UK to assess the optimal conditions for the ferrihydrite to hematite transformation experiments planned for the *in situ* and time resolved ED-XRD study. For each of these, 15 ml of a 50gL^{-1} ferrihydrite slurry either pure or co-precipitated with either molybdenum or vanadium (1% molar ratio) as described above (subchapter 3.1.2.) were brought to pH 8 with 1M NaOH and ionic strength 0.7 using NaCl in order to simulate seawater conditions. The slurries were transferred at room temperature into 20ml Teflon® (polytetrafluoroethylene) liners inside a steel Parr® hydrothermal reaction cell that was subsequently transferred into a heater block.

Three sets of test experiments were carried out at temperatures between 130ºC and 240ºC:

- Ferrihydrite pure at pH 8 and ionic strength 0.7;
- Ferrihydrite co-precipitated with 1% molybdenum at pH 8 and ionic strength 0.7;
- Ferrihydrite co-precipitated with 1% vanadium at pH 8 and ionic strength 0.7;

Additionally, a transformation experiment at 160ºC was also conducted at lower ionic strength (0.1) and pH 8 with the ferrihydrite co-precipitated with molybdenum to assess the effect of ionic strength and to allow a comparison and data extrapolation of the longer term low temperature transformation experiments at 4ºC and 10ºC (see subchapter 3.6.2.).

3.7.3. *In-situ* experiments

ED-XRD measurements were performed at Daresbury Laboratories UK, on Station 16.4. The station is equipped with a Laue-Bragg monochromator white beam able to produce high energy photons which generate powder diffraction patterns. The high energy white radiation is generated by a 6-Tesla Wiggler magnet.

Ferrihydrite samples were placed in the hydrothermal cell (high- pressure-resistant steel vessel Parr® hydrothermal reaction vessel with a thinned-down area of the wall) which was housed in a aluminum holder heated by 4 cartridge controlled heaters, with temperature regulated by a thermocouple system (Figure 3. 1.). Isothermal transformation experiments were carried out at temperatures from 130ºC to 240ºC. Once the samples in the Parr autoclave were inserted into the heater at the set temperature (between 130-240ºC), the cell content reached the desired temperature in ~ 2 minutes.

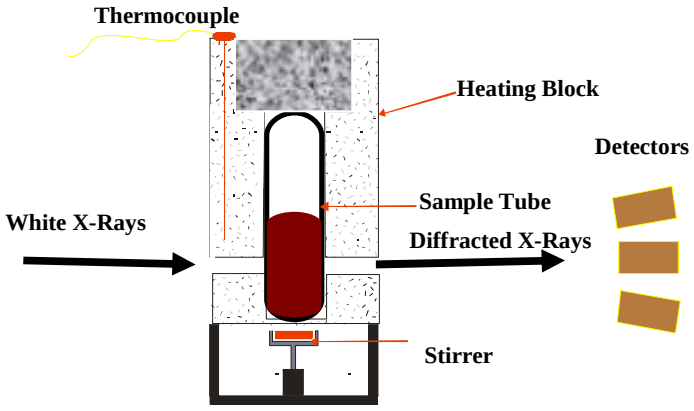

Figure 3. 1. Schematic diagram of ED-XRD *in situ* isothermal transformation experimental set up

Once an experiment was started, the incident polychromatic beam passed through slots in the heated aluminum block, the transmitted X –ray beam is diffracted by the cell content and collected via three collimators by a set of 3 discriminating liquid nitrogen cooled solid state detectors. The collimators are set at slightly different 2θ (2-theta) angles (separated by ~ 2.8° in 2θ), so that each detector collected XRD patterns at an extended ranged of *d*-spacing simultaneously. This allowed a continuous range of *d*-spacings at energies that are easily seen on at least one of the detectors to be collected. In this configuration, the bottom detector collected spectra at high *d*-spacings (or 2θ), while the top detector collected the low *d*-spacings.

For each detector, the energy, *E* (in keV), is defined by an equation of the form

$$E(keV) = [Channel\ Number]^* b + a \qquad \text{(Eq. 3.17.)}$$

where *a* and *b* are specific calibration constants given in Table 3.3.

The calibration of the detectors is usually carried out with a Si standard and the following calibration constants were used in this study for converting the data and 3 D plotting of the ED-XRD spectra.

Table 3. 3. Detectors calibration constants (provided by the Dr. Dave Taylor (principal station scientist) from the latest calibration):

	Top detector	Middle detector	Bottom detector
(a) Intercept	2.692944804	2.56821033	2.563793451
(b) Slope	0.026448999	0.026559535	0.026508852
2θ - *d*-spacing conversion constant	7.324	4.4885	1.6075

For each isothermal transformation consecutive XRD patterns were collected every minute with experiments carried out for up to 4 hours.

Using the constants from Table 3.3. the data were converted from *d*-spacing to 2θ with the DL converter V 1.32 software. The converted XRD patterns were 3D plotted with the Surfer software (Golden 2002). The area under specific peaks were evaluated using the software XFIT (Cheary and Coelho 1996) while the software Origin Pro (OriginLab 2007) was used to evaluated the kinetic parameters described below.

3.7.4. Data processing

The transformation progress was followed from the changes in the peak area of newly formed mineral phases, which in our specific systems were the hematite peak (110) and the goethite peak (111). By evaluating the area under these peaks from consecutively collected XRD patterns, the time when the transformation started, t_o (the induction time) as well as the completion of the transformation (time corresponding to the point after which the peak area remained constant) defined the duration of the transformation. To express the kinetics of the transformation, time resolved peak areas were normalised from 0 to 1, giving the degree of transformation, α, using the empirical formula:

$$\alpha = (A_t - A_{min})/(A_{max} - A_{min}) \qquad \text{(Eq. 3.18.)}$$

Where: A_t is the peak area at time t, A_{min} and A_{max} are the minimum and maximum peak area values of the specific peak.

The kinetics of the transformation: mechanistic information

The kinetics of the transformations were evaluated from the time resolved degree of transformation, α, for the growth of the hematite or goethite peaks (where applicable). The data were fitted with the Johnson-Mehl-Avrami-Kolmogorov (JMAK) model (Avrami 1939; Avrami 1940; Avrami 1941) which is expressed as:

$$\alpha = 1 - e^{-k(t-t_0)^m} \qquad \text{(Eq. 3.19.)}$$

where *k is* the reaction rate constant in s^{-1}; *t is* time in s; t_0 is the induction time (first appearance of a peak) also in s, and *m is* a variable that depends on the nucleation rate, reaction mechanism, and dimensionality of growth (Hulbert 1969).

The values of *m* were interpreted according to Hulbert (1969), who classified the various regimes for nucleation and crystallization mechanisms (Table 3.4.).

Table 3. 4. Interpretation of the JMAK model constant, *m*, according to Hulbert (1969).

Growth dimensionality	**Nucleation rate**	**Values of *m***	
		Surface-controlled	**Diffusion-controlled**
3-D	constant	4	2.5
	decreasing	3 – 4	1.5 – 2.5
	zero	3	1.5
2-D	constant	3	2
	decreasing	2 – 3	1 – 2
	zero	2	1
1-D	constant	3	1.5
	decreasing	1 – 2	0.5 – 1.5
	zero	1	0.5

The activation energies of the transformation

For a better understanding of this part of the work it is important to note that the 'ferrihydrite transformation' notation will from here on be termed as 'end-product (hematite or goethite) nucleation or crystallisation'.

The apparent activation energies for each system were calculated from the kinetic parameters obtained from the fittings of the JMAK model (Equation 3.19.).

The logarithmic form of the Arrhenius equation (Equation 3.20.), but in terms of the rate constant, *k*, expressed as a temperature dependent parameter (Equation 3.21.) was used to calculate the apparent activation energy of crystallisation for the end-products.

$$k = A \cdot e^{-E_a / RT} \qquad \text{(Eq. 3.20.)}$$

with *k* being the rate constant, *A* the frequency or pre-exponential factor, E_a the activation energy in kJ mol^{-1}, R the gas constant (8.314 J mol^{-1} K^{-1}), and *T* the absolute temperature in Kelvin (K).

$$\ln k = \ln A_{(cryst.)} - \frac{E_{a(cryst.)}}{RT} \qquad \text{(Eq. 3.21.)}$$

The logarithmic form of the Arrhenius equation in terms of induction time and temperature (Equation 3.19.) was used to extract information about the end-product apparent nucleation activation energies.

$$\ln t_0 = \ln A_{(nuc.)} - \frac{E_{a(nuc.)}}{RT} \qquad \text{(Eq. 3.22.)}$$

These equations (Equation 3.21.- 22.) assume that E_a and *A* are constant or nearly constant with respect to temperature.

By plotting ln *k vs.* 1/*T*, and ln t_0 *vs.* 1/T a linear relationship is obtained and E_a of crystallization and nucleation, respectively, can be determined from the slope ($-E_a/R$).

For comparison the "time to a given fraction method" (Putnis 1992), was used to determine E_a of the hematite crystallization. This method provides a simpler approach that relies solely on the fraction of time of transformation and can be expressed as:

$$\ln t_\alpha = const. - \ln A + (E_a/R)(1/T) \qquad \text{(Eq. 3.23.)}$$

where: t_α is time to a given fraction (α) of transformation; A is the frequency or pre-exponential factor; E_a is the activation energy, kJ mol^{-1}; R is the gas constant (8.314 J mol^{-1} K^{-1}) and T is the absolute temperature in Kelvin (K)

3.8. Partitioning of molybdenum and vanadium in the transformation end-product

The partitioning of metal associated with the solid structure, the surface and the supernatant solution at the end of the transformation experiments were also quantified.

3.8.1. Experimental set up

Freshly co-precipitated ferrihydrite (with molybdenum or vanadium) as well as molybdenum and vanadium adsorbed samples were transformed to hematite (end-product) at 200ºC as described above (Subchapter 3.6). During the transformation, the slurry was shaken manually to assure its homogeneity. Experiments were carried out for 24 hours and at the end of an experiment the resulting solids were separated from the supernatants by centrifugation (8000 rpm for 15 minutes) and characterized by XRD. The supernatant was filtered through 0.2µm Acetate Cellulose syringe filters and analysed for molybdenum and vanadium concentrations with ICP-MS as described in subchapter 3.1.3 a and b. The measurements were done at Portsmouth University with the help of Dr. Gary Fones. In parallel, 0.1g of the resulting solids phases were fully digested in 10mL 6M HCl overnight in the dark. From the mass balance of digested solid and supernatant solution, the amount of molybdenum and vanadium release into solution during ferrihydrite (co-precipitated and adsorbed) transformation was evaluated.

Furthermore, a desorption step was employed in order to quantify the amount of molybdenum and vanadium associated potentially with the end-product material surface after the transformation. An aliquot of the solid phase was equilibrated with a 2 M NH_4OH solution for 30 minutes under constant stirring (Carvahlo et al. 1997). The resulting supernatant was collected via centrifugation, and after filtration analysed for molybdenum and vanadium concentration. Finally, the remaining solid fraction was fully digested in 6 M HCl and the resulting solution analysed using the methods described above.

3.9. X-Ray Adsorption Fine Structure Spectroscopy

X-Ray Adsorption Spectroscopic (XAFS or XAS) measurements were conducted to derive information about the bonding and coordination of molybdenum in the starting ferrihydrite (co-precipitated and adsorbed) as well as in the transformation end-products.

3.9.1. XAS theory

X-ray Absorption Spectroscopy is a technique that measures the absorption of X-rays by a sample as a function of specific X-ray energy.

The intensity of the X-ray beam is measured before (I_0) and after (I) passing through the sample for transmission mode (Figure 3. 2. A) or the energy scattered by the sample in fluorescence mode (Figure 3. 2. B). The measured X-ray intensities can be expressed by the absorption coefficient (μ(E) or just μ), which is described by Beer's Law - Equation 3.24. for transmission mode and Equation 3.25 for fluorescence mode (Newville 2008):

$$I = I_0 \cdot e^{-\mu x} \qquad \text{(Eq. 3.24)}$$

$$\mu(E) \propto I / I_0 \qquad \text{(Eq. 3.25)}$$

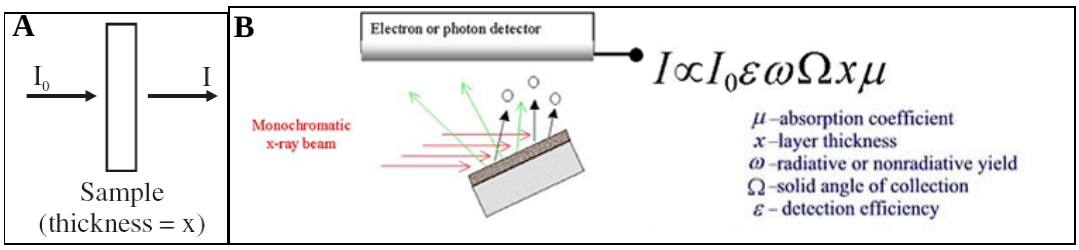

Figure 3. 2. X-Ray absorption measurements: (A) transmission mode: an incident X-ray beam of intensity I_0 passes through a sample of thickness, x, and the transmitted beam has an intensity I; (B) fluorescence mode: a incident X-ray beam is reflected by the sample and the emitted beam intensity is collected by an electron/photon detector (Kodre et al. 2004).

For the samples containing low concentrations (ppm levels) of interested element or thick samples it is recommended that the XAS scan is done in fluorescence mode. In fluorescence XAFS measurements, the x-rays reflected from the sample are both elastically and inelastically scattered x-rays and they are not emitted isotropicaly. This effect is due to the polarization (suppression at 90º to the incident beam, in the horizontal plane) of the x-rays from a synchrotron in its plane. Therefore, fluorescence detectors (Figure 3. 2.B) are normally placed at a right angle to the incident beam. More sophisticated formulas and additional information for understanding the intensity of the reflected beam in fluorescence mode are described, for example, by Matthew Newville (2008).

Plotting the absorption coefficient, μ(E), as a function of X-ray energy (in eV) gives a plot in which two features can be distinguished (Figure 3. 3) (Binstead 1998):

(a) X-ray absorption near edge structure (XANES) which is the region close to the sharp rise in the absorption coefficient (absorption edges);

(b) Above this edges small oscillations in the absorption coefficient are evident and this represents the Extended R-ray fine structure region (EXAFS);

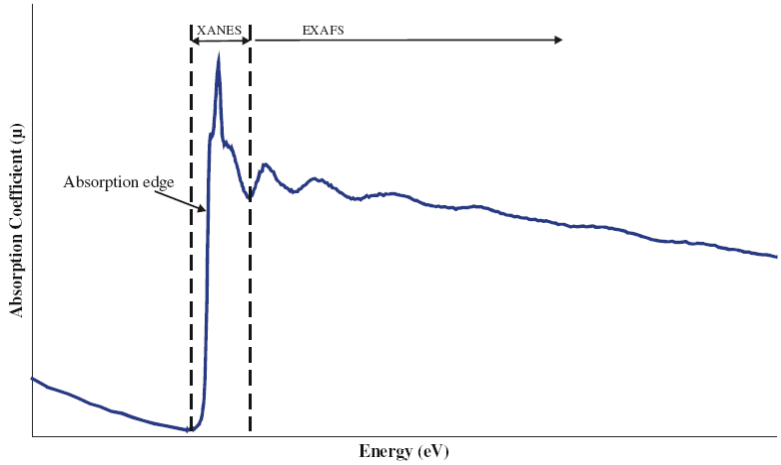

Figure 3. 3. X-ray absorption spectroscopy trace showing an absorption edge (edge step) and the XANES and EXAFS regions as well as the decrease in the absorption coefficient with increasing energy (Bunker 2005).

The energy of the absorption edge is unique to each element because it is due to the energy required to excite one of the inner-shell electrons of a specific atom. The XANES region is defined as the area ~50eV below and ~100eV after the edge and small energy changes (few eV) in the edge position are common since the energy required to

excite an inner-shell electron is dependent on the oxidation state and local bonding of the atom in question (Bennett 2005).

The oscillations in the EXAFS region give detailed structural information about the local atomic environment of the element of interest. In practice, the local structure is defined as up to 5Å from the atom of interest, therefore information on a first, second, third and occasionally fourth shell of neighboring atoms located adjacent to the atom of interest can be derived (Bennett 2005). Three types of parameters can be determined from the EXAFS region: (a) inter-atomic distances between the probed atom and the neighbouring atoms; (b) neighbouring atom coordination number; (c) neighbouring atom type.

3.9.2. XAS measurements

XAS measurements were carried out at the Synchrotron Radiation Source (SRS), Daresbury Laboratory on the beam line at station 16.5 which is ideal for ultra dilute systems due to the high flux and high count rate fluorescence detector (30 element Ge solid state detectors).

Non parallel bent Si (220) crystals were used as monochromator crystals and this way only ~ 50% to 80% of the maximum beam intensity is used (Figure 3. 4.).

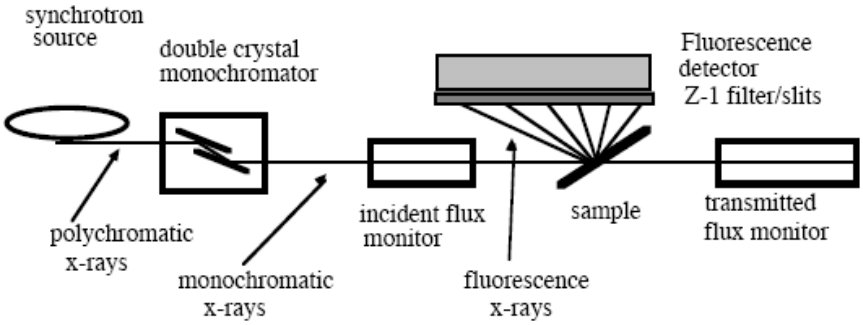

Figure 3. 4. Schematic diagram sowing a XAFS beam line set up (Bunker 2005).

Station 16.5 is ideal for quantifying the XAS features of samples which contain low concentrations of metals. In this study the work was carried out on samples that contained max 1% molybdenum.

XAS data for all samples were collected at the Mo K1 edge in fluorescence mode with the electron binding energy specific to molybdenum for the K 1s shell being 20000eV.

Freshly prepared ferrihydrite samples (with molybdenum co-precipitated and adsorbed) as well as the transformation end-products (both desorbed and non-desorbed), were placed in cryo-resistant plastic holders and frozen in liquid nitrogen where they were stored prior to measurements. The measurements were also carried out in cryo-mode using a cryogenic sample holder available on station 16.5.

Commercial standard materials: sodium molybdate, potassium molybdate, molybdenum trioxide (Aldrich), and natural standards: molybdite ((MoO_3)-Karben, S-W Norway, Leeds University Earth Science collection no: EMF 49); wulfenite ($Pb(MoO_4)$-Yugoslavia, Leeds University Earth Science collection no: EMJ 24) and powellite (Ca(MoO4)-Toropah Nevada USA; collection no: 48132) where used to compare our results. All standards were examined by XRD to check their identity and purity.

The standards were run in transmission mode and due to their high molybdenum content they were diluted with an inert boron nitride salt.

3.9.3. Data processing

From the raw XAS data a number of mathematical procedures were followed in order to derive structural information. The data were processed using the computer programs EXCALIB, EXBROOK, EXSPLINE (Dent and Mosselmans 2003; Spadini et al. 2003) and EXCURV98 (Binstead 1998) compiled at the SRS Daresbury Laboratory, UK.

The first step was to sum the scans collected at the same edge for the same sample using the EXCALIB program (Spadini et al. 2003). This process also converted the monochromator angle into X-ray energy.

For analysis of the EXAFS oscillations, the background was subtracted from the raw XAS spectra and the data were normalized. This was achieved using the EXSPLINE program (Dent and Mosselmans 2003; Ellis 1995). The first step was pre-edge background subtraction. Following this, the post-edge background was subtracted. This was achieved by determining a spline curve, which estimates the smooth background absorbance. A number of spline points were established, which model the curve from which the data were subtracted to provide the EXAFS data. The data were then normalised so that the edge step was equal to 1. The final step was the Fourier Transform (FT) of the data in order to convert the energy into a radial distribution function.

For XANES analysis, the edge position was determined and the data normalized such that the edge step was equal to 1 using the EXBROOK program.

Finally, the EXCURV98 software was used to find a structural model (type of neighborhoods atoms, coordination numbers and distance between the atoms) for the interested element within the sample (Binstead 1998).

3.10. Molybdenum and vanadium pre-concentration on Toyopearl 650M cationic resin from a seawater matrix

Column adsorption experiments were conducted to assess the maximum adsorption capacity of the Toyopearl 650M cationic resin for molybdenum and vanadium in seawater matrices. The aims of these experiments were to check the feasibility of using Toyopearl 650M resin for molybdenum and vanadium pre-concentration from seawater matrices, followed by measuring detectable concentrations of molybdenum and vanadium with ICP OES/AES/MS. Similar tests were conducted by Warnken and collaborators (2000), as well as by Willie et al (1998) using Mn. Ni, Cu, Cd and Pb and Cu, Ni, Zn, Mn, Co, Pb, Cd, and vanadium respectively on Toyopearl AF-Chelate 650M (Warnken et al. 2000; Willie et al. 1998).

3.10.1. Resin description

The Toyopearl 650M resin (CAS No:122985-81-3) is a commercial cationic hydrophobic interaction media resin (registered trademark of TosoH Corp) with the following characteristics: strong affinity for water-soluble proteins; high recovery of mass and activity; high sample capacity: up to 2-4 times that of gel media; fluctuating salt concentrations do not change bed volume; mechanical stability to 7kg/cm^2 (7 bar/100psi); stable at wide pH range: 2-12; can be cleaned in place with 0.5M NaOH; autoclavable; matrix: polymer (65 µm) and particle size: 40-90 µm (www.separations.us.tosohbioscience.com/Products).

3.10.2. Experimental protocols:

Seawater was collected by Dr Micha Rijkenberg, National Oceanography Centre (NOC), Southampton, from the Canary Basin, North-West Atlantic Ocean. Immediately after collection, the seawater was filtered through a 0.2 µm filter and subsequently stored in a temperature controlled room at 4ºC at National Oceanography Center, Southampton.

The experiments were carried out using 100ml of seawater spiked with 100 µM of either molybdenum or vanadium. Four columns (A, B, C, D) and a control column (E) (Figure 3. 5.) were dosed with ~ 0.05g, dry weight (0.0523; 0.0511; 0.0530; 0.0533g and 0-

control, respectively) of the Toyopearl resin and seawater was passed through the columns with a peristaltic pump via Teflon® tubes (internal volume 5μLcm^{-1}). Before the adsorption experiment, the columns were washed with 10 ml of nitric acid (0.7M, or 5% v/v). The volume of the seawater passed, as well as the dead volume in the tubes and columns, were measured gravimetrically taking into account the density of the seawater (1.023 g mL^{-1} for 25ºC, 1 atm and salinity of 35). In order to achieve the optimum adsorption capacity the seawater pH was adjusted to low pH values (i.e., 3.5 for molybdenum adsorption and 4.5 for vanadium adsorption (Hirata et al. 2001).

After the columns were saturated, desorption of the retained anions was done using 10 ml of nitric acid (0.7M or 5% v/v) as the eluent. The collected eluent was diluted 100 times and analyzed with ICP-OES (analyzed at National Oceanography Center with the help of Dr. Darryl Green) to check the mass balance obtained from the column adsorption test and to eliminate the background seawater content of molybdenum and vanadium. The limit of detections (LOD) for molybdenum and vanadium for the ICP-OES analyses were: 0.8μgL^{-1} for molybdenum at a wavelength λ=202.022 nm and 0.4μgL^{-1} for vanadium at a wavelength λ=309.299 nm, respectively.

The experiments were run at two flow-rates and the results were expressed as molybdenum and vanadium concentrations *vs.* volume passed through the column (*i.e.,* breakthrough curves). From this data the maximum adsorption capacities were calculated as mmol Mo/V per g resin.

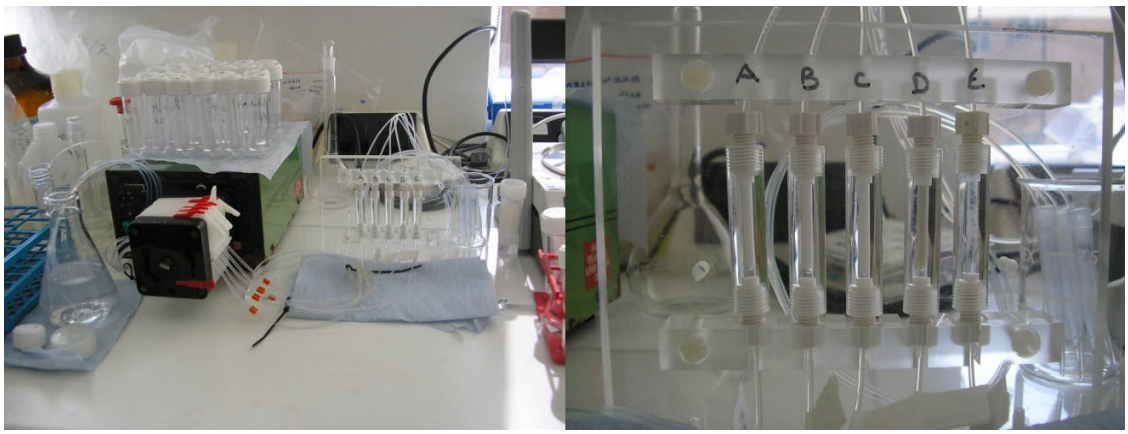

Figure 3. 5. Experimental set up for molybdenum and vanadium pre-concentration column adsorption experiments: left- peristaltic pump loading the adsorption columns and right - closer view of the pre-concentration columns with the resin (A to D) and control (E).

The metal uptake capacities, q, mmol g^{-1} were calculated with the following equation:

$$q_r = \frac{V \cdot (C_f - C_i)}{S_r} \qquad \text{(Eq. 3.26.)}$$

Where: q_r is resin uptake capacities, mmol g^{-1};

V is the volume of seawater passed through the column (100mL), L;

C_i is initial metal concentration in the effluent, mmol L^{-1};

C_f is final (equilibrium) metal concentration in the effluent, mmol L^{-1};

S_r is resin dry weight from the adsorption column, g.

The results represent data from preliminary tests which can be further used for designing an on-line pre-concentration unit for ICP MS/OES measurements of molybdenum and vanadium in seawater matrixes.

Chapter 4
Adsorption and co-precipitation studies of molybdenum and vanadium onto/with ferrihydrite

4.1. Introduction

Ferrihydrite is a well known poorly ordered iron oxyhydroxide which forms in different terrestrial environments mostly under neutral conditions (*i.e.,* deep sea hydrothermal systems, soils, rivers, acid mine drainage). One of the most important characteristics of ferrihydrite is its small size and extremely high surface area and this leads to its high affinity to adsorb different cations and anions. Among anions, the interaction between molybdenum (molybdate) and vanadium (vanadate) and ferrihydrite have so far been little studied.

In this chapter primarily the molybdenum and vanadium uptake via co-precipitation and adsorption were evaluated in typical batch systems. Adsorption experiments were run under varying conditions as presented in Table 4. 1.

Table 4. 1. Adsorption experimental conditions varied.

PARAMETER OR EXPERIMENTAL CONDITIONS	VALUE
pH	4 to 10
Particle concentration	0.1, 1 and 2 gL^{-1}
Metal concentration	1 to 1000µM
Phosphate as a competitive ion	P, P +Mo and P+V.
Matrix	Fresh water, seawater with organics and seawater without organics.

Adsorption kinetic data were fitted with a pseudo second order kinetic model. From the co-precipitation experiments a comparison with adsorption uptake capacity via isotherms was derived. The adsorption processes were modeled using Visual MINTEQ 2.32 software (Gustafsson 2005) with a Diffuse Layer surface complexation Model (DLM).

4.2. Materials and methods

4.2.1. Ferrihydrite synthesis and characterization

A detailed description of synthesis and characterization methods is given in the methods chapter (Chapter 3.).

Ferrihydrite was synthesized following Cornell and Schwertmann (2000), by neutralizing a ferrous nitrate solution (0.2M) with NaOH (1M) under vigorous stirring to pH 7. After synthesis, the slurry was washed by successive centrifugation/dispersion cycles using distilled water. Solids were characterized by X-Ray Diffraction, BET, Scanning Electron Microscopy and Transmission Electron Microscopy after drying, while slurries were analyzed with potentiometric titrations, Dynamic Light Scattering and Mastersizer laser diffraction. The dry weight (DW) of the solids was determined after drying overnight in an oven at 40ºC. Surface area measurements of the ferrihydrite were performed following the standard protocol of Micrometrics Gemini V – based on Brunauer, Emmett and Teller (BET) theory. Potentiometric titrations at different ionic strengths were carried out using a Man-Tech auto-titration system equipped with an automatic burette in order to obtain the point of zero charge of the ferrihydrite. Particle shapes, sizes and aggregation states were analyzed with a High Resolution Transmission Electron Microscope (HR-TEM) equipped with an Energy Dispersive Spectrometer (EDS). The ferrihydrite aggregate size was also evaluated in a static regime with Dynamic Light Scattering and in a dynamic regime (3000 rpm) with a Malvern Mastersizer laser diffraction technique.

4.2.2. Batch experiments setup

Molybdenum and vanadium stock solutions (1000µM) were made from sodium ortho-molybdate and sodium vanadate, respectively. Bach experiments were conducted in 0.5L glass beakers, under N_2 atmosphere, using 100µM molybdenum and vanadium solution and 0.1g (dried weight - DW) L^{-1} ferrihydrite. The experiments were carried out at pH 7 at a mixing speed of 300 rpm (rotations per minute) and at room temperature (23±2ºC). During the adsorption, solution samples for molybdenum and vanadium analyses were collected following a geometrical time scale of 0-1280 min. Prior to dilution and analysis, the solutions were filtered through 0.2µm Cellulose Acetate Filters.

molybdenum and vanadium concentrations were measured using a Perkin Elmer Optima ICP-OES with a detection limit of 0.6 µg $L^{-1}$for molybdenum and 0.9 µg L^{-1} for vanadium. The metal uptake was calculated from the system mass balance using Equation 4.1. (Polihrohiade 1967):

$$q = \frac{V \cdot (C_i - C_e)}{S_a} \quad \text{(Eq. 4.1.)}$$

where, V is the solution volume (L), S_a = the DW of ferrihydrite used in the adsorption study (g), C_i = the initial concentration of the metal (mmol L^{-1}), C_e = the equilibrium concentration of the metal (mmol L^{-1}) and q = the uptake capacity of the metal via adsorption (mmol Mo or V g^{-1} DW ferrihydrite).

The data were also expressed as metal removal efficiency using Equation. 4.2.

$$E = \frac{(C_i - C_e)}{C_i} \cdot 100 \quad \text{(Eq. 4.2.)}$$

where C_i is the initial concentration of the metal in solution, C_e is the equilibrium concentration of the metal .

4.2.3. Kinetics of adsorption

The uptake rates were calculated by fitting the experimental uptake capacities to an empirical pseudo second order model (Herrero et al. 2006).

$$\frac{dq_t}{dt} = k \cdot (q - q_e)^2 \quad \text{(Eq. 4.3.)}$$

where k (g $mmol^{-1}min^{-1}$) is the rate constant of adsorption, q_e (mmol g^{-1}) is the amount of metal adsorbed at equilibrium (calculated with Equation 4.1.) and q_t (mmol g^{-1}) is the amount of metal adsorbed per g ferrihydrite at any time, t (min).

Effect of different parameters:

(a) Effect of pH

The dependence of the metal uptake capacity on pH was followed via batch adsorption experiments (using the procedure described previously) at pH values between 4 and 9. The pH was adjusted with NaOH (0.1M) and HCl (0.1M) using a pH stat titration unit - Radiometer 856. The average ionic strength (over the pH interval) derived from the acid and base addition was ~ 0.01M.

(b) Effect of particles concentration

Ferrihydrite at particle concentrations of 0.1, 1 and 2 gL^{-1} was added into metal solution (100µM) and samples were collected and analyzed as described above. The results were plotted using Equation 4.1.

(c) Effect of metal concentration

Solutions with metal concentrations between 1-1000µM were mixed with 0.1gL^{-1} ferrihydrite at pH 7 and solution samples were taken for analysis as described above. The results were plotted as adsorption isotherms (q (the amount of metal adsorbed at equilibrium) *vs.* C_e (the concentration of the metal at equilibrium)) and fitted with the Langmuir model.

(d) P-competitive studies of molybdenum and vanadium adsorption

Competitive batch adsorption tests were performed in the following three binary systems (P-Mo, P-V, and V-Mo) as well as in the mono-ion systems (P, Mo or V) in order to assess the effect of phosphorus on the uptake of molybdenum and vanadium uptake onto ferrihydrite. The phosphorus in all the samples was analyzed using a standard spectrophotometric acid acetate–molybdenum blue method (Kuo 1996). The results were expressed as phosphorus uptake using Equation 4.1.

(e) Effect of different matrices on molybdenum and vanadium adsorption

Molybdenum and vanadium adsorption studies were carried out at pH 7 in three different matrices: distilled water, seawater with organics and seawater without organics. Solutions of 1000µM molybdenum and vanadium were stirred at 300 rpm in a batch system with 0.1g ferrihydrite for 1280 min. Samples were collected and analyzed with ICP-OES at the National Oceanography Center in Southampton with the help of Dr. Darryl Green. The origin of the natural seawater is described in Chapter 3. For the experiments with seawater without organics the natural seawater was UV treated prior to use.

4.2.4. Surface chemistry and adsorption modeling and simulation

The experimental studies carried out at different pH values were modelled with the Visual MINTEQ 2.32 software (Gustafsson 2005). The parameters used for the modeling are tabulated in Chapter 3, Table 3.2.

Using the Origin 8 software (OriginLab 2007) the data from the adsorption studies were plotted in 3D diagrams (pH, particle concentration, metal concentration, uptake capacity) to show the independency between these parameters. The full details of these methods are described in Chapter 3.

4.3. Results and discussions

4.3.1. Ferrihydrite characterization

(i) High resolution microscopy and X-ray diffraction

Images of the ferrihydrite (Figure 4. 1. A) by Field Emission Gun- Scanning Electron Microscope (FEG-SEM) and the mineralogical identification (Table 4. 2.B) by X-Ray diffractometer (XRD) showed typical ferrihydrite nanoparticle aggregates and classical broad peaks at d-spacing 1.5 Å and 2.5Å that represent 2-line ferrihydrite.

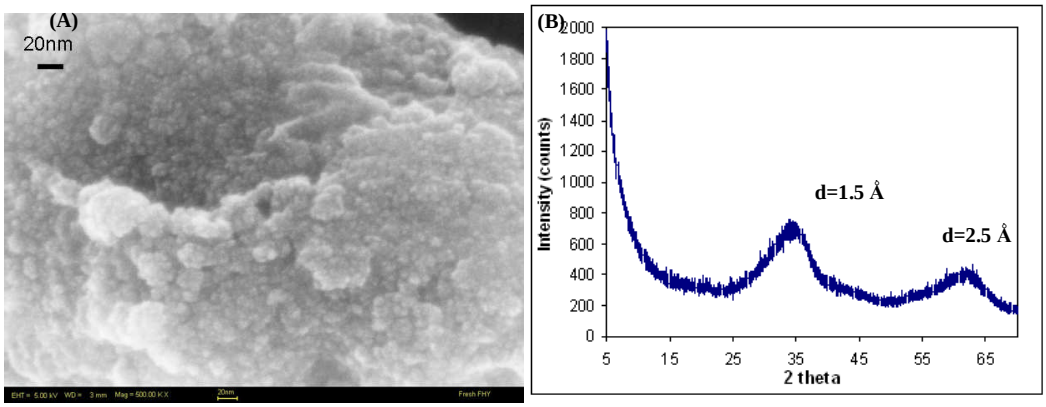

Figure 4. 1. (A) FEG-SEM micrograph of the starting ferrihydrite shows small (≤5nm) particles forming big aggregates. Scale bar is 20nm; (B) XRD spectrum of 2-line ferrihydrite.

Ferrihydrite nanoparticles were also imaged at higher resolution using Field Emission Gun Transmission Electron Microscopy (FEG-TEM). The images showed particles of 3-5 nanometers in size forming large aggregates (Figure 4. 2).

Energy Dispersive Spectroscopy (EDS) patterns were taken in triplicate to assess the elemental composition and semi quantitative composition of the solid. In the EDX pattern (Figure 4. 2.B left inset), the high peaks of O and Fe detect the presence of these elements in the ferrihydrite structure while Cu and C appeared from the grid and carbon film, respectively.

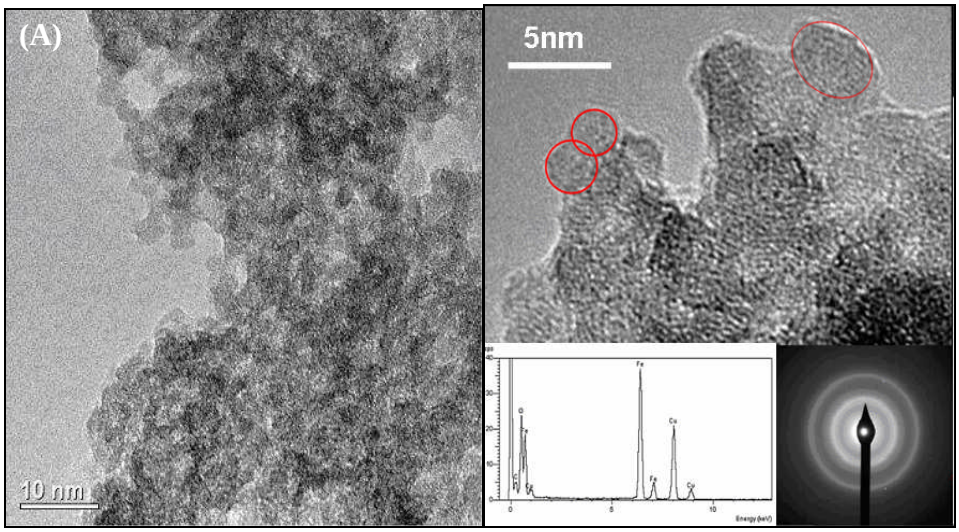

Figure 4. 2. FEG-TEM micrograph of the ferrihydrite aggregate showing individual particles forming clusters. Insets in (B) are (left) Energy dispersive spectra (EDS) and (right) Selected Area Electron Diffraction (SAED) of the imaged sample

Diffuse diffraction rings characteristics of 2 - line ferrihydrite (inset Figure 4. 2B) could be assigned to d-spacing values of 2.5Å and 1.5Å which are typical XRD diffraction peaks positions for 2 –line ferrihydrite. The d-spacing values were calculated from SAED wth Equation 3.1.

The microscopic investigations showed that the ferrihydrite formed aggregates made of poorly ordered ferrihydrite nanoparticles and this is in accordance with other literature findings (Janney et al. 2000a; Janney et al. 2000b).

(ii) Dynamic Light Scattering and Laser Diffraction measurements- Particle size measurement

Masterizer (laser diffraction) and dynamic light scattering measurement were done to determine the range of ferrihydrite aggregate sizes in the liquid phase at different particle concentrations and ionic strength, in the dynamic and static regime, respectively.

(a) Effect of particle concentration on ferrihydrite particle size - Dynamic Light scattering measurements

The effect of particle concentration on the average size of ferrihydrite aggregates was studied using dynamic light scattering in the static regime at zero ionic strength.

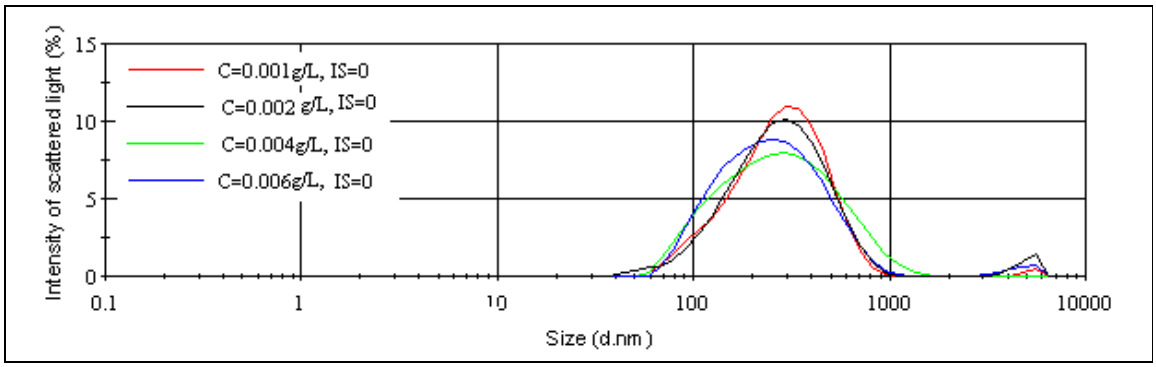

Figure 4. 3. Particle size distribution at ionic strength 0 for four different particle concentrations (Average of 3 measurements, 10 runs per measurement)

For particle concentrations of 0.001; 0.002; 0.004 and 0.006 gL^{-1} the average size of the aggregates at zero ionic strength was calculated by the DTS (Nano) software as: 261; 252; 226 and 221nm respectively, showing a small decrease in aggregate size with increasing particle concentrations in the system (Figure 4. 3). The Dynamic Light Scattering measurements showed that, in the static regime, at zero ionic strength, as the particle concentrations increased the particle size slightly decreased. This effect can be explained by the fact that Brownian motion in the system enhances particle dispersion and separation. From the shape of the plots (their broadness) it can be concluded that as the particle concentration decreases the particles become slightly more monodispersed (particle distributions curve narrows at small particle concentration).

(b) Effect of ionic strength on ferrihydrite particle size – Mastersizer measurements

Particle size distribution analysis in the dynamic regime (3000 rpm) was performed with Mastersizer laser diffraction. The effect of ionic strength on the particle (aggregate) / diameter is shown in Figure 4.4.

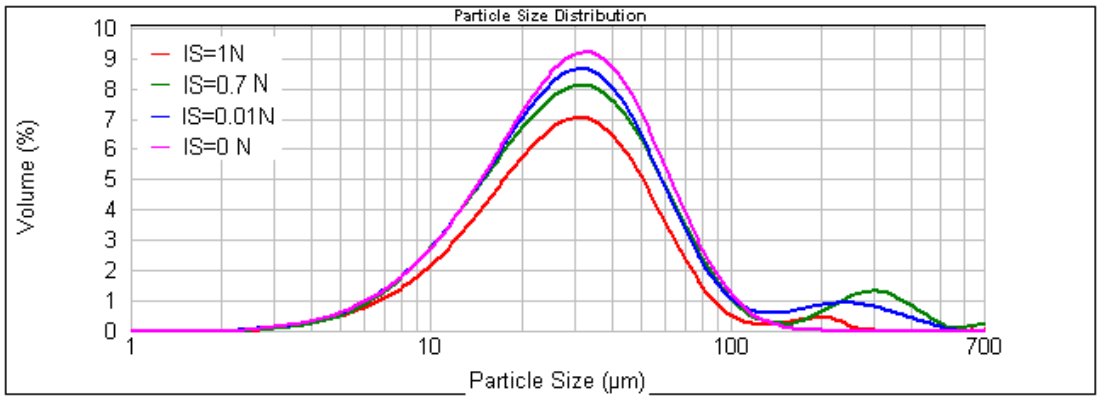

Figure 4. 4. Particle size distribution at different ionic strength and same particle concentration (0.002 gL^{-1}). Average of 20 measurements from Malvern Mastersizer 2000 (laser diffraction).

Figure 4. 4 shows the distribution of the median particle size (d_{50} or d (0.5)) of ferrihydrite aggregates at ionic strengths between 0 and 1N. On a scale of 1-10 % volume scattered, for all ionic strengths, the distributions of the aggregates with sizes between 30-40µm are cc. 6.97%, 8.06%, 8.92% and 9.17%, respectively. As the ionic strength increases the aggregates become bigger. In addition, it is notable that as ionic strength increases, small fractions (0.37-1.27%) of bigger particles form in the range of 150-400µm, although the average colloid sizes range between 10-80µm.

In the dynamic regime, the measurements of the ferrihydrite aggregates in the ionic strength interval of 0-1 showed that the aggregate size distribution is between 10-80µm (Figure 4.4.).

First trial measurements of average diameter of the ferrihydrite aggregates were carried out by Scheinost and collaborators (2001), who obtained a value of 30 µm. In addition, they also found that the aggregates of freeze dried ferrihydrite were smaller with a mean diameter of 15 µm (Scheinost et al. 2001).

More recently, Dynamic Light Scattering measurements of ferrihydrite colloids (iron concentration ~1.4 M) of Bosch and collaborators (2010) gave a value for colloidal ferrihydrite size of 336 ±40nm (Bosch et al. 2010). Their result agrees very well with our Dynamic Light Scattering measurement for the particle concentration range 0.001-0.005gL^{-1}.

Our data showed a difference between the particle sizes measured with the Dynamic Light Scattering *vs.* the Mastersizer measurements for the suspension with zero ionic strength and particles concentration of 0.002 gL^{-1} (200nm vs. 30µm). Explanations for this difference could be: (i) the fact that these techniques have different detection limits

(eg., the reason why the set of samples at different ionic strengths were not suitable to be measured with Malvern Zetasizer); (ii) the fact that these techniques calculate the diameter of the particle (assumming that the particle is spherical) from the measurement of different parameters of the particles (volume, weght, surface area, hydrodynamic diameter, etc) further converting it to radius or diameter; (iii) the fact that measurement regimes are different (i.e., static *vs.* dymnamic); thus the results given by both techniques for the sample with zero ionic strength and Cp = 0.002 gL^{-1}, differ by two orders of magnitude.

(iii) Potentiometric titration – surface charge characterization

The influence of ionic strength on the ferrihydrite surface properties is evident from the volume of base added to reach the same pH value. As the ionic strength increases, less volume of base is required (Figure 4. 5. A-C) and the buffer capacity of the ferrihydrite surface increase as the ionic strength decreases. The flocculation phenomenon was also visually observed in the ferrihydrite slurries before each titration. Even if the slurries were sonicated before titration and all samples were treated the same, at high ionic strength the ferrihydrite particles tended to form larger visible aggregates (*i.e.*, they flocculated). This qualitative effect is possibly due to a decrease in the thickness of the electrical double layer surrounding the individual nanoparticles. With increasing ionic strengh the particles aggregate more and at low ionic strength the electrical double layer is thicker and the particles aggregate less.

(A)

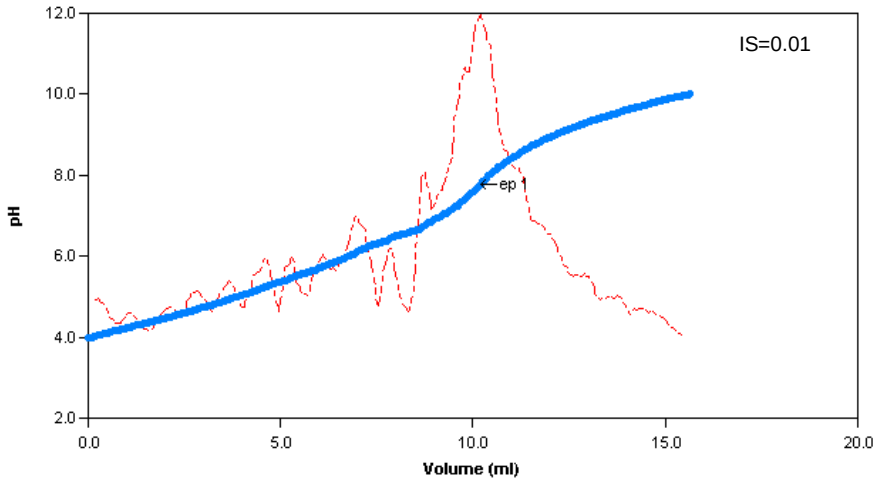

Figure continued on next page

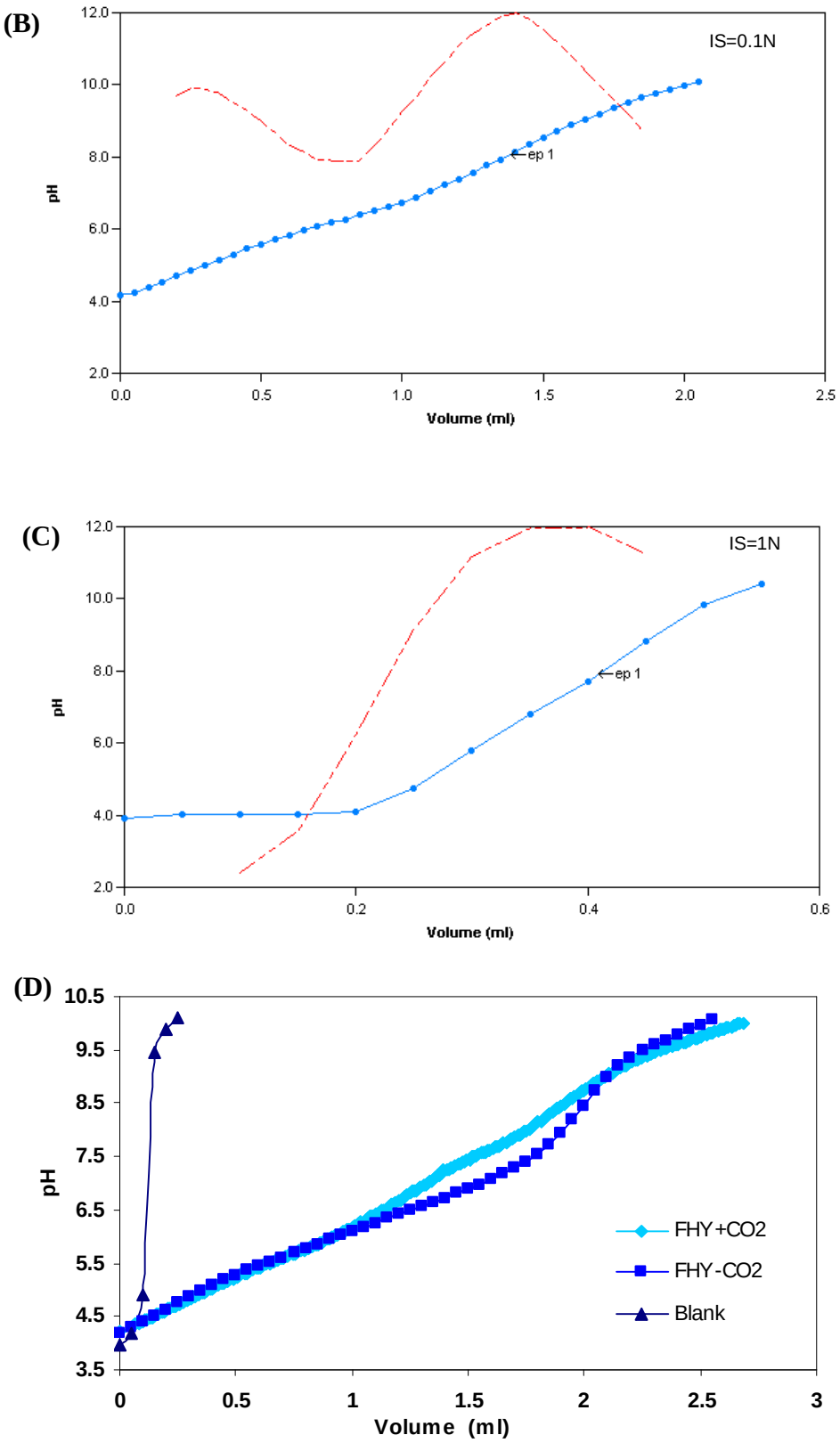

Figure 4. 5. Surface charge characterization of the ferrihydrite at different ionic strengths: (A) 0.01N; (B) 0.1N; and (C) 1N, and (D) the effect of CO_2 on ferrihydrite surface charge.

Blue curves are the volume of base added to titrate the sample from pH 4 to 10 and red curves are the first derivative of the pH *vs.* the base volume (mL)

At the end of the reverse potentiometric titration all samples at different ionic strength were kept at pH 4 at room temperature. After one month the slurries were filtered and characterized by XRD. The results showed that at high ionic strength a small proportion of ferrihydrite transforms to goethite (see Appendix A).

The first derivatives of the pH/V plots provide the pH value that corresponds to the end point (ep) and thus the pH value where the number of positive charges is equal with the number of negative charges (Figure 4.5.A-C). The end point pH values for the interval of the ionic strength studied are presented in Table 4. 2; the average is 7.96 ±0.11.

Table 4. 2. Summary of the results from potentiometric titration: point of zero charge of the ferrihydrite at different ionic strengths and appropriated pKa value

IS electrolyte	Vol $_{NaOH}$ (ml)	End point pH	pKa
0.01	15.65	7.96	6.23
0.1	2.05		
1	0.55		

The potentiometric titration results presented here confirmed that the point of zero charge of ferrihydrite was 7.96 which is in agreement with previous studies (Dyer et al. 2003; Trivedi et al. 2003). In addition, when the slurries were titrated in the presence or absence of CO_2 the data showed that the CO_2 influences the surface properties of the ferrihydrite between pH 6 and 9. The pKa value derived from each ionic strength titration is 6.23 +/-0.05 (Table 4. 2.). From comparison with literature this value can be assigned to be the dissociation constant of cis-CO_2H isomer.

(iv) BET-surface area measurements

BET measurements of starting ferrihydrite gave a surface area of 198 (± 2.18) m^2g^{-1}. Important to note is that in the literature surface area values for ferrihydrite vary between 200 and 700 m^2g^{-1} and in surface complexation models a theoretical value of 600m^2g^{-1}

(Dyer et al. 2003; Dyer et al. 2004; Trivedi et al. 2003; Trivedi and Lisa 2001) is usually used. However, some studies also obtained a surface area of 200 m^2g^{-1}: Song and collaborators (2008) - 206 m^2g^{-1}, (Vu et al. 2010) – 200 m^2g^{-1}, and Scheinost and collaborators (2001) - 245 ±10 m^2g^{-1}.

Our experience and literature studies have shown that despite the fact that the same synthesis method is followed, small to large differences (±50 m^2g^{-1}) in surface area have been measured. This behavior is due to factors which are related to the synthesis protocol: rapidity of iron solution titration, the washing method, the number of washings after synthesis, storage method and storage time etc. Gustafsson (2003), as well as Cornell and Schwertmann (2003) state that even if the same synthesis method is used ferrihydrite surface areas can vary between 200 and 320 m^2g^{-1} and that this variation may also be due to the outgassing conditions during BET measurements (Cornell and Schwertmann 2003; Gustafsson 2003).

4.3.2. Adsorption kinetics

The adsorption kinetic data reveals that molybdenum and vanadium adsorption at low pH is fast (<20min), with vanadium adsorbed about twice as fast as molybdenum. This is the first indication that ferrihydrite has a higher affinity for vanadium compared to molybdenum (Figure 4. 6).

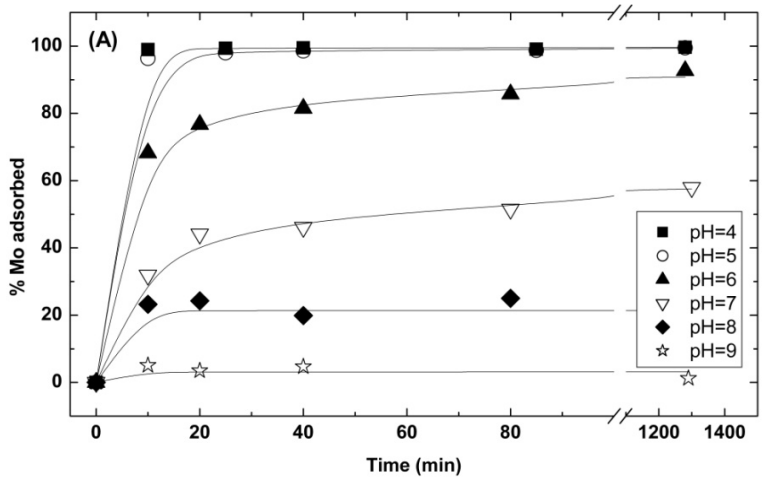

Figure continued on next page

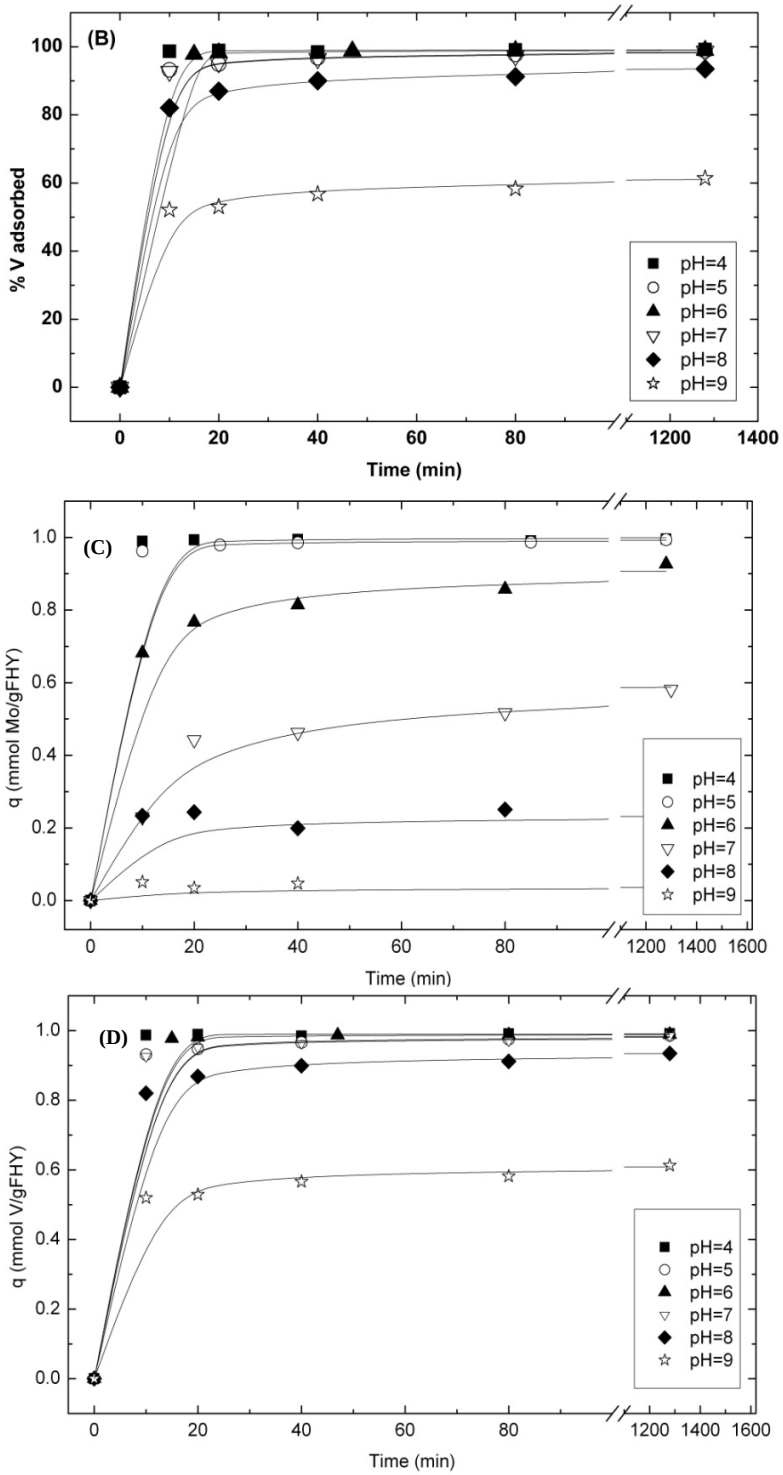

Figure 4. 6. The kinetics of molybdenum (A) and vanadium (B) adsorption on ferrihydrite at different pH values in the mono-sorbate systems: molybdenum (A) and vanadium (B) removal efficiency by ferrihydrite (C_i=100µM metal and C_{FHY} =0.1gL^{-1}) and (C) molybdenum and (D) vanadium adsorption uptake capacities onto ferrihydrite. Symbols

represent experimental data and lines show the fits to a pseudo-second order kinetic model. Errors in metal concentrations were smaller than the size of the symbols.

The molybdenum and vanadium removal efficiencies (Figure 4. 6.A and B) indicate that the adsorption/removal efficiency for molybdenum is high at pH below 6 (90-100%) but decreased with increasing pH (i.e., pH 7 < 60 %, pH 8 < 20 % and pH 9 < 3%), while for vanadium the adsorption efficiency decreased to ~ 60 % only at pH 9. This pH dependent behavior revealed that below pH 6, both vanadium and molybdenum have the highest affinity for the ferrihydrite binding sites (Figure 4. 6.A and B).

Ferrihydrite loading in the molybdenum and vanadium adsorption studies is also expressed as uptake capacities (q) and plotted in Figure 4. 6.C and D.

For both molybdenum and vanadium the uptake capacities and removal efficiencies follow the same trend: but there is a bigger decrease with increasing pH for the molybdenum system compared to the vanadium system. Within the molybdenum and vanadium set of experiments, the results from the uptake capacities are proportional with the ones expressed as removal efficiencies.

Both sets of plots were fitted with a pseudo second order kinetic model which assumed that the adsorption mechanism is chemo sorption (Herrero et al. 2006) Eq. 4.3. Table 4. 3. summarizes the weighted uptake capacities from the kinetic fittings. Note that the goodness of fit (R^2) for the vanadium system is very good (close to 1) over the entire pH interval, while for the molybdenum system R^2 is decreasing with increasing pH (*i.e.,* at pH 8 R^2 =0.6685 and at pH 9 R^2 =0.3537).

Table 4. 3. Summary of the pseudo-second order kinetic model parameters

Mo	**Q (mmol/g)**	**Error**	**R^2**
4	0.999	0.0022	0.9996
5	0.993	0.0005	0.9999
6	0.909	0.0048	0.9984
7	0.592	0.0113	0.9904
8	0.232	0.0158	0.6685
9	0.036	0.0098	0.3537
V			
4	0.999	0.0049	0.9998
5	0.983	0.0015	0.9999
6	0.988	0.0004	0.9999
7	0.980	0.0010	0.9999
8	0.935	0.0019	0.9998
9	0.609	0.00772	0.992

These results give a macroscopic view of the molybdenum and vanadium adsorption mechanism within the studied pH interval. Very good fits to a pseudo second order kinetic model indicate that the adsorption takes place following a chemo-sorption mechanism (strong chemical bonding), whereas a poor fit implies a change in adsorption mechanism, most probably towards physical-sorption (weak bonds).

Hartzog et. al.,(2009) described the best protocol to compare, normalize and scale pH dependent adsorption data. They did experiments with As-goethite on sand. By varying individual parameters such as absolute adsorbant and/or adsorbent concentration and relative adsorbate concentration in an arsenate goethite batch adsorption system at pH between 3 and 10, they found that the log Kd (distribution coefficient) approach is the most sensitive measure of adsorption studies compared to q and E. Their results in association with other literature findings (Belova et al. 2008) suggested that normalizing the adsorption data to surface area rather than adsorbent mass reduces the variability in Kd and q for adsorption (Hartzog et al. 2009). Thus, below our uptake capacity data along with other literature findings were normalized to surface area and compared.

Table 4. 4. Anions adsorption onto iron oxides - literature comparison

Anion	Iron oxides - adsorbent and conditions	q (mmol/gFe)	q (mmol/m^2)	References
V	FHY – slurry; SA=200m^{2}g^{-1}; pH 7; Ci = 100µM;	1.333	0.0049*	This study
Mo	FHY – slurry; SA=200m^{2}g^{-1} ; pH 7; Ci = 100µM;	0.986	0.0027*	This study
P	Biogenic oxides; pH 6.4; Ci = 100µM;	1.77	n.a.	(Rentz et al. 2009)
As	Goethite coated sand; SA=178m^{2}g^{-1}; pH 7; Ci = 67µM	0.134	$2.82 \cdot 10^{-6}$ §	(Hartzog et al. 2009)
As	Goethite; SA= 20m^{2}g^{-1}; pH 7; Ci = 100 µM; Cp=0.9gL^{-1}	0.0760	0.0024	(Kersten and Vlasova 2009)
P	FHY slurry; SA=200-320m^{2}g^{-1}; pH 7.18; Ci=200uM	0.182	0.0039‡	(Gustafsson 2003)
W	FHY slurry; SA=200-320m^{2}g^{-1}; pH 7.29; Ci=50uM	0.086	0.0019‡	(Gustafsson 2003)
Mo	FHY slurry; SA=200-320m^{2}g^{-1}; pH 7.09; Ci=50uM	0.062	0.0021‡	(Gustafsson 2003)

*conversion to mmolg^{-1} Fe was made taking into account that 1 g ferrihydrite contains 600 mg of Fe (measured value);

§ for comparison a synthesized goethite coated sand with SA = 178 m^{2}g^{-1} and $6.83 \cdot 10^{-5}$ mol Fe g^{-1} material was used.

‡ An averaged surface area of 260 m^{2}g^{-1} and iron content per g ferrihydrite of 558 mg Fe g^{-1} ferrihydrite was used.

Comparing our results in term of anion adsorption (mmol) per iron oxide mineral surface (m^2) (Table 4. 4.) revealed that the uptake capacities for all anions are within the same order of magnitude (0.0019 to 0.0049 mmol m^{-2}). An exception is the As adsorption on goethite co-precipitated sand study by Hartzog et al. (2009), which showed a adsorption capacity of three orders of magnitude smaller than all other values. This

difference may be explainable by the fact that they used goethite coated sand and not a pure mineral phase.

Potentiometric stat data from the pH effect adsorption experiments

In order to maintain the pH constant during the adsorption of molybdenum and vanadium at low pH (4 and 5 respectively) volumes of acid of 1.2 ml for molybdenum (pH 4) and 3 ml for vanadium (pH 5) and volumes of base of 1 ml for molybdenum and 2.8 ml for vanadium were needed (Figure 4. 7. A and C). Note that in both adsorption studies slightly more acid was added as the anions were adsorbed onto the protonated ferrihydrite surfaces. In other words, anion adsorption onto the protonated ferrihydrite surface (pH below point of zero charge) takes place with hydroxyl release (which raises the pH and requires more acid to keep the pH of the system stable at 4 and 5 respectively). Comparatively, at high pH values (above the ferrihydrite point of zero charge) more base (1.7 ml for molybdenum and 3.2 ml for vanadium) than acid was required for the system to maintain its pH constant during the molybdenum and vanadium adsorption onto the negatively charged ferrihydrite (Figure 4. 7. B and D). Molybdate and vanadate adsorption onto ferrihydrite surfaces at high pH take place by proton release.

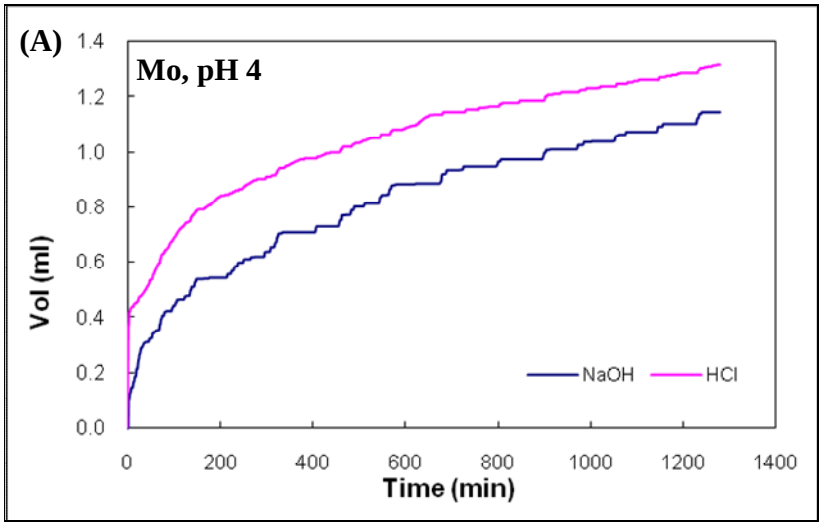

Figure continued on next page

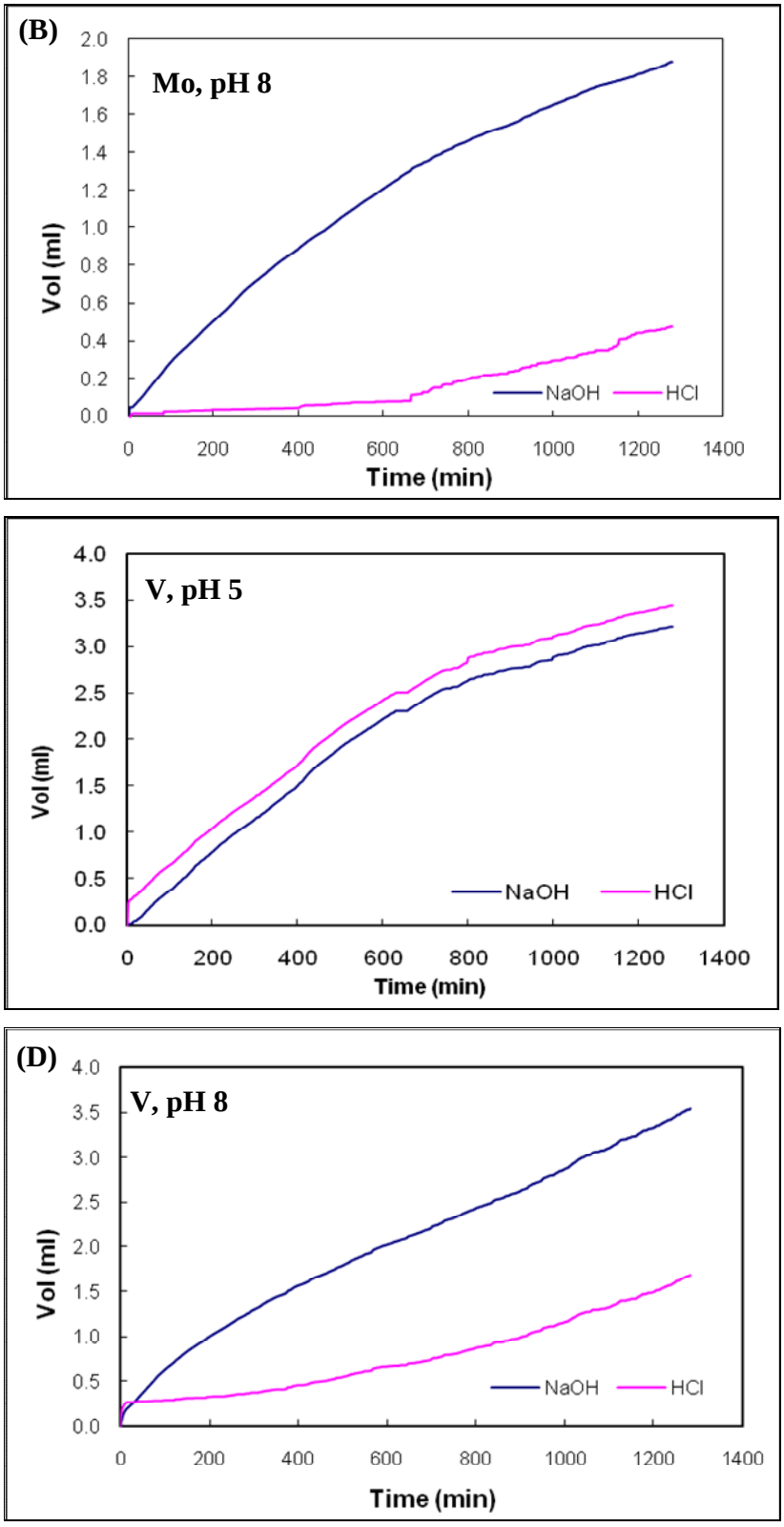

Figure 4. 7. The profiles of hydrochloric acid (pink line) and sodium hydroxide (blue line) added to molybdenum (A and B) and vanadium (C and D) absorbtion systems during their

adsorption onto ferrihydrite at low pH (4 for molybdenum and 5 for vanadium) and high pH (8 for both: molybdenum and vanadium).

From this data, it can be deduced that the adsorption mechanism changes with pH. How exactly the molybdate and vanadate molecules are linked to the ferrihydrite surfaces can only qualitatively be assessed at this stage : at low pH multi protonated anions are losing H^+ from their structure to be able to strongly bind to the positively charged ferrihydrite surfaces; conversely at high pH (>8, PZC) low adsorption of bi and tri valent anions (molybdate and vanadate, respectively) is taking place probably via a outer sphere type of complex onto the negatively charged ferrihydrite surface (as more hydroxyl groups are needed during adsorption). The acid and base volumes added during the adsorption of the two anions differed. This difference may be related to (a) anion size and (b) valence, both these parameters dictate the adsorption bonding environment. However, surface modeling (see later 4.3.4) was used to derive more information about adsorption mechanism at this macro scale.

4.3.2.1. pH effects

In Figure 4. 8. the efficiencies of molybdenum and vanadium removal by ferrihydrite from the solution at different pH values are shown. At pH below 7, vanadium has the highest affinity for ferrihydrite binding sites. The removal efficiency of vanadate by ferrihydrite decreases significantly at pH 9 (60 %). From the molybdenum profile it can be seen that molybdenum has been removed from the solution almost entirely at pH below 6. The removal efficiency decreased considerably from 60% at pH 7 to 22 % at pH 8 and only 5 % at pH 9.

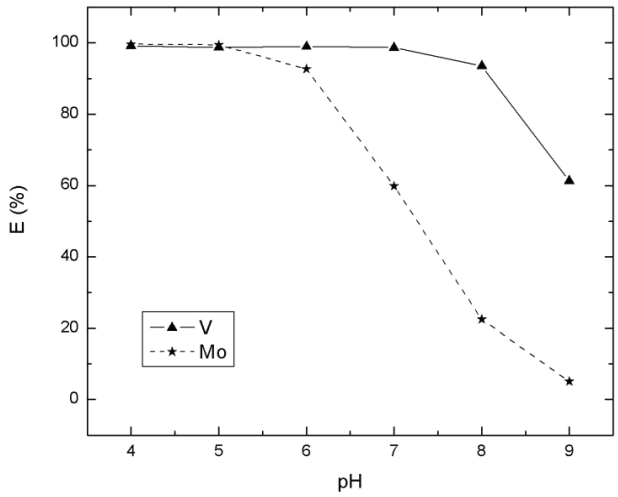

Figure 4. 8. The influence of pH on molybdenum and vanadium adsorption onto ferrihydrite. ($C_{Mo/V} \approx 100\mu M$, $C_{FHY} = 0.1gL^{-1}$)

These results agree well with the ferrihydrite surface charge results which showed that ferrihydrite has a protonated surface charge at pH below 7.9 (point of zero charge) and a negatively charged surface at pH above it. Thus, below pH 8, both anions: vanadium (vanadate) and molybdenum (molybdate) have high affinities for the ferrihydrite surface. However, note that vanadium is taken up by ferrihydrite over a larger pH interval compared to molybdenum.

Table 4. 5. Molybdenum and vanadium adsorption studies – literature comparative view

System	Conditions	Results (sorption efficiency)	Reference
Mo adsorption onto FHY	C_{Mo} = *50μM*; C_{FHY} =1g L^{-1} ; *pH 3-8*	pH below 6.5: 95-100%; pH 7: 68 %; pH 8 ~ 15 %; and pH 9 ~ 1.5%	Gustafsson, 2003
	C_{Mo} = *100μM*; C_{FHY} = 0.1g L^{-1} ; *pH 4-9*; IS=0.01	pH below 6: 90-100%; pH 7 ~ 60 %; pH 8 ~ 20 % and pH 9 ~ 3%	This study
V adsorption onto FHY	C_V = 200μM V, C_{FHY} =2gL^{-1} , pH 8, *IS= 0.7(seawater)*	>80 %	Trefry and Metz 1989
	C_V = *100μM*; C_{FHY} = 0.1g L^{-1} ; pH = 7; *IS=0.01*	>90 %,	This study

Only one other study on molybdenum adsorption onto ferrihydrite (Gustafsson 2003) and one on vanadium (Trefry and Metz 1989) are available in the literature, yet those were carried out at different conditions (Table 4. 5.). Briefly, Gustafsson (2003) found similar trends of molybdenum adsorption onto ferrihydrite within the pH interval of 3 to 9. Using molybdenum concentration of 50 μM and ferrihydrite concentration of 1g L^{-1} he obtained 95-100% removal of molybdenum below pH 6.5; 68 % at pH 7; ~ 15 % at pH 8 and ~ 1.5% pH 9.

Trefry and Metz (1989) showed that 80% of the vanadium was removed within two minutes from synthetic seawater (pH 8 and ionic strength 0.7) spiked with 200μM vanadium, in the presence of 2gL^{-1} ferrihydrite. Comparing their results with our findings shows that vanadium is rapidly taken up by ferrihydrite both in distilled water (at pH 7- this study) and in seawater (at pH 8 - Trefry and Metz, 1989).

4.3.2.2. Particle concentration effects

The data from the experiments with variable particle concentrations (Figure 4. 9.A and D) indicate that for the molybdenum system at concentrations above $1gL^{-1}$ all molybdenum was removed from the solution. At a particle concentration of $0.1gL^{-1}$ however, only 40% of molybdenum was adsorbed (ferrihydrite binding sites being saturated). Conversely, for the vanadium system, 100% of vanadium was removed in all three conditions. These results underline the higher affinity of vanadium compared to molybdenum for ferrihydrite surfaces at pH 7 within the studied conditions. In addition, in the molybdenum system the removal efficiency data show that at a particle concentration of $0.1gL^{-1}$, ferrihydrite binding sites become saturated at 40% of the total 100µM molybdenum, whereas at the same particle concentration all vanadium (100µM) was removed from the solution. Thus, the ferrihydrite available binding sites might not be saturated in the molybdenum system at concentration above 1 g L^{-1}, while in the vanadium system at all working particle concentrations the vanadium was removed.

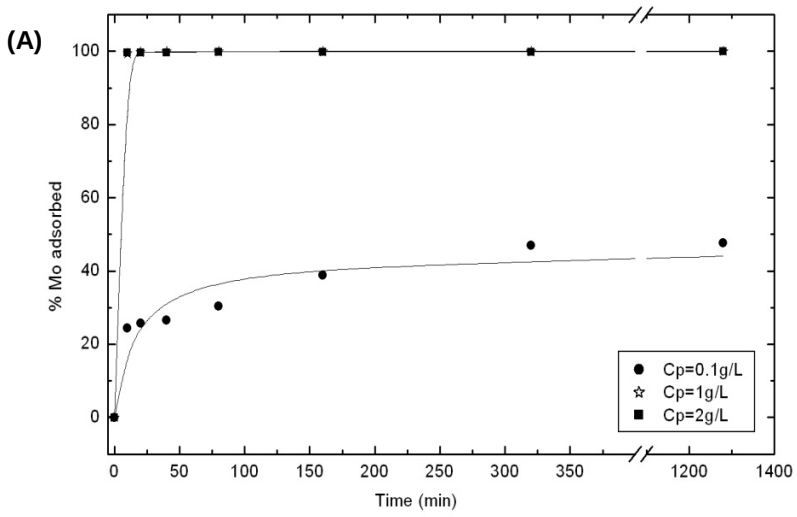

Figure continued on next page

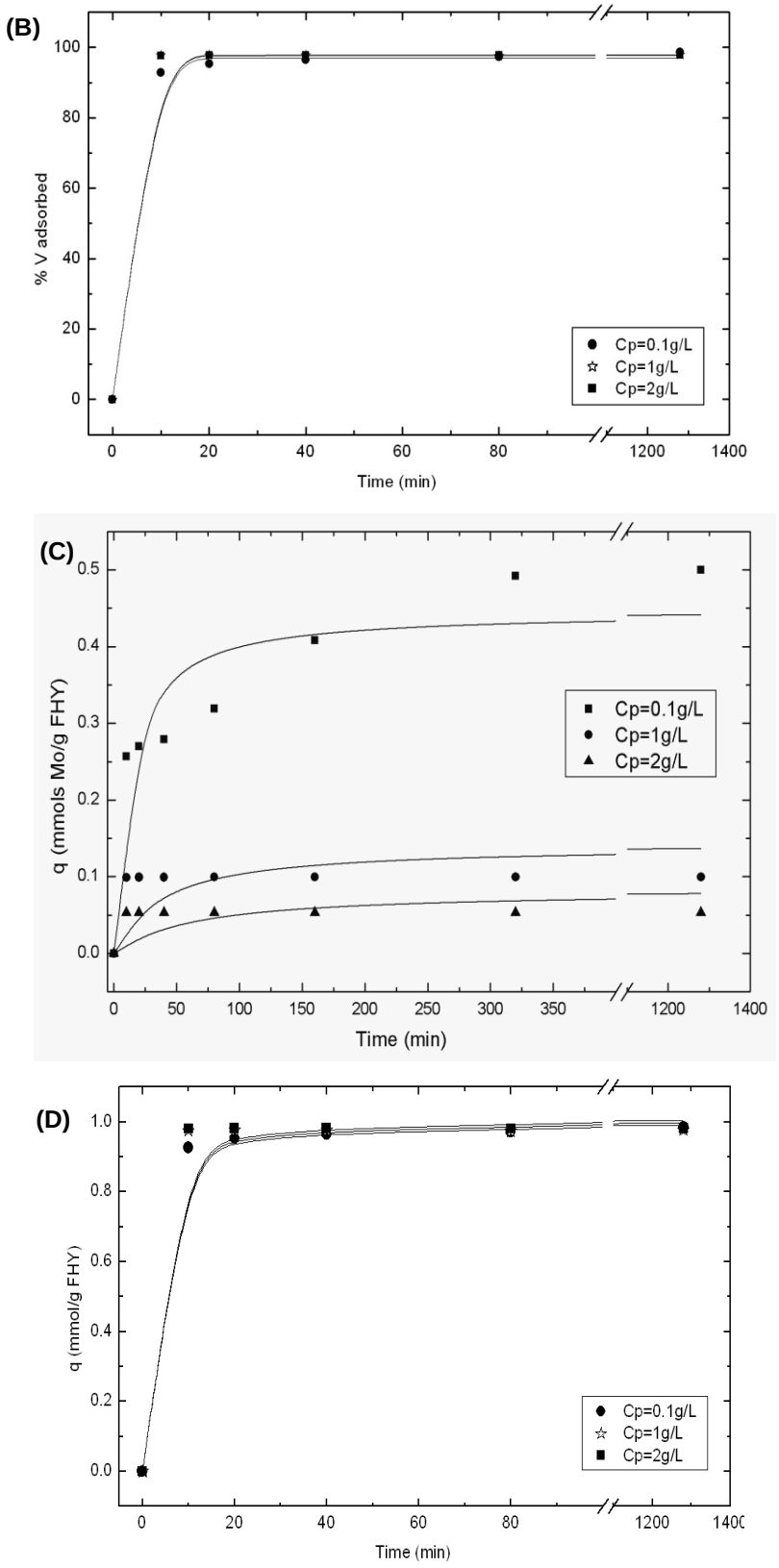

Figure 4. 9. The kinetics of molybdenum (A and C) and vanadium (B and D) adsorption onto ferrihydrite at different particle concentrations ($C_{Mo/V}$=100 µM; C_{FHY} = 0.1-2 gL^{-1}, T=

23±2ºC, pH 7) expressed as: (A) and (B) removal efficiencies and (C) and (D) uptake capacities. Dots are experimental data and lines are fits with a pseudo-second order kinetic model.

Figure 4. 9. C indicates that at lower particle concentrations molybdenum is adsorbed onto ferrihydrite surface with a maximum capacity of 0.44 mmol g^{-1}. As the particle concentration increases to 1gL^{-1} and 2gL^{-1}, respectively, less molybdenum per g ferrihydrite (0.14 mmol g^{-1} and 0.08 mmol g^{-1}) was taken up. This trend can be explained by considering the distribution of a constant amount of molybdate ions onto an increasing number of binding sites available (high particle concentration). For the vanadium system, a high uptake capacity (ca 1.02 mmol g^{-1}) was reached for all particles concentrations (Figure 4. 9. D). In other words, as the particle concentration increases between 0.1 to 1 g L^{-1}, ferrihydrite can adsorb progressively longer amounts of vanadium from solution and above this interval ferrihydrite reaches its maximum uptake capacity.

Comparing the trends of molybdenum and vanadium uptake in the particle concentration interval of 0.1 to 1g L^{-1}, it can be deduced that for 100µM initial metal concentration the saturation ratio of metal: binding sites available is: between 0.1 and 1g L^{-1} for molybdenum and above 2g L^{-1} for vanadium.

Empirically, if we consider a ferrihydrite surface area of 200 m^2g^{-1}, a ferrihydrite site density of 2.3 sites/nm^2 and a metal concentration of 100µM (= $1x10^{-4}$ molL^{-1} = $10x10^{-5}$ molL^{-1}), the surface sites available for adsorption can be calculated (Table 4. 6.). Theoretically at a particle concentration of 0.1 gL^{-1}, 100µM of molybdenum or vanadium should cover all ferrihydrite surfaces to saturation and 25% of the available molybdenum and vanadium should still be free. Conversely at 1gL^{-1} and 2gL^{-1} only 13% and 7%, respectively of the surface is covered. These empirically calculated values do not match the experimental results.

Table 4. 6. Summary of the pseudo-second-order kinetic model parameters the molybdenum and vanadium adsorption onto ferrihydrite at three different particle concentrations

System	Surface sites available (mols site/L)	Theoretical coverage	Q (mmol/g FHY)	Error	R^2
V - Cp=0.1gL^{-1}	7.54x10^{-5}	100%	0.997	0.0009	0.991
V - Cp=1gL^{-1}	7.54x10^{-4}	13%	1.003	0.0198	0.995
V - Cp=2gL^{-1}	15.08x10^{-4}	7%	0.990	0.0193	0.993
Mo - Cp=0.1gL^{-1}	7.54x10^{-5}	100%	0.444	0.0213	0.999
Mo - Cp=1gL^{-1}	7.54x10^{-4}	13%	0.140	0.0172	0.979
Mo - Cp=2gL^{-1}	15.08x10^{-4}	7%	0.081	0.0120	0.979

A summary of the molybdenum and vanadium uptake parameters, weighted by the pseudo-second order kinetic model are given in the Table 4. 6. A direct comparison between molybdenum and vanadium uptake capacities expressed per gram ferrihydrite indicated that for vanadium an average of 0.997 mmol g^{-1} ferrihydrite were adsorbed at all particle concentrations while for molybdenum the ferrihydrite loading decreased (from 0.444; to 0.140 and to 0.081 mmol g^{-1}) with increasing particle concentration (from 0.1 to 2 g L^{-1}).

4. 3. 2. 3. P-competitive studies

The experimental data obtained from the phosphorus competitive adsorption studies at pH 7 (Figure 4. 10) showed that in the mono-sorbate (P) and bi-sorbate studies (P-Mo and P-V), the phosphorus uptake achieved steady state within 80-100 minutes. However, as shown above, in the mono-sorbate molybdenum and vanadium systems, the adsorption process was significantly faster (within 10 minutes for vanadium and 20 minutes for molybdenum) than in the phosphorus bi-sorbate system (up to 80 min).

The weighted maximum uptake capacity of phosphorus in the mono-sorbate system was 0.69 mmol g^{-1} (Table 4. 7.), while when equal concentrations of vanadium and phosphorus (100 µM) were added to the system, the maximum phosphorus uptake efficiency decreased to 0.381 mmol g^{-1} suggesting that almost half of the available binding sites on the ferrihydrite surface were occupied by vanadate ions. In the presence of

molybdenum, no significant effect on the phosphorus maximum uptake capacity was observed (Figure 4. 10. B).

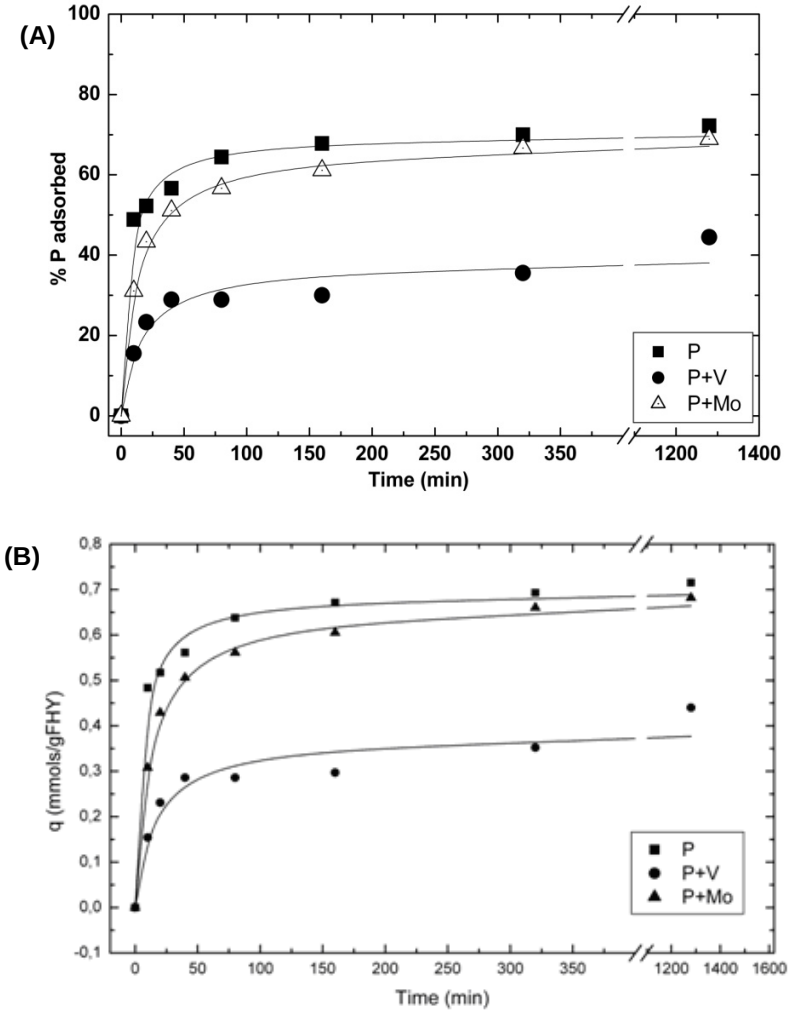

Figure 4. 10. Pseudo second order kinetics of phosphorus adsorption onto ferrihydrite in mono and binary systems with molybdenum and vanadium; (Ci=100µM; C_{FHY} =0.1gL^{-1}, T= 23±2ºC, pH 7) - expressed as: (A) removal efficiency and (B) uptake capacity. Symbols are experimental data and lines are fits to pseudo-second order kinetic model.

Table 4. 7. Summary of the pseudo-second-order kinetic model parameters for mono and binary (with molybdenum and vanadium) adsorption studies of phosphate onto ferrihydrite

System	Q (mmol/g FHY)	Error	R^2
P	0.691	0.01656	0.9860
P + V	0.381	0.02425	0.9332
P + Mo	0.670	0.00996	0.9957

For comparison, Gustafsson (2003) showed that in the presence of phosphorus (200µM) a Mo-ferrihydrite adsorption system (pH 7; 50µM Mo; 0.1g ferrihydrite L^{-1}) reduced the molybdenum adsorption efficiency from 80% to 8%. His study revealed that at pH = 7 and at P:Mo ratio of 4:1, phosphorus out competed molybdenum (~ 8% molybdenum and 92% phosphorus). In the present study conducted at a lower P:Mo ratio of 1:1, phosphorus still out competes molybdenum (< 3 % molybdenum and 97 % phosphorus).

Comparable results were obtained by Rentz and collaborators (2009), who studied the kinetics of phosphate adsorption onto natural biogenic iron oxides separated from microbial mats collected from a freshwater wetland system. They obtained a modelled (with pseudo-second order kinetic model) uptake capacity of 46 $mg_P\ g_{Fe}^{-1}$ or 1.48 $mmol_P\ g_{Fe}^{-1}$ for a phosphorus initial concentration of 84µM (Rentz et al. 2009). Scaling their uptake capacity value from 84µM to 100µM, a new phosphorus uptake capacity at pH 6.4 of 1.76 $mmol_P\ g_{Fe}^{-1}$ can be calculated. Specifically, assuming that 1g of ferrihydrite contains ca 600 mg iron (average value measured from ferrihydrite digestion in 6M HCl) our phosphorus uptake capacity at pH 7 would be 1.15 $mmol_P\ g_{Fe}^{-1}$. Taking into account the difference between the nature of the samples and the pH these results are similar within error of each other.

4. 3. 2. 4. Influence of different matrices on molybdenum and vanadium adsorption onto ferrihydrite

Batch adsorption studies of 1000µM molybdenum and vanadium (high metal concentration to avoid seawater interference in metal analyses with ICP-OES) were conducted in three different matrices: distilled water, seawater with organics and seawater without organics. These studies aimed to assess the influence of seawater compounds onto vanadium and molybdenum adsorption specifically: organic and inorganic compounds and inorganic compounds only. In addition, the results obtained from these studies will

help scale up all previous laboratory adsorption studies run in distilled water to seawater environments.

As shown in Figure 4. 11. A about 9% molybdenum was removed by the seawater with organics and only 6.5% by the seawater without organics, thus the content of organics in natural seawater removes 2.5% of the molybdenum added. Figure 4. 11. B presents clear evidence that vanadium has higher affinity for ferrihydrite surfaces in seawater matrices compared with distilled water (20% removed in DW vs. 32% removed in SW). This behaviour might be due to the formation of inorganic vanadium complexes with seawater compounds which may enhance vanadium adsorption onto the ferrihydrite surfaces. No specific interactions of vanadium with organics from the seawater could be noted.

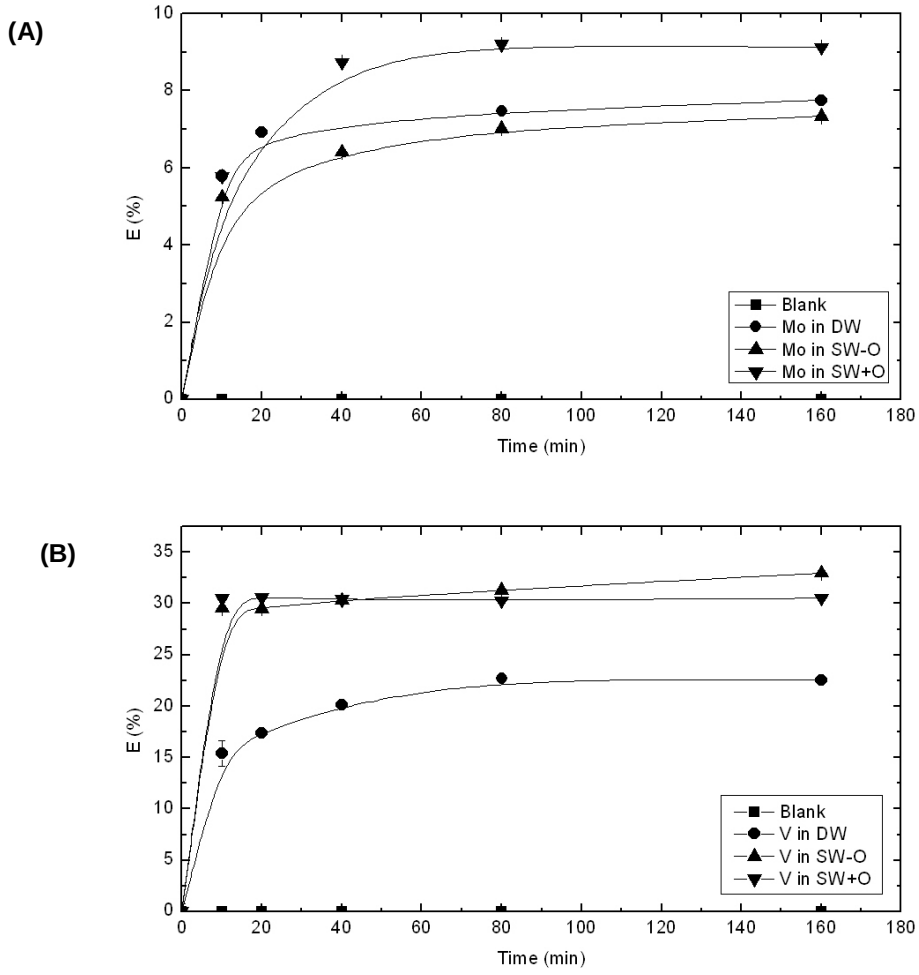

Figure 4. 11. Kinetic profile of molybdenum (A) and vanadium (B) adsorption onto ferrihydrite (Ci=1000µM; C_{FHY} =0.1gL^{-1}, T= 23±2ºC, pH 7±0.2), expressed as removal

efficiency *vs*. time, in three different matrices: distilled water, (DW); seawater without organics, (SW-O) and seawater with organics, (SW+O). Symbols are experimental data and lines are fits to a pseudo-second order kinetic model.

For scaling up the adsorption studies, 22% for molybdenum and 33% for vanadium needs to be added to the values obtained from all the experiments carried out in distilled water to transpose the values to seawater environments

A comparison of the two results (molybdenum and vanadium removal efficiencies in seawater matrices (Figure 4. 11. A and B)) reveals that vanadium is removed much more efficiently (max. 31%) by ferrihydrite than molybdenum (max 9%).

No molybdenum adsorption studies in seawater conditions are available in the literature. However, Trefry and Metz (1989) have conducted an adsorption study using 200µM vanadium and 2gL^{-1} ferrihydrite in a synthetic seawater matrix from which they obtained an 80% removal efficiency of vanadium (Trefry and Metz 1989). It is interesting to note that even if the ratio of V: ferrihydrite (expresses as µM V:g FHY) differs by 100 times between our study (10000µM V:1g FHY) and Trefry and Metz study (100µM V :1gFHY), the vanadium uptake efficiency differs with only 49%.

4.3.3. Adsorption and co-precipitation isotherms

Adsorption and co-precipitation isotherms were obtained in order to compare the uptake capacities of the ferrihydrite for molybdenum and vanadium via two distinct processes. From the experiments where 1g of ferrihydrite was co-precipitated with 1-10000µM molybdenum or vanadium at pH 7 and room temperature, the maximum uptake (sequestration) capacities of molybdenum and vanadium via co-precipitation could be derived. These are 3.36 mmol g^{-1} for vanadium and 2.48 mmol g^{-1} for molybdenum (Figure 4. 12. A). The results showed that the maximum uptake capacities for molybdenum and vanadium were lower via adsorption [Mo (0.43 mmol g^{-1}) and V (1.28 mmol g^{-1})] in comparison with the co-precipitation [Mo (2.48 mmol g^{-1}) and V (3.36 mmol g^{-1})] for the same experimental conditions.

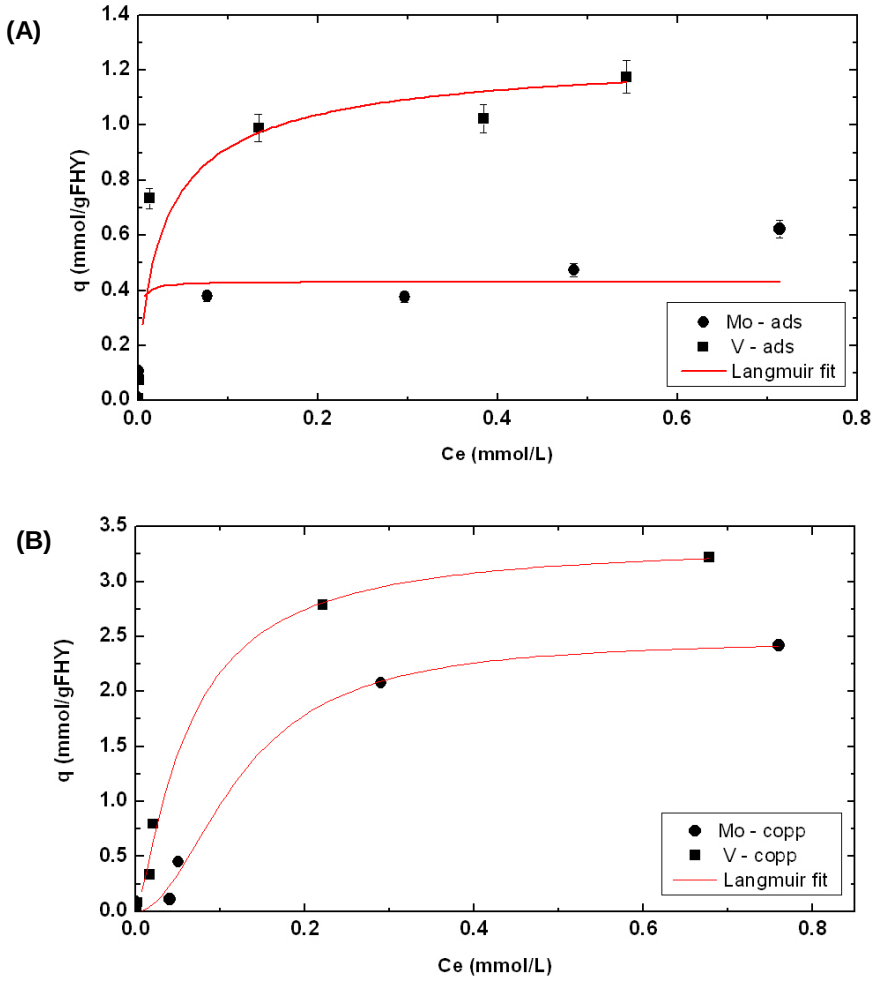

Figure 4. 12. Adsorption (A) and co-precipitation (B) isotherms of molybdenum and vanadium onto/with ferrihydrite at pH 7, ionic strength 0.01, C_{FHY}=1g L^{-1}, $C_{Mo/V}$= 1-10000µM.

Fitting the experimental results with the Langmuir Isotherm Model, gave good regression factors (Table 4. 8.).

The Langmuir model assumes that adsorption takes place as a monolayer; all adsorption sites are energetically equal and also are homogenously spread over the substrate surface.

Maximum metal-loading capacities or maximum uptake capacities given by a Langmuir isotherm allow the comparison of the potential of different sorbents to remove and control the availability of molybdenum and vanadium. It is important to note that such comparisons are valid only if the process conditions are specified and equivalent.

Table 4. 8. Summary of the maximum uptake capacities of vanadium and molybdenum via adsorption and co-precipitation at pH 7, ionic strength 0.01, Cp of 1gL^{-1} and $C_{Mo/V}$ interval of 1-10000µM

System	qmax (mmol/g FHY)	R^2
Mo - ads	0.431	0.949
V - ads	1.28	0.920
Mo - copp	2.48	0.980
V – copp	3.36	0.991

As an approximated comparison with other anion adsorptions onto ferrihydrite, Sannino and collaborators (Sannino et al. 2009) recently published the Langmuir maximum uptake capacities of As (V) and Cr (VI) onto ferrihydrite, but at pH 4, as being 0.743mmolAs g^{-1} and 0.254mmolCr g^{-1}, respectively. The values are in the same order of magnitude as those from this study, but the small difference might be explained by the fact that their pH was lower than in the present study, which also explains the higher affinity of anions for ferrihydrite surface (*e.g.,* Figure 4. 8.)

4.3.4. Surface chemistry modeling and adsorption simulation

Experimental molybdenum and vanadium adsorption studies onto ferrihydrite at different pH values were simulated with Visual MINTEQ 2.32 (Gustafsson 2005) to compare the experimentally derived uptake capacities with the model at equivalent conditions and to assess the modeling errors (accuracy). In addition, information about vanadium and molybdenum speciation as well as ferrihydrite surface species at different pH values can be extracted to derive mechanistic information about the adsorption processes.

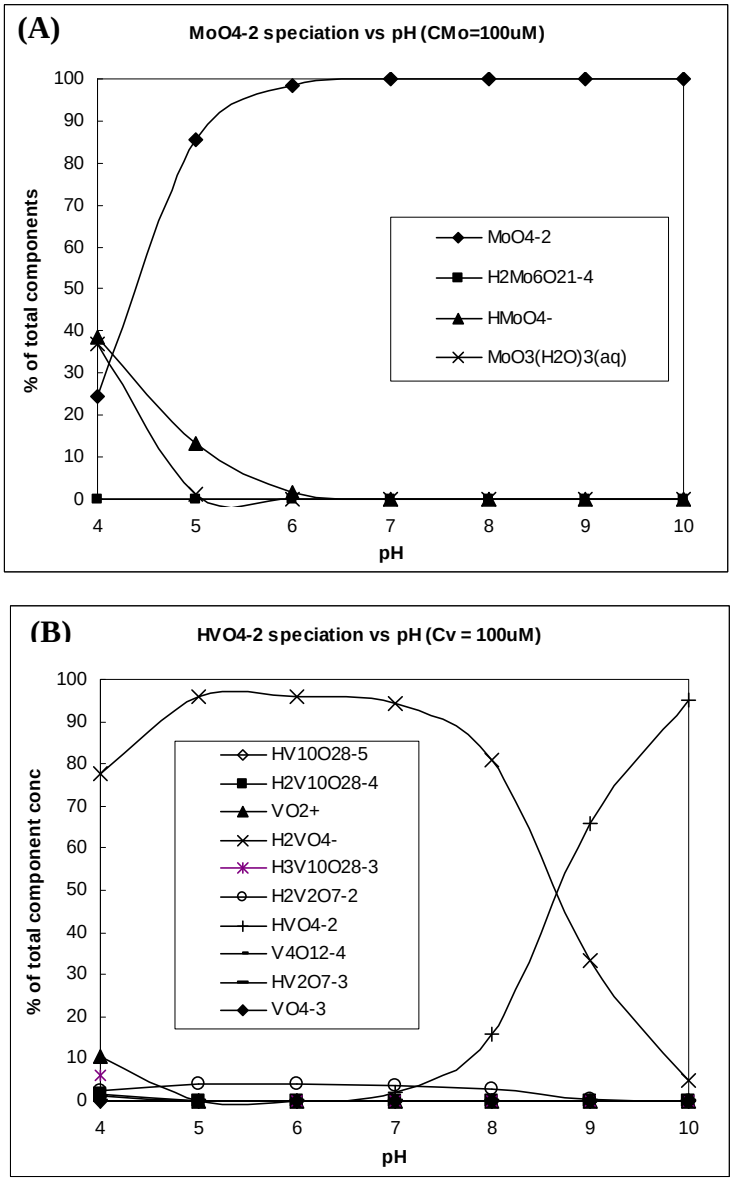

Figure 4. 13. Molybdenum and vanadium speciation at different pH values in distilled water at 25ºC and metal concentration of 100µM.

In the studied system, 100% of the molybdenum is present as MoO_4^{2-} (molybdate) at pH 6 to 10, while at pH 5, only 85% of molybdenum is molybdate and 13% $HMoO_4^-$ and 2% MoO_3 (molybdenum trioxide) three hydrated (Figure 4. 13. A). Conversely, $H_2VO_4^-$ is the most common species (80-97%) at pH between 4 and 8 and above pH 8 HVO_4^{2-} becomes the dominant species. About <5-10% of other vanadium species (*e. g.,* VO_4^{3-}; $HV_2O_7^{3-}$; VO^{2+} et al., are also present in solution at most pH values. These diagrams help us understand the species which are able to interact with the ferrihydrite surfaces during adsorption.

Furthermore, the adsorption of molybdenum and vanadium and the speciation of iron, at different pH values were modeled using DLM (Diffuse Layer Model) (Figure 4. 14. and Figure 4. 15.)

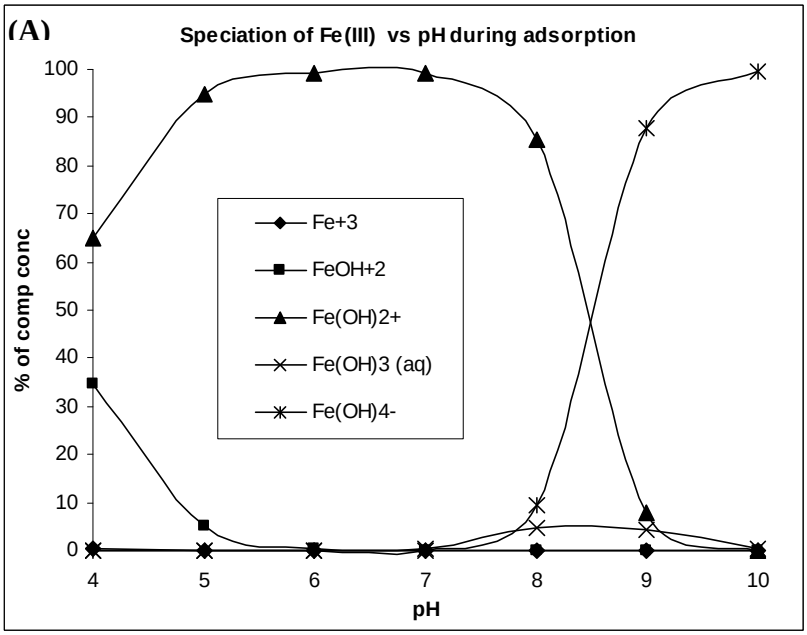

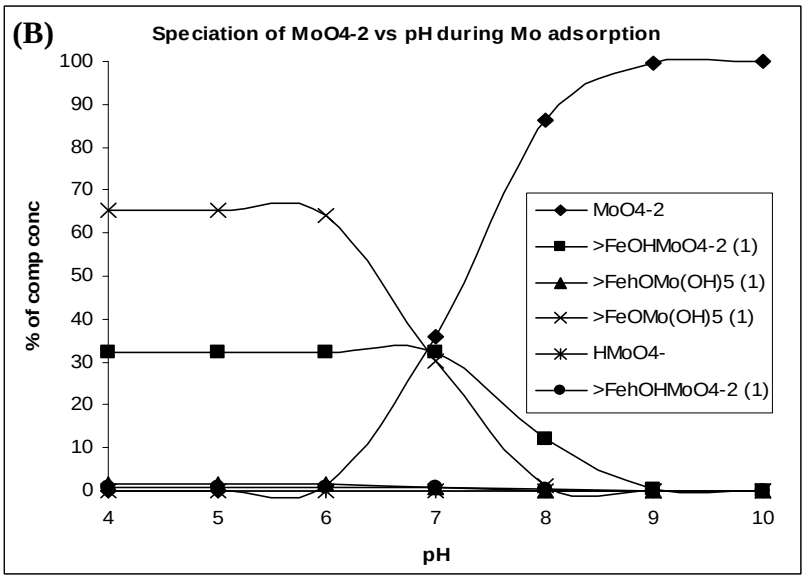

Figure continued on next page

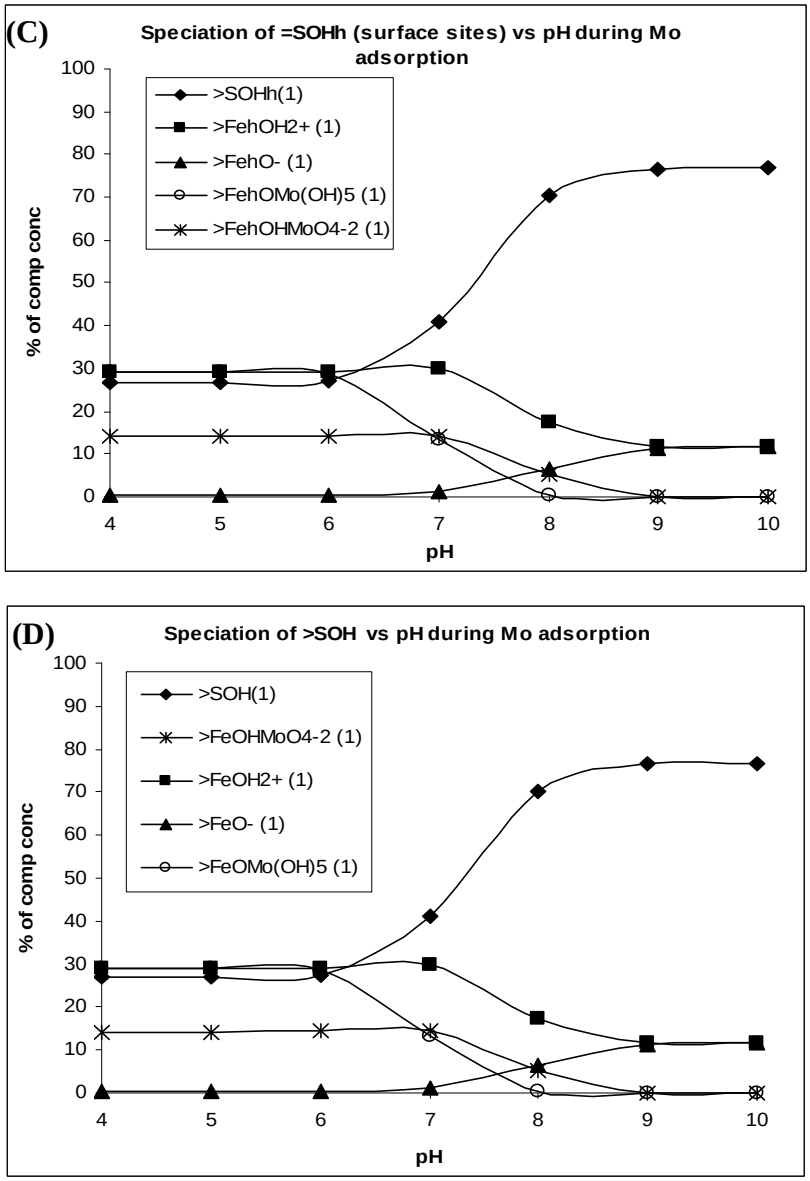

Figure 4. 14. Iron, molybdenum and surface sites distribution among the dissolved and adsorbed species as a function of pH

The speciation of Fe at the conditions at which all adsorption experiments were carried out is presented in Figure 4. 14.A. Over a wide pH interval (*i.e.,* 5-8) most of the aqueous iron (>88%) is present as mono-protonated iron hydroxide species, $Fe(OH)_2^+$. At pH 4, only 64% of the iron is present as $Fe(OH)_2^+$ while 36% is present as the di-protonated iron oxihydroxide species ($Fe(OH)^{+2}$). Negatively charged hydroxide species ($Fe(OH)_4^-$) are only present in the system at pH above 8, reaching 100% at pH 10. Finally, max 10% of the iron is present as dissolved hydroxyl species $Fe(OH)^3_{(aq)}$ between pH 7 and 10.

Figure 4. 14.B shows the molybdate speciation during the adsorption process at different pH values. Free molybdate species in solution are found at pH above 6, increasing rapidly and reaching 100% at pH 9 and above. At pH below 6 molybdate is associated with the ferrihydrite surface as the $FeOMo(OH)_5$ species (65%) and $FeOHMoO_4^{-2}$ species (33%). If these results are correlated with the molybdenum adsorption profile vs. pH (Figure 4. 8.), than it can be deduced that during the adsorption of 100 µM molybdenum at pH 4-6 most of the molybdenum is adsorbed to the ferrihydrite surfaces as $FeOMo(OH)_5$ (65%) and $FeOHMoO_4^{-2}$ (33%) and these are bound to the surface via inner-sphere complexes. The amounts of these complexes decrease with increasing pH and at pH 7 almost equal % of surface species ($FeOMo(OH)_5$, $FeOHMoO_4^{-2}$) and free molybdate (MoO_4^{-2}) were found in the system. This explains the decrease in the removal efficiency of the molybdenum to 60% in the pH adsorption edge diagram (Figure 4. 8.) obtained from the experimental work. Previous studies (Gustafsson 2003) had to include the $FeOMo(OH)_5$ species in the database in order to describe better the molybdenum adsorption onto their ferrihydrite experimental results when simulating the adsorption with DLM (Diffuse Layer Model).

Figure 4. 14. C and Figure 4. 14. D, show that the distribution of ferrihydrite surface sites and ferrihydrite functional groups follow the same trend as a function of pH. This similarity suggests that all surface sites are charged and available for sorption.

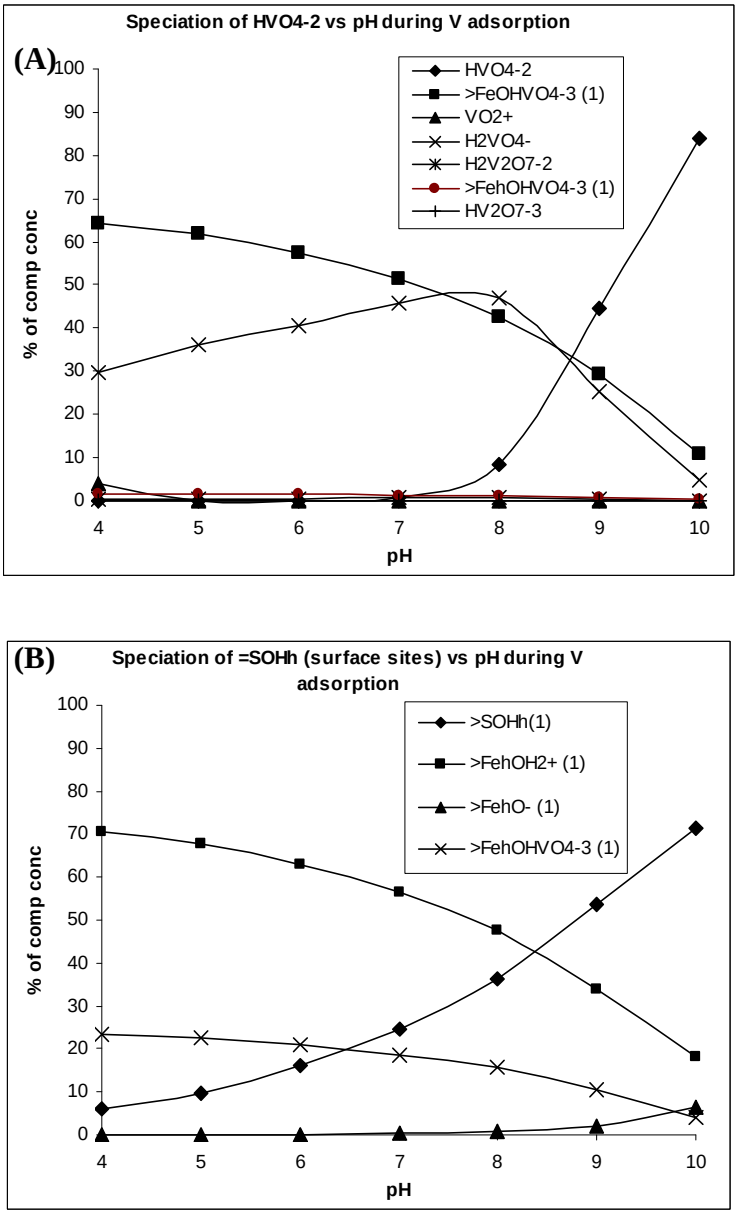

Figure 4. 15. Vanadium speciation and surface sites distribution among the dissolved and adsorbed species as a function of pH in similar conditions as experimental adsorption studies.

For the vanadium system (Figure 4. 15.), the percent of vanadate (HVO_4^{-2}) in solution is very low at pH below 8 (< 8%) and increases to 45% at pH 9 and 85% at pH 10. These outputs reveal that most of the vanadium in the system is adsorbed onto the ferrihydrite surface at pH below 8. These modeling results respect the same trend as the experimental results (Figure 4.8.) which showed that at pH below 8 vanadium was adsorbed 100%. However, quantitatively, looking at chemical speciation, this high affinity

seems more complex. From simulation at pH 4 ~ 64% of the vanadium species are adsorbed onto the ferrihydrite surface as the inner-sphere complex: $FeOHVO_4^{-3}$ while 30% is present as the monovalent vanadate ($H_2VO_4^-$). The contribution of the surface complexes decreases with increasing pH while monovalent vanadate reaches a maximum of 50% at pH 8, after which a sharp decrease is observed. At pH 8, the vanadium adsorption is due to only 40 % of $FeOHVO_4^{-3}$ complexes. The rest of 10% divalent vanadate anion (HVO_4^{-2}) and 50% monovalent vanadate anion ($H_2VO_4^-$) – aqueous species- are probably able to complex weakly with neutral charge ferrihydrite surface (Figure 4. 5.). Above pH 8, the amount of vanadium species associated with the surface and the monovalent vanadate decreases while soluble divalent vanadate increases.

From point of view of the surface (Figure 4. 15.B): only 23 to 5 % of the vanadium seems to be associated with the ferrihydrite surface as inner-sphere complexes (>$FeOHVO_4^{-3}$) and this value decreases almost linearly with pH. Conversely, protonated sites ($FehOH^{+2}$) dominate (70 %) at pH 4 and decrease with pH to 20% at pH 10. There was no difference between ferrihydrite surface sites and surface functional groups on ferrihydrite surfaces modeled for the vanadium system, therefore only the surface sites *vs.* pH diagram was presented (Figure 4. 15.B).

In order to quantify the amount of molybdenum and vanadium taken up by the ferrihydrite from the simulation outputs, the concentrations of the molybdenum or vanadium – surface associated species (in mols) were summed and normalized per g of ferrihydrite and the simulation outputs were compared with the experimental data expressed as removal efficiency (E,%) and uptake capacity (q, mmol metal/g ferrihydrite) (Figure 4. 16.).

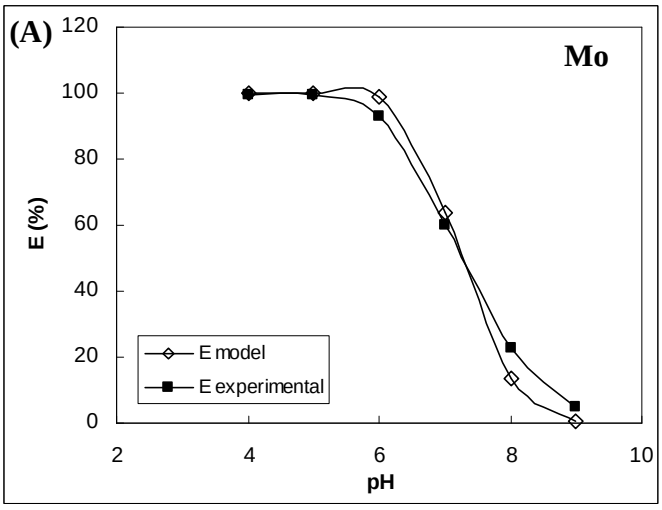

Figure continued on next page

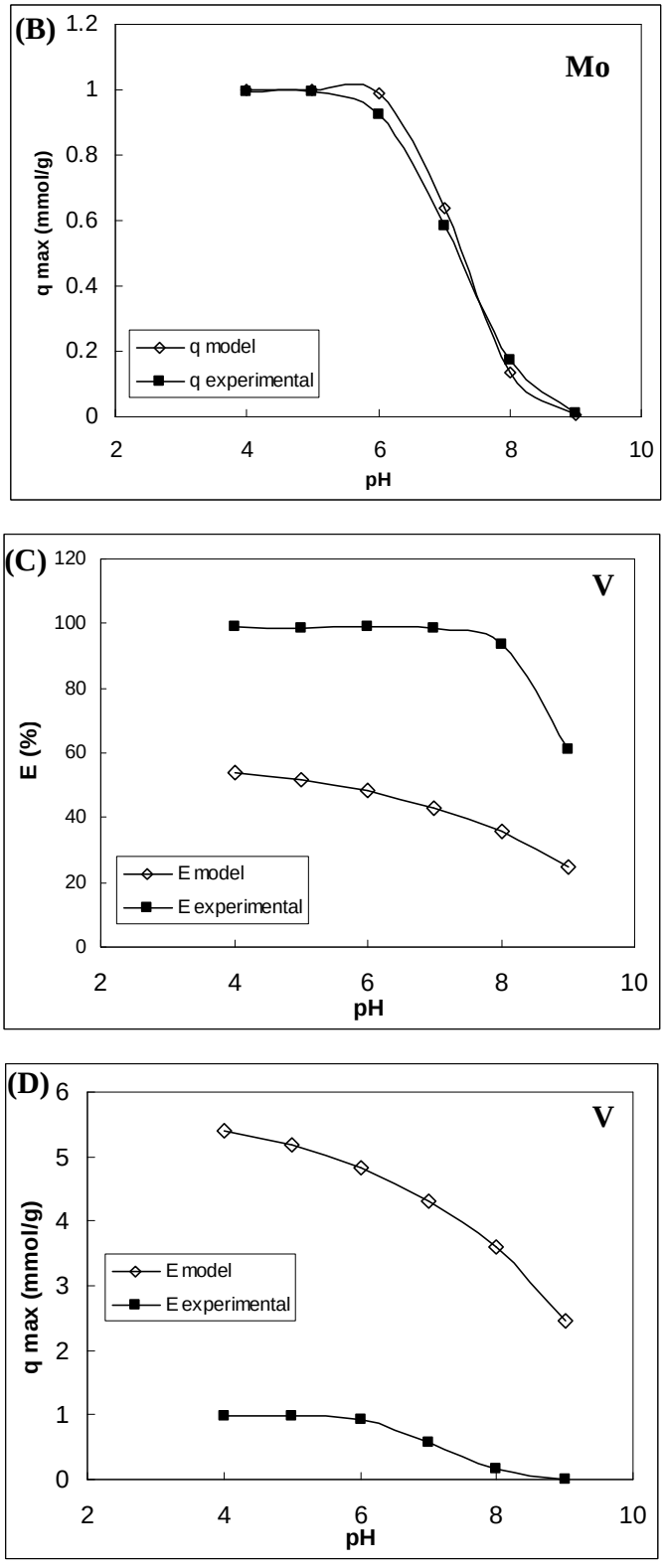

Figure 4. 16. Comparison of the molybdenum (A and B) and vanadium (C and D) experimental adsorption profile with adsorption simulation profile expressed as E (%) (A and C) and q (mmol g^{-1}) (B and D).

The results show that the amount of molybdenum taken up by ferrihydrite as predicted by the adsorption simulation (see Appendix A.) was in very good agreement with the experimentally derived data (Figure 4. 16. B). However the amount of vanadium taken up per g ferrihydrite predicted was ca 5 times higher than the uptake capacity obtained experimentally (Figure 4. 16.D). From the efficiency point of view, the molybdenum experimental profile matched very well the simulation output (Figure 4. 16. A), whereas vanadium removal efficiency measured experimentally was ~40% higher than the efficiency predicted by the model (Figure 4. 16. C). These differences in the adsorption simulation outputs *vs.* experimental measurements with regards to the vanadium adsorption systems may be explain by:

(a) Incomplete database information: presence or absence of un/appropriate species,

(b) Incorrect intrinsic constants,

(c) Differences in practical *vs.* theoretical adsorbent characteristics (*i.e.,* surface area, surface site densities, dissociation constants, etc).

In order to refine some of factors which may cause these differences, various databases were searched and compared and empirical simulations were carried out to elucidate the effect of the individual parameters such as: intrinsic constants of the surface coupled species, ferrihydrite surface area and the presence and/or the absence of specific species (see Appendix A).

Differences in intrinsic values for the surface associated vanadium species ,$>FehOHVO_4^{-3}$, from -0.73 to -16.63 were found in various databases. This difference (20 times smaller) lead to a decrease in the amount of the surface associate species of 12 orders of magnitude (Appendix A). Unfortunately none of these databases gave the reference where these constants were obtained from, to allow tracking back more details which can explain this difference.

A three times decrease in ferrihydrite surface area (from 600 m^2g^{-1} to 200 m^2g^{-1}) lead to only 0.4% decrease in the amount of adsorbed species.

The database species comparison revealed that for vanadium, both databases contained the same type and number of species whereas for molybdenum, the $FeOMo(OH)_5$ specie was replaced by $>FeMoO_4^-$ with its appropriated intrinsic constant. Detailed descriptions of these compilations are present in the Appendix A.

Concluding, a rigorous check of the databases with regards to intrinsic constants and appropriated type of species as well as other thermodynamic parameters needs to be

covered. However, this was outside the purpose of this chapter and is recommended as future work.

4.3.5. Modeling and 3D plotting of the adsorption parameters

3D modelling of the adsorption parameters varied in the experimental studies was aimed at elucidating the inter-correlations between these parameters and also providing guidelines of how laboratory data can be used to scale up and transpose the experimental data to real systems.

In Figure 4. 17. A and B, the molybdenum and vanadium uptake capacities, derived from the experimental data (ionic strength 0.01 and $C_{Mo/V}$ =100µM) are plotted as a function of pH and particle concentration (Cp). For the molybdenum system, the uptake capacity decreases with increasing pH (4 to 10) and increasing particle concentration (from 0.1 to 2gL^{-1}). However, considering that the total amount of molybdenum to be adsorbed was 100µM (the initial concentration of molybdenum), the decreasing trend in uptake capacity with increasing particle concentration can be explained by the fact that the amount of molybdenum available to be sorbed becomes limited with the increasing number of sites. For the vanadium system (Figure 4. 17. B) the decrease in uptake capacity with increasing pH and particle concentration follows comparable trends to the molybdenum system. Vanadium has a higher affinity for the ferrihydrite surface over a larger pH interval, a fact which explains better the difference between molybdenum and vanadium in the 3D diagrams.

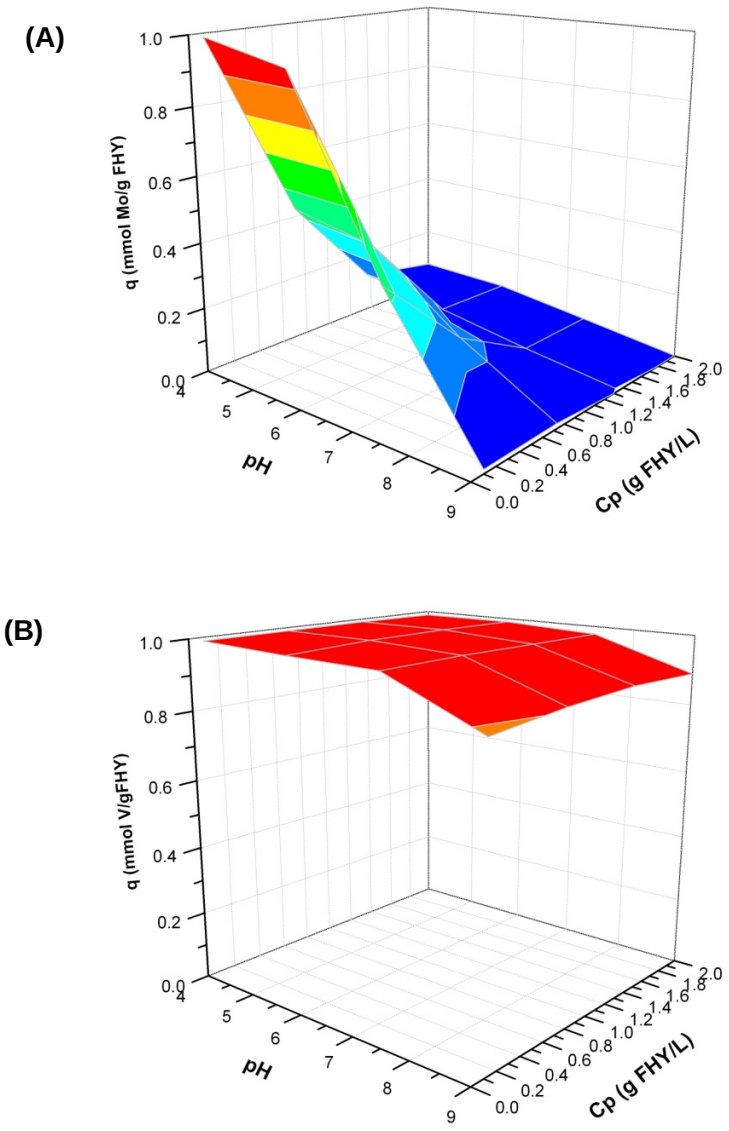

Figure 4. 17. The profile of molybdenum (A) and vanadium (B) adsorption uptake capacities onto ferrihydrite at metal concentration of 100μM, as a function of pH and ferrihydrite particle concentration (Cp) at ionic strength ~ 0.01. Red color indicates high uptake capacity (1 $mmol g_{FHY}^{-1}$), whereas blue color indicates uptake capacity close to 0.

3D modeling of the variation of metal concentration, particle concentration and uptake capacities of molybdenum (Figure 4. 18. A) and vanadium (Figure 4. 18. B) shows that both systems follow the same trend and shape. However, the profile of vanadium differs from the molybdenum, reaching more than twice the uptake of molybdenum (q axis) over the same metal and particle concentration interval.

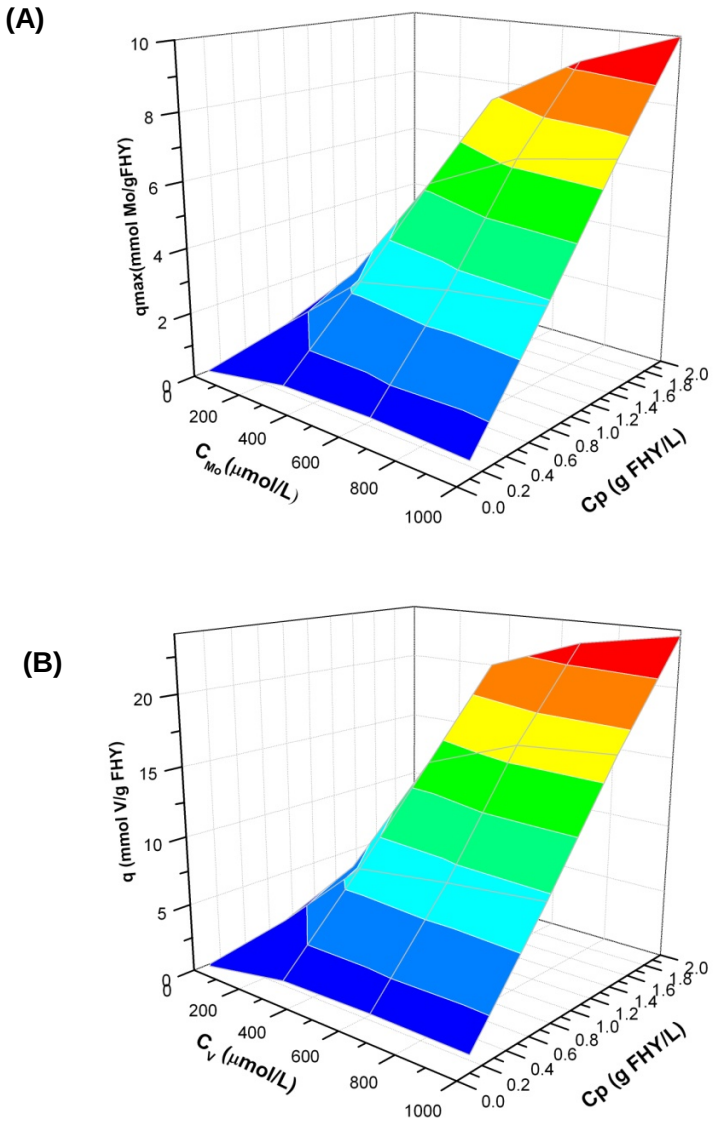

Figure 4. 18. The profile of molybdenum (A) and vanadium (B) adsorption uptake capacities onto ferrihydrite at pH 7, as a function of metal concentration (C_{Mo} and C_V, respectively) and ferrihydrite particle concentration (Cp) at ionic strength ~ 0.01. Red color indicates high uptake capacity, whereas blue color indicates uptake capacity close to 0.

Thus, over the interval of 0-1000 µM, with increasing particle concentration to $2gL^{-1}$, the maximum uptake capacity of the ferrihydrite at pH 7 for molybdenum was 10 mmol g^{-1} and for vanadium was 23.6 mmol g^{-1}.

As an application of this type of modeling we can use deep sea hydrothermal processes. If the variations of ferrihydrite input into seawater from a hydrothermal vent and the molybdenum or vanadium concentration in the surrounding seawater are known, these

data can be used (via interpolation or extrapolation) to predict how much molybdenum and vanadium can be scavenged along a deep sea hydrothermal plume.

Specifically, the continuous uptake of molybdenum and vanadium from the seawater reservoir via adsorption onto ferrihydrite particles which form in the plume can be calculated by: assuming a molybdenum concentration in the seawater of 10 μgL^{-1} (Chester 1990) and a vanadium concentration of ~ 2-3 $\mu g\ L^{-1}$ (Ferreira et al. 2002) and if we arbitrarily take a value of 1.5gL^{-1} for ferrihydrite input in the seawater, than by interpolating on the appropriated plots and by taking into account the influence of the matrix (add 22% for molybdenum and 33% for vanadium) (Figure 4. 11), we estimated 0.0183 mmol molybdenum and 0.0065 mmol vanadium per g of ferrihydrite can be removed in these processes. This may explain why the molybdenum and vanadium concentration in the sediments near the vent are a few orders of magnitude higher that in surrounding seawater.

4.4. Summary

Ferrihydrite characterization analysis gave useful information about:

- particle shape: small sphere;
- particle size: 3-5 nm individual particles which aggregate forming clusters of 3-150µm in dynamic regime and 60-1000nm in static regime;
- Crystalinity: poorly ordered;
- Surface charge features: PZC is 7.89;
- Surface area: ~ 200 m^2g^{-1}.
- The effect of CO_2 on its surface: CO_2 adsorbs onto ferrihydrite surface sites at pH 6 to 9;
- Thermodynamic stability at neutral pH: transforms to mainly hemaite, with minor amount of goethite.

All this information is helpful and supports further studies and results on molybdenum and vanadium adsorption and co-precipitation affinities and mechanisms. The adsorption studies conducted in different pH conditions revealed that vanadium has a higher affinity in comparison with molybdenum over a larger pH interval in the same environmental conditions ($C_{Mo/V}$=100µM; Cp=0.1gL^{-1}; pH 4-9, dynamic regime: 300 rpm): molybdenum removal efficiency was high at pH below 6 (90-100%) but decreased with increasing pH (i.e., pH 7 < 60 %, pH 8 < 20 % and pH 9 < 3%), while vanadium removal efficiency decreased to ~ 60 % only at pH 9. In addition, studies of molybdenum and vanadium adsorption in batch systems at the same particle concentration (0.1gL^{-1}) but over a larger metal concentration interval (1-1000µM) at pH 7, allowed a direct comparison of the maximum adsorption capacities of the ferrihydrite for both anions. Thus, in such conditions, molybdenum maximum uptake capacity was 0.43 mmol g^{-1} whereas vanadium uptake capacity was almost 3 times bigger: 1.28 mmol g^{-1}.

The competitive adsorption studies of molybdenum and vanadium (100µM) with phosphorus (100 µM) suggested that phosphorus affects vanadium adsorption, competing almost equally for the ferrihydrite surface sites (0.69 mmol P g^{-1} in single system and 0.38 mmol P g^{-1} in V- binary system), while molybdenum did not significantly influence the phosphorus sorption.

In order to transpose all the laboratory results obtained from experiments carried out in distilled water to seawater environments, the results from the effect of seawater matrices on the molybdenum and vanadium adsorption suggested that all the values

obtained on molybdenum and vanadium adsorption onto ferrihydrite in distilled water studies should be increased with 22% and 33%, respectively.

Information about adsorption mechanisms were extracted from modelling the experimental adsorption studies. An empirical approach (usually used for non-homogenous surfaces), of fitting the kinetics of molybdenum and vanadium adsorption onto ferrihydrite at different pH values with a pseudo-second order kinetic model suggested that ferrihydrite adsorbs molybdenum and vanadium via chemo-sorption mechanism at pH below 6 and 8 respectively, and above these pH values via a physico-sorption mechanism. Chemo sorption mechanisms infer the formation of strong chemical bonding (ionic or covalent bonds) between molybdenum or vanadium species and ferrihydrite surface sites, while physico-sorption is via weak bonding (van der Waals bonds) between molybdenum and vanadium species and hydroxylated ferrihydrite surface groups (outer-sphere complexes).

Qualitatively, using modelling (such as Visual MINTEQ 2.32 (Gustafsson 2005) and Diffuse Layer Model) to simulate the experimental adsorption studies, more information about molybdenum and vanadium – ferrihydrite surface associated species were deducted. The inner-sphere complexes formed at pH below 6 for molybdenum are $FeOMo(OH)_5$ (65%) and $FeOHMoO_4^{2-}$ (33%) and at pH 8 for vanadium they are ($FeOHVO_4^{3-}$) (40%). In addition, potentiometric titration results (*e. g.,* PZC = 7.89) supports this mechanism of molybdenum and vanadium adsorption onto ferrihydrite protonated surface via inner-sphere complexes. Further information about the molybdenum adsorption mechanism at pH 8 are present in Chapter 5, which contains a nano-scale approach of the mechanism using Synchrotron based technique (XAS) to assess the bonding environment of molybdenum adsorption.

By using geochemical modelling software, Visual MINTEQ 2.32, and the appropriate database to compare the experimental results obtained from the pH dependent adsorption experiments it was found that experimental molybdenum pH adsorption edge and pH molybdenum removal trends matched very well with the modelling outputs. However vanadium experimental adsorption edge was 5 time smaller than the modelled edge and the vanadium removal efficiency obtained experimentally was ~40% higher than the efficiency predicted from the modeling, over the whole pH interval. Furthermore, detailed database search and comparison explained only partially this discordance in vanadium practical *vs.* vanadium theoretical behaviours (*e.g.,* incomplete list of vanadium species with appropriate intrinsic constant and other yet unknown database issues). This discordance agrees well with the vanadium species during the vanadium adsorption, where 23-5% of vanadium appears to be associated with ferrihydrite

surface, in modelling outputs, rather than up to 100%, as experimental results gave. From this it can be concluded that most probably the dissociation constant of the main vanadium ferrihydrite associated specie has an incorrect value in the database.

However, more research can be done with regards to this matter (*e.g.,* identifying the source of intrinsic constants from the database and choosing the correct one for each stoichiometrically real specie which respects the elemental mass balance or calculating the correct one from the experimental result obtained in this thesis).

Important to note is that not all the databases are reliable for the geochemical modelling and if used, special attention has to be given to the database content by checking quantitatively and qualitatively the species involved and updating values, if possible.

Molybdenum and vanadium scavenging, from the environments where ferrihydrite forms (*i.e.,* deep sea hydrothermal vents), occur also via co-precipitation - a process which takes up metals during the mineral formation. As a comparison, isothermal studies at pH 7 in batch reactors allowed quantification of the molybdenum and vanadium uptake capacities via co-precipitation *vs.* adsorption. The results showed that molybdenum and vanadium were better removed (5.7 times molybdenum and 2.6 times vanadium) via co-precipitation than via adsorption.

Molybdenum and vanadium adsorption and co-precipitation experiments from this chapter have implications in quantifying the uptake processes which take place in real environments and then controls the availability of these micro-nutrients. Thus, the inter-correlation of parameters which influence molybdenum and vanadium uptake onto ferrihydrite (by coupling them in 3D diagrams) helps transpose these laboratory results to real ecosystems.

Chapter 5
The fate of molybdenum and vanadium and the speciation of molybdenum during ferrihydrite transformation to hematite

5.1. Introduction

Ferrihydrite is a thermodynamically metastable poorly ordered iron oxyhydroxide phase. Under specific environmental conditions (i.e., pH, red-ox, T, ionic strength, etc) it transforms into crystalline iron oxides such as goethite, hematite and magnetite (Cudennec and Lecerf 2006; Davidson et al. 2008; Shaw et al. 2005; Sumoondur et al. 2008). It is well known that ferrihydrite can control the availability and the cycles of different elements. Thus, it is important to study and quantify the fate of these ions during such transformations. In this chapter, the effect and the fate of molybdenum and vanadium during the transformation of ferrihydrite to hematite were quantified. Such quantifications play a major role in evaluating the molybdenum and vanadium budgets in different environments where ferrihydrite forms (*i.e.,* oceans, fresh waters and soils) and transformations into geologically stable phases (Trefry and Metz 1989, Cornell and Schwertmann 2003).

This chapter aims to evaluate the interactions of molybdenum with ferrihydrite at the molecular scale and quantify the fate of molybdenum and vanadium during the ferrihydrite transformation to hematite. In addition, the molybdenum and vanadium partitioning pools after the transformation (i.e., structure, surface and solution) and the bonding environments of molybdenum in these different pools were quantified. Interactions such as adsorption and co-precipitation of molybdenum and vanadium onto and with ferrihydrite were the basic processes studied.

5.2. Materials and methods

The full details of the off line adsorption and co-precipitation experiments were described in Chapter 3. Here only a brief summary is given.

Ferrihydrite synthesis was done following the method described by Cornell and Schwertmann (2000). The starting material was then characterized by XRD and FEG-TEM to certify its crystallinity, particle size and purity.

Adsorption studies were performed in batch reactors where 1g of ferrihydrite was suspended in 1000µM molybdenum and vanadium solution. The process conditions were: room temperature; pH = 7±0.1, mixing speed ≈ 300 rpm, ionic strength 0.01. Solution samples were collected at different times (0; 10; 20; 40; 80 to 1280 min). The solutions were filtered through 0.2µm filters, diluted, acidified and subsequently analysed by Inductively Coupled Plasma-Mass Spectrometry.

Co- precipitation experiments were done by synthesizing 1g of ferrihydrite in the presence of molybdenum or vanadium at pH 7. The quantification of the molybdenum and vanadium uptake by ferrihydrite structure during co-precipitation was done via solid phase digestion in HCl 6M and subsequent solution analysis with ICP-MS and also by analysing the molybdenum and vanadium concentrations in the supernatant from the co-precipitation experiments.

Partitioning of molybdenum / vanadium during ferrihydrite transformation

Freshly molybdenum or vanadium - co-precipitated ferrihydrite as well as the ferrihydrite with molybdenum and vanadium adsorbed were transformed to hematite at 200ºC for 2 days under hydrothermal hydrated conditions. The transformation end-product was confirmed by XRD as being hematite. The transformation of the Mo-associated ferrihydrite was carried out at two different pH values (7 and 8) - in order to assess the influence of pH during the transformation. The transformed samples were centrifuged at 8000 rpm for 15 minutes in order to separate the solid phase and the supernatant. The supernatants were filtered through 0.2µm Acetate Cellulose syringe filter and the molybdenum and vanadium concentrations in solutions were quantified by ICP-MS. From the mass balance between molybdenum and vanadium concentrations in the solid phase (from digestion) and solution (supernatant), the amount of molybdenum and vanadium released into solution during the ferrihydrite (co-precipitated and adsorbed) transformation could be assessed.

In addition, a solid desorption procedure was devised in order to quantify the amount of molybdenum or vanadium associated with the hematite surface after the transformation. Therefore, after centrifugation, the separated solid phases were equilibrated with 2 M NH_4OH for 30 minutes under constant stirring (Carvahlo and Abrao 1997). The supernatant was collected by centrifugation, filtered and analysed for molybdenum and vanadium concentrations (with ICP-MS) (surface molybdenum and vanadium pool). The remaining hematite was digested and then analysed for molybdenum and vanadium (these values representing the molybdenum and vanadium structural pool).

X-Ray Adsorption Fine Structure Spectroscopy

X-Ray Adsorption Spectroscopic measurements were used to derive information about molybdenum speciation in the co-precipitated and on adsorbed ferrihydrite as well as the transformation-product - hematite.

XAS (or XAFS) measurements were carried out at the Synchrotron Radiation Source (SRS), Daresbury Laboratory at Station 16.5 which is ideal for ultra dilute systems due to the high flux and high count rate fluorescence detector (30 element Ge solid state). Using these settings samples which contained low concentrations of molybdenum (<1%) could be quantified. The electron binding energy for the Mo K 1s shell is 20000eV.

Two regimes were considered from the X-Ray adsorption spectrum: X-ray adsorption near edge (XANES) and extended X-ray fine-structure (EXAFS). The interpretation of the XANES gives information about the oxidation state and coordination chemistry of the adsorbing atom, while EXAFS is used to determine the bond distances, coordination number and species of the neighbors of the absorbing atoms.

The data were processed using the computer programs EXCALIB, EXBROOK, EXSPLINE and EXCURV98; (Dent and Mosselmans 2003; Spadini et al. 2003). To quantify the results, synthetic and natural standards (Na_2MoO_4; K_2MoO_4 and MoO_3) were also analyzed. All standards were analyzed by conventional X-Ray Diffraction for their identity and purity. The samples from the co-precipitation and adsorption experiments were examined in fluorescence mode, while the standards were run in transmission mode. Where necessary the standards were diluted with an inert salt - boron nitride.

5.3. Results and discussions

5.3.1. Molybdenum and vanadium associated ferrihydrite and transformation end-product characterization

Transmission Electron Microscopy results (Figure 5. 1.) showed that 1% molybdenum and vanadium co-precipitated ferrihydrite have individual particles slightly better defined comparing with pure ferrihydrite.

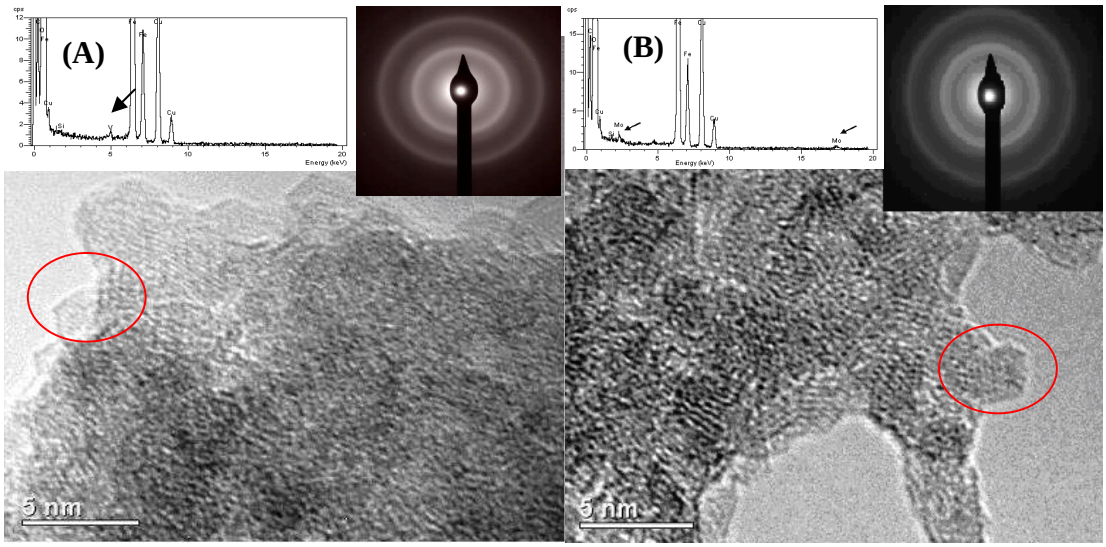

Figure 5. 1. FEG-TEM micrograph of the vanadium (A) and molybdenum (B) co-precipitated ferrihydrite showing individual particles forming clusters. Insets are Energy dispersive spectra (EDS) (left) and Selected Area Electron Diffraction (SAED) (right) of the imaged sample.

Selected Area Electron Diffraction patterns (Figure 5. 1. A and B right side insets) identify the crystallography of the ferrihydrite co-precipitated with molybdenum and vanadium, whereas Energy Dispersive Spectra (Figure 5. 1.A and B left side insets) indicate the presence of 1% molybdenum and vanadium, respectively.

FEG-TEM micrographs showed that the presence of 1% molybdenum and vanadium in ferrihydrite structure slightly changed the nanoparticles crystalinity making them less “amorphous”. Similar effects were seen by Punnoose and collaborators (2004), who doped ferrihydrite with 5% Ni, Mo and Ir. In addition, their XRD data also supports this change - the Ni doped ferrihydrite had sharper Bragg’s peaks and some weak lines characteristic of 6-line ferrihydrite.

The transformation end-product of the molybdenum- or vanadium-associated ferrihydrite was characterised by XRD (Figure 5. 2). The results showed that under those specific conditions (pH 8 and ionic strength 0.001) the end-product was hematite with goethite being a minor intermediate.

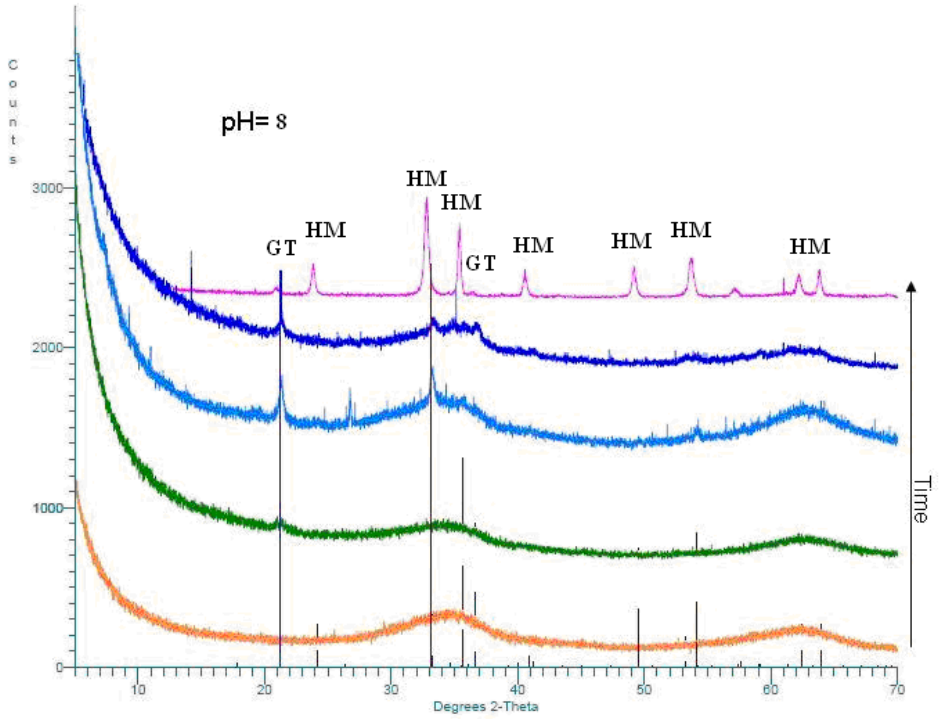

Figure 5. 2. XRD patterns showing the transformation of the ferrihydrite to hematite with a minor amount of goethite as intermediate

5.3.2. Partitioning of molybdenum and vanadium during ferrihydrite transformation

Figure 5.3. shows the three different pools of vanadium associated with the hematite end-product. After vanadium co-precipitation with ferrihydrite and its transformation, all vanadium associated with the initial ferrihydrite became incorporated in the end-product structure (Figure 5. 3.A). No vanadium has been released into the solution during the transformation or was associated with the hematite surface. On the other hand, for the experiments where vanadium was adsorbed onto the initial ferrihydrite surface, only 96% were incorporated in the hematite structure, while 4% of the vanadium was transferred to the hematite surface, yet no vanadium was released into the supernatant after the transformation (Figure 5. 3.B).

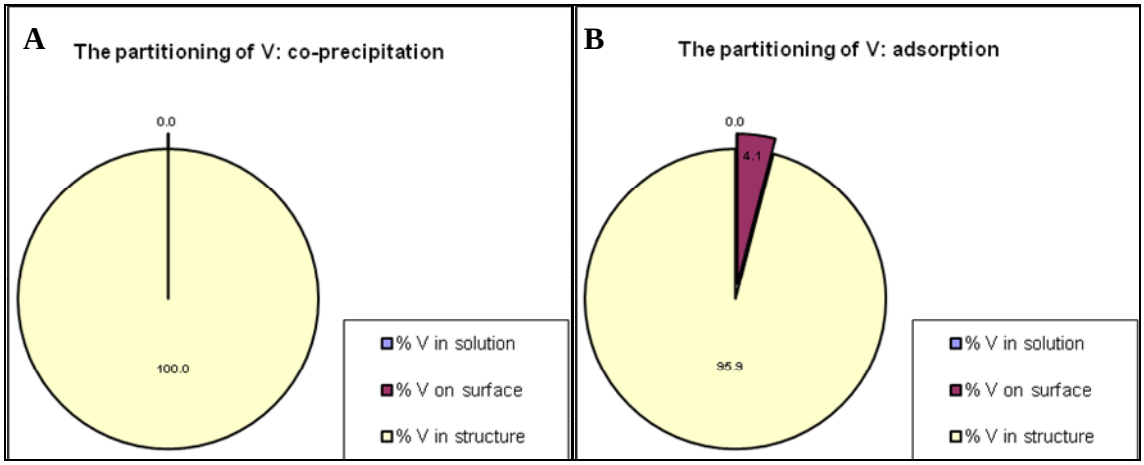

Figure 5. 3. Partitioning of vanadium from co-precipitation (A) and adsorption (B) on ferrihydrite end-product.

The results show that regardless if vanadium was co-precipitated with ferrihydrite or adsorbed onto ferrihydrite, at the end of the transformation the vast majority of the vanadium became incorporated into the hematite structure.

Interestingly the partitioning of molybdenum (Figure 5.4.) in the co- precipitated and adsorbed samples after ferrihydrite transformation and after molybdenum desorption from the transformation end-product revealed a slightly different picture. In both cases ca. 3% of the molybdenum was released back into the solution during the transformation (Figure 5.4.A and B) and 6% of the total molybdenum (for adsorption experiment) and ca 3% of the total molybdenum (for the co-precipitation experiment) were bound to the surface of the hematite.

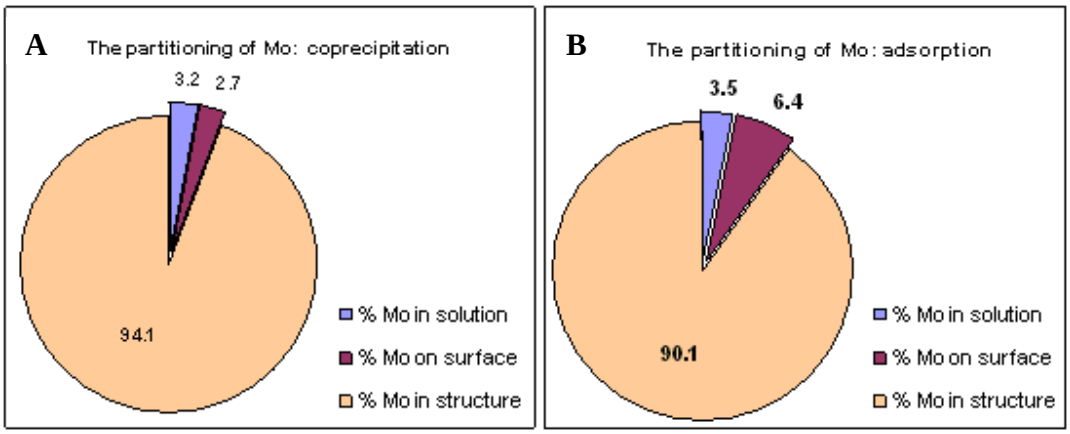

Figure 5. 4. Partitioning of molybdenum in the transformation end-products from co-precipitation (A) and adsorption (B) experiments

However, again the majority of the molybdenum in both systems became sequestered in the end-product structure: 94% via co-precipitation and 90% via adsorption respectively (Figure 5. 4).

Comparing the two uptake processes studied for both molybdenum and vanadium: co-precipitation *vs.* adsorption, and taking into account the nature of the processes, structure uptake *vs.* surface uptake, respectively the results revealed that the co-precipitation process sequestered slightly more molybdenum and vanadium than the adsorption process.

The above data indicates that scavenging processes which take place at the bottom of the ocean, within the hydrothermal sedimentary systems, does influence molybdenum and vanadium cycles in the ocean.

Previous studies with regards to V/Fe ratio in natural sample from the Juan de Fuca Ridge showed that V/Fe ratio in the hydrothermal fraction of the sediments (0.003) is almost the same as in the hydrothermal plume particles in the overlying water column (Feely et al. 1998). Our results confirmed their assumption with regards to the oxic metalliferous sediments which maintain constant V/Fe ratio that was established in the ferrihydrite particles as they were formed in the hydrothermal plume. The same authors, found a linear correlation between the V/Fe ratio in the hydrothermal particles and dissolved phosphate for several hydrothermal vents systems on the global ridge-crest spreading centers. This correlation may have important implication in monitoring the phosphate (as a very important macronutrient) and vanadium (as an important micronutrient) concentrations along the time within the ocean and earth evolution.

Partitioning data showed that during the ferrihydrite transformation to hematite most vanadium (>96%) and molybdenum (>90%) became incorporated into the end-product structure. Thinking of the nature of the process (*e.g.,* co-precipitation and adsorption) the results from the partitioning experiments agree with this consideration, specifically if the high surface to volume nature of the ferrihydrite is taken into account. Our data clearly showed that vanadium and molybdenum can be sequestered by crystalline iron oxyhydroxides at near neutral pH conditions.

5.3.3. Speciation of molybdenum in the fresh co-precipitated and adsorbed ferrihydrite

The full XANES spectra of the co-precipitated and adsorbed ferrihydrite samples with different concentrations of molybdenum as well as the standards (Na_2MoO_4, K_2MoO_4,

and MoO_3) are shown in Figure 5. 5. From the finger print assessment, no big differences between the shapes of the sample plots and the MoO_4^{2-} standards could be observed, except that as the content of molybdenum in the sample decreases the spectra become noisier. All XANES spectra show a pre-edge feature and the main absorption edge is well defined at energy of about 20035 eV. From the finger print comparison of the XANES spectra, the molybdenum speciation in all samples could be assigned as being molybdate.

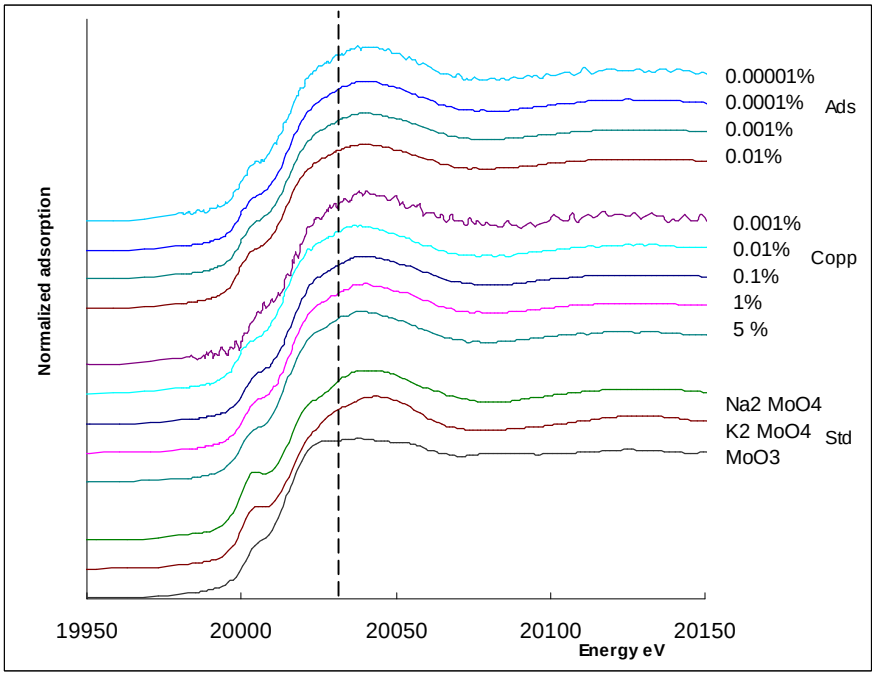

Figure 5. 5. Molybdenum XANES spectra for the fresh co precipitated ferrihydrite with molybdenum and molybdenum adsorbed onto ferrihydrite (X axis: energy, E (eV); y axis: normalized adsorption).

In Figure 5. 6. the k^3 weighted EXAFS and the calculated Fourier-Transforms are shown. Fitting the experimental data with the Fourier theoretical model, allowed the bond distances between the atoms from and the coordination number of the neighboring atoms as well as the type of the neighboring atoms to be determined.

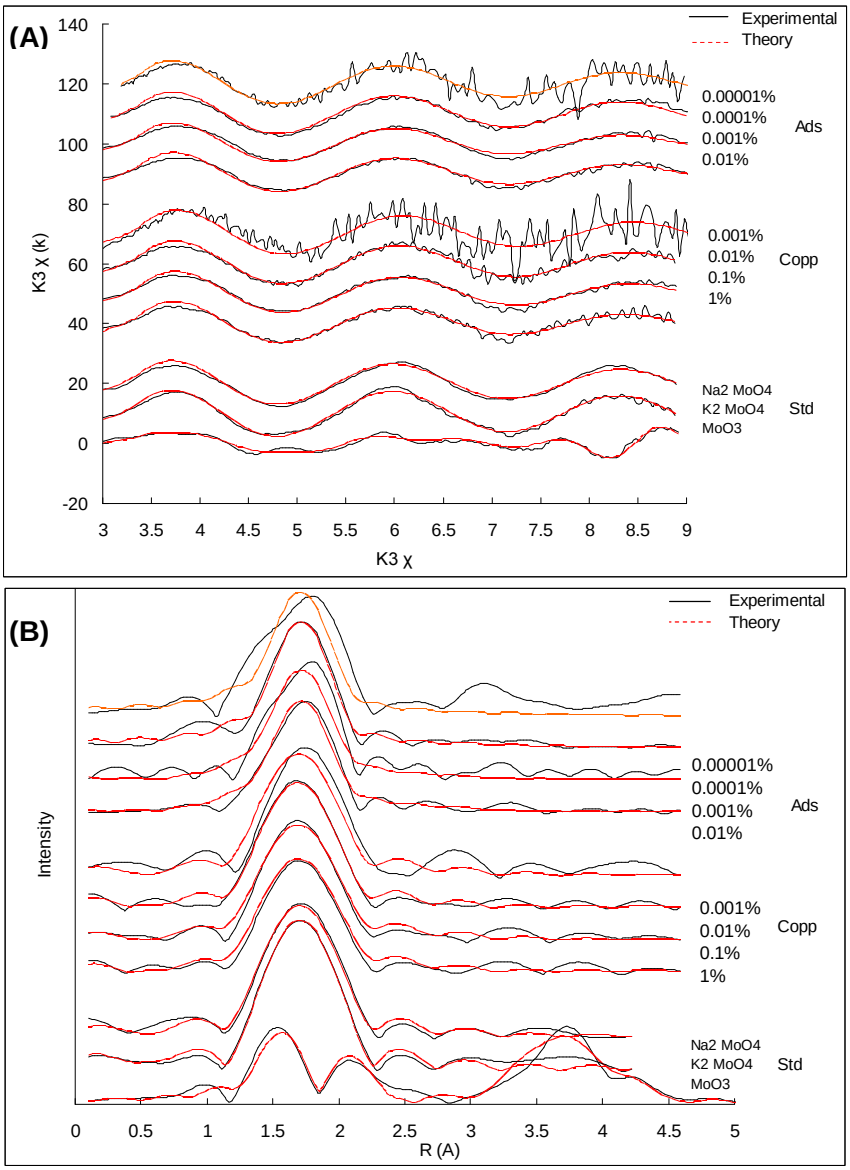

Figure 5. 6. k^3 weighted EXAFS spectra (A) and calculated Fourier-Transforms (B) for EXAFS spectra for fresh co-precipitated and adsorbed samples at different molybdenum contents and standards.

A summary of the types of the neighboring atoms, coordination numbers and bonding distances are presented in Table 5. 1.

The data show that in both co-precipitated and adsorbed Mo-associated ferrihydrite samples, four O atoms are situated in the first shell at a distance of 1.76Å from the main molybdenum atom corresponding to a molybdate speciation.

Table 5. 1. Summary of the parameters obtained from Fourier Transformed fittings of the EXAFS spectra of the fresh co-precipitated and adsorbed ferrihydrite samples with different molybdenum contents

Sample name	**Bond type**	**Coord. number, N**	**Distance between atoms (Å)**	**R factor (goodness of fit)**	**Debye Waller factor**
STD- Na_2MoO_4	Mo-O 1st shell	4 (3.7)	1.76	15.14	0.008
STD – K_2MoO_4	Mo-O 1st shell	4 (3.7)	1.76	13.27	0.004
STD – MoO_3	Mo-O 1st shell	2	1.68	37.12	0.007
	Mo-O 2nd shell	2	1.92		0.008
	Mo-O 3rd shell	2	2.28		0.021
FHY+5%Mo co-precipitated	Mo-O 1st shell	4 (3.6)	1.75	22.17	0.019
FHY+1%Mo co-precipitated		4 (3.7)	1.76	31.11	0.014
FHY+0.1%Mo co-precipitated		4 (3.6)	1.75	19.61	0.014
FHY+0.01%Mo co-precipitated		4 (3.7)	1.75	23.07	0.011
FHY+0.001%Mo co-precipitated		4 (3.7)	1.75	58.65	0.011
FHY+0.01% adsorbed Mo		4 (3.6)	1.76	29.48	0.015
FHY+0.001% adsorbed Mo		4 (3.8)	1.76	29.88	0.015
FHY+0.0001% adsorbed Mo		4 (3.8)	1.76	26.29	0.011
FHY+0.00001% adsorbed Mo		4 (4.1)	1.75	39.09	0.012

Analyses of the molybdenum EXAFS show clear evidence that molybdenum is adsorbed via *outer-sphere* molybdate complexes on the surfaces of the amorphous ferrihydrite.

Not many XAFS studies on molybdenum speciation in molybdenum-associated ferrihydrite are found in the literature. However, Zhao and his collaborators (1994) looked at molybdenum speciation into Mo-ferrihydrite catalysts and suggested that their samples containing atomic ratios of 5 and 35% have molybdenum associated mostly with ferrihydrite surface - as molybdate (Zhao et al. 1994). Their results agrees well with this thesis and this comparison shows that even at high concentration of molybdenum in the co precipitated ferrihydrite, molybdenum speciation remains the same.

5.3.4. XAFS results of transformed end-product

Figure 5.7. displays the XANES part of the spectra of the HM- end-products, from the transformation of both adsorbed and co-precipitated samples (Ads-Trans and Copp-Tranf, respectively). In addition, the transformed samples after desorption - identifying the molybdenum speciation in the hematite structure only (termed Ads-Trans-Des and Copp-Trans-Des, respectively) are also displayed together with the used standards.

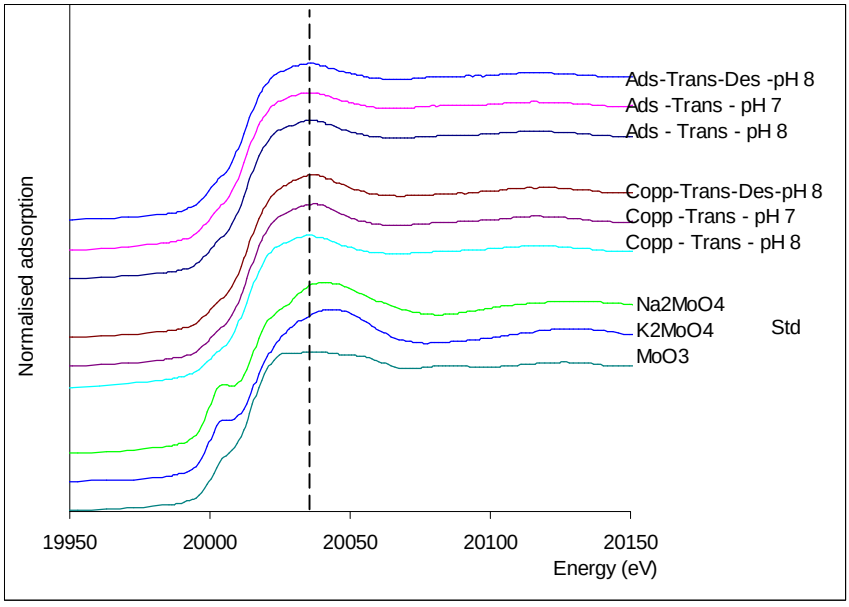

Figure 5. 7. Molybdenum XANES spectra for the hematite end-product from the transformation (Copp-Trans and Ads-Trans) and transformation followed by desorption (Copp-Trans-Des and Ads-Trans-Des). On X axis is energy, E (eV) and on y axis is normalized adsorption coefficient,μ(E)).

The XANES spectra (Figure 5. 7) revealed that the pre-edge feature observed in the starting materials – ferrihydrite (Figure 5. 5.) was much weaker indicating that the speciation of molybdenum in the hematite, end-product, has changed.

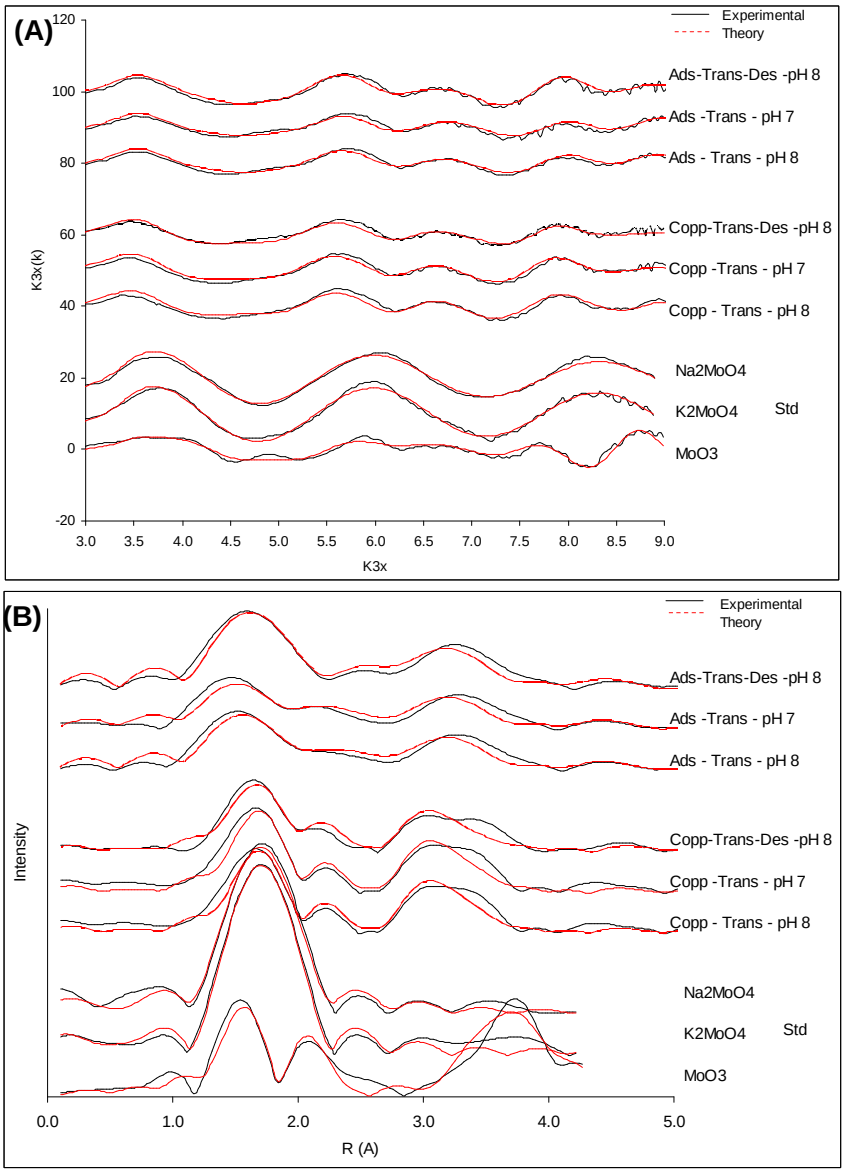

Figure 5. 8. k^3 weighted EXAFS spectra (A) and calculated Fourier-Transforms (B) for end-product hematite from the co-precipitated and adsorbed experiments

The Fourier Transformed data could be fitted with up to three shells (Figure 5. 8 B.): two with Mo-O bond distances and one with Mo-Fe bond distances (Table 5. 2.). The results reveal that molybdenum speciation in the co precipitated samples differs slightly from molybdenum speciation in the adsorbed samples

Table 5. 2. Summary of the parameters obtained from Fourier Transformed fittings of the EXAFS spectra of the co-precipitated and adsorbed samples after transformation at two different pH values and after transformation and desorption (at pH 8)

Sample Name	**Bond type**	**Coord. number, N**	**Distance between atoms (Å)**	**R factor (goodness of fit)**	**Debye-Waller factor**	**Chi 2**
Copp-Trans pH 8/pH 7	Mo-O 1st shell	2.0/2.1	1.79/1.80	33.11/ 32.56	0.012/0.010	4.0188 E-6/ 3.396 E-6
	Mo-O 2nd shell	1.9/2.2	2.03/2.04		0.021/0.024	
	Mo-Fe 3rd shell	2.7/2.7 1.0/1.1	3.07/3.08 4.68/4.68		0.023/0.018; 0.025	
Copp-Trans-Des pH 8	Mo-O 1st shell	2.0	1.79	35.11	0.013	4.155 E-6
	Mo-O 2nd shell	1.9	2.03		0.021	
	Mo-Fe 3rd shell	2.7 1.0	3.07 4.67		0.023 0.020	
Ads-Trans-pH 8/pH 7	Mo-O 1st shell	1.5/1.5	1.75/1.75	28.62 /36.39	0.001 /0.007	4.66 E-6 /8.39E-6
	Mo-O 2nd shell	1.3/1.3	1.95/1.96		0.003 /0.002	
	Mo-Fe 3rd shell	1.6/1.7	3.05/3.04		0.012 /0.012	
Ads-Trans-Des pH 8	Mo-O 1st shell	1.5	1.75	25.38	0.003	4.188 E-6
	Mo-O 2nd shell	1.3	1.96		0.005	
	Mo-Fe 3rd shell	1.6	3.05		0.007	

The co-precipitated samples show three consecutive major peaks at distances of 1.79 (±0.01) Å, 2.03 (±0.01) Å and 3.07 (±0.01) Å. They correspond to two Mo-O bonds on

the first shell, another two Mo-O bonds in the second shell and four Mo-Fe bonds on the third shell. These results, demonstrate that the speciation of molybdenum, initially co-precipitated as molybdate with ferrihydrite, changed as a result of its sequestration into the hematite structure. Interestingly, no significant difference between co-precipitated molybdenum incorporated in the hematite structure and the molybdenum associated with the surface- structure could be seen, again confirming that the majority of the molybdenum is incorporated into the structure.

On the other hand, for the adsorbed samples a change in the distance of oxygen from the main molybdenum atom (the first peak has slightly shifted towards the left) was noticeable. Fitting parameters gave a bonding environment of 1.75 Å for two coordinated O atoms in the first shell. Additionally, information about the second and the third shell were extracted: one atom of O at a bonding distance of 1.95 (±0.01) Å, and two Mo-Fe bonds of a length of 3.05 (±0.01) Å, respectively. Again, no difference between surfaces *vs*. structural adsorbed molybdenum in hematite was observed.

Important to note is that the pH at which the transformation started did not influence the speciation of molybdenum in the hematite samples.

5.4. Summary

Quantitative evaluation of different pools of molybdenum and vanadium during the transformation of ferrihydrite to hematite suggested that from all co-precipitated molybdenum and vanadium: 100% and 94 % remain associated with the hematite structure; 0% and 3% goes back into the solution and 0% and 3% is associated with the surface whereas from adsorbed molybdenum and vanadium the percents are 96% and 90%, 0% and 4% and 4% and 6%, respectively.

Our partitioning experiments played a major role in demonstrating the affinity of ferrihydrite for molybdenum and vanadium which was taken up via adsorption and co-precipitation as well as in quantifying the fate of molybdenum and vanadium during the transformation of ferrihydrite to hematite. With these approaches, some other studies are worth considering:

- studies of the vanadium partitioning during ferrihydrite transformation in the anoxic conditions: it is assumed that in oxygen free conditions vanadium is released back into the pore water via diagenetic remobilization of Fe from Fe-oxyhydroxides (Feely et al. 1998);
- Quantitative comparison of the fate of the vanadium associated with ferrihydrite during the transformation to hematite in oxic *vs.* anoxic conditions.

XAFS results found that molybdenum was taken up via co-precipitation and adsorption as molybdate (MoO_4^{2-}). After ferrihydrite transforms to hematite its speciation changed when molybdenum became incorporated into hematite structure making it less bio-available. These results are the first data which give information about how molybdenum is incorporated into hematite structure. Molybdenum incorporated via co-precipitation has a different speciation than that sequestered via adsorption during ferrihydrite transformation. In both, co-precipitated and adsorbed samples, structural molybdenum seems not to differ from the structural/surface molybdenum, speciation wise. The pH of transformation did not influence the molybdenum speciation in adsorbed and co-precipitated samples.

However, our results suggest that molybdenum in co-precipitated samples might replace the iron six coordinated from edge-sharing octahedral of hematite structure. This theory can be explained by the fact that the Fe-Fe bond distance in hematite structure is 2.9Å and from our fittings we found a Mo-Fe bond distance of 3.05Å which is a very close value – an a reasonable comparison taking into account the vibrations of the atoms and the nature of the sample (not perfect crystalline).

The XAS results confirmed that molybdenum is incorporated into the hematite structure and remains immobilised for a long period of time. Molybdenum immobilisation by hematite formation from ferrihydrite, has important implications for metal sequestration in sediments the bio-availability for living organisms but also for water and soil remediation technologies.

From crystallographic point of view more data are necessary to certify that molybdenum has fully replaced Fe in the hematite unit cell. A suggestion could be: additional experimental approaches such as: XRD scanning of the products with an internal standard which might allow the hematite unit cell calculation in the presence and absence of molybdenum.

Chapter 6

The effect of molybdenum and vanadium on the crystallization of hematite from ferrihydrite at neutral pH: an *in situ* EDXRD study

6.1. Introduction

Iron (oxyhydr)oxide phases (*i.e.,* goethitę,ά-FeOOH) are common naturally occurring mineral phases important in many environmental systems (*i.e.,* rivers). These phases are also used in many industrial processes *(i.e.,* pigment and dyes factories, waste-water treatment plants etc). These phases have a high capacity to adsorb trace elements from solution due to their high surface area (up to >200m^2g^{-1}) and their reactivity (Cornell and Schwertmann 2003). Ferrihydrites (Fe_5O_3 $(OH)_9$) are group of metastable poorly-ordered iron oxyhydroxide phases that tend to be the first phase to form from solution when dissolved ferric iron is hydrolysed. These poorly ordered phases will tend to transform to different crystalline end-products (*i.e.,* goethite and hematite, Fe_2O_3). The kinetics of crystallization and the crystalline phase formed is influenced by a number of factors including pH (Schwertmann and Murad 1983), temperature (Shaw et al. 2005), presence of different anions and cations which can act as inhibitors (Lin et al. 2003; Shaw et al. 2005) or catalysts (Yee et al. 2006), solid:solution ratio(Cornell and Schwertmann 2003), etc. During the crystallisation process, any co precipitated or adsorbed metals will be either be released back into solution or sequestered by the newly formed phases (German et al. 1997; Metz and Trefry 1988). Also, the presence of adsorbed species (*i.e.,* phosphate) can have a significant effect on the crystallization rates (Shaw et al. 2005). Molybdenum and vanadium are considered important micronutrients for micro fauna habiting different ecosystems including those where the ferrihydrite forms *(i.e.,* the ocean floor). They play a major role in many enzymatic processes which drive the metabolism of all living organisms. The budget and availability of vanadium and molybdenum is strongly correlated to natural processes *(i.e.,* riverine inputs; (Chester 1990), sediment sequestration) many of which occur in marine systems and are controlled by interactions with iron oxyhydroxides (such as ferrihydrite).

However, the kinetics and mechanisms of the ferrihydrite transformation to goethite/hematite in the presence of co precipitated ions (in this study molybdenum and vanadium), as well as the fate of the metals during this process are poorly understood. In

these studies we also focused on the effect of temperature, ionic strengths, presence of the molybdenum and vanadium in ferrihydrite structure on transformation kinetics using an innovative *in-situ* Synchrotron-based Energy Dispersive X-Ray Diffraction technique.

6.2. Materials and methods

6.2.1. Ferrihydrite - starting materials

Pure 2-line ferrihydrite was synthesized following Cornell and Schwertmann (2000). In addition, molybdenum and vanadium co-precipitated ferrihydrite (Mo-ferrihydrite and V-ferrihydrite), were prepared by adding appropriate amounts (1000µM per batch) of molybdenum (as MoO_4^{2-}) and vanadium (as HVO_4^{2-}) to the starting base (NaOH) or acidic $Fe(NO_3)_3 \cdot 9H_2O$ solutions respectively. All ferrihydrite slurries were stored in the dark at 4ºC for a maximum of 1 week prior to use. For each ferrihydrite batch the density was determined by dry weight (in triplicate, at 50ºC, overnight). The amounts of co-precipitated molybdenum and vanadium were determined from the mass balance between the initial concentration and the concentrations in the supernatant after precipitation, as well as from the molybdenum and vanadium concentration in the fully digested solid phases (6 M HCl), using Inductively Coupled Plasma Optical Emission Spectrometry (ICP-OES).

6.2.2. Transformation experiments

On-line, in situ, transformation experiments

Energy dispersive X-ray diffraction (EDXRD) measurements were performed at Daresbury Laboratory, UK, Station 16.4. Details of the station set up and data acquisition can be found in Shaw et al. (2005) and Davidson et al (2008). All *in-situ* time resolved isothermal transformation experiments were carried out at a starting pH of 8 (adjusted with HCl or NaOH) either at an ionic strength (IS) of 0.7 (adjusted with NaCl, pure ferrihydrite, Mo-ferrihydrite and V-ferrihydrite, at temperatures between 130ºC to 240ºC) or at ionic strength 0.1 (Mo-ferrihydrite, 160ºC). For each experiment 15 ml of a 50 gL^{-1} ferrihydrite slurry were placed into a Teflon® liner enclosed in a Parr® hydrothermal reaction cell. A magnetic stirring bar provided a constant stirring of the reaction process. At the beginning of each isothermal transformation experiment the hydrothermal cell was placed inside a heating jacket set at the temperature of interest (Davidson et al. 2008). Experiments were conducted between 10 and 160 minutes, with diffraction patterns recorded every minute. Initial and final pH values (ORION 710A pH meter) of the mixtures as well as iron concentrations (ferrozine method, Viollier et al., 2000) in the filtered final solutions were

measured and upon completion of each experiment the solid end-products were separated by filtration from the solutions, washed and analyzed with a conventional X-Ray diffractometer (XDR, Philips PW 1730/10, CuKα, λ=1.54Å) to check for possible contributions from minor proportions of phases not detectable with EDXRD (Parise 2000). The reaction progress was evaluated from the change in peak area of growing Bragg peaks (Xfit, (Cheary and Coelho 1996)) with the induction time, t_o (time of appearance of a peak), as well as the completion of the transformation (time where peak area remained constant) defining the timeframe of the transformation. To express the transformation kinetics, the time resolved peak areas were normalised from 0 to 1, giving the degree of transformation, α:

$$\alpha = (A_t - A_{min})/(A_{max} - A_{min}) \qquad \text{(Eq. 6.1.)}$$

where A_t is the peak area at time t, A_{min} and A_{max} are the minimum and maximum peak area values of the specific peak.

Off-line (ex-situ) transformation experiment

Off-line experiments designed in the equivalent manner to the on-line experiments described above were carried out at 160˚C (Mo-ferrihydrite and pure ferrihydrite) and 73±2.5˚C (pure ferrihydrite) but with no *in situ* EDXRD data collection. For the Mo-ferrihydrite experiments, 3 equivalent sets were carried out and at specific time steps (0, 2 and 6 hours) the reactions were quenched and the solids separated from the supernatants, washed and analyzed by high-resolution Field Emission Gun Transmission Electron Microscopy (HR-FEG-TEM, Philips/FEICM200) operated at 197keV and fitted with energy dispersive X-Ray detector (EDS). The lower temperature experiment (in an oil bath on a stirrer plate) was carried out in order to follow the pH variations during the transformation. This experiment lasted for 6 days and the pH was recorded every 10 minutes using a PC controlled ORION 710A pH meter. The initial and end-product solids were analyzed with conventional XRD to confirm their mineralogical composition.

6.2.3. Kinetic evaluation and activation energies

The degree of transformation for the growth of the observed Bragg peaks from the EDXRD data, were fitted with the Johnson–Mehl-Avrami-Kolmogorov (JMAK) model (Avrami 1939; Avrami 1940; Avrami 1941):

$$\alpha = 1 - e^{-k(t-t_0)^m} \qquad \text{(Eq. 6.2.)}$$

where k is the rate constant for the reaction (s^{-1}), t is time (s), t_0 is the induction time (s) and m is a variable that depends on the nucleation rate, reaction mechanism, and dimensionality of growth (Hulbert 1969). The apparent activation energies of nucleation and crystallisation for the transformation end-products were calculated from the temperature dependent kinetic parameters derived from JMAK and applying the Arrhenius equation:

$$k = A \cdot e^{-E_a / RT} \qquad \text{(Eq. 6.3)}$$

where k is the rate constant; A is the frequency or pre-exponential factor; Ea is the activation energy (kJ mol^{-1}), R is the gas constant (8.314 J mol^{-1} K^{-1}) and T is the absolute temperature in Kelvin (K). For comparison the “time to a given fraction method” (Putnis 1992), was also used to determine the activation energy of crystallization. This approach relies solely on the time to a given fraction of transformation (*t**) and can be expressed as:

$$E_a = -RT \ln (t^*_\alpha / A) \qquad \text{(Eq. 6.4.)}$$

6.3. Results and discussions

In all on-line, *in-situ* transformation experiments > 140°C the only Bragg peaks observed to grow from the initial poorly ordered ferrihydrite were those for hematite (HM). The growth of the hematite (110) diffraction peak as a function of time is shown in Figure 6. 1. The EDXRD data revealed that at the lowest temperature (130°C) minor amounts of goethite were present during the transformation (Figure A6.2 in Appendix B). The low resolution of the EDXRD method due to the fact that the analyses were done in solution with high background causes the minor phases (5-10 %) to be poorly distinguished (Parise 2000). However, in the equivalent off-line experiments both at 160°C and at 73±2.5˚C (Apendix B - Figure A6.1.A and B) small proportions (estimated >1 and < 5 %) of goethite were observed as a minor intermediate phase during the transformation to hematite. The EDXRD data showed that the degree of transformation of ferrihydrite to hematite was temperature dependent (Figure 6. 1 and Figure 6. 4) and that the induction times for the appearance of hematite peaks increased with decreasing temperature. For example, in the pure-ferrihydrite system at 240ºC the (110) peak of hematite was observed after 8 minutes and the reaction was competed after 15 minutes, while at lower temperatures (130ºC) hematite started to form only after 40 minutes and the reaction was completed after ~100 minutes (Figure 6. 1.). Similar trends were observed in the Mo-ferrihydrite system and V-ferrihydrite system (Figure 6. 4.A and B).

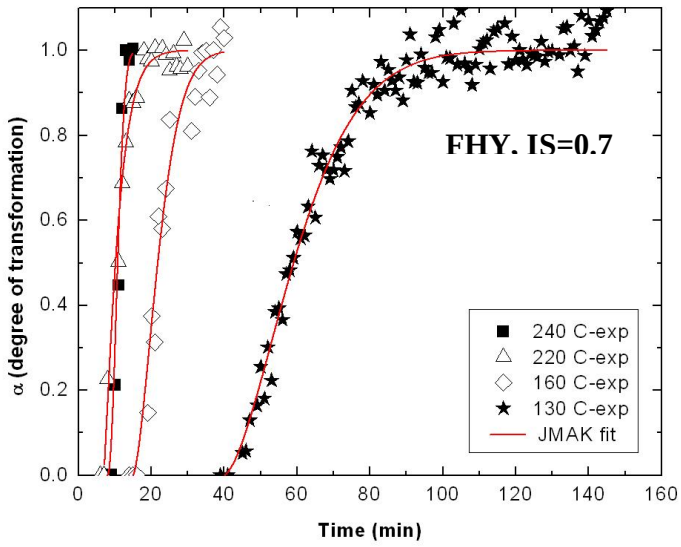

Figure 6. 1. The degree of transformation of pure ferrihydrite to hematite from the *in situ* EDXRD experiments as a function of temperature

The XRD data from the quenched high temperature off-line experiment (Mo-ferrihydrite experiment, XRD patterns recorded for 14 hours in order to determine the presence of minor phases) showed that even at 160°C small proportions (estimated > 1 % and < 5 %) of goethite were present during the transformation and in the solid end product (Figure A6.1A), yet in the EDXRD data this could not be observed. The presence of goethite as an intermediate was also supported by the high-resolution images of the quenched materials. The starting (0 min), quenched intermediate (1 hour) and end-product (6 hours, Figure 6. 2.A-C) from the off-line experiment with pure ferrihydrite at 160˚C revealed that the initial poorly ordered ferrihydrite aggregates, were converted to hexagonal hematite plates and minor quantities of goethite (needles in Figure 6. 2.B), yet the end-product was pure hematite (Figure 6. 2.C).

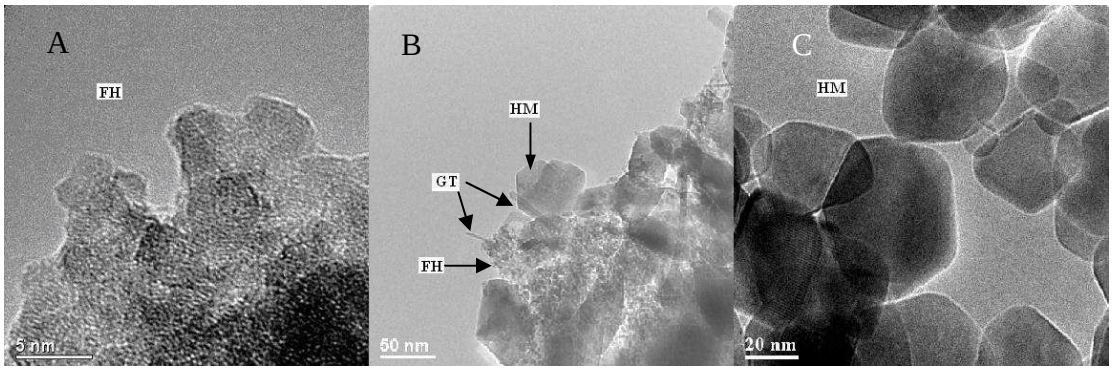

Figure 6. 2. Representative FEG-TEM images from quenched samples from the off-line pure ferrihydrite transformation experiment at T=160ºC showing minor goethite as an intermediate phase; (A) 0 hours, (B) 2 hours and (C) 6 hours; FHY = ferrihydrite, GT = goethite and HM = hematite.

Previous studies by Schwertmann and Murad (1983) and Schwertmann et al., (1999) showed that at a pH close to the point of zero charge (PZC) of ferrihydrite (7-8), hematite is favored over goethite and that the formation rate of hematite decreased with increasing temperature. In addition, at low temperatures and alkaline pH (>10-11) goethite is the favored solid end-product (Cudennec and Lecerf 2006; Schwertmann et al. 1999; Schwertmann and Murad 1983), although at high temperatures goethite is an intermediate and hematite is the final solid end product (Davidson et al. 2008; Shaw et al. 2005; Vu et al. 2010). These studies concluded that the ferrihydrite to hematite or goethite transformation was driven by the pH-dependent iron solubility (Jolivet et al. 2004). Thus, hematite was the dominant end-product at near neutral pH where the iron solubility is

lowest, while at acidic and alkaline pH values (2–5 and 10–14), the iron solubility increases and therefore goethite was the dominant end-product. However the results from the present study confirm that at near neutral pH and under aerobic conditions, *hematite* is the principal transformation end-product.

A comparison between the data collected at 130ºC, pH 8, ionic strength 0.7 in the pure ferrihydrite system from this study with data from Shaw et al., (2005) at 137ºC (pH 10.7 and ionic strength 0.1) revealed that in the current study the induction time at lower pH and higher ionic strength was 40 min while at higher pH and lower ionic strength (Shaw et al. 2005) the induction time was only 15 minutes.

Interestingly, the quenched samples collected at the end of the low temperature experiment revealed that the transformation end product consisted of a mixture of hematite with minor goethite. The goethite peaks were present in minor amounts even after 6 days of reaction (Figure A6.1.B in Appendix B). This result indicates that at low temperatures the transformation to hematite was not completed and that goethite may be an intermediate product. These results are in line with a previous study (*i.e.,* (Schwertmann et al. 1999)), where the photomicrographs of the solids revealed that even after 84.5 days at 70ºC the transformation of ferrihydrite was not complete and minor amounts of goethite needles were still present in the hematite matrix (Schwertmann et al. 1999). Furthermore these results are also in agreement with other high pH transformation experiments (Davidson et al. 2008; Vu et al. 2010), where hematite was the sole final solid end product yet goethite was an intermediate in the transformation reaction.

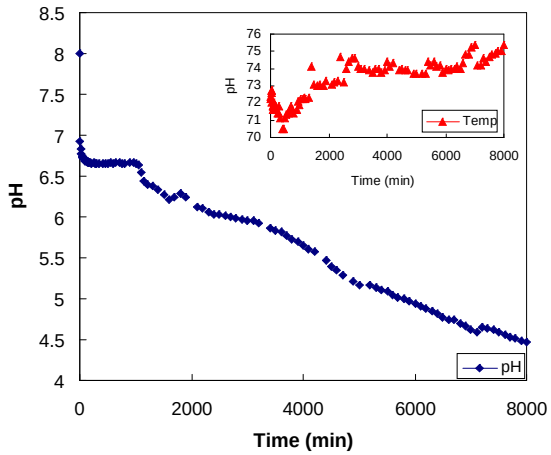

Figure 6. 3. The pH profile recorded for the low temperature (73±2.5˚C) off-line transformation experiment; the inset shows the ~ 2.5ºC temperature variations during the experiment.

In the present high temperature EDXRD study as well as other off-line and on-line transformation studies (Davidson et al. 2008; Lin et al. 2003; Schwertmann et al. 1999; Schwertmann and Murad 1983; Yee et al. 2006) usually only the initial or the end-pH values are reported (specially in long-term or high-temperature experiments, (Lin et al. 2003; Schwertmann and Murad 1983; Shaw et al. 2005). Here, for the first time the pH profile was recorded for the low temperature (73±2.5°C) off-line experiment (Figure 6. 3), to extract more mechanistic information. The pH profile recorded in time revealed that in the first 100 min the pH gradually dropped from 8 to ~ 6.7. On a longer time scale (*i.e.,* ~ 100 min to 8000 min) the pH decreased further reaching a final value of 4.5. Within the time of the current on-line EDXRD experiments (max 160 min), although the initial pH in all cases was 8, the end pH usually dropped to 6.5 - 7 at the end of the experiments. The first pH drop (8 to 6.7) was in agreement with the observations from the high-temperature *in situ* EDXRD results, where in all experiments the end pH reached values between 6.5 and 7.

Further to the results obtained from pH recording experiment which revealed that ferrihydrite transformation near neutral pH occurred with proton production or hydroxyl consumption, a short consideration of mechanistic information is given. So far no indication of proton production during ferrihydrite transformation at neutral pH, could be found in the literature. Nevertheless, if it can be agreed that the chemical formula of ferrihydrite is $Fe_5O_3\ (OH)_9$ (Jolyon 2009), and stoichiometricaly the indirect hematite formation from ferrihydrite can be written as:

$$2Fe_5O_3\ (OH)_9 \Rightarrow 10Fe\ OOH + 4H_2O \quad \text{and} \quad 10Fe\ OOH \Rightarrow 5Fe_2O_3 + 5H_2O$$

Or at high temperature - direct transformation to HM:

$$2Fe_5O_3\ (OH)_9 \Rightarrow 5Fe_2O_3 + 9H_2O$$

which is in agreement with the mechanism supposed by Cudennec et al., 2006 and also Loan et al., 2005 who used as ferrihydrite formula $Fe_5O_7(OH)\ 4H_2O$ (Cudennec and Lecerf 2006) and $5Fe_2O_3\ 9H_2O$ (Loan et al. 2005), respectively:

All presented equations show a dehydration mechanism. The importance of water during the ferrihydrite to hematite transformation has previously also been shown based on isotopic analyses (Bao and Koch 1999) - overall the fact that ferrihydrite transforms to hematite via dehydration and rearrangement is a well known mechanisms, but the fact that

during the reaction the pH drops, either via H^+ production or HO^- consumption, was not shown previously.

6.3.1. The effect of co-precipitated molybdenum and vanadium on the ferrihydrite transformation to hematite

The analyses of digested molybdenum and vanadium co-precipitated ferrihydrite revealed that the starting materials used in the transformation experiments contained 1 molar% metal (±0.01).

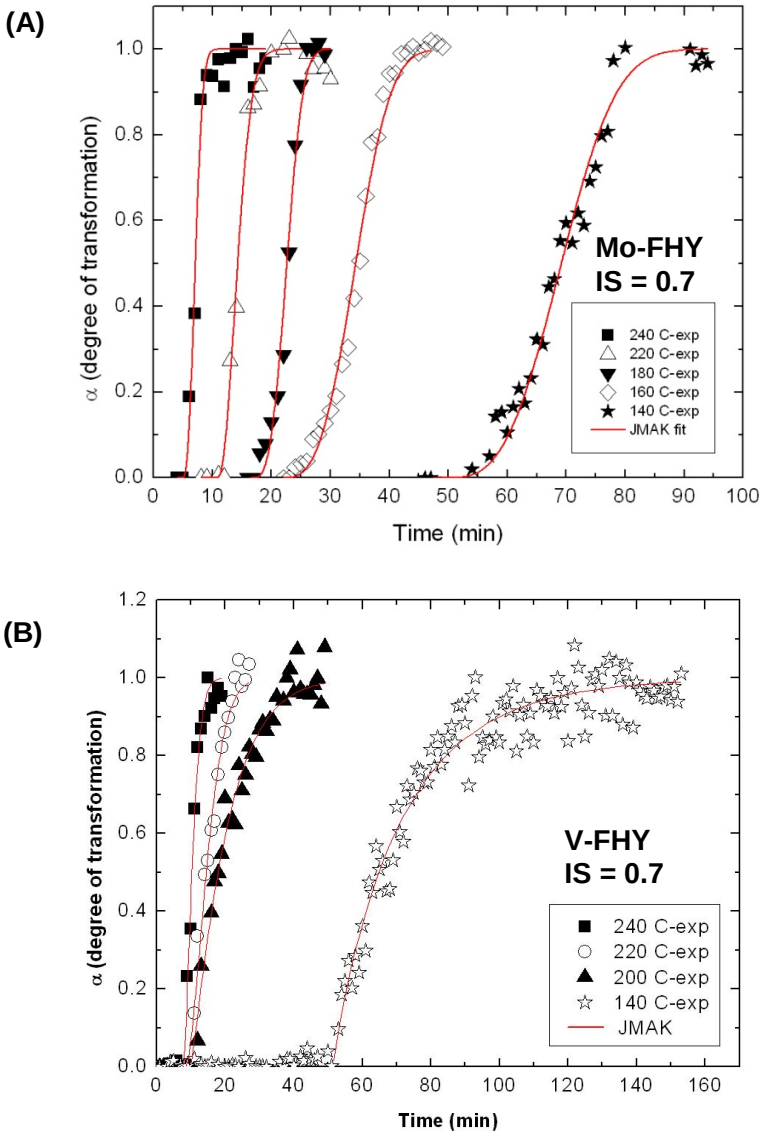

Figure continued on the next page

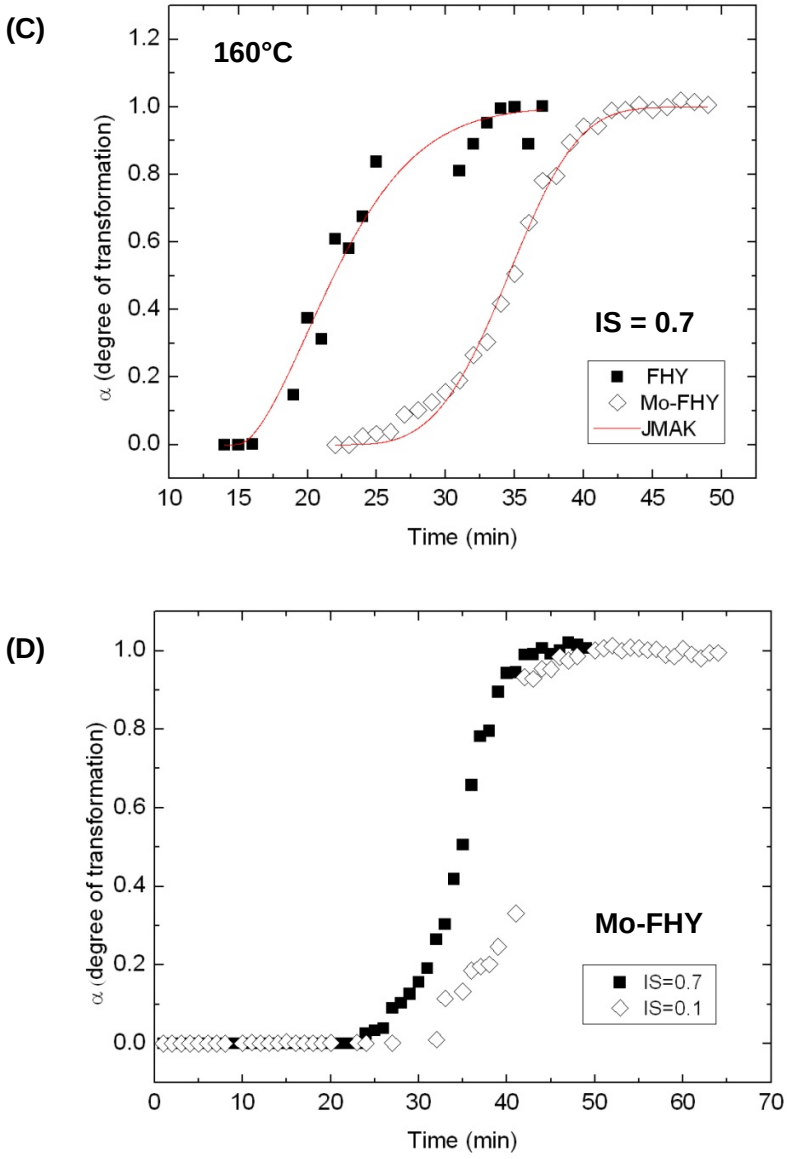

Figure 6. 4. The degree of transformation of ferrihydrite to hematite as a function of time, temperature and ionic strength for: (A) Mo-ferrihydrite at ionic strength 0.7; (B) V-ferrihydrite at ionic strength 0.7; (C) pure ferrihydrite and Mo-ferrihydrite at 160ºC and ionic strength 0.7; (D) Mo-ferrihydrite at 160ºC and ionic strengths 0.7 and 0.1. Symbols are experimental data points and lines represent the JMAK fits.

Comparing the pure ferrihydrite system (Figure 6. 1.) with the molybdenum and V-ferrihydrite systems (Figure 6. 4.A and B) indicates that both of the metals retard the ferrihydrite transformation. Also comparing the reaction rates in Mo-ferrihydrite system at high and low ionic strength (Figure 6. 4.D) revealed that lowering the ionic strength also

retarded the ferrihydrite transformation to hematite. For example, at 160ºC in the Mo-ferrihydrite system the data showed that higher ionic strength reduced the induction time of the transformation from 32 minute to 23 minutes (Figure 6. 4.D). Conversely, the presence of metals (at equivalent ionic strength) when compared to the metal-free system increased the induction times by 32% in the Mo-ferrihydrite system (Figure 6. 4.C) and by up to 38% in the V-ferrihydrite system (Figure 6. 4.B and Table 6.1). These data also indicate that vanadium as a trivalent anion (VO_4^{3-}) delays the induction of the transformation reaction slightly more than the divalent molybdate (MoO_4^{2-}) anion,

Long term batch transformation experiments (up to 1 year, T = 20ºC and pH between 7-11) carried out by Lin et al., (2003), showed that the presence of Cl^-, NO_3^- and SO_4^{2-} all retarded the transformation of 1 mol % Cd doped ferrihydrite and that the transformation rate decreased as the negative valence on the anion increased ($NO_3^- > Cl^- > SO_4^{2-}$). In addition, the induction time increased with increasing anion valence at constant pH (7 and 8) and temperature (Lin et al. 2003). Moreover, Shaw et al., (2005) showed that at 90ºC in the presence of 3 % PO_4^{3-} and under more alkaline conditions (pH=13.2) the end-product of the transformation was goethite and not hematite. They concluded that when compared to a phosphate free system, the presence of the PO_4^{3-} ion reduced the goethite formation rate and the induction time of the transformation by ~70 %. Finally, a study by Davidson and collaborators (2008) on the transformation of schwertmanite at alkaline pH (13) found that the presence of sulfate (SO_4^{2-}) also significantly retarded the dissolution of the ferrihydrite intermediate to goethite and that at high temperatures hematite is favored over goethite.

Zhao's studies on molybdenum effects on a ferrihydrite catalyst surface found that co-precipitated molybdenum (atomic concentration ratios of 5 and 35%), inhibits hematite crystal growth and prevents the formation of large hematite particles, allowing the catalyst to maintain dispersion and thereby enhance its catalytic activity (Zhao et al. 1994). Their results are general and agree well with our fundings but are limited with regards to quantifing the retardation time and the end-product formation kinetics.

The experiments at different ionic strength presented above suggest that a 0.6 unit difference in ionic strength enhanced the induction time of hematite formation by about 30% (Figure 6. 1.D) (or 1 ionic strength unit promotes a 50% faster nucleation). Comparing the data collected at 130ºC (pH 8, ionic strength 0.7) in the pure ferrihydrite system from the present study with data from Shaw et al., (2005) at 137ºC (pH 10.7 and ionic strength 0.1) shows that by taking into account the corrections due to the difference in ionic strength (0.6 units) and temperature (ΔT=7ºC), the 2.7 pH units difference in experimental conditions would decrease the induction time by ~50% (or one pH unit gives a decrease of

~18%). This pH trend agrees with the well known strong pH dependence of the ferrihydrite to hematite transformation previously published (Schwertmann and Murad 1983).

6.3.2. Kinetic interpretation

The JMAK parameters (*k,* t_o and *m*) obtained from the fitting of the degree of the transformation of ferrihydrite to hematite (Table 6. 1.) showed that in all three systems studied, the hematite crystallization rate increased with temperature, while concomitantly the induction time decreased with increasing temperature.

Table 6. 1. JMAK fitting parameters and activation energies for hematite formation with and without molybdenum and vanadium for the experiments at ionic strength 0.7

Mo-FHY				**V-FHY**				**FHY**			
Temp (^{o}C)	k *10^{-4} (s^{-1})	t_o (s)	m	Temp (^{o}C)	k *10^{-4} (s^{-1})	t_o (s)	m	Temp (^{o}C)	k *10^{-4} (s^{-1})	t_o (s)	m
240	69	300	2.4	240	52	469	1.5	240	49	480	2.2
220	42	660	2.0	220	22	512	1.7	220	38	420	1.2
180	26	1020	3	200	15	599	1.1	160	19	900	1.6
160	12	1320	3	140	8	3087	1.0	140	n.d.	1900*	n.d.
140	8	3000	3					130	7	2400	1.6
$E_{a\ nucl.}$ (kJ/mol)	35 (±5)			35 (±6)				26 (±6)			
$E_{a\ crys.AA}$ (kJ/mol)	38 (±3)			28 (±9)				29 (±4)			
$E_{a\ cryst.TGF}$‡ (kJ mol^{-1})	39 (±3)			26 (±9)				26 (±5)			

* only the beginning of the transformation was recorded for this experiment.

‡ $E_{a\ cryst.TGF}$ is the apparent activation energy of crystallization derived using 'Time to a given fraction" method (Putnis 1992)

The m values obtained from the JMAK fits (Table 6. 1.), ranged between 1 and 3: averaging 1.6 for pure ferrihydrite, 1.3 for V-ferrihydrite and 2.6 for Mo-ferrihydrite respectively. The classification of Hulbert (1969) for m values (Table 3.4.) indicates that, hematite crystallized via a 2D phase boundary controlled growth.

Using the Arrhenius approach the apparent activation energies of nucleation and crystallization for hematite for all three systems were derived (Figure 6. 5. and Table 6. 1.).

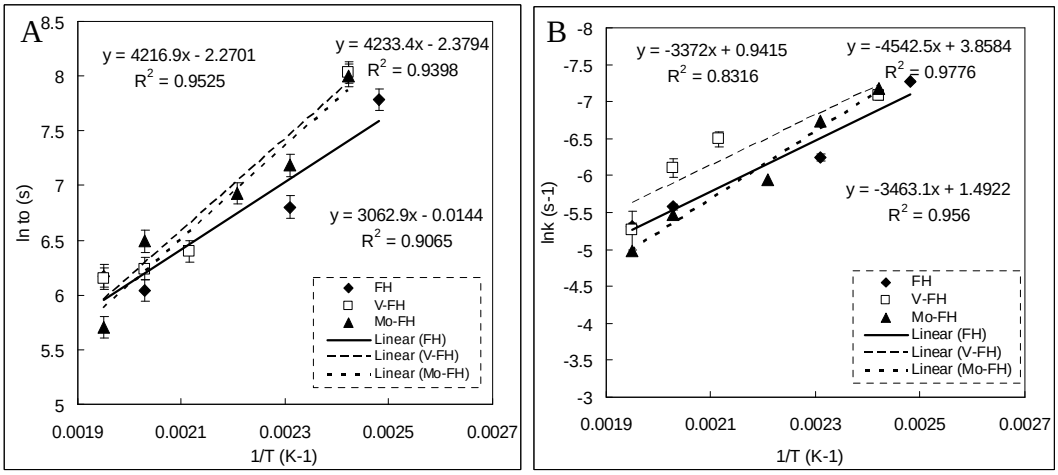

Figure 6. 5. Arrhenius plots for (A) induction time, t_o and (B) rate of growth, k, of hematite nucleation and crystallization in the three studied systems.

The E_a for nucleation and crystallization for all three studied systems were within the range of 26-39 kJmol^{-1} (Table 6. 1.). The apparent activation energies of nucleation for the pure ferrihydrite system was ~ 10 kJmol^{-1} lower than the $E_{a\ nucl.}$ for the molybdenum or vanadium systems, indicating that the presence of these anions increased the activation energy of nucleation. Interestingly, for the crystallization stage only the Mo-ferrihydrite system required slightly higher apparent activation energy, while the V-ferrihydrite and pure-ferrihydrite systems had both the same activation energy. Shaw et al., (2005) calculated activation energy of hematite nucleation (at pH 10.7 and ionic strength 0.1) of 24 (±1) kJmol^{-1}, while their activation energy of hematite crystallization (calculated from the Arrhenius approach (AA)) was 69 (±6) kJmol^{-1}. Their high crystallization activation energy for hematite formation (2.6 times higher than in the present study) can easily be explained by the 2.7 pH units difference in experimental conditions, which also produced a change in the transformation mechanism (i.e. aqueous added transformation mechanism). In the present study, when the apparent activation energies of crystallization were calculated using the “time to a given fraction” (TGF) approach (Putnis 1992) the results revealed

activation energy values ($E_{a\ cryst,\ TGF}$, Table 6. 1) that matched those obtained from the Arrhenius approach. Similarly, if the crystallization activation energy of Shaw et al (2005) was recalculated using the "time to a given fraction' approach (Putnis 1992) again a very good agreement (67 (±4) $kJmol^{-1}$ vs. 69 (± 6) $kJmol^{-1}$) with the activation energy calculated via the Arrhenius approach was obtained. These calculations indicate that both models used to calculate activation energies of crystallization are suitable and valid.

Comparing the data from this study with literature data on hematite crystallization at pH 10.7, ionic strength 0.1 (69 (±6) $kJmol^{-1}$; (Shaw et al. 2005)) or at pH 13.2 and ionic strength 0.1 (103 (±3) $kJmol^{-1}$; (Davidson et al. 2008)) revealed that at higher pH and lower ionic strength, a much higher activation energy was needed for hematite to crystallize. In addition, at pH 13.2, there is a competitive effect given by goethite formation (Davidson et al. 2008) which explains the requirement of higher activation energy. In Figure 6.6, taking into account that the ionic strength affected primarily the nucleation stage (the induction time) and not the crystallization (Figure 6. 4.D), the results from this study together with those from the literature (Davidson et al. 2008; Shaw et al. 2005; Vu et al. 2010) for both goethite and hematite are plotted as $E_{a\ cryst}$ vs. pH (Figure 6.6.A) and k (s^{-1}) vs. pH (Figure 6. 6.B). Hematite crystallization activation energy (E_a) increases with increasing pH. Figure 6.6.A shows that at pH below 10.7 higher activation energy is needed for goethite to form, thus the hematite is favoured and above it the predominant transformation end-product is hematite. The apparent activation energy vs. pH dependence for hematite and goethite are given by the Equations 6.5 and 6.6, respectively. Notice that despite the fact the Vu's (2009) and Davidson's (2008) work were conducted at the same pH, activation energies for hematite crystallization at pH 13.2 are ~30% different. This difference is explained by the presence of sulphate in the system, which is derived from the schwertmannite – the initial transformation product in Davidson's work (Davidson et al. 2008; Vu et al. 2010).

$$E_{a(HM)} = 14.6\ pH - 84.39 \qquad \text{(Eq. 6.5.)}$$

$$E_{a(GT)} = -9.06pH + 157.87 \qquad \text{(Eq. 6.6.)}$$

The equations 6.5. and 6.6. were obtained from limited but still *in-situ* EDXRD experiments found in the literature, considering different assumptions with regards to the similarity of the transformation conditions such as possible presence of the different ions *(i.e.,* sulphate or chloride) from starting material content or pH and ionic strength adjustment or solid:liquid ratios.

Factors as solid:liquid ratio, ionic strength, pH and temperature influence the type and the kinetics of the end product formation. Over all the ferrihydrite transformation mechanism is a different function of pH: goethite is predominantly forming at high pH competing with hematite whereas at pH neutral hematite is the main transformation end-product (Schwertmann and Murad 1983).

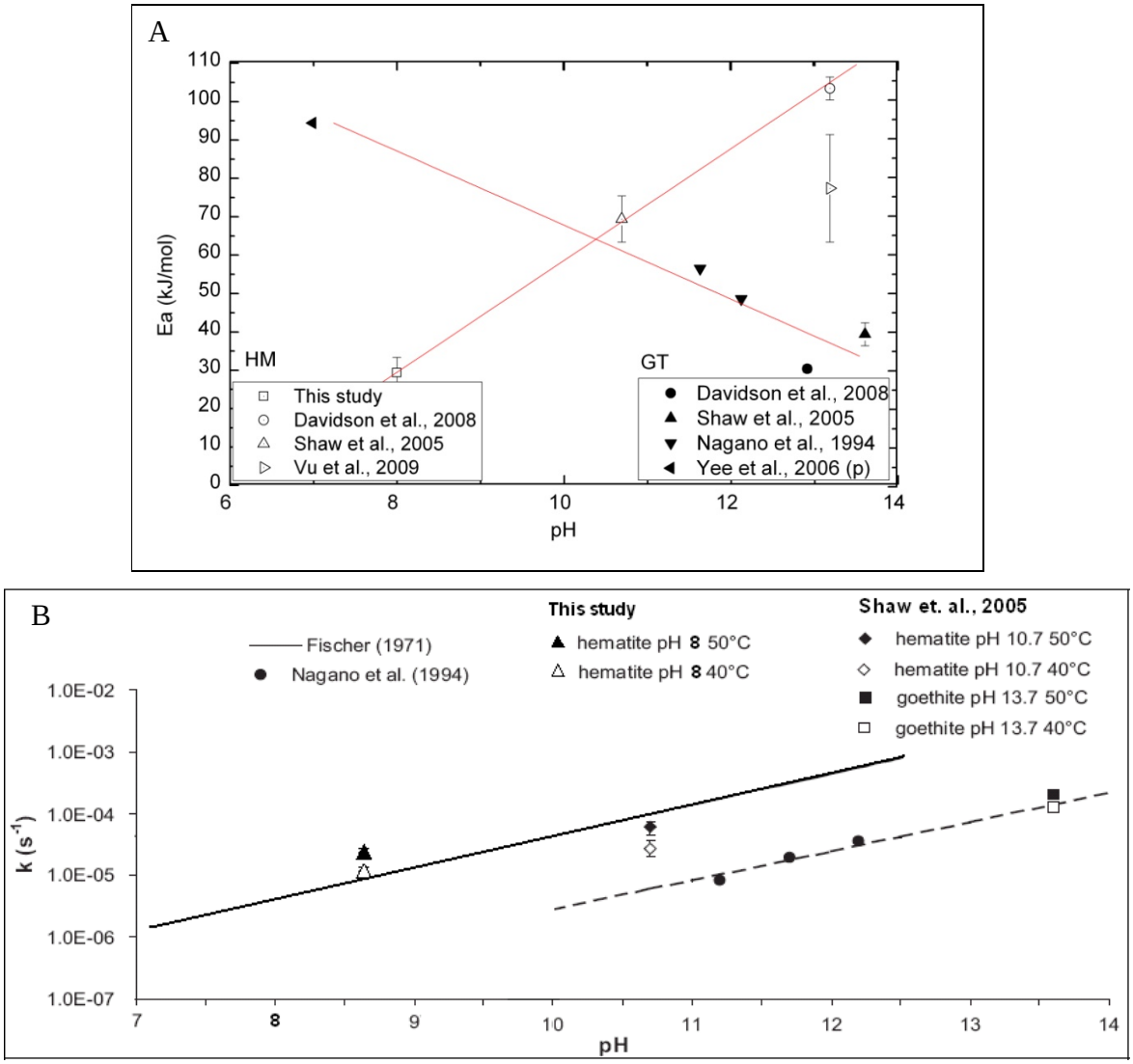

Figure 6. 6. (A) Ea_{cryst} *vs.* pH for hematite and goethite from this study and the literature. Note: p – values predicted from published results; empty symbols are values for hematite and full symbols are goethite values (B) rate constant *vs.* pH dependences of the hematite and goethite formation from ferrihydrite at 40 and 50°C found in the literature: values from this study and Shaw et al., (2005) are extrapolated from *in situ* EDXRD study, whereas Fisher (1971) and Nagano et al., (1994) studies are *ex situ* transformation studies.

Information about the faster transformation of ferrihydrite as the pH increases in alkaline pH range were found in the literature (*e.i.,* (Schwertmann et al. 1999; Schwertmann and Murad 1983)), however a linear dependence of k *vs.* pH for only hematite formation could never be plotted because of the insufficiency of the *in-situ* time resolved data.

The Shaw et al., (2005) data compilation in terms of k *vs.* pH, used Fisher's and Nagano's ferrihydrite ex situ transformation results to compare his in situ transformation results at pH 10.7 and 13. It can be noted that our data fits well on the trend predicted by Fisher in 1971 (Figure 6. 6.B). It is important to mention that Fisher (1971) conducted his isothermal kinetic experiments at pH 6.4 to 12.5 and a temperature of 50°C following a rudimentary oxalate extraction technique, which could not define the crystalline end product (hematite or goethite) of the transformation. Comparing the data, in terms of hematite formation *vs.* time, from this study with the results obtained by Shaw et al (2005) (Figure A6.3 in Appendix B) at pH 8 and 10.7, respectively, it confirms the same trend (as in Figure 6. 6.B) of increasing transformation rate with the increasing pH, which is extendable and valid towards the neutral pH. On another hand, this trend is supported by our *ex situ* ferrihydrite transformation results at 73°C, which suggested that the ferrihydrite transformation occurs via HO^- consumption (pH decreases, Figure 6. 3).

Using the rate constant and the induction time dependence *vs.* temperature Arrhenius plots obtained in the *in-situ* experiments, ferrihydrite under experimental conditions presented in our off-line experiment monitoring the pH (at 73 ± 2.5ºC) is expected to start transforming after ~ 148 minutes with a rate constant of $2.0 \cdot 10^{-4}$ s^{-1}. The extrapolation was done taking into account ionic strength influence, but for a closer approximation small corrections could be done considering the physical dynamicity of the systems (the mixing speed) and water/solid ratio influence.

6.4. Summary

The results from the current study confirmed that the transformation of ferrihydrite to hematite is dependent on temperature, pH, ionic strength as well as the presence or absence of different anions. However, new data on rate constants, induction times and activation energies are presented for three different systems at near neutral conditions that are important for a variety of natural systems (*i.e.,* seawater hydrothermal systems, neutral soil adsorption processes, acid mine drainage, etc.,). The *in-situ* and time resolved EDXRD data showed that the ferrihydrite to hematite transformation occurred via the nucleation and 2D growth and that high temperature, pH and high ionic strength primarily enhanced the crystallization process, whereas the presence of molybdenum and vanadium principally retarded the nucleation stage while the crystallization rate was similar with the process without anion addition.

These studies support the fact at near neutral pH the ferrihydrite transformation to hematite takes place following a dehydration/rearrangement, but is associated with the H^+ production or HO^- consumption. Further investigations of the transformation kinetics at the molecular scale are suggested by monitoring the HO^- consumption in consistent conditions by varying sequentially each parameter influencing the transformation process (pH, temperature, ionic straight, water:solid ratio, the presence of different ions: co-precipitated and adsorbed which can act as catalysts or inhibitors, dynamicity of the system: static or dynamic regime). The comparison of our transformation data with Vu et al., (2010) and Davidson et al., (2008) indicates that it is necessary to study the influence of solid to solution ratio on the transformation end-product. This suggestion came from the fact that although they transformed the ferrihydrite at high pH (i. e., 13), conditions under which they should have obtained goethite as a main end product, their end-product was ultimately hematite (end-product expected to form at neutral pH).

These results play an important role in quantifying the time scale of molybdenum and vanadium sequestration from their environments, their availability as well as has important implications in their budget within the environments ferrihydrite occur and co-precipitate. For example, if the whole ocean reservoir is passing through the hydrothermal systems ones every 10^3-10^4- years (Statham et al. 2005; Tuner and Hunter 2001); molybdenum and vanadium concentration along the water column is 10 mg L^{-1} (Chester 1990) and 2-3 µg L^{-1} (Ferreira et al. 2002), respectively, and that molybdenum and vanadium have a high affinity for ferrihydrite particles (Brinza et al. 2008) the impact of

hydrothermal systems on molybdenum and vanadium budget to the ocean could be estimated. Also, the data may be applied to soil and wastewater remediation field.

In Appendix B available:

XRD analyses of the intermediate transformation product from the off-line ferrihydrite transformation experiments at 160ºC and 73±2.5ºC, IS =0.1 as well as the initial and end-product diffractograms of the pH-recorded off line experiment are presented in Appendix. In addition, the t_o (sec) *vs*. T (C) and k (s^{-1}) *vs.* T (C) profiles of all transformation systems following an exponential trend are plotted to help the interpolation or extrapolation of any desired temperature, induction times or rate constants.

In Appendix C available:

XRD spectra of the ferrihydrite transformation at 4°C and 10 °C, showing a very slow transformation process after 33 months. A small difference between the processes monitoized at 4°C and 10°C could be observed (slightly higher (110) hematite peack is visipble in the XRD spectra at 33 months for the 10ºC transformation experiment) suggesting that at 10°C the transformation process occurs slightly faster.

Chapter 7
Molybdenum and vanadium pre-concentration on Toyopearl 650M cationic resin from a seawater matrix

7.1. Introduction

Molybdenum and vanadium concentrations in seawater are usually very low, yet their chemistry is important for both metabolic and mineral interaction effects. In order to be able to accurately quantify their concentrations new approaches are needed specially as the complexity of seawater matrices usually creates problems for the exiting high-resolution and high-precision mass spectrometric techniques (*i.e.,* ICP-MS, etc). Such effects may include: species interferences, salts effect/deposition on the instrument components etc. These limitations reduce the overall instrument sensitivity and in this sense, the development of on-line pre-concentration techniques using different ion exchange resins, are necessary to reduce the volume and the time required for analysis.

Previous work in this field have used resins such as Muromac A-1 for Al, V, Mn, Co, Ni, Cu, Zn, Mo, Cd, Pb, and U (Hirata et al. 2001) and Toyopearl AF-Chelate 650M for Cu, Ni, Zn, Mn, Co, Pb, Cd, Ni, Cu, Cd and V (Warnken et al. 2000; Willie et al. 1998), and they found good outputs making the on line pre-concentration column/ICP-MS technique applicable to different environmental samples. Their work is based on improvements in the resin performance and optimization of flow injection system as well as ICP-MS instrument and plasma conditions for on line pre-concentration system.

For the first time, we decided to test the capacity of the Toyopearl 650M resin to retain and pre-concentrate molybdenum and vanadium anions from seawater matrices. In order to proceed to more sophisticated experimental designs of the pre-concentration/analysis unit, in this case - preliminary studies are needed to evaluate the potential of the resin to uptake molybdenum and vanadium. Thus, the aim of this study was to primarily investigate the ability of the Toyopearl 650M resin to remove and concentrate molybdenum and vanadium from natural seawater spiked with relative high concentrations of these anions.

7.2. Materials and methods

The resin description and experimental methods employed have been detailed in Chapter 3.9. Briefly, a flow through column set up was used to test the feasibility of using a commercial resin (Toyopearl 650M (CAS No:122985-81-3)) to pre-concentrate molybdenum and vanadium from seawater matrices. Natural seawater spiked with 100uM molybdenum and vanadium was used in the preliminary tests. The pH for molybdenum adsorption was set to 3.5, while for vanadium adsorption the pH was set to 4.5. Elution of the molybdenum and vanadium was done with nitric acid (0.7M or 5% v/v). The collected samples from both adsorption and desorption were appropriately diluted and analyzed with ICP-OES (at National Oceanography Center with the help of Dr. Darryl Green).

The metal uptake capacities, q, mmol g^{-1} were calculated with the following equation:

$$q_r = \frac{V \cdot (C_f - C_i)}{S_r} \qquad \text{(Eq. 7.1.)}$$

Where: q_r is the metal uptake capacity of the resin, mmol g^{-1};
V is the volume of seawater passed through the column (100mL), L;
C_i is the initial metal concentration in the effluent, mmol L^{-1};
C_f is final (equilibrium) metal concentration in the effluent, mmol L^{-1};
S_r is the dry weight of the resin in the adsorption column, g.

7.3. Results and discussions

These data from preliminary tests, which can be further used for designing an on-line pre-concentration unit for ICP MS measurements of molybdenum and vanadium in seawater matrices, are discussed. Note that further work to fully implement and validate this protocol is needed but here first insights into the possibilities of this approach are discussed.

Figure 7. 1. shows the molybdenum concentration profile in the column effluent as a function of the effluent volume. The increase in molybdenum concentration with volume of the seawater passing through the column indicated that the column became progressively saturated with molybdenum. The initial molybdenum concentration in the test seawater (before passing through the column) was 0.115 mmol L^{-1}. The molybdenum concentration in the effluent reached a value close to the one in the influent and a equilibrium plateau is reached that indicates that the resin is saturated. In our tests the equilibrium plateau was reached after passing 40 mlL of seawater containing 100uM molybdenum. Runs at two different flow rates (measured by quantifying the mean flow-through time of three 10 mL replicate thorough the column) were carried out. When comparing the uptake profile of the column at a flow rate of 1mL min^{-1} (the uptake capacity = 0.228 $mmolg^{-1}$) with the one corresponding to the flow rate of 2 mL min^{-1} (the uptake capacity =0.220 $mmolg^{-1}$) it is obvious that a flow rate of 1-2 mL min^{-1} does not significantly influence the uptake capacity of the molybdenum on the Toyopearl 650M resin in our column settings. Specifically because the flow measurement was subjective we can consider the two runs as replicates. In this context we expressed the uptake capacity of the resin as an average of the two runs as being 0.224 mmol g^{-1} (or 21.586 mg g^{-1}) (Table 7.1.)

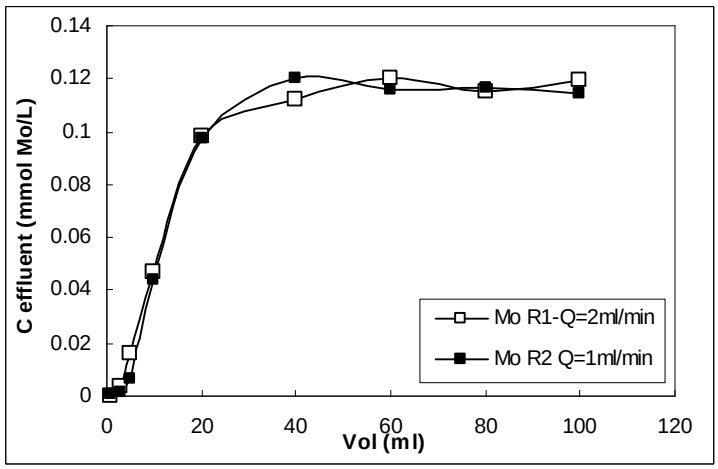

Figure 7. 1. The profiles of molybdenum adsorbed on Toyopearl 650M resin in the column type adsorption experiments: breakthrough curves expressed as CMo (mmolL-1) *vs.* Vol (mL) at two different flow rates (1 and 2 mL min^{-1}).

The profile of the vanadium concentration in the effluent *vs.* the volume of seawater (spiked with 100uM V) passed through the column is displayed in Figure 7.2. The vanadium concentration in the seawater before passing through the column was 0.125 mmol L^{-1}.

Interestingly, the shape of the curve indicates that the first 5 mL of the effluent had already had a content of vanadium of ~0.035 mmolL^{-1} and after 5 mL of seawater passed through the column a high vanadium uptake started. This trend can be seen in both replicates. The low adsorption within the first 5 mL can be explained either by a competitive effect with some other ions in the seawater matrix (that had a bigger affinity), or more probably the formation of complexes on the resin surface which enhanced the adsorption of vanadium. Once a volume of 5 mL of sample passed through the column, vanadium adsorption became faster and reached the equilibrium plateau after 40 mL of seawater beuing passed. The maximum uptake capacity was calculated as an average of the two runs as 0.145 mmol g^{-1} (or 7.386 mg g^{-1}) (Table 7.1.). Notably a marginally bigger difference between the two flow rate runs can be observed in vanadium experiments. This suggested that a slower flow rate of the seawater through the column will favour vanadium uptake capacity: (0.138 mmol g^{-1} for a flow rate of 2 mL min^{-1} and 0.153 mmol g^{-1} for a flow rate of 1 mL min^{-1}).

Comparing the affinities of molybdenum and vanadium for the same resin, it can be deduced that vanadium is adsorbed ~ 35% less than molybdenum on Toyopearl 650M resin.

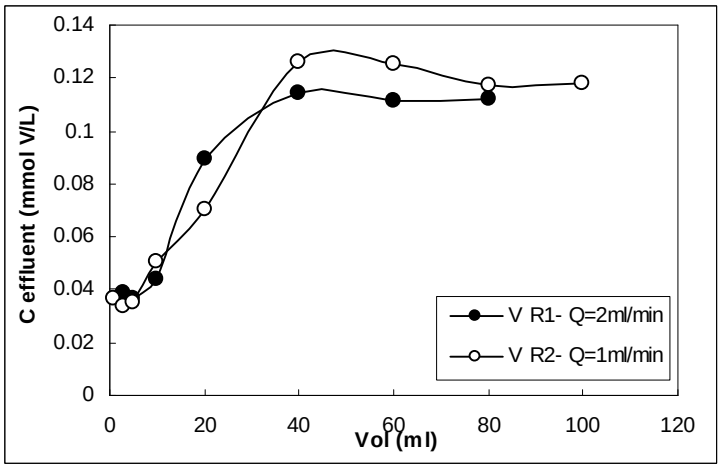

Figure 7.2. The profiles of vanadium adsorbed on Toyopearl 650M resin in the column type adsorption experiments: breakthrough curves expressed as C_V ($mmolL^{-1}$) *vs.* Vol (mL) at two different flow rates (1 and 2 mL min^{-1}).

Figure 7.3 shows the normalized plot of the adsorption progress, expressed as effluent concentration (C) / influent concentration (C_0), as a function of the volume of the samples, indicating that the resin became saturated when the effluent concentration equals the influent concentration. Interestingly for both systems (Mo and V) this occurred after the first 40 mL of the solution passed through the column.

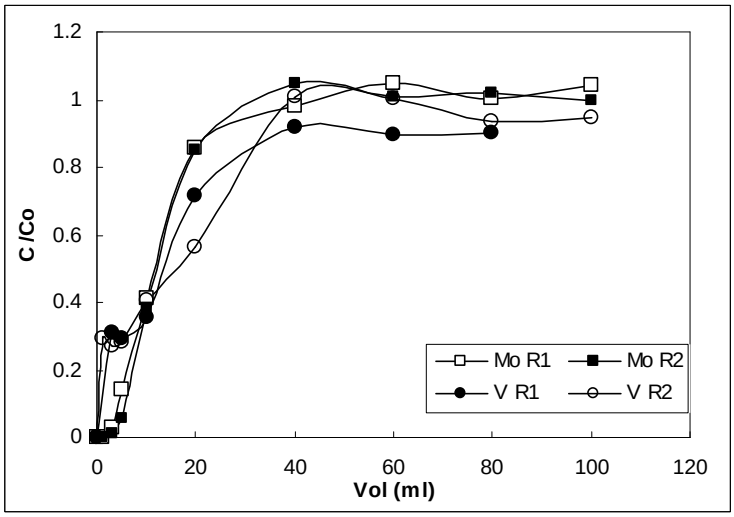

Figure 7.3. The progress of vanadium and molybdenum adsorption on Toyopearl 650M resin in column type adsorption experiments: breakthrough curves expressed as C_V ($mmolL^{-1}$) *vs.* Vol (mL)

Table 7.1. Uptake capacities of molybdenum and vanadium adsorbed onto Toyopearl 650M resin from seawater matrices:

Element	**q_r, averaged uptake capacity from R1 and R2, mmol g^{-1}**	**q_r, averaged uptake capacity from R1 and R2, mg g^{-1}**
Mo	0.22	21.59
V	0.15	7.38

7.4. Summary

The results from these preliminary studies showed that the Toyopearl 650M resin is a useful ion exchange support for molybdenum and vanadium pre-concentration from seawater matrices. However, further investigationsand optimization work needs to be carried out.

Future recommended developments:

- running standards to determine the precision and accuracy (and detection limit);
- method optimization by repeating the studies using a range of lower concentration of molybdenum and vanadium;
- use of different eluents, such as perchloric acid and ammonium hydroxide for sequential extraction of the different species of vanadium (*e.g.,*: V(IV) and V(V))(Wang and Sañudo-Wilhelmy 2008);
- building a flow injection system (on line column pre-concentration unit) and optimizing the unit by varying/testing:
    - (a) unit parameters: flow rate, volume of sample passed through the column; time, volume of eluent needed for optimum recovery;
    - (b) process parameters: pH, reagents mixing speed (*i,e.,* acid or base addition for pH correction or on line dilution of the eluent prior to sample inlet into ICP technique, etc);
    - (c) the number of reusable cycles of the raisin;
- ICP MS/OES/AES parameters: optimize mass spectrometer settings and plasma conditions.

Chapter 8
Summary and concluding remarks

8.1. Ferrihydrite characterization

Ferrihydrite physical and chemical characterizations were done with a variety of conventional and high-resolution techniques looking at particle shape and size, aggregate size, surface area, composition, purity and surface charge properties.

Our results revealed that ferrihydrite is present as non-mono-dispersed spherical particles of 3-5 nanometers in size forming aggregates of 0.3-30 µm. The aggregate size is dependent on the ionic strength of the solution: a high ionic strength favours the formation of bigger aggregates. The ferrihydrite surface area in the present study was measured to be ~200m^2g^{-1}. This value is in accordance with other findings from the literature where the surface area can vary between 150 and 700 m^2g^{-1}. In addition, we found that different methods of synthesis, the way how individual steps for the ferrihydrite synthesis are carried out, as well as post synthesis washing and drying treatments, have a significant effect on ferrihydrite surface area. Important to note is the fact that, for the modelling the the adsorption of metals onto ferrihydrite in order to compare our data with the literature a surface area of 600 m^2g^{-1} was used.

The chemical characterization of the ferrihydrite surface concluded that the point of zero charge was 7.8, which implies that the ferrihydrite surface is negatively charged above this pH and positively charged below it. In addition, the ferrihydrite surface charge was independent of the ionic strength of the solution. Interestingly, we found that CO_2 adsorbs onto the ferrihydrite surface over the pH interval of 4 to 9, modifying its surface properties.

These findings helped further our understanding of the molybdenum and vanadium interactions with ferrihydrite via adsorption and co-precipitation: specifically the quantification of the adsorption/co-precipitation processes, the interaction mechanisms, the comparison between uptake capacities and removal efficiencies, as well as comparison between adsorption *vs.* co-precipitation uptake. Finally, we also assessed the effect other ions, organics and complex matrices have on the molybdenum and vanadium adsorption character.

8.2. Molybdenum and vanadium adsorption and co-precipitation

Molybdenum and vanadium adsorption studies were carried out in order to quantify the affinity of these elements for the ferrihydrite surface sites under different experimental conditions: *e.g.,* varying the pH, anion concentration, particle concentration, different matrices and also study the competition with other anions (*e.g.,* phosphate).

In all adsorption studies, the kinetic results showed that the adsorption of both elements was fast and reached equilibrium after 20-30 minutes.

The pH dependence adsorption experiments from a system with initial metal concentration of 100uM and ferrihydrite concentration of 0.1gL^{-1}, gave maximum uptake capacity of 0.999 mmol L^{-1} for molybdenum and vanadium at pH 4 and a minimum uptake capacity of 0.036 mmolL^{-1} for molybdenum and 0.609 mmolL^{-1} for vanadium. In other words, the results indicated that the adsorption efficiency for molybdenum was high at pH below 6 (90-100%) but decreased with increasing pH (i.e., pH 7 < 60 %, pH 8 < 20 % and pH 9 < 3%), while for vanadium the adsorption efficiency decreased to ~ 60 % only at pH 9, while below pH 7 the adsorption efficiency was 100%.

Monitoring the addition of base and acid during the adsorption of molybdenum and vanadium onto ferrihydrite at different pH values, we deduced that the mechanism of adsorption clearly changed with pH. This was the first time that this approach was taken for studying mechanistic related properties related to molybdenum and vanadium adsorption systems. The results showed that at low pH multi protonated anions were losing H^+ from their structure and are strongly bonded to the positively charged ferrihydrite surface forming *inner-sphere* complexes. Conversely, at high pH adsorption was low probably because of OH^- layers interposed between the negatively charge ferrihydrite surface and the molybdate and vanadate anions (as more base is required during adsorption) forming mostly *outer-sphere* complexes. We found consistent differences in the volume of acid and base added during the adsorption of the two anions onto ferrihydrite at low and high pH. This difference may be related to the anion size or valence, both parameters dictating the adsorption bonding environment. Based on these results and literature data, surface modelling was used to derive more information about the adsorption mechanism at this macro scale.

Our result from the particle concentration effect experiments on molybdenum and vanadium adsorption onto ferrihydrite, suggested that for a system with initial metal concentration of 100µM, the saturation ratio of metal to available binding sites was at

particle concentrations between 0.1 and 1g L^{-1} for molybdenum and above 2g L^{-1} for vanadium.

Typically is is assumed that particle concentration influences the uptake capacity as follows: high particle concentrations will lead to a higher uptake capacity, whereas a smaller number of particles will uptake less adsorbent. Equally, if metal concentration is high in an adsorption system, higher uptake is expected then at low metal concentrations. In theory, all these assumptions are valid only if the surface sites saturation approach which derive the optimum metal (adsorbent) or particles (adsorbant) concentrations at which all adsorption sites are occupied it taken into account.

In other words, a specific metal concentration as well as particle concentration is characteristic to each adsorbent - adsorbant system - concentrations at which surface sites are fully occupied. Assessing the values of these concentrations can only be achieved by varying metal or particle concentrations in different ranges or alternatively calculating the surface coverage of the adsorbent using known parameters like surface area, site density, particle size, *etc*. Our results showed that the second approach (i.e., surface coverage calculation) is not always the best way to calculate the surface saturation, because that it includes empirical parameters, which can be different from the practical ones (*e.g.,* surface area, site density) function by environmental conditions. Thus, theoretically at a particle concentration of 0.1gL^{-1}, a concentration of 100µM of molybdenum or vanadium (our fixed metal concentration) should have covered all ferrihydrite surfaces to saturation and 25% of the available molybdenum and vanadium still should be free. Conversely, at 1gL^{-1} and 2gL^{-1} only 13% and 7%, respectively of the surface sites should have been saturated/ covered. Practically, our results found that no molybdenum was left in the solution at 1 and 2 gL^{-1} and all vanadium was adsorbed from solution at concentration between 0.1 to 2 gL^{-1}. From these results we concluded that mathematical models are only an empiric way to estimate the adsorption potential and care should be taken at times with their interpretation.

By varying the matrices of the adsorption systems (*e.g.,* distilled water, seawater with organics and without organics) we found that molybdenum adsorption onto ferrihydrite from seawater with organics was enhanced by 30% comparing with molybdenum adsorbed from seawater without organics, whereas for vanadium no specific interactions with the organic content of the seawater could be noted. The results also showed 22% for molybdenum and 33% for vanadium less adsorption in the seawater experiments compared to all the experiments carried out in distilled water.

From all seawater constituents, phosphate was the only one which we studied closely as a competitive anion for molybdenum and vanadium sorption onto ferrihydrite surface sites. The results showed that phosphorus and vanadium compete equally for the ferrihydrite surface sites whereas, phosphorous outcompetes almost entirely molybdenum.

The comparison between adsorption *vs.* co-precipitation uptake capacities showed that: (i) vanadium was preferentially taken up compared with molybdenum at neutral pH (1.28 $mmol_V g^{-1}$ via adsorption and 3.36 $mmol_V g^{-1}$ via co-precipitation vs. 0.431 $mmol_{Mo} g^{-1}$ via adsorption and 2.48 $mmol_{Mo} g^{-1}$ via co-precipitation); (ii) both, molybdenum and vanadium were scavenged more efficiently via co-precipitation then via adsorption. The first finding was in accordance with the results from the pH effect studies, where vanadium has been found to have a higher affinity for ferrihydrite surface sites over a larger pH interval then molybdenum. The second finding was a surprising result, if it is accepted that ferrihydrite particle sizes are small and that its particle volume is much smaller than the surface area. However, this unexpected difference can be explained by the fact that in aqueous solutions ferrihydrite particles form big aggregates, and are non-mono-dispersed and ferrihydrite surface sites are not entirely accessible for metals to bind.

8.3. Adsorption modelling and simulation

Mechanistic information at the macroscopic scale were extracted from fitting the adsorption data to different kinetic modes as well as from simulation of the adsorption experiments with DLM surface complexation models.

The kinetic profiles of all adsorption experiments were modelled with a pseudo-second order kinetic model and adsorption comparison between weighted uptake capacities were thus possible. In addition, a very good fit of the data with a pseudo-second order kinetic model (the case of vanadium adsorption over the pH interval of 4-9 and molybdenum adsorption over pH interval 4-7) implies a chemical adsorption mechanism (or strong chemical bonds) whereas a poor fit (molybdenum sorption onto ferrihydrite at pH 8 and 9) implies a physical sorption mechanism (or weak electrostatic bonds).

Visual Minteq speciation modelling of molybdenum and vanadium allowed a better understanding of the adsorption mechanisms by deriving the types of complexes which these anions can form and how they are bound onto the ferrihydrite surface. The results showed that at pH 4-8 vanadium forms *inner-sphere* complexes via $H_2VO_4^-$ species (80-97%) on the ferrihydrite surface, while a maximum of 10% of other vanadium species (e. g., VO_4^{3-}; $HV_2O_7^{3-}$; VO^{2+} et al.,) are present in solution at most pH values. As pH increases, above 8, these complexes decrease quantitatively and aqueous divalent vanadate forms and complexes weakly with the neutrally and slightly negatively charged ferrihydrite surface (PZC 7.8, see ferrihydrite surface charge characterization). 100% of the molybdenum in solution is present as MoO_4^{2-} (molybdate) at pH 6 to 10 and this will all bind to the available ferrihydrite surface sites, while at pH 5, only 85% of the molybdenum is present as molybdate while 13% is present as $HMoO_4^-$ and 2% as MoO_3 (molybdenum trioxide) three hydrated. The data showed that molybdenum can be adsorbed onto the ferrihydrite surface as molybdate via *outer-sphere* complexes.

The pH dependennt adsorption experimental data were also simulated with the DLM model in the Visual MINTEQ 2.32 software. The comparison between the results from the practical experiments with the DLM simulation outputs, revealed interestingly that for the molybdenum systems the simulation outputs, expressed either (i) as molybdenum uptake onto ferrihydrite surface or (ii) as its removal efficiency from the solution agreed well, whereas for the vanadium system some differences were found. Vanadium uptake predicted from adsorption simulation was ~ 5 times higher than the experimentally obtained uptake capacitiy. Thus, removal efficiencies measured experimentally were ~40% higher than the removal efficiencies predicted by the simulations. We argue that these

differences may be due to incomplete database information, incorrect intrinsic constants for specific species in the databases or differences in practical *vs.* theoretical adsorbent parameters (*i.e.,* surface area, surface site densities, dissociation constants, etc). From our findings we can conclude that it is very important to check the validity of the database with regard to each element species, parameters and constants before simulating processes or modelling any elemental speciation.

Finally, the adsorption experimental results were scaled up to different realistic environments via interpolation and by plotting various combinations of three parameters which influenced the adsorption (*e.g.,* pH, uptake capacity and particles concentration or pH, particles concentration and metal concentration) in 3D with the Origin Pro 8 software. As an example, to transpose the molybdenum and vanadium maximum adsorption capacities onto ferrihydrite from a fresh water environment (with ionic strength 0.1) at pH 7 to a seawater environment (ionic strength 0.7 and pH 8) showed that up to 22% for molybdenum and 33% for vanadium need to be added to achieve the maximum uptake capacities corresponding to fresh water system at pH 7 (1.28 $mmolg^{-1}$ for molybdenum and 0.431 $mmolg^{-1}$for vanadium). In addition, 36% for molybdenum and 5% for vanadium need to be subtracted to take into account the pH difference (from 7 to 8).

The adsorption kinetic modelling and surface complexation simulation gave a macroscopic view of the mechanism of molybdenum sorption onto ferrihydrite at pH 8 (e.g., physical sorption mechanism - forming mostly *outer-sphere* types of complexes with ferrihydrite surface sites via hydrogen bonds or electrostatic long-range Coulumbic forces). Conversely, the XAS studies on the speciation of molybdenum associated with solid phases were able to give a molecular scale view of the sorption mechanism.The XAS results showed that molybdenum taken up by ferrihydrite via adsorption as well as via co-precipitation was tetra coordinated surrounded by four oxygen atoms at a distance of 1.75Å. These findings suggested that molybdenum is bonded to ferrihydrite surface sites as molybdate, as an *outer-sphere* complex. These results are supported by the adsorption simulation outputs, which showed that molybdenum in the system at pH 8 was found to be a combination of free molybdate in solution and as >$FeOHMoO_4^{2-}$ *outer-sphere* complexes. In addition, again, the pseudo second order kinetic modelling of the pH dependency showed a poor fit for the adsorption of molybdenum to ferrihydrite at pH 8 (R=0.668). The assumptions which the model has (a very good fit of the adsorption data with a pseudo-second order model and adsorption by chemo sorption) means that the adsorption mechanism in such conditions is most likely to be physical type - driven by weak electrostatic forces – a fact confirming the outer-sphere complex nature of the interactions.

Moreover, potentiometric titration results, which showed that at pH close to the PZC (7.8) the ferrihydrite surface is almost neutrally charged, and this again supports the fact that *outer-sphere* complexes are favored.

8.4. The fate of molybdenum and vanadium during ferrihydrite transformation to hematite.

Solid and solution quantitative assessment of the distribution of molybdenum and vanadium in the transformation end-product hematite were carried out, in order to calculate the potential of these elements to be sequestered and immobilised in the hematite structure.

The partitioning results showed that at pH 8 most of the molybdenum (>90%) and vanadium (>95%) which are scavenged via co-precipitation and adsorption become sequestered into the hematite structure.

In accordance with the partitioning data, XAS results confirmed that molybdenum was sequestered into the hematite structure. The, XAS results showed that molybdenum most likely replaces octahedrally coordinated iron in the hematite structure. Unfortunately the circumstances did not allow XAS measurements for the vanadium samples, and thus the full evaluation of the molecular level binding environment of vanadium in the hematite structure remains still open for future research.

These results have important implications on molybdenum and vanadium budgets in different environments where they are present and where they may interact with ferrihydrite. As an example, hydrothermal vent activities at mid ocean ridges create an enrichment gradient of molybdenum and vanadium in the plume and more specifically at the sediment level. The fact that molybdenum and vanadium are sequestered and enriched at the sediment level has important implications in controlling the availabilities and the cycles of these elements in the oceans. In the upper water column, where such interactions may also occur with terrestrial inputs, the scavenging of molybdenum and vanadium (which are limiting micronutrients for the metabolic and enzymatic processes of zooplankton) will also affect the metal cycling.

The partitioning results revealed new interesting questions with regard to the time scales of such elemental sequestration. However, the kinetic and thermodynamic approaches elucidated in part the effects of molybdenum, pathways and vanadium taken up by ferrihydrite on the stability and transformation mechanism provided insights in the time scale frame required for these elements to be immobilised into the hematite structure.

8.5. Molybdenum and vanadium effect on ferrihydrite transformation kinetic and thermodynamic

The ferrihydrite transformation to hematite, in the presence and the absence of molybdenum and vanadium were evaluated in *in situ* simulated hydrothermal system conditions, using synchrotron ED-XRD technique.

The kinetic models used revealed important parameters from the fitting of our experimental results which suggested that: (i) ferrihydrite transformation to hematite is strongly dependent on temperature and ionic strength; (ii) ferrihydrite transformation at pH 8 occurs via dehydration and/or rearrangement mechanisms, (iii) molybdenum and vanadium associated with ferrihydrite affect the transformation kinetic but not its pathway. Although low temperatures will slow down the transformation of ferrihydrite to hematite, a high ionic strength (i.e, seawater) speeds up the transformation by enhancing the aggregation (the surface layer and the diffuse layer of counter-ions in solution create a high surface charge density allowing particles to combine).

Interestingly, the presence of molybdenum and vanadium in the ferrihydrite structure retarded the formation of the hematite. This effect seems to be correlated with the size and the valence of the anion. Vanadium (tri-valent) retards the hematite formation by slightly more (6%) than molybdenum (di-valent) and this is clearly revealed in the longer induction time of the reactions.

The *in situ* data also allowed the evaluation of the apparent activation energy for hematite nucleation and crystallisation for all three systems studied. The results revealed that a slightly higher (ca. 30%) activation energy of nucleation is needed for the Mo- and V-systems to overcome the transformation barrier in comparison with the pure system. This result is in very good agreement with the above mentioned kinetic findings where molybdenum and vanadium delayed the transformation by prolonging the induction time of hematite formation.

Interestingly, the comparison between apparent activation energy of hematite crystallisation for all three systems calculated via the Arrhenius equation and also via “time to a given fraction method”, showed, for the first time, that both models are equally valid for mineral transformation thermodynamics.

Off-line transformation experiment of the ferrihydrite at 73°C indicated that ferrihydrite transforms to hematite with goethite as an intermediate phase and also that during the transformation the pH pf the system decreased supporting the findings from the

in-situ experiments about the fact that the transformation occurs with OH^- consumption / H^+ production. This is one of the important and original result of this project, yet further transformation experiments at different temperatures with known amounts of ferrihydrite and solid to solution ratios in which the pH would be constantly monitored could help elucidate a more accurate stoichiometry of the transformation reaction.

Our kinetic and energetic results of the ferrihydrite transformation to hematite play an important role in quantifying the time scale of molybdenum and vanadium sequestration from environments where ferrihydrite forms and scavenges them via co-precipitation. As example, these results can contribute to quantifing the impact of the molybdenum and vanadium scavenging at deep sea hydrothermal vents/plumes and its effect on metal cycles and their retention times in the ocean. Furthermore, in terrestrial settings, these results can also be applied to soil and wastewater remediation applications.

8.6. Molybdenum and vanadium pre-concentration from seawater matrix.

Molybdenum and vanadium determination in seawater, is most of the time (as their concentration is very low) a difficult task to do with ICP techniques because of interferences. Therefore, pre-concentration methods onto different ion exchange resins were tested as a useful intermediary step. We carried out preliminary studies on a cationic ion exchange resin, called Toyopearl 650M, to pre-concentrate molybdenum and vanadium from an enriched seawater matrix. The results showed that the Toyopearl 650M resin is a promising substrate for both anions to pre-concentrate them from seawater. Molybdenum is concentrated slightly more efficiently than vanadium: 0.22mmolg^{-1} *vs.* 0.15mmolg^{-1}.

However there are numerous studies which could be recommended for future work, to make this analytical technique applicable. From the pre-concentration point of view, run of pre-concentration tests with low molybdenum and vanadium concentrations in seawater and use of various eluents (i.e., perchloric acid and ammonium hydroxide for sequential extraction of the different species of vanadium) are few suggestions which could be done before optimising the process (e.g., running standards to determine the precision and accuracy and detection limits). In addition, further studies on building a flow injection system (on line column pre-concentration unit) and its optimization would be another suggestion for future work.

References

Abbasse G, Ouddane B, Fischer JC. 2002. Determination of trace levels of dissolved vanadium in seawater by use of synthetic complexing agents and inductively coupled plasma-atomic emission spectroscopy (ICP-AES). Analytical and Bioanalytical Chemistry 374:873-878.

Avrami M. 1939. Kinetics of phase change. I General Theory. Journal of Chemical Physics 7:1103 - 1112.

Avrami M. 1940. Kinetics of Phase Change. II Transformation-Time Relations for Random Distribution of Nuclei. Journal of Chemical Physics 8:212-224.

Avrami M. 1941. Granulation, Phase Change, and Microstructure Kinetics of Phase Change. III. Journal of Chemical Physics 9:177.

Bao H, Koch PL. 1999. Oxygen isotope fractionation in ferric oxide-water systems: Low temperature synthesis. Geochimica et Cosmochimica Acta 63(5):599-613.

Belova DA, Lakshtanov LZ, Stipp SLS. 2008. Experimental study of Ni adsorption on chalk: preliminary results. Mineralogical Magazine 72(1):377-379.

Bennett AJ. 2005. Relationship between gold and arsenic in hydrothermal pyrite: experimental results and applications to submicroscopic gold in massive sulphide deposits. Leeds: The University of Leeds. 231 p.

Bethke CM. 2002. The Geochemist`s Workbench - A User`s Guide to Rxn, Act2, React, and Gtplot. Version Release 4.0. University of Illinois.

Binstead N. 1998. EXCURV98: CCLRC Daresbury Laboratory computer program.

Bosch J, Heister K, Hofmann T, Meckenstock RU. 2010. Nanosized Iron Oxide Colloids Strongly Enhance Microbial Iron Reduction. Applied and Environmental Microbiology 76(1):184-189.

Bradl HB, editor. 2005. Individual behaviour of selected heavy metals, Heavy metals in the environment: origin, interaction and remediation: Elsevier Academic Press. 124-125 p.

Brinza L, Benning LG, Statham PJ. 2008. Adsorption studies of Mo and V onto ferrihydrite. Mineralogical Magazine 72(1):107-110.

Brinza L, Dring MJ, Gavrilescu M. 2005. Biosorption of Cu (2+) ions from aqueous solution by-Enteromorpha sp. Environmental Engineering and Management Journal 4(2):41-51.

Brinza L, Gavrilescu M. 2003. pH effect on the biosorpion of Cu2+ from aqueous solution by *Saccharomyces Cerevisiae*. Environmental Engineering and Management Journal 2(3):243-254.

Brown GE, Henrich VE, Casey WH, D. L. Clark, Eggleston C, Felmy A, D. W. Goodman ea. 1999. Metal oxide surface and their interaction with aqueous solutions and microbial organisms. Chemistry Reviews 99:77-174.

Brunauer S, Emmett PH, Teller E. 1938. Adsorption of gases in multimolecular layers. Journal of American Chemical Society 60:309-319.

Bunker G. 2005. Elements of XAFS. Physics Department, Illinois Institute of Technology, Chicago, Illinois pAPS XAFS School, July 26-29, 2005.

Cahn JW. 1956. The kinetics of grain boundary nucleated reactions. Acta Metallurgica 4(5):449.

Carvahlo FMS, Abrao A. 1997. Sorption and desorption of molybdenum in alumina microspheres. Jurnal of Radioanalitical and Nuclear Chemistry 218(2):259-262.

Cheary RW, Coelho AA. 1996. Programs XFIT and FOURYA deposited in CCP14 Powder Diffraction Library, Engineering and Physical Sciences Research Council, Daresbury Laboratory. Warrington, England.

Chester R. 1990. Marine Geochemistry. London: Unwin Hyman Ltd.

Cornell RM, Schwertmann U. 2000. The Oxides in the Laboratory. Weinheim: Wiley-VCH.

Cornell RM, Schwertmann U. 2003. The Iron Oxides: Structure, Proprieties, Reactions, Occurances and Uses. Weinheim: Wiley-VCH GmbH&KGaA.

Crawford RJ, Harding IH, Mainwaring DE. 1996. The Zeta potential of iron and chromium hydrous oxides during adsorption and coprecipitation of aqueous heavy metals. Journal of Colloid and interface science 181:561–570.

Croker D, Loan M, Hodnett BK. 2009. Kinetics and Mechanisms of the Hydrothermal Crystallization of Calcium Titanate Species. Crystal Growth Design 9(5):2207-2213.

Cruz CC, Costa ACD, Henriques CA, Luna AS. 2004. Kinetic modeling and equilibrium studies during cadmium biosorption by dead Sargassum sp. biomass. Bioresour Technollogy 91:249-257.

Cudennec Y, Lecerf A. 2006. The transformation of ferrihydrite into goethite or hematite, revisited. Journal of Solid State Chemistry 179:716–722.

Davidson LE, Shaw S, Benning LG. 2008. The kinetics and mechanisms of schwertmannite transformation to goethite and hematite under 2 alkaline conditions. American Mineralogist 93:1326-1337.

Dent AJ, Mosselmans JFW. 2003. An introduction to EXCALIB. EXAFS for beginers Course. Daresbury Laboratory, UK.

Dyer JA, Trivedi P, Scrivner NC, Sparks DL. 2003. Lead sorption onto ferrihydrite. 2. Surface complexation modeling. Environmental Science Technology 37:915-922.

Dyer JA, Trivedi P, Scrivner NC, Sparks DL. 2004. Surface complexation modeling of zinc sorption onto ferrihydrite. Journal of Colloid and Interface Science 270:56–65.

Dzombak DA, Morel FMM. 1990. Surface Complexation Modeling: Hydrous Ferric Oxide: A Wiley Intersciences Publications.

Ellis P. 1995. EXSPLINE-a program for EXAFS background subtraction. CCLRC Daresbury Laboratory.

Feely RA, Trefry JH, Lebon GT, German CR. 1998. The relationship between P/Fe and V/Fe ratios in hydrothermal precipitaes and dissolved phosphate in seawater. Geophisical Research Letters 25(13):2253-2256.

Ferreira SLC, dosSantos HC, Costa ACS, delaGuardia M. 2004. Procedures of separation and preconcentration for molybdenum determination using atomic spectrometry—a review. Applied Spectroscopy Reviews 39(4):457–474.

Ferreira SLC, Queiroz AS, Fernandes MS, Santos HCd. 2002. Application of factorial designs and Doehlert matrix in optimization of experimental variables associated with the preconcentration and determination of vanadium and copper in seawater by inductively coupled plasma optical emission spectrometry. Spectrochimica Acta Part B 57:1939–1950.

Ferreira SLC, Santos HCd, Jesus DSd. 2001. Molybdenum determination in iron matrices by ICP-AES after separation and preconcentration using polyurethane foam. Fresenius J Anal Chem 369:187–190.

Field MP, Sherrell RM. 2000. Dissolved and particulate Fe in a hydrothermal plume at 9°45*N, East Pacific Rise: Slow Fe (II) oxidation kinetics in Pacific plumes. Geochimica et Cosmochimica Acta 64(4):619–628,.

Fujiwara K, Morikawa T, Fuwa K. 1986. Determination of molybdenum and vanadium in seawater by carbon furnace atomic-absorption spectrometry with metal chelate coprecipitation. Bunseki Kagaku 35(4):361-367.

Furnace RW, Rainbow PS. 1990. Heavy metals in the Marine Environments. Boca-Raton, FL: CRC Press.

German CR, Bourles DL, Brown ET, Hert J, Colley S, Higgs NC, Ludford EM, Nelsen TA, Feely RA, Raisbeck G and others. 1997. Hydrothermal scavenging on the Juan de

Fuca Ridge: Evidence from ridge-flank sediments Geochimica Cosmochimica Acta 61(19):4067-4078.

German CR, Colley S, Palmer MR, Khripounoff A, Klinkhammer GP. 2002. Hydrothermal plume - particle fluxes at 13N on the East Pacific Rise. Deep-Sea Research I 49(11):1921-1940.

German CR, Sparks RSJ. 1993. Particle recycling in the TAG hydrothermal plume. Earth and Planetary Science Letters 116:129-134.

Goldberg S, Lesch SM, Suarez DL. 2002. Predicting molybdenum adsorption by soils using soil chemical parameters in the constant capacitance model. Soil Science Society American Journal 66:1836–1842.

Golden. 2002. Surfer - Surface Mapping System. Version 8.01. Colorado.

Greenfield S, Durrani TM, Kaya S, J.F.Tyson. 1989. Pre-concentration of refractory elements for inductively coupled plasma atomic-fluorescence spectrometry. Analytical Proceedings 26(11):382-384.

Gustafsson JP. 2003. Modelling molybdate and tungstate adsorption to ferrihydrite. Chemical Geology 200:105– 115.

Gustafsson JP. 2005. Visual MINTEQ. Version 2.32. Stockholm, Sweden: KTH.

Haese RR. 2000. The reactivity of iron. Schultz HD, Zabel M, editors. Verlag Berlin Heidelberg: Springer. 233-261 p.

Hanson G, Szabo A, Chasteen ND. 1977. Determination of Molybdenum in Seawater by Electron Paramagnetic Resonance Spectrometry. Analytical Chemistry 49(3):461-463.

Hartzog OK, Loganathan VA, Kanel SR, Jeppu GP, Barnett MO. 2009. Normalization, comparison, and scaling of adsorption data: arsenate and goethite. J Colloid Interface Sci 333(1):6-13.

Herrero R, Cordero B, Lodeiro P, Rey-Castro C, SastreDeVicente ME. 2006. Interactions of cadmium(II) and protons with dead biomass of marine algae *Fucus sp*. Marine Chemistry 99(1-4):106-116.

Hiemstra T, Riemsdijk WHV, Rossberg A, Ulrich K-U. 2009. A surface structural model for ferrihydrite II: Adsorption of uranyl and carbonate. Geochimica et Cosmochimica Acta 73(15):4437-4451.

Hirata S, Ishida Y, Aihara M, Honda K, Shikino O. 2001. Determination of trace metals in seawater by on-line column preconcentration inductively coupled plasma mass spectrometry. Analytica chimica acta 438(1-2):205-214.

Hongshao Z, Stanforth R. 2001. Competitive adsorption of phosphate and arsenate on goethite. Environmental Science and Technology 35,:4753-4757.

Hulbert SF. 1969. Models of solid-state reactions in powder compacts: A review. Journal of the British Ceramics Society 6:11-20.

Jambor JL, Dutrizac JE. 1998. Occurrence and constitution of natural and synthetic ferrihydrite, a widespread iron oxyhydroxide. Chemical Reviews 98(7):2549-2586.

Janney DE, Cowley JM, Buseck PR. 2000a. Transmission electron microscopy of synthetic 2- and 6-line ferrihydrite. Clays and Clay Minerals 48(1):111–119.

Janney DE, Cowley JM, Buseck PR. 2000b. Structure of synthetic 2-line ferrihydrite by electron nanodiffraction. American Mineralogist 85:1180–1187.

Jentzsch TL, Penn RL. 2006. Influence of Aluminum Doping on Ferrihydrite Nanoparticle Reactivity. Journal of Physical Chemistry B 110(35):11746-11750.

Jin L, Wu D, Ni Z. 1987. Determination of lead, cadmium, cobalt, copper, tin, arsenic and molybdenum in sea-water and biological samples by graphite-furnace atomic-absorption spectrometry after pre-separation and pre-concentration with APDC [ammonium pyrrolidine-1-carbodithioate] precipitation. Huaxue Xuebao 45(8):808-812.

Jolivet J-P, Chaneac C, Tronc E. 2004. Iron oxide chemistry. From molecular clustters to extended solid networks. Chemistry Communications 5:481-487.

Jolyon R. 2009. Mineral database website (http://www.mindat.org/min-1493%20html). Jolyon & Ida Ralph

Kersten M, Vlasova N. 2009. Arsenite adsorption on goethite at elevated temperatures. Applied Geochemistry 24(1):32-43.

Khawam A, Flanagan DR. 2006. Solid-State Kinetic Models: Basics and Mathematical Fundamentals. Journal of Physical Chemistry B 110(35):17315–17328.

Kodre A, Arčon I, Gomilšek JP. 2004. X-ray absorption spectroscopy and related techniques. Acta Chim. Slov. 51:1-10.

Kooner ZS. 1993. Comparative study of adsorption behavior of copper, lead, and zinc onto goethite in aqueous systems. Environmental Geology 21:242-250.

Kuo S, editor. 1996. Phosphorus. WI, USA: Soil Science Society of America, Inc, Madison. 869-919 p.

Langmuir D. 1997. Aqueous Environmental Geochemistry New Jersey: Prentice Hall, Inc.

Langmuir I. 1916. The constitution and fundamental properties of solids and liquids. Journal of American Chemical Society 38:2221-2295.

Lilley MD, Feely RA, Trefry JH, editors. 1995. Chemical and biochemical transformation in hydrothermal plumes. Washington: American Geophysical Union. 369-391 p.

Lin X, Burns RC, Lawrance GA. 2003. Effect of cadmium (II) and anion type on the ageing of ferrihydrite and its subsequent leaching under neutral and alkaline conditions. Water, Air and Soil Pollution 143:155-177.

Liu H, Guo H, Li P, Wei Y. 2008. The transformation of ferrihydrite in the presence of trace Fe(II): The effect of the anionic media. Journal of Solid State Chemistry 181(10):2666-2671.

Liu H, Li P, Zhu M, Wei Y, Sun Y. 2007. Fe(II)-induced transformation from ferrihydrite to lepidocrocite and goethite. Journal of Solid State Chemistry 180(7): 2121-2128.

Loan M, Parkinson GM, Richmond WR. 2005. The effect of zinc sulfide on phase transformations of ferrihydrite. American Mineralogist 90:258–261.

MalvernLab. 2000. Mastersizer 2000- Integrated systems for particle sizing.

Metz S, Trefry JH. 1988. Scavenging of vanadium by Iron Oxides in Hydrotermal Plumes. Eos 69(44):148.

Michel FM, Ehm L, Antao SM, Lee PL, Chupas PJ, Liu G, Strongin DR, Schoonen MAA, Phillips BL, Parise JB. 2007. The Structure of Ferrihydrite, a Nanocrystalline Material. Science 316(5832):1726-1729.

Naeem A, Westerhoff P, Mustafa S. 2007. Vanadium removal by metal (hydr)oxide adsorbents. Water Research 41(7):1596-1602.

Newville M. 2008. Fundamentals of XAFS. University of Chicago, Chicago, Illinois. p http://xafs.org/Tutorials.

Ofer R, Yerachmiel A, Shmuel Y. 2004. Mechanism of biosorption of different heavy metals by brown marine macroalgae. Biotechnology and bioengineering 4:451-458.

OriginLab. 2007. Origin Pro. Version 8. Northampton, USA.

Parise JB, editor. 2000. Synchrotron studies of phase transformations. Transformation Processes in Minerals Chantilly, Virginia: Mineralogical Society of America. 318 p.

Pichler T, Veizer J. 1999. Precipitation of Fe(III) / oxyhydroxide deposits from shallow-water hydrothermal fluids in Tutum Bay, Ambitle Island, Papua New Guinea. Chemical Geology 162:15-31.

Polihrohiade A. 1967. Absorbtia - Adsorbtia. Polihrohiade A, editor. Bucuresti: Editura Tehnica.

Poulton SW, Raiswell R. 2002. The low temperature geochemical cycle of iron: from continental fluxes to marine sediment deposition. American Journal of Science 302:774–805.

Punnoose A, Phanthavady T, Seehra MS, Shah N, Huffman GP. 2004. Magnetic properties of ferrihydrite nanoparticles doped with Ni, Mo, and Ir. Physical Review B (69):054425 1-9.

Putnis A. 1992. Introduction to mineral sciences: Cambridge University Press. 457 p.

Raiswell R, Tranter M, Benning LG, Siegert M, D'Death R, Huybrechts P, Payne T. 2006. Contributions from glacially-derived sediment to the global iron (oxyhydr)oxide cycle: Implications for iron delivery to the oceans. Geochimica et Cosmochimica Acta 70(11):2765-2780.

Rentz JA, Turner IP, Ullman JL. 2009. Removal of phosphorus from solution using biogenic iron oxides. Water Research 43(7):2029 - 2035.

Sannino F, De Martino A, Pigna M, Violante A, Di Leo P, Mesto E, Capasso R. 2009. Sorption of arsenate and dichromate on polymerin, Fe(OH)(x)-polymerin complex and ferrihydrite. Journal of Hazardous Materials 166(2-3):1174-1179.

Sarkar D, Essington ME, Misra KC. 2000. Adsorption of Mercury(II) by Kaolinite. Soil Science Society America Journal 64(6):1968-1975.

Schaller T, Moor HC, Wehrli B. 1997. Reconstructing the iron cycle from the horizontal distribution of metals in the sediment of Baldeggersee. Aquatic Science 59:326–344.

Scheinost ASC, Bend S, Pandya KI, Sparks DL. 2001. Kinetic controls on Cu and Pb sorption by ferrihydrite. Environmental Science and Technology 35:1090-1096.

Schwertmann U, Friedl J, Stanjek H. 1999. From Fe(III) ions to ferrihydrite and then to hematite. Journal of colloid and interface science 209(1):215-223.

Schwertmann U, Murad E. 1983. Effect of pH on formation of goethite and hematite from ferrihydrite. Clays and Clay Minerals 31(4):277-284.

Shaw S, Pepper SE, Bryan ND, Livens FR. 2005. The kinetics and mechanisms of goethite and hematite crystallization under alkaline conditions, and in the presence of phosphate. American Mineralogist 90:1852.1860.

Shieh C-S, Duedall IW. 1988. Role of amorphous ferric oxyhydroxide in removal of anthropogenic vanadium from seawater. Marine Chemistry 25(2):121-139.

Spadini L, Schindler PW, Charlet L, Manceau A, Ragnarsdottir KV. 2003. Hydrous ferric oxide: evaluation of Cd–HFO surface complexation models combining CdK EXAFS data, potentiometric titration results, and surface site structures identified from mineralogical knowledge. Journal of Colloid and Interface Science 266:1–18.

Statham PJ, German CR, Connelly DP. 2005. Iron (II) distribution and oxidation kinetics in hydrothermal plumes at the Kairei and Edmond vent sites, Indian Ocean. Earth and Planetary Science Letters 236:588– 596.

Stumm W, Morgan JJ. 1996. Aquatic chemistry: Chemical equilibria and rates in natural waters. New York: John Wiley & Sons, INC. 1022 p.

Sumoondur A, Shaw S, Ahmed I, Benning LG. 2008. Green rust as a precursor for magnetite: an *in situ* synchrotron based study. Mineralogical Magazine 72(1):201-204.

Sunda WG, editor. 2000. Bioavailability and bioaccumulation of iron in the sea, The biogeochemistry of Iron in Seawater. New York: John Wiley & Sons Ltd. 41-78 p.

Ting YP, Mittal AK. 1999. An evaluation of equilibrium and kinetic models for gold biosorption. Res. and Environ. Biotechnology 2:311-326.

Tobler DJ. 2008. Molecular pathways of silica nanoparticle formation and biosilicification. Leeds: University of Leeds. 259 p.

Trefry JH, Metz S. 1989. Role of hydrothermal precipitates in the geochemical cycling of vanadium. Letters to Nature 432:531-534.

Trivedi P, Dyer JA, Sparks DL. 2003. Lead sorption onto ferrihydrite. 1. A macroscopic and spectroscopic assessment. Environmental Science Technology 37:908-914.

Trivedi P, Lisa A. 2001. Ni and Zn sorption to amorphous versus crystalline iron oxides : Macroscopic studies. Journal of Colloid and Interface Science 244:221-229.

Tuner DR, Hunter KA. 2001. The Biogeochemistry of Iron in Seawater. England: John Wiley &Son Ltd.

Viollier E, Inglett PW, Hunter K, Roychoudhury AN, Cappellen PV. 2000. The ferrozine method revisited: Fe(II)/Fe(III) determination in natural waters. Applied Geochemistry 15:785 - 790.

Volesky B. 2004. Sorption and Biosorption. Montreal, Canada. p 320.

Volesky B, Holan ZR. 1995. Biosorption of heavy metals. Biotechnology Progress 11:235-250.

Vu HP, Shaw S, Brinza L, Benning LG. 2010. Crystallization of hematite (a-Fe2O3) under alkaline condition: the effects of Pb. Crystal Growth and Design Crystal Growth and Design 10(4):1544–1551.

Wang D, Sañudo-Wilhelmy SA. 2008. Development of an analytical protocol for the determination of V (IV) and V (V) in seawater: Application to coastal environments. Marine Chemistry 112:72-80.

Warnken K, Tang D, Gill G, Santschi P. 2000. Performance optimization of a commercially available iminodiacetate resin for the determination of Mn, Ni, Cu, Cd and Pb by on-line preconcentration inductively coupled plasma-mass spectrometry. Analytica Chimica Acta 423(2):265-276.

Waychunas GA, Fuller CC, Davis JA. 2002. Surface complexation and precipitate geometry for aqueous Zn(II) sorption on ferrihydrite I: X-ray absorption extended fine structure spectroscopy analysis. Geochimica et Cosmochimica Acta 66(7):1119-1137.

Waychunas GA, Fuller CC, Rea BA, Davis JA. 1996. Wide angle X-ray scattering (WAXS) study of “two-line” ferrihydrite structure: Effect

of arsenate sorption and counterion variation and comparison with EXAFS results. Geochimica et Cosmochimica Acta 60(10):1765-1781.

Wen X, Du Q, Tang H. 1998. Surface Complexation Model for the Heavy Metal Adsorption on Natural Sediment. Environmental Science & Technology 32(7):870-875.

Willie S, Ilda Y, McLaren J. 1998. Determination of Cu, Ni, Zn, Mn, Co, Pb, Cd, and V in seawater using flow injection ICP-MS. Atomic spectroscopy 19(3):67-72.

Yee N, Shaw S, Benning LG, Nguyen TH. 2006. The rate of ferrihydrite transformation to goethite via the Fe(II) pathway. American Mineralogist 91:92-96.

Zhang F, Du F-s. A model for prediction of phase transformation

during quenching of steel; 2008; Shanghai, China. IEEE Computer Society.

Zhao J, Feng Z, Huggins FE, Shah N, Huffman GP, Wender I. 1994. Role of molybdenum at the iron oxides surface. Journal of Catalisys 148:194-197.

Appendix A. (for Chapter 4)

Ferrihydrite behavior in different ionic strengths at pH 4 and 25ºC

Due to the fact that solubility of iron decreases considerably at low pH values few simple experiments were run to test ferrihydrite solubility at ionic strength of 1, 0.1 and 0.001 N , pH 4 and T = 25ºC.

Three samples of ferrihydrite slurries ($0.1gL^{-1}$) at three ionic strengths (0.01; 0.1 and 1) were titrated to pH 4 and kept closed on a bench at room temperature in static regime. After 30 days the slurries were filtrated and analyzed with XRD to assess the room temperature reaction progress.

The results are presented in the figure below.

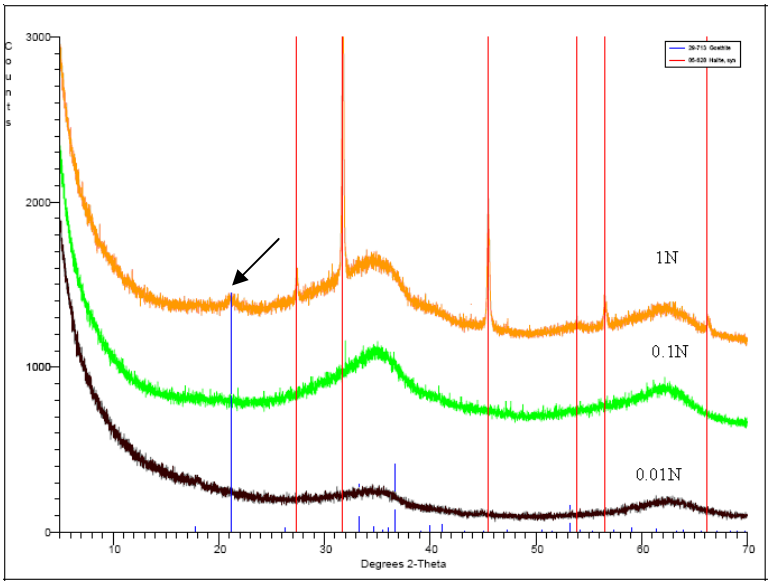

Figure A4.1. XRD pattern showing the transformation of ferrihydrite at different ionic strengths and pH 4. The blue line shows goethite whereas the orange lines shows the halite peaks (halite appeared as result of drying effect of the sample with ionic strength of 1). Lines are scaled to peak intensities.

At low ionic strength (0.01N) ferrihydrite dissolves and re-precipitates forming goethite – with the predominant peak showed by the arrow in Figure A4.1. At high ionic strength the process is faster due to the decrease in the Stern layer which enhances the formation of goethite needles.

Various outputs of empirical adsorption simulation with the MINTEQA2 software

Recently, a newer version of the database (last update on 16.01.2009), called M4-feo-dlm.vdb was found. Comparing the data from the old database (feo-dlm.mdb) and the new database for the MINTEQA2 software (M4-feo-dlm.vdb.) huge differences in the intrinsic values (log K) of the "=FehOHVO$_4^{-3}$" and the "=FeHHVO$_4^{-3}$" were found (from -0.73 to -16.63). Replacing the old intrinsic constant (-0.73) with the new value (-16.63), the amount of the adsorbed species in the output significantly decrease (12 orders of magnitude smaller). Unfortunately, the data base did not specify the source of these constants were taken from. However it can be concluded that the variations in intrinsic constant (ca 20 times smaller) have a major effect on the adsorption modeling with respect to the surface associated species. Further research could be done in this respect to find and establish the correct constant (for the vanadium system) and reconsider the adsorption simulation.

For the molybdenum system, small difference (23.5% smaller) for the intrinsic constant of the main Mo-surface associated specie (=FeOHMoO$_4^{2-}$) between the "feo-dlm.mdb" database for the Visual MINTEQ 2.32 code and the "M4-feo-dlm.vdb" database for the MINTEQA2 software resulted in only 7.5% lees of the total amount of molybdenum adsorbed species, after some of the =FeOHMoO$_4^{2-}$ specie.

Table A4.1. Influence of log $K_{FeOMoO42-}$ on the distribution and quantification of molybdenum – surface associated species during the adsorption onto ferrihydrite at pH 7.

Species	**Database: "feo_dlm_vdm" log K for $FeOMoO_4^{2-}$ = 3.14**	**Database: "feo_dlm_vdm" updated with log K from "M4_feo_dlm_mdb" log K for $FeOMoO_4^{2-}$ = 2.4**
	Concentration (M)	Concentration (M)
$=FeHO^-$	7.83E-08	1.47E-07
$=FeHOH_2^+$	1.74E-06	1.31E-06
$=FeHOHMoO_4^{-2}$	7.28E-07	4.31E-07
$=FeHOMo(OH)_5$	6.43E-07	8.38E-07
$=FeO^-$	3.13E-06	5.89E-06
$=FeOH_2^+$	6.94E-05	5.22E-05
$=FeOHMoO_4^{-2}$	2.91E-05	1.72E-05
$=FeOMo(OH)_5$	2.57E-05	3.35E-05
=SOH	9.74E-05	1.16E-04
=SOHh	2.44E-06	2.90E-06
H^+	1.11E-07	1.11E-07
$H_2Mo_6O_{21}^{-4}$	4.54E-32	7.85E-32
$H_3Mo_8O_{28}^{-5}$	3.58E-43	7.43E-43
$HMo_7O_{24}^{-5}$	8.57E-36	1.62E-35
$HMoO_4^-$	5.58E-08	6.11E-08
$Mo_7O_{24}^{-6}$	5.09E-34	9.63E-34
$Mo_8O_{26}^{-4}$	6.17E-46	1.28E-45
$MoO_3(H_2O)_3(aq)$	5.02E-11	5.50E-11
MoO_4^{-2}	4.38E-05	4.79E-05
OH^-	1.12E-07	1.12E-07
Total adsorbed species	5.62E-05	5.2E-05

Modeling only the vanadium adsorption experiments at pH 7 using the "2-pk_a with the "Diffuse Layer Model" (which allowed the variation of the ferrihydrite surface area at different values: at 600 m^2g^{-1} and 200 m^2g^{-1}), revealed that at the same adsorption conditions, a decrease in surface area of three times lead to only a 0.4% decrease in the absorbed species (see below). Thus, although unexpected, the effect of the surface area on the surface associated species was not significant.

Table A4.2. Influence of surface area on the distribution and quantification of vanadium – surface associated species during the adsorption onto ferrihydrite at pH 7.

Species	**Modeled with SA=600m^2g^{-1} (HFO with DLM)**	**Modeled with SA=200m^2g^{-1} (2-pka with DLM)**
	Concentration (M)	Concentration (M)
$=FehO^-$	1.45E-08	1.45E-08
$=FehOH_2^+$	3.14E-06	3.15E-06
$=FehOHVO_4^{-3}$	1.05E-06	1.05E-06
$=FeO^-$	5.80E-07	5.78E-07
$=FeOH_2^+$	1.26E-04	1.26E-04
$=FeOHVO_4^{-3}$	4.21E-05	4.19E-05
=SOH	5.64E-05	5.64E-05
=SOHh	1.41E-06	1.41E-06
Total adsorbed species	4.31E-05	4.29E-05

A comparison between databases species revealed that both databases contained the same species with regards to vanadium, while for the molybdenum system along with the $=FeOHMoO_4^{2-}$ specie (which was present in both databases) the $FeOMo(OH)_5$ specie (log K = 17.96) from the “feo_dlm.mdb” database (used for Minteq Visual code) was replaced with $=FeMoO_4^-$ specie (log K = 9.5) in the “M4_feo_dlm.vdb” (used for MINTEQA2 code).

Suppressing the vanadium mono-valent specie, $H_2VO_4^-$, from the adsorption system at pH 7, for example, the concentration of the V-surface associated specie, $=FeOHVO_4^{-3}$, increased by 11% and the species like HVO_4^{-2} and $H_2V_2O_7^{-2}$ increased by 5 and 29 times respectively (see below). Thus, neither of these species could explain the big differences between the experimental results and modeling outputs.

Table A4.3. Influence of $H_2VO_4^-$ species suppression on the distribution and quantification of vanadium – surface associated species during the adsorption onto ferrihydrite at pH 7.

Species	HFO with DLM - all species considered	HFO with DLM - $H_2VO_4^-$
	Concentration (M)	Concentration (M)
$=FehO^-$	1.24E-08	5.87E-09
$=FehOH_2^+$	3.21E-06	3.47E-06
$=FehOHVO_4^{-3}$	1.08E-06	1.20E-06
$=FeO^-$	4.97E-07	2.35E-07
$=FeOH_2^+$	1.28E-04	1.39E-04
$=FeOHVO_4^{-3}$	4.32E-05	4.79E-05
=SOH	5.28E-05	3.77E-05
=SOHh	1.32E-06	9.44E-07
H^+	1.11E-07	1.11E-07
$H_2V_{10}O_{28}^{-4}$	5.22E-27	1.08E-19
$H_2V_2O_7^{-2}$	6.91E-07	2.01E-05
$H_2VO_4^-$	5.31E-05	NA
$H_3V_{10}O_{28}^{-3}$	1.21E-29	2.50E-22
$HV_{10}O_{28}^{-5}$	8.36E-24	1.72E-16
$HV_2O_7^{-3}$	2.91E-09	8.45E-08
$HV_4O_{13}^{-5}$	1.49E-13	1.25E-10
HVO_4^{-2}	1.29E-06	6.93E-06
OH^-	1.12E-07	1.12E-07
$V_{10}O_{28}^{-6}$	1.14E-23	2.34E-16
$V_2O_7^{-4}$	3.01E-13	8.73E-12
$V_4O_{12}^{-4}$	1.09E-09	9.20E-07
$V_4O_{13}^{-6}$	7.70E-17	6.49E-14
$V_5O_{15}^{-5}$	6.20E-13	2.81E-09
$V_6O_{18}^{-6}$	9.69E-17	2.37E-12
VO_2^+	7.33E-12	3.95E-11
VO_4^{-3}	6.98E-13	3.76E-12
Total adsorbed species	4.43E-05	4.91E-05

Appendix B. (for Chapter 6)

Results to support ED-XRD findings

Off line transformation experiment of ferrihydrite to hematite were carried out in order to check the presence of the intermediate product. 14h X-ray Diffraction scans were taken at different time scale so that accurate patterns could be collected and even small amount of goethite could be detected.

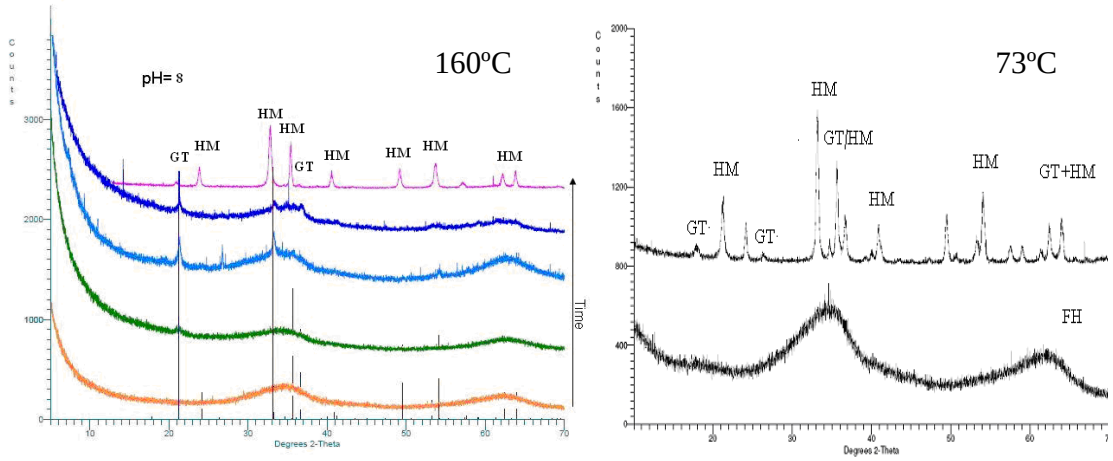

Figure A6.1. XRD patterns supporting the transformation of ferrihydrite to hematite: (A) from TEM imaging *off-line* experiments and (B) from pH recording *off line* experiment: initial and final product.

The XRD patterns presented in figure A6.1 indicate that during the ferrihydrite transformation to hematite at neutral pH, small amounts of goethite formed, but that the dominant process was the ferrihydrite conversion to hematite. The XRD results are in agreement with the FEG-TEM (Figure 6.2., Chapter 6) and in agreement with previous literature findings (Cornell and Schwertmann 2003; Schwertmann et al. 1999).

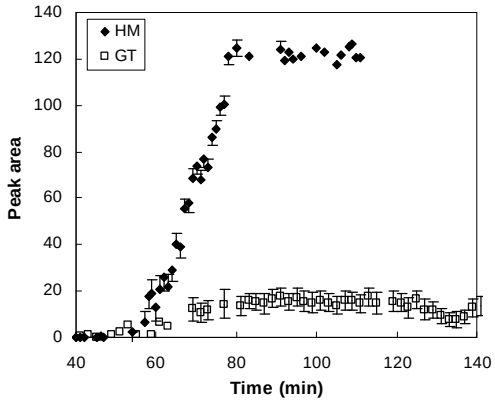

Figure A6.2. Hematite (110) and goethite (110) peak areas as function of time for the Mo-ferrihydrite system, at 140ºC and ionic strength 0.7.

Figure A6.2. shows that small proportions of goethite [GT (110)] formed along with hematite [HM (110)]. Note that from the peak area it can be concluded that goethite was a minor phase and (also note error) and that this peak fully disappeared at the end of the reaction with hematite remaining the sole end-product. The peak area of the goethite (110) peak was 7 times smaller, than that of the hematite (110) peak indicating that only small amounts of goethite formed as an intermediate in the reaction.

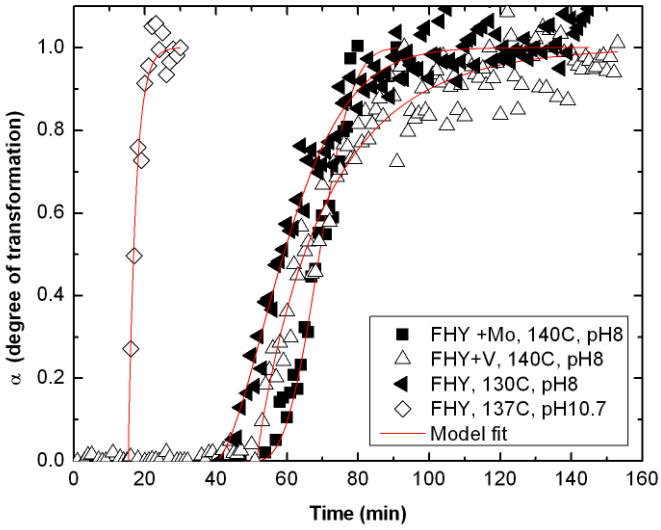

Figure A6.3. The degree of transformation as a function of time for pure ferrihydrite, Mo-ferrihydrite and V- ferrihydrite (this study at 130 and 140ºC respectively, ionic strength = 0.7 and pH 8) and pure ferrihydrite (Shaw et. Al., 2005; 137ºC, ionic strength = 0.1, pH

10.7) as a function of temperature. For the data from this study symbols are experimental data points and red lines are the JMAK fits.

Figure A6.3. shows the transformation of the various starting materials (pure ferrihydrite, Mo- and V- ferrihydrite) from this study and the comparison with the literature at temperatures between 130ºC to 140ºC. The degree of hematite formation with time profile indicates that the induction time of the transformation is increasing as the temperature decreases. In addition, a higher pH induces a faster induction time and transformation of the ferrihydrite to hematite, but also implies a competitive effect of goethite formation if pH is very basic (> 11-13, see Chapter 6, Figure 6.5.B).

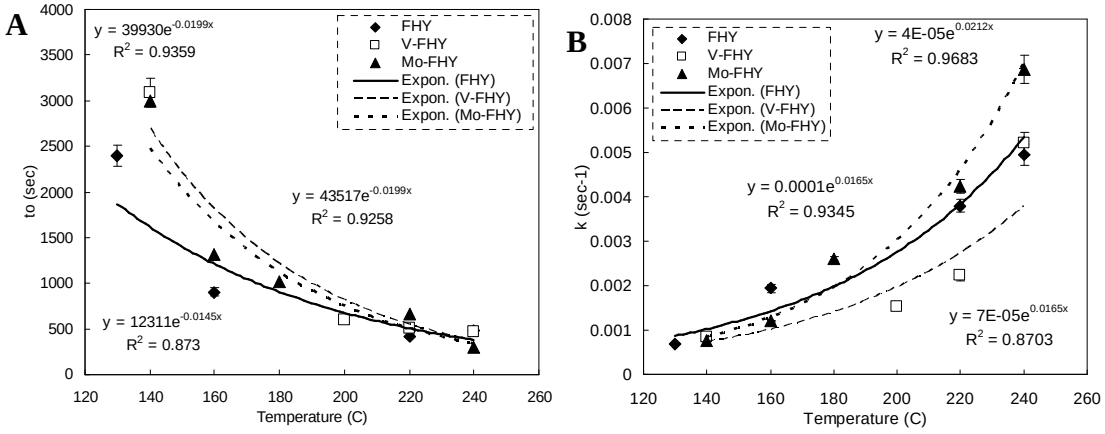

Figure A6.4. The profiles of the rate constant and induction times as a function of temperature for the three studied systems

Comparing the transformation rates (k), and induction times (t_o) for hematite crystallization in the presence and absence of molybdate and vanadate as a function of temperature illustrates and again confirms that in all systems the induction time increases with decreasing temperature (Figure A6.4.A) while the crystallization rate increases with increasing temperature (Figure A6.4. B).

Appendix C. Off-line ferrihydrite transformation at 4°C and 10°C

Ferrihydrite transformation at 4°C during 33 months

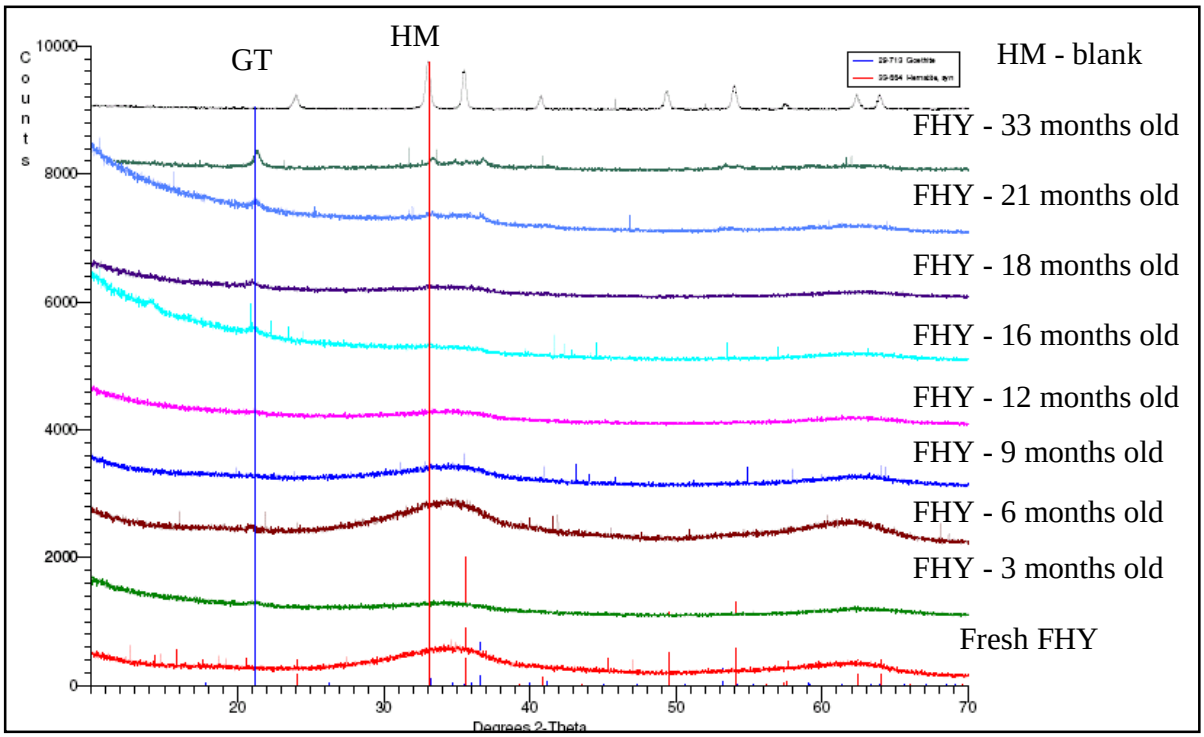

Figure A6.5. XRD patterns of the pure ferrihydrite showing its transformation at 4°C for a time frame of 33 months

Figure A6.5 shows off - line ferrihydrite slurry transformation at 4°C– recorded with XRD patterns for a time frame of 33 months. Interestingly, goethite main peak 110 (from 2-theta value - 21.24) is shown after 6-18 months suggesting that the goethite –intermediate product appears. In addition, the 110 peak of hematite (2-theta 33.180) can be seen only after 33 months – in small quantities (>10%) suggestion that the transformation is very slow. The experiment is on going and will be monitored from time to time in the future. This is the first experiment at this low temperature (mimicking hydrothermal sediments as an example): previews literature contains, yet, only one *off line* transformation record of ferrihydrite at 21°C (Schwertmann and Murad 1983).

Ferrihydrite transformation at 10°C during 33 months

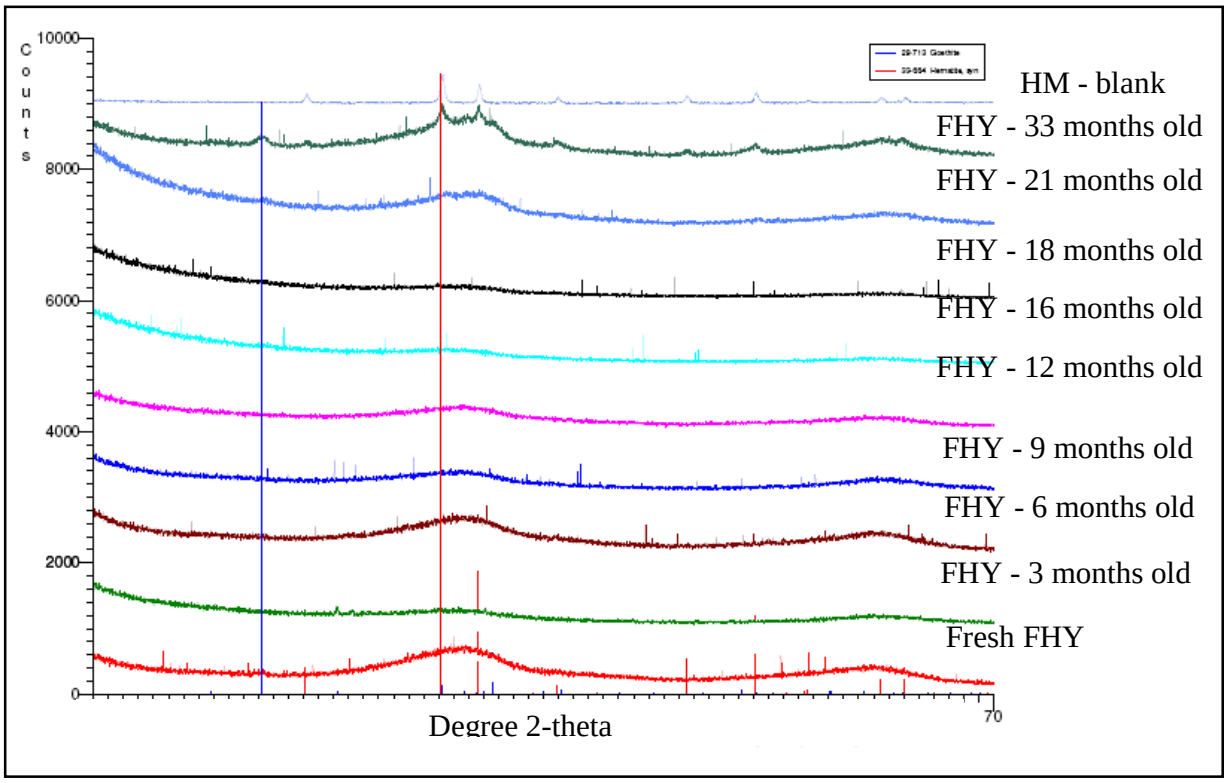

Figure A6. 6. XRD patterns of the pure ferrihydrite showing its transformation at 10°C for a time frame of 33 months

From figure A6. 6. it can be seen ferrihydrite slurry transformation at 10°C during the same time frame as at 4°C. Following the XRD patterns up to 21 months scan not much difference between the patterns could be seen. However, small goethite and hematite packs are present after 33 months. By comparing the height of the peaks from the pattern taken at 33 months at the 2 temperatures studied, the result shows that ferrihydrite transforms to hematite a bit faster at 10°C than at 4°C (slightly better defined hematite peaks can be seen .in the XRD pattern from the transformation carried out at 10°C). This finding supports the *in-situ* transformation experimental results: the transformation of ferrihydrite to hematite is temperature dependent and is faster as temperature increases. In plus, low temperature transformation results confirm again that goethite appears as an intermediary product of the transformation even at neutral pH.